Tectonic geomorphology and paleoseismology of the Lake Heron and Torlesse faults, mid-Canterbury, New Zealand

A thesis submitted in partial fulfilment of the requirements
for the degree of Master of Philosophy in the School of Earth and Environment,
University of Canterbury by

Santosh Dhakal

2022

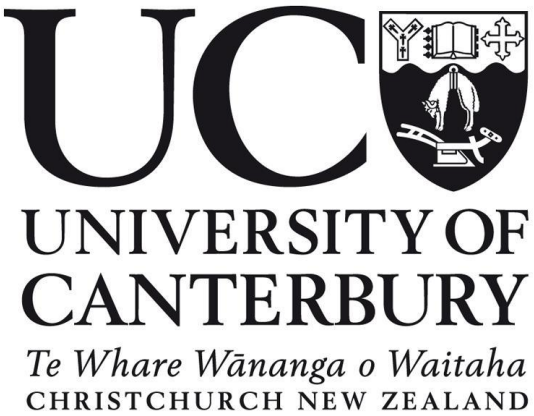

“All nature’s wilderness tells the same story: the shocks and outbursts of earthquakes, volcanoes, geysers, roaring, thundering wave and floods, the silent uprush of sap in plants, storms of every sort, each and all, are the orderly, beauty-making love beasts of nature’s heart.” **John Muir**

Acknowledgements

This study has been supported by New Zealand Scholarships and UC Mason Trust Grants. New Zealand Scholarships made it happen to enrol me in the field of geological sciences in the one of the world's renown university.

I am thankful to my supervisory team. It was a pleasure to work with Tim Stahl, my primary supervisor throughout the journey. He helped me to understand active fault science in South Island, New Zealand. He supported in the ups and downs of the journey and used his maximum effort to motivate me every single minute. Jarg Pettinga, assistant supervisor, also gave valuable comments and suggestions during meetings. I am grateful for his deep understandings on geomorphology and tectonics.

I am thankful to the technical and administrative staff, Sacha Baldwin, Matt Cockcroft, Janet Warburton, Rebekah Hunt, Chris Grimshaw, Anekant Wandres, John Southward, John Thyne, Rob Spiers, all of whom helped to run field work, lab work and office study.

My thank goes to Kate Pedley to provide me an opportunity to deal with undergrad students in the lab during one semester. I also thank office mates Rasool, Julia, Dorji, Adam, Gilles, Nick, Pedro, Sulaiman with whom I shared non-academic discussion in and out of the office.

Most importantly, I am thankful to Peter Scott who assisted me for two weeks in the field. I also thank Ethan Walsh, Milap Dhakal, Andy Howell, Jaime Delano, Colin Bloom, Sushant Aryal who helped me to carry out hard field work. Ethan Walsh also ran the multi-fault rupture model for me. I thank Andy Nicol and Russ van Dissen to guide me to perceive faulting situation of the 2016 Kaikōura Earthquake and other events in the trenches. I thank Willy Amidon of Middlebury College, Vermont USA for helping to date OSL samples and assisting in the field with trenching. Useful discussion with above mentioned persons and other people in New Zealand made my stay and study easy.

I also thank to Clare Wilkinson and Walter Raymond for proofreading my chapters and for suggestions to make thesis adequate.

I also thank to landowners of Castle Hill Station and Brook Dale Station to allow me to access into their lands to study. I also thank Department of Conservation, New Zealand to allow me to dig trenches and collect samples from the conservation area.

I am thankful to Department of Mines and Geology, Government of Nepal for providing study leave to pursue study in New Zealand.

I cannot forget to thank my wife (Bijaya) my son (Ashraya) and my parents (Hari and Bhawani) to support me every minute to pursue degree. I am happy to be a father of my beautiful daughter (Aashvi) during this study period.

Abstract

A number of reverse and strike-slip faults are distributed throughout mid-Canterbury, South Island, New Zealand, due to oblique continental collision. There is limited knowledge on fault interaction in the region, despite historical multi-fault earthquakes involving both reverse and strike-slip faults. The surface expression and paleoseismicity of these faults can provide insights into fault interaction and seismic hazards in the region. In this thesis, I studied the Lake Heron and Torlesse faults to better understand the key differences between these two adjacent faults located within different 'tectonic domains'.

Recent activity and surface expression of the Lake Heron fault was mapped and analysed using drone survey, Structure-from-Motion (SfM) derived Digital Surface Model (DSM), aerial image, 5 m-Digital Elevation Model (DEM), luminescence dating technique, and fold modelling. The results show a direct relationship between deformation zone width and the thickness of the gravel deposits in the area. Fold modelling using fault dip, net slip and gravel thickness produces a deformation zone comparable to the field, indicating that the fault geometry is sound and corroborating the results. This result Is consistent with global studies that demonstrate deposit (or soil thickness) correlates to fault deformation zone width, and therefore is important to consider for fault displacement hazard.

A geomorphological study on the Torlesse fault was conducted using SfM-DSM, DEM and aerial images Ground Penetrating Radar (GPR) survey, trenching, and radiocarbon and luminescence dating. The results indicate that the Torlesse fault is primarily strike-slip with some dip slip component. In many places, the bedding-parallel Torlesse fault offsets post-glacial deposits, with some evidence of flexural slip faulting due to folding. Absolute dating of offset terraces using radiocarbon dating and slip on fault determined from lateral displacement calculating tool demonstrates the fault has a slip rate of around 0.5 mm/year to 1.0 mm/year.

The likelihood of multi-fault rupture in the Torlesse Range has been characterised using paleoseismic trenching, a new structural model, and evaluation of existing paleoseismic data on the Porters Pass fault. Identification of overlapping of paleoseismic events in main Torlesse fault, flexural-slip faults and the Porters Pass fault in the Torlesse Range shows the possibility of distinct or multi-fault rupture on the Torlesse fault. The structural connectivity of the faults in the Torlesse zone forming a 'flower structure' supports the potential of multi-fault rupture. Multi-fault rupture modelling carried out in the area shows a high probability of rupture in the Porters Pass fault and Esk fault which also supports the co-rupture probability of faults in the region.

This study offers a new understanding of the chronology, slip distribution, rupture characteristics and possible structural and kinematic relationship of Lake Heron fault and Torlesse fault in the South Island, New Zealand.

Table of Contents

List of Figures

List of Tables

List of Symbols and Abbreviation

BP	before present
Cal	calibration age
CE	common era
cm	centimetre
CMP	common mid-point
COP	common offset profile
DEM	digital elevation model
DSM	digital surface model
GNSS	global navigation satellite system
GPS	global positioning system
km	kilometre
LaDiCaoz	lateral displacement calculator
LGM	last glacial maximum
m	metre
MCSST	monte carlo slip statistics toolkit
MIS	marine isotope stage
pix	pixel
SfM	structure-from-motion
UAV	unmanned aerial vehicle

1 Introduction

1.1 Background

Active fault studies are vital to assess seismic hazard. Several major earthquakes after European settlement in New Zealand (c. 1850 CE) have occurred on surface rupturing faults (e.g., Beanland et al. 1989; Van Dissen et al. 1996; Elliott et al. 2012; Hamling et al. 2017). Houses, roads, tunnels, and bridges destroyed in the 2016 Mw 7.8 Kaikōura earthquake, New Zealand demonstrates that characterisation of multi-fault earthquakes and displacement on faults (Hamling et al. 2017; Langridge et al. 2018; Nicol et al. 2018) are important to reduce impacts to infrastructure and minimize the destruction caused by such events.

More than 600 active faults have been identified offshore and onshore in New Zealand (Litchfield et al. 2014; Langridge et al. 2016; Van Dissen et al. 2021); however, all faults are not well characterised, and some lack any on-fault data. Many faults offsetting geomorphic surfaces have been studied based on aerial image and limited field data (e.g., Pettinga et al. 2001; Litchfield et al. 2014). Connectivity of active faults is important to understand the multi-fault rupture potential. Thus, knowledge regarding the precise locations and orientations of faults are important using both field data and a high-resolution remote sensing data.

Different slip senses on faults have been identified in the South Island, New Zealand (Pettinga et al. 2001; Litchfield et al. 2014; Van Dissen et al. 2021). Strike-slip faults are mostly present in the northern part of South Island while reverse faults in the southern part, south of the Alpine fault. Combinations of reverse, oblique, and strike-slip faults are found in the central part of the South Island in the Canterbury region (Pettinga et al. 2001; Litchfield et al. 2014; Van Dissen et al. 2021). Characterisation of faults and the structural relationships between them helps to examine how they might interact, with some indications that faults in this region operate as a crustal-scale flower structure (Harding 1985; Sylvester 1988)

Both high slip rate faults (Norris et al. 2001; DeMets et al. 2010) and low slip rate faults (e.g., Van Dissen et al. 2011; Quigley et al. 2012; Stahl et al. 2016) contribute to seismic hazard in mid-Canterbury (Stirling et al. 2012). The Lake Heron and Torlesse faults, located in mid-Canterbury, were previously designated low slip rate faults, located in two distinct tectonic domains (Pettinga et al. 2001).

With additional field data, remote sensing data and chronological data, there is an opportunity to understand the structural relationships of the Lake Heron and Torlesse faults across domains, and

to adjacent structures, as well as determine their contribution to seismic hazard to Christchurch city and rural areas in the mid-Canterbury.

1.2 Scientific Context

In the northeast of the South Island, New Zealand, plate motion transfer between the dextral-reverse Alpine Fault and Hikurangi Subduction Zone is accommodated primarily by the Marlborough Fault System (MFS). The MFS consists of dextral strike-slip and oblique–slip faults. The MFS accommodates approximately 40 mm/year relative plate motion (Beavan et al. 2007; DeMets et al. 2010). Regional shortening rates of 2-3 mm/year are estimated in the North Canterbury domain (Nicol et al. 1994; Barnes 1996). Plate-normal shortening of the Southern Alps is accommodated by reverse faults and related folds (Pettinga et al. 2001; Litchfield et al. 2014). The Porters Pass-Amberley Fault Zone has been recognized as the developing southern boundary of MFS (Cowan 1992). Deformation related to the oblique continental collision is primarily accommodated between the Southern Alps and the Canterbury plains. Back thrusts of the Alpine fault and folding related to back thrusting are propagating eastward from the Alpine fault, and extend to beneath the Canterbury plains (Norris et al. 1990; Pettinga et al. 2001; Jongens et al. 2012). Progressive migration of deformation towards the south on the younger faults of the MFS (Estrada 2003) is also expected in Canterbury.

Based on earthquake source parameters, the South Island has been divided into different tectonic domains (Pettinga et al. 2001; Litchfield et al. 2014). Reverse/thrust faulting are the dominant slip type south of the Rakaia River, with east-northeast strike-slip and oblique faulting becoming more frequent in the mid and northern part of Canterbury. South Canterbury Zone consists of the margin of the Southern Alps double-sided wedge style of thrust deformation (Pettinga et al. 2001). The Porters Pass-Amberley Fault Zone and Torlesse fault zone consist of hybrid system of interconnected east-northeast trending strike-slip transfer faults, oblique thrusts and or reverse faults with associated fault propagated folds (Pettinga et al. 2001).

Faults with variable orientation, sense of movement, slip rates and recurrence intervals ruptured in the Kaikōura earthquake (Hamling et al. 2017; Litchfield et al. 2018; Little et al. 2018). The faults that ruptured during Kaikōura earthquake were assigned to two different tectonic domains (Pettinga et al. 2001; Litchfield et al. 2014) the contractional North Canterbury domain and the strike-slip Marlborough Fault System. Surface displacements of >0.5 m and up to c. 12 m were observed on multiple faults (Litchfield et al. 2018). Many previously unknown faults, or those not identified as being active, were also identified in Kaikōura earthquake (Hamling et al. 2017; Litchfield et al. 2018; Little et al. 2018; Nicol et al. 2018). Termination of rupture was limited by geometric complications of the fault

system (Hamling et al. 2017). This kind of deformation style can be expected in other strike-slip fault zones in the South Island.

"Flower structures" (Harding 1985; Sylvester 1988) have been identified in different parts, and at different scales, in the South Island (Pettinga et al. 1994; Carpentier et al. 2012; Barth 2013). This structural model offers one way of conceptualising how faults might interact in both the long-term and during single earthquakes. For example, the tectonic domain boundaries may simply be demarcating different parts and accommodation styles within a crustal scale flower structure (Pettinga et al., 1994). Thus, several parts of this overall structure may rupture in a single earthquakes, perhaps explaining why earthquakes in the South Island are inherently complex. (Pettinga et al. 2001). At a more local scale, knowledge is limited on the possibility of rupturing the Lake Heron and Torlesse faults together, located in two tectonic domains, 45 km apart (Pettinga et al. 2001; Litchfield et al. 2014), during future events. Additionally, knowledge is limited on whether the neighbouring Torlesse and Porters Pass faults may rupture together.

1.3 Aims

The primary aim of this thesis was to improve the knowledge of earthquake source parameters− characterisation of individual faults is important to assess regional seismic hazard. In undertaking this primary aim, several other questions regarding controls on the surface expression of faulting arose, and these are explored further in individual chapters. Table 1.1 lists the goals, research questions, and the relevant chapters.

Table 1-1. Thesis goals and questions

Thesis Goal	Research Questions	Relevant Chapter (s)
Define fault deformation zones on the Lake Heron fault and better understand structural-geomorphic relationships	What are the controls on fault deformation zone width?	Chapter 2
	What is the structure of the Lake Heron fault and can e.g. single event displacements be refined?	
Obtain ages using trenches, Quaternary geochronology and geomorphological inference	How can faulted geomorphic features and their displacements and surface age be compared?	Chapter 2, Chapter4
	Are paleoseismic slip rates consistent? How does slip rate change with boarder scale fault structure?	
Improve seismic source information on the Lake Heron and Torlesse faults	Is there variation in the slip rate along strike of the faults? How does the slip rate vary in different segments of the Torlesse fault?	Chapter 2, Chapter 3 and Chapter 4 and Chapter 5

	Are the Torlesse and Lake Heron faults capable of rupturing together due to their structural relationships?	
Document the relationship between the Torlesse fault and other faults in the region	Is it possible to link the Torlesse fault with other faults in the Canterbury region (e.g., the Porters Pass) in an earthquake?	Chapter 3, Chapter 4 and Chapter 5
	Does the structure and kinematics of the Torlesse fault and other faults in the region support the plate boundary scale "flower structure" model?	

1.4 Thesis Format

This thesis is divided into 5 chapters. Following the Introduction (Chapter 1), Chapters 2-4 each address at least two of the main research questions. Chapters 2-4 were developed to be standalone academic contributions (i.e. journal articles), and therefore each contain an introduction, background, and methods section. Thus, there is some repetition of material in these chapters.

Chapter 2 addresses research questions 1 and 2 by quantifying the deformation around the Lake Heron fault zone. Characterisation of faults and folds related to the fault is carried out using high resolution remote sensing and field data. Fault kinematics are calculated from surveying and slip rate are estimated from the inferred age scenarios.

Chapter 3 addresses research question 3 by identifying slip sense, measuring possible single event displacements, and quantifying slip rate in different offset geomorphic surfaces on the Torlesse fault.

Chapter 4 analyses the paleoseismicity of the Torlesse fault and evaluates it as a distinct seismic source (from the Porters Pass fault). I discuss the likelihood of multi-fault rupture of the Torlesse fault and Porters Pass fault and on the basis of the new structure model and modelling of paleoseismic event ages.

Finally, Chapter 5 is a synthesis and conclusion of previous chapters. A new multi-fault rupture model is run to view the relative likelihoods of multi-fault rupture in mid-Canterbury. This chapter revisits the research questions and show how they have been tackled. The main conclusions derived from findings are reiterated. Finally, possible pathways for future research in the study area are presented.

1.5 References

Barnes PM 1996. Active folding of Pleistocene unconformities on the edge of the Australian-Pacific plate boundary zone, offshore North Canterbury, New Zealand. Tectonics 15: 623-640.

Barth NC 2013. A tectono-geomorphic study of the Alpine Fault, New Zealand. Unpublished thesis, University of Otago.

Beanland S, Berryman KR, Blick GH 1989. Geological investigations of the 1987 edgecumbe earthquake, New Zealand. New Zealand Journal of Geology and Geophysics 32: 73-91.

Beavan J, Ellis S, Wallace L, Denys P 2007. Kinematic constraints from GPS on oblique convergence of the pacific and Australian plates, Central South Island, New Zealand. Geophysical Monograph Series. Pp. 75-94.

Carpentier SFA, Green AG, Langridge Ret al. 2012. Flower structures and Riedel shears at a step over zone along the Alpine Fault (New Zealand) inferred from 2-D and 3-D GPR images. Journal of Geophysical Research: Solid Earth 117.

Cowan HA 1992. Structure, seismicity and tectonics of the Porter's Pass-Amberley fault zone, North Canterbury, New Zealand.

DeMets C, Gordon RG, Argus DF 2010. Geologically current plate motions. Geophysical Journal International 181: 1-80.

Elliott JR, Nissen EK, England PCet al. 2012. Slip in the 2010-2011 Canterbury earthquakes, New Zealand. Journal of Geophysical Research: Solid Earth 117.

Estrada BE 2003. Seismic hazard associated with the Springbank Fault, North Canterbury Plans.

Hamling IJ, Hreinsdóttir S, Clark Ket al. 2017. Complex multifault rupture during the 2016 M<inf>w</inf> 7.8 Kaikōura earthquake, New Zealand. Science 356.

Harding TP 1985. Seismic characteristics and identification of negative flower structures, positive flower structures, and positive structural inversion. AAPG Bulletin 69: 582-600.

Jongens R, Barrell DJA, Campbell JK, Pettinga JR 2012. Faulting and folding beneath the Canterbury Plains identified prior to the 2010 emergence of the Greendale Fault. New Zealand Journal of Geology and Geophysics 55: 169-176.

Langridge RM, Rowland J, Villamor Pet al. 2018. Coseismic Rupture and Preliminary Slip Estimates for the Papatea Fault and Its Role in the 2016 Mw 7.8 Kaikōura, New Zealand, Earthquake. Bulletin of the Seismological Society of America 108: 1596-1622.

Langridge RM, Ries WF, Litchfield NJet al. 2016. The New Zealand Active Faults Database. New Zealand Journal of Geology and Geophysics 59: 86-96.

Litchfield NJ, Villamor P, Dissen RJVet al. 2018. Surface rupture of multiple crustal faults in the 2016 M w 7.8 Kaikōura, New Zealand, earthquake. Bulletin of the Seismological Society of America 108: 1496-1520.

Litchfield NJ, Van Dissen R, Sutherland Ret al. 2014. A model of active faulting in New Zealand. New Zealand Journal of Geology and Geophysics 57: 32-56.

Little TA, Van Dissen R, Kearse J, Norton K, Benson A, Wang N 2018. Kekerengu Fault, New Zealand: Timing and Size of Late Holocene Surface Ruptures. Bulletin of the Seismological Society of America 108: 1556-1572.

Nicol A, Alloway B, Tonkin P 1994. Rates of deformation, uplift, and landscape development associated with active folding in the Waipara area of North Canterbury, New Zealand. Tectonics 13: 1327-1344.

Nicol A, Khajavi N, Pettinga JRet al. 2018. Preliminary Geometry, Displacement, and Kinematics of Fault Ruptures in the Epicentral Region of the 2016 Mw 7.8 Kaikōura, New Zealand, Earthquake. Bulletin of the Seismological Society of America 108: 1521-1539.

Norris RJ, Cooper AF 2001. Late Quaternary slip rates and slip partitioning on the Alpine Fault, New Zealand. Journal of Structural Geology 23: 507-520.

Norris RJ, Koons PO, Cooper AF 1990. The obliquely-convergent plate boundary in the South Island of New Zealand: implications for ancient collision zones. Journal of Structural Geology 12: 715-725.

Pettinga JR, Wise DU 1994. Paleostress adjacent to the Alpine fault: Broader implications from fault analysis near Nelson, South Island, New Zealand. Journal of Geophysical Research: Solid Earth 99: 2727-2736.

Pettinga JR, Yetton MD, Van Dissen RJ, Downes G 2001. Earthquake source identification and characterisation for the Canterbury region, South Island, New Zealand.

Quigley M, Van Dissen R, Litchfield Net al. 2012. Surface rupture during the 2010 Mw 7.1 darfield(canterbury) earthquake: Implications for fault rupture dynamics and seismic-hazard analysis. Geology 40: 55-58.

Stahl T, Quigley M, Bebbington M 2016. Tectonic geomorphology of the Fox Peak and Forest Creek Faults, South Canterbury, New Zealand: slip rates, segmentation and earthquake magnitudes. New Zealand Journal of Geology and Geophysics 59: 568-591.

Stirling M, McVerry G, Gerstenberger Met al. 2012. National seismic hazard model for New Zealand: 2010 update. Bulletin of the Seismological Society of America 102: 1514-1542.

Sylvester AG 1988. Strike-slip faults. Geological Society of America Bulletin 100: 1666-1703.

Van Dissen R, Barrell D, Litchfield Net al. 2011. Surface rupture displacement on the Greendale Fault during the Mw 7.1 Darfield (Canterbury) earthquake, New Zealand, and its impact on man-madestructures.

Van Dissen R, Seebeck H, Litchfield Net al. 2021. Development of the New Zealand Community Fault Model–version 1.0. 96.

Van Dissen RJ, Berryman KR 1996. Surface rupture earthquakes over the last ∼1000 years in the Wellington region, New Zealand, and implications for ground shaking hazard. Journal of Geophysical Research: Solid Earth 101: 5999-6019.

2 Surface deformation of the Lake Heron fault, mid-Canterbury, New Zealand

Abstract

Surface expressions of continental reverse faults are not commonly characterised in detail due to their positions in steep, rapidly eroding landscapes. However, surface rupture hazard associated with reverse faults is a critical issue globally. Here, I use field mapping and a high-resolution Digital Surface Model (DSM) to present an analysis of the reverse-sense Lake Heron fault in localities where it deforms late Pleistocene-Holocene fans and terraces in mid-Canterbury, New Zealand. Results show that deformation is expressed as multiple discrete fault traces and two folds at the surface. Analysis of 54 topographic profiles across the multiple fault scarps obtained from a c. 10 cm DSM and differential Global Positioning System transects indicate that the average net slip along the Lake Heron Fault ranges from 0.3-3.5 m across individual scarps and cumulative net slips vary from 2-58 m across terraces and fan sequences. Two age scenarios of the offset geomorphic surfaces based on calibrated ages and regional glacial advanced ages of offset surfaces are utilized to estimate the slip rates on the Lake Heron fault. The best slip rate for the Lake Heron fault ranges from 1.21 mm/year to 2.76 mm/year at the 95% confidence in two scenarios. The maximum deformation zone width is around 396 m in the terraces where the Lake Heron fault has accommodated the most slip. Around 55% of the vertical deformation is associated with folding in a prominent fan deposit, while around 70% of vertical deformation is linked to folding in the terraces. A crestal graben has developed in the hanging wall due to bending moment faulting. Trishear fold models reliably reproduce surface deformation of the terrace sequence using fault geometries inferred from field data. The results show that there is an analogous relationship between the thickness of unconsolidated deposits and the width of the deformation zone in the Lake Heron area. This approach highlights the utility of using offset geomorphic markers to investigate specific properties of reverse fault surface deformation and may be applicable to evaluating surface rupture hazard. Fault avoidance zone calculated using formula shows narrow width of deformation in comparison to the wider deformation zone in the field which raises question of how fault avoidance zone is calculated for the cumulative number of events in the reverse fault systems.

2.1 Introduction

Reverse faults are found throughout continental plate boundaries around the world and therefore represent important sources of seismic and fault displacement hazard. Reverse faults can be challenging to identify because they do not always reach the surface (Lettis et al. 1997) or, if they do reach the surface, may be poorly preserved due to erosion or burial (Boyer et al. 1974; Cox et al. 2012). Deformed geomorphic features, such as folded terraces, may be more useful in identifying fault displacement hazard than fault surface expressions (i.e. scarps representing past surface ruptures) themselves. Identifying reverse faults and their deformation zones by examining offset geomorphic features has been applied in various landscapes around the world (e.g., King et al. 1981; Philip et al. 1983; Rockwell et al. 1984; Stein et al. 1984; Molnar 1994; Nicol et al. 2001; Thompson et al. 2002; Campbell et al. 2003; Gold et al. 2006; Amos 2007; Schaefer et al. 2015). Characterising reverse fault deformation expressed on landforms of different age and origin may provide opportunities to better understand controls on surface deformation patterns.

The Lake Heron fault located to the east of New Zealand's Southern Alps in the South Island's mid-Canterbury region, is an ideal place to study surface expressions of reverse faulting across multiple geomorphic markers (Fig. 2-1). The Lake Heron fault has previously been mapped as a west-dipping reverse fault (Gair 1967; Mabin 1980; Oliver et al. 1990; Pettinga et al. 1998; Pettinga et al. 2001; Cox et al. 2007; Barrell et al. 2009; Barrell et al. 2011; Litchfield et al. 2013; Litchfield et al. 2014; Langridge et al. 2016). A total vertical separation of around 20 m on late Quaternary glaciofluvial features has been estimated for the Lake Heron fault (Barrell et al. 2011; Jacobson 2015). Previous efforts to characterise the Lake Heron fault and surrounding landscape include mapping and relative age dating of terraces by Stahl (2014) and paleoseismic trenching, further mapping, surveying, and calibrated-age dating by Jacobson (2015). However, analysis of the Lake Heron fault on high-resolution topography, to better understand the distribution and modes of deformation, are lacking.

In this study, I used field and remote mapping, including a high-resolution Digital Surface Model (DSM) developed from Structure-from-Motion (SfM) photogrammetry, to characterise the fault geometry and deformation zone of the Lake Heron fault. Topographic profiles across the fault obtained from the DSM and Global Navigation Satellite System (GNSS) were used to characterize the style of deformation, which, along with fault dips, were analysed to calculate net slips. I used DSM derived net slips and two scenarios of geomorphic surface ages to calculate fault slip rates. I used fold models to better understand the control of deposit thickness on ground deformation. The results of this study show that the fault geometry and sediment thickness are important controls on the deformation width and number of faults in the late Pleistocene to Holocene terraces and fans. The

study demonstrates trishear type of folding model mostly matches in the area. This study also provides important constraints on displacement hazards of reverse faults that could be used to develop avoidance zones or setback distances elsewhere.

2.2 Geological background

2.2.1 Regional active tectonics

New Zealand straddles the Pacific-Australian plate boundary and there are numerous active faults throughout the country. Oblique convergence between the Pacific and Australian plates occurs at a rate of c. 36-48 mm/year and is accommodated across the 150 - 450 km wide boundary zone by active faults and folds (Beavan et al. 2002; DeMets et al. 2010) (Fig. 2-1).

The Alpine fault and the Marlborough fault zone (MFZ) are major fault systems in the South Island that connect two oppositely dipping subduction zones (Fig. 2-1). The Puysegur Subduction Zone dips southeast and is located in the southwest end of Fiordland. The Hikurangi Subduction Zone dips northwest is situated in the northeast of the South Island and east of the North Island. The 480 km-long Alpine fault accommodates 70-75% of the plate motion along most of the South Island (Berryman 1979; Norris et al. 2001). The remaining component of oblique continental collision is primarily accommodated by numerous faults and folds in the Canterbury and Marlborough regions. The Lake Heron fault and Maori Lakes fault discussed in this study are located within the thrust/reverse faulting tectonic domain of the central South Island (Pettinga et al. 1998; Pettinga et al. 2001).

2.2.2 Regional geology and geomorphology

The bedrock of the study area is primarily Triassic to Jurassic quartzofeldspathic greywacke sandstone of the Rakaia Terrane, Torlesse Group (Cox et al. 2007). Within the survey area, bedrock outcrops are present in a small area on the right bank of the South Branch Ashburton River (Fig. 2-2). Unconsolidated late-Pleistocene to Holocene fluvial and glacial deposits (Barrell et al. 2011) lie unconformably over the Torlesse greywacke in the survey area (Fig. 2-2). The thickness of unconsolidated sediments that cover bedrock in the Lake Heron area is not available. However, the maximum thickness of unconsolidated sediments is thought to be higher in the central part of the survey area (Fig. 2-1B), assuming that the bedrock exposed on the right bank of the South Branch Ashburton River follows the same level beneath the Quaternary deposits.

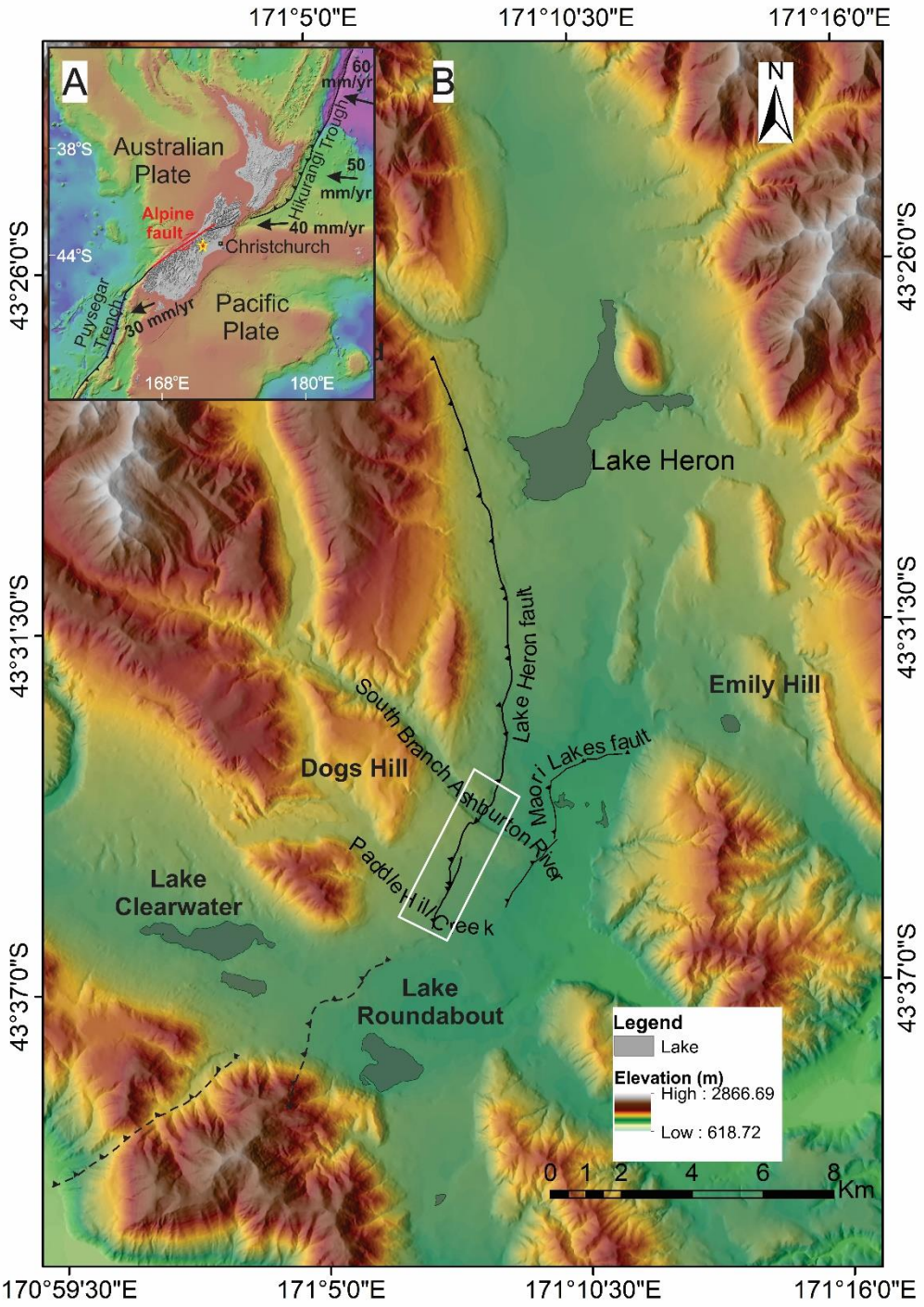

Figure 2-1. A) New Zealand outline map in the inset showing major faults. Star (yellow coloured) indicates the location of the study area. B) Location map of the Lake Heron fault shown in 8-m Digital Elevation Model (DEM). The Maori Lakes fault is present c. 1.7 km southeast of the Lake Heron fault. The study is mainly confined to the area, denoted by white box, from the Paddle Hill Creek to c. 1 km north of the South Branch Ashburton River. DEMs obtained from LINZ Data Service (https://data.linz.govt.nz/layer/51768-nz-8m-digital-elevation-model-2012/) and fault traces provided by GNS Science, available at http://data.gns.cri.nz/af/ (Langridge et al. 2016).

Landform age correlations in the Lake Heron area are heavily dependent on mapping glacial and glacio-fluvial deposits. Formation of different landforms in the study area is related to glaciation

that occurred at various phases in Pleistocene (Mabin 1980; Mabin 1984; Suggate 1990; Suggate et al. 1999; Pugh 2008; Barrell et al. 2011). Mabin (1980) identified five glacial advances in the South Island. From oldest to youngest, the events are the Pyramid advance, Dogs Hill advance, Trinity advance, Emily advance and the Lake Heron advance. In contrast, Pugh (2008) identified four Quaternary glaciations in the South Island: one of them is late Quaternary Otira glaciation (Marine Isotope Stage (MIS) 2 and 4). Barrell et al. (2011) differentiated the glacial geomorphology of the Lake Heron area into different units based on Mabin's terminology (Fig. 2-3). In the Lake Heron area, the glacial and glacio-fluvial deposits belong to MIS 2 and MIS 1 (Pugh 2008; Barrell et al. 2011) (Table 2-1).

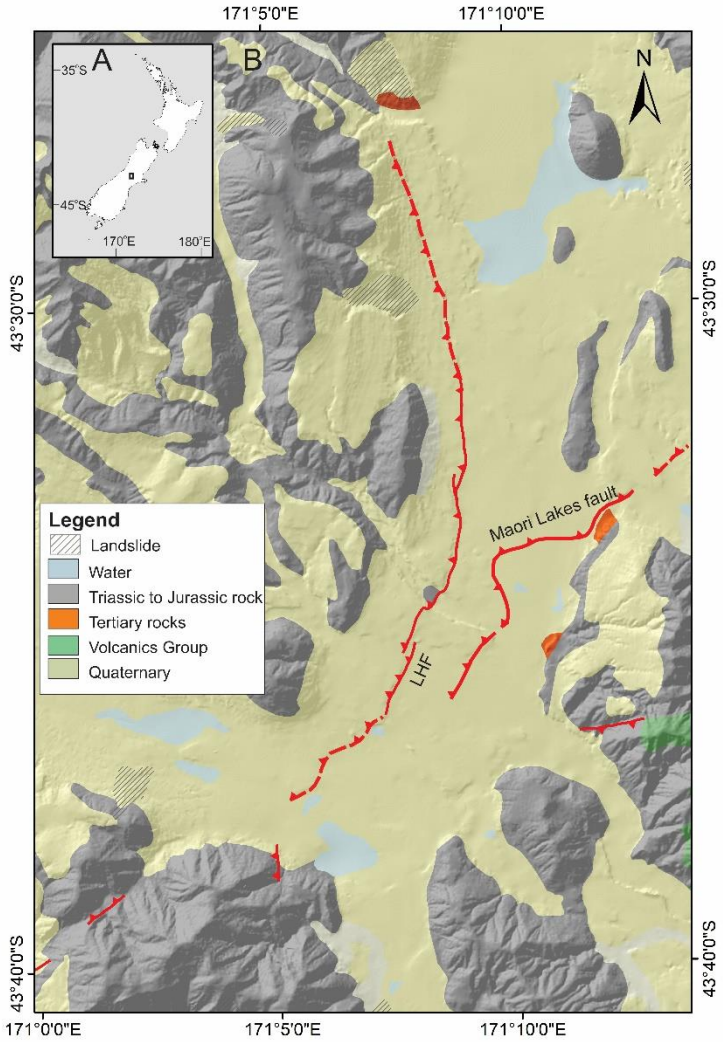

Figure 2-2.A) Location of the study area. B) Regional geological map of the study area. Most of the area consists of Triassic to Jurassic (Torlesse) rocks and Quaternary deposits. Tertiary and volcanic rocks are present at the surface in select locations. The red line with teeth displays reverse fault while the dashed red line with teeth indicates likely reverse fault. Sporadic landslides are present to the north and south of the Lake Heron fault, mostly in the hanging wall. Modified after Cox and Barrell (2007).

Glaciofluvial deposits between Paddle Hill Creek and the South Branch Ashburton River in the study area are associated with the Hakatere advance (Pugh 2008), which is associated with MIS 2.

Based on previous work, the geomorphic surfaces in the study area formed at Late Otiran, Late Glacial and Holocene time (Table 2-1).

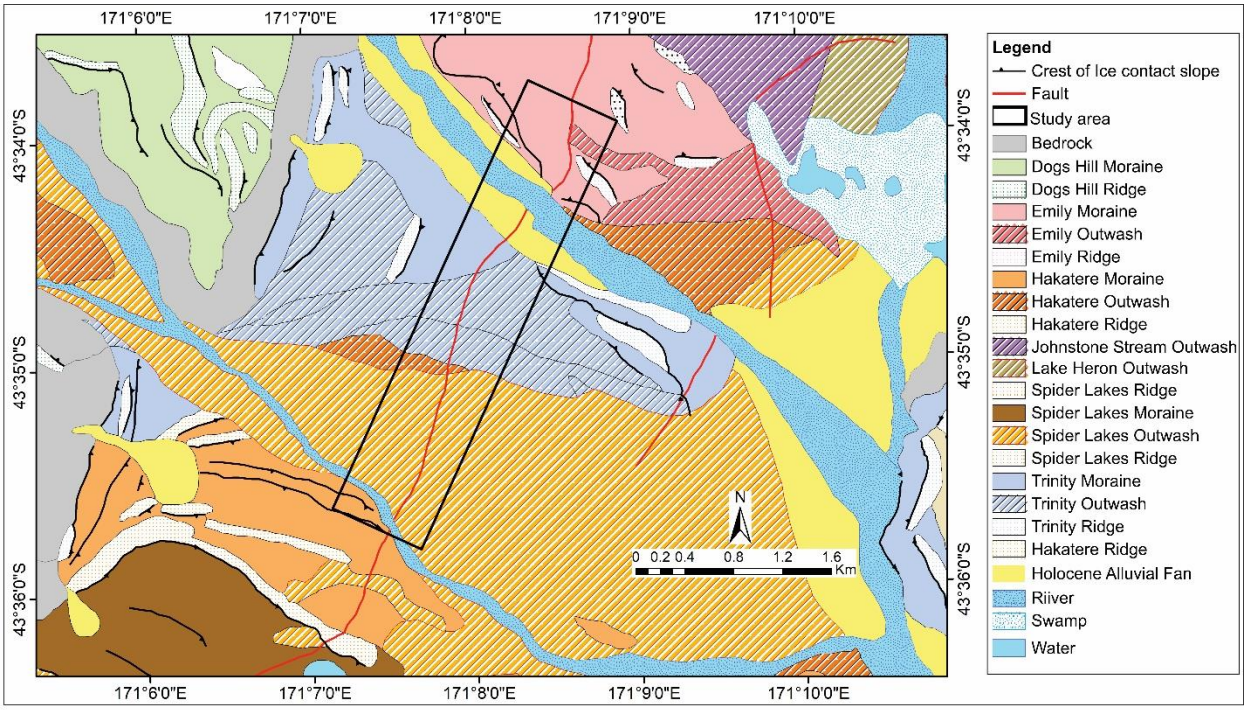

Figure 2-3. Geomorphic map of the Lake Heron area. Deposits of the Emily, Trinity, and Hakatere advances are considered to have been deposited simultaneously in adjacent valleys during Late Otiran glaciation. The Dogs Hill advance in the west is an Early Otiran deposit, while the Spider Lake Outwash is the latest Late Otira deposit. The rectangular box in grey colour shows the drone survey/study area. Modified after Barrell et al. (2011). Fault trace in the figure is slightly different from the former figure as the maps belong to different authors.

Table 2-1: Glaciation up to MIS 4 of New Zealand (Suggate, 1990; Suggate and Waight, 1999; Barrell et al., 2011). Oldest deposit is at the bottom and youngest is at the top.

MIS Stage	**Glaciation**	**Approximate Age (cal. Ka)**	**Relative age of deposit (Barrell et al., 2011)**
1		0 - 11.5	Holocene Alluvial Fan
2	Late-Glacial	11.5 – 18	Spider Lakes Lake Heron Hakatere Johnstone Stream
	Late Otiran	18 - 30	Trinity Emily
3	Mid-Otiran	30 - 50	
4	Early Otiran	~65	Dogs Hill

2.3 Methods

2.3.1 Photogrammetric DSM

I created a high-resolution DSM of the area from Paddle Hill Creek to the South Branch Ashburton River, an area containing known fault traces associated with the Lake Heron fault (Jacobson, 2015). A Phantom Pro Quadracore Unmanned Aerial Vehicle (UAV) was flown at an altitude of ~100 m to capture nearly 1,500 images of the 3.87 km^2 study area. Twelve drone flight stations across the survey area were selected to capture the whole study area. The fault zone was situated in the centre of the survey. Image overlap of 60% to 80% with fixed zoom photography resulted in a DSM with a vertical resolution of around 10 cm.

I used Agisoft Metashape Professional, version 1.5.2 to generate the DSM using the SfM technique (Westoby et al. 2012). Point clouds were generated from the UAV photos. The point cloud (1,189,435,552 points) was generated from the imagery data (1,482 images and 13 GCPs) by using 'feature points detection and matching' procedures. A DSM was then generated from the dense point cloud. An orthomosaic was also produced from the high-resolution imagery, based on the source photos of the survey area and the topography in the DSM.

2.3.2 Mapping

Mapping was carried out at a scale of 1:500 in the UAV survey area to identify different geomorphic features. Terrace treads, terrace risers, moraines, fans, paleochannels, and fault scarps were mapped to constrain fault displacements and kinematics. Topographic profiles were extracted from the DSM and GNSS/Global Positioning System (GPS) lines, which were used to characterise original and deformed geometries of the geomorphic features.

2.3.3 Topographic profiling

Topographic profiles were extracted directly from the photogrammetric DSM in most instances. Topographic profiles across the fault scarps located outside the UAV survey area were extracted using a Geo7x GNSS/ GPS system to calculate slip on the fault and to identify any surface warping. Two traces were surveyed c. 1.7 km to the east of the main fault traces near the South Branch Ashburton River using the Geo7x. An elevation profile across a fault scarp near the South Branch Ashburton River was also extracted. Likewise, one elevation profile c. 1.5 km in length was obtained along the track in the Hakatere Conservation area. Differential corrected vertical and horizontal values of the GPS were taken to get the precise locations of the surveyed points and lines. The vertical precision of the data obtained from the Geo7x was in the range of 10 to 15 cm. After differential correction of the horizontal and vertical components of the GPS, the precision of the profile locations was improved by ~5 cm.

2.3.4 Faulting, folding, and surface deformation zone widths

Surface deformation caused by faulting and fault-associated-folding was quantified by mapping and analysing topographic transects taken perpendicular to the fault strike. Parallel terrace and fan surface slopes on the hanging wall and footwall, outside the zones of deformation, were taken as baseline references for deformation. The extent of deformation is delineated by the change of local slope in comparison with these baseline slopes. Short wavelength modifications of slopes due to non-tectonic forcings (e.g., erosion and deposition) were not classified as deformation and ignored.

To understand the relationship of faulting and folding in the study area, I determined the percentage of deformation due to faulting and folding. Faulting percentage is calculated by taking the cumulative net slip (described below) across all reverse fault scarps at a particular location. Folding percentage is the remaining deformation after subtracting the vertical separation attributable to single fault scarps.

Fold modelling was used to compare deformation zone widths for different estimated gravel thicknesses. Fold modelling was performed in FaultFold software version 7.2 0 (Allmendinger 1998) using a propagation to slip ratio (1.5), trishear angle (60^o), fault dip (~20^o to ~30^o) and various net slips. In the models, terraces of different deposit thicknesses were modelled as growth strata, such that the oldest terrace was represented by the most recent and least deformed stratum – this was done to specifically test the effect that fault propagation through the greater gravel thickness in older terrace units has on deformation zone width. Deformed beds and deformation zone widths generated from three models were compared with correlative topographic profiles in the area.

2.3.5 Net slips

Topographic profiles were used to determine net slips across the fault scarps by applying linear regressions across fault scarp component and using equations of Thompson et al. (2002). Slopes of the hanging wall, footwall and scarp were obtained from the same geomorphic surface to minimize the error during calculation of the net slip. I used the semi-automated python code of the Monte Carlo Slip Statistics Toolkit (MCSST) (Wolfe et al., 2020) following the Monte Carlo method (Thompson et al., 2002) to calculate net slips (Fig. 2-4). Net slips were calculated for deformation due to the formation of each small scarp in the profiles, as well as total net slip on the inferred 'master' fault at depth. Parameters for the calculations were determined from mapping and are summarized in Table 2-2 (further discussed in the results section). A total of 54 profiles were used to calculate net slips in the Lake Heron area. Planar scarps were selected rather than concave or convex surfaces to minimize the error of net slips calculation. Normal fault scarps were not used during slip calculations, as these

were interpreted to have formed in response to shallow bending moments and do not contribute to overall fault slip at depth.

Vertical separation, the distance measured perpendicularly to projections of undeformed hanging wall surface and footwall surface (Fig. 2-4), was measured to display the vertical offset of surfaces without interpreting fault dip

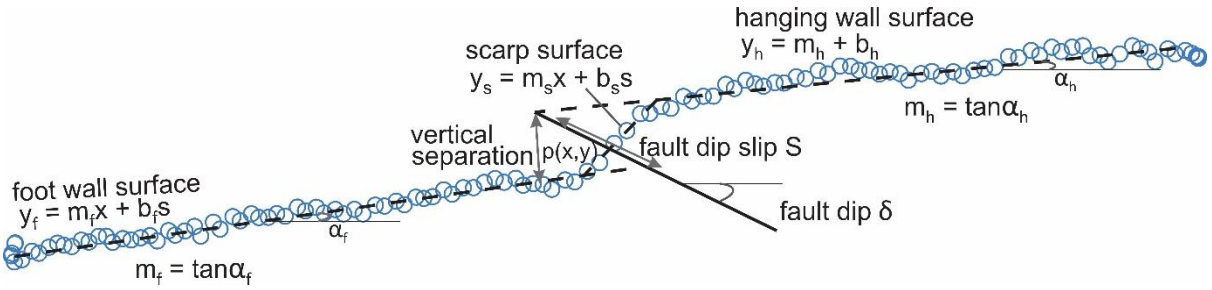

Figure 2-4. Calculation of net slip using the Monte Carlo method (Thompson et al., 2002). Linear equations represent the surfaces (hanging wall, scarps and footwall) and the surfaces are connected by blue circles. The fault is represented by the solid black line, and positioned at the middle of the scarp p(x, y). Fault dip δ is the angle of the fault plane with respect to the horizontal, measured perpendicular to the strike in the vertical plane. Linear regressions are run using slopes of the hanging wall, footwall scarps, and fault dip. Modified after Thompson et al. (2002).

Table 2-2: Fault geometry used to calculate net slip.

Fault geometry along	**Dip Model**	**Dip Model Constraints**	**Position constraints**
Surface profile	Trapezoidal	Min1, Min2, Max1, and Max2	Min1, Min2, Max1, and Max2

2.3.6 Geochronology

2.3.6.1 Optically Stimulated Luminescence (OSL)

There is limited absolute age control for the terraces un the field area. One OSL sample was obtained from the left bank of the Paddle Hill Creek to limit the burial age of near-surface deposits in the Paddle Hill outwash surface. A sample consisting of coarse sand was collected from the left bank of the Paddle Hill Creek, 120 cm below the surface. An OSL tube of 20 cm length and 5 cm diameter was inserted in the wall by pounding to collect the sample.

The sample was processed at the Luminescence Dating Laboratory of the University of Victoria Wellington, New Zealand. The fine grain (4-11 µm) preparation technique was applied in the laboratory. Infrared simulation of fine grain feldspar (Smith et al. 1986) was run to compute blue luminescence from feldspar. The blue luminance of small aliquots of the feldspar sample were

measured. The Single Aliquot Regenerative method (SAR) (Murray et al. 2000, 2003) was used to determine the luminescence age based on gamma spectrometry measurement (Appendix C).

Age determination comprised measurement or equivalent doses and dose rate. The sample age was determined by dividing the equivalent dose value by mean dose rate:

2.3.7 Fault slip rates

The time-averaged slip rate, displacement formed in the surface over a certain period, was calculated based on the net displacement measured on the surface and the displaced surface's age. The slip rate on the Lake Heron fault at Paddle Hill outwash, T3, and T2 were calculated following the Monte Carlo method at the 95% confidence range (Thompson et al. 2002) using MCSST (Wolfe et al. 2020) (Fig. 2-4). I used the minimum and maximum age range and performed 10,000 trials to calculate the slip rate. Different ages of the surfaces based on the two scenarios were used to calculate slip rate, which gave a range of slip rate for the fault at each geomorphic surface.

2.4 Results

2.4.1 DSM and geomorphic mapping

The DSM developed from a point cloud using the UAV derived images consists of a density of 249 point/m^2. The final DSM was 3.87 km^2 with a resolution of 6.33 cm/pix (Fig. 2-5A).

Faults, folds, moraines, terraces, outwash fans, alluvial plains, bedrock and landslides were identified from mapping in the field on the hill-shaded DSM (Fig. 2-5B). Discrete faults displace terraces, outwash fans, and moraine landforms in the survey area. Landforms and deposits identified in the study area are consistent with geomorphic maps prepared by previous researchers (Mabin 1980; Oliver et al. 1990; Cox et al. 2007; Pugh 2008; Barrell et al. 2009; Barrell et al. 2011; Stahl 2014; Jacobson 2015; Stahl et al. 2016). Moraines are present in the southern, central, and northern extents of the study area. The relief between the Paddle Hill Outwash and the central moraine deposit is around 45 m (Fig. 2-6). The moraine deposits in the northern part and moraines in the southern parts of the study area are displaced by the Lake Heron fault (Fig. 2-5B), but the central moraine does not have a correlative on the downthrown side of the fault, so it is difficult to interpret its potential deformation history.

Scarp heights on the terraces range from 0.3 m to 3.5 m. Overall, the scarp is compound and consists of multiple individual scarps, including fold scarps, that contribute to the total height. The height of the compound scarp ranges from 2 to 32 m, depending primarily on age of the surface.

The central and southern moraine deposits in the survey area have been inferred as the oldest deposits in the study area (e.g., Mabin 1980; Barrell et al. 2011), and are classified as Late Otiran

deposits (MIS2; 18-30 ka), based on the weathering rate of boulders on the surface of moraine deposits (Barrell et al. 2011) (Table 2-1). Cosmogenic exposure-age dating carried out on the boulders of a terrace deposit near Lake Heron (out of the survey area), were dated at 27 to 30 ka (Rother et al. 2014), corroborating the age of the moraine deposit within reasonable uncertainty. One central moraine in the study area, the Hakatere moraine, was dated at 18.3 ka B.P (^{10}Be).

Eight fluvial terraces, succeeding the central moraine in age, were identified in the study area (Fig. 2-5). T1-T5 are Late Otiran in age (Barrell et al. 2011) and formed due to progressive cut-in-fill sequences and incision of Paddle Hill Creek to its present level in its fan. It is likely that the terraces and the Paddle Hill Outwash are related because the source of terraces 1 to 5 and the Paddle Hill Outwash is the same. Terraces 6-8 are younger in age, inferred to have formed in the Holocene (Barrell et al. 2011) by incision of the South Ashburton River. Terrace 6 (T6) is a degradational terrace that consists mainly of fluvial gravels and sand deposits. Terrace 7 (T7) spans the Lake Heron fault, and Terrace 8 (T8) continues on both sides of the Lake Heron fault as well as on both sides of the South Branch Ashburton River (Fig. 2-5B). No offsets of T8 were observed in the study area, but it is possible that faulting could have happened with minor displacement (e.g., a few cm), or the scarp may have been reworked by fluvial erosion and deposition.

The Paddle Hill Outwash fan is the youngest surface abandoned by Paddle Hill Creek and is observable in the southern extent of the study area (Fig. 2-5). The outwash surface is a glaciofluvial deposit that is currently inactive. Cosmogenic dating determined for boulders on a terrace deposit outside of our study area that may correlate with the Paddle Hill Outwash fan dates from 15-21 ka (Rother et al. 2014). Jacobson (2015) estimated the Paddle Hill Outwash surface at around 10.15 ±2.95 ka using calibrated Schmidt hammer exposure age dating (Stahl et al., 2013). Thus, some uncertainty exists in the age of the outwash surface. Barrell et al. (2011) has estimated the age range of the Paddle Hill Outwash from 11.5 to18 ka based on field inspection, photo interpretation, regional geological mapping and correlation to other units (Imbrie 1984; Martinson et al. 1987; Suggate et al. 2005).

Torlesse greywacke sandstone bedrock is present on the surface on the right bank of the South Branch Ashburton River (Fig. 2-7). The outcrop consists of greywacke overlain by river gravel deposits 3 m thick. No displacement in the bedrock outcrop is observable despite the proximity of the outcrop to the fault. In this area, the fault plane is not prominent; however, Stahl (2014) and Jacobson (2015) measured fault planes and striations in the bedrock. Except for this one location, bedrock is not observed in the study area.

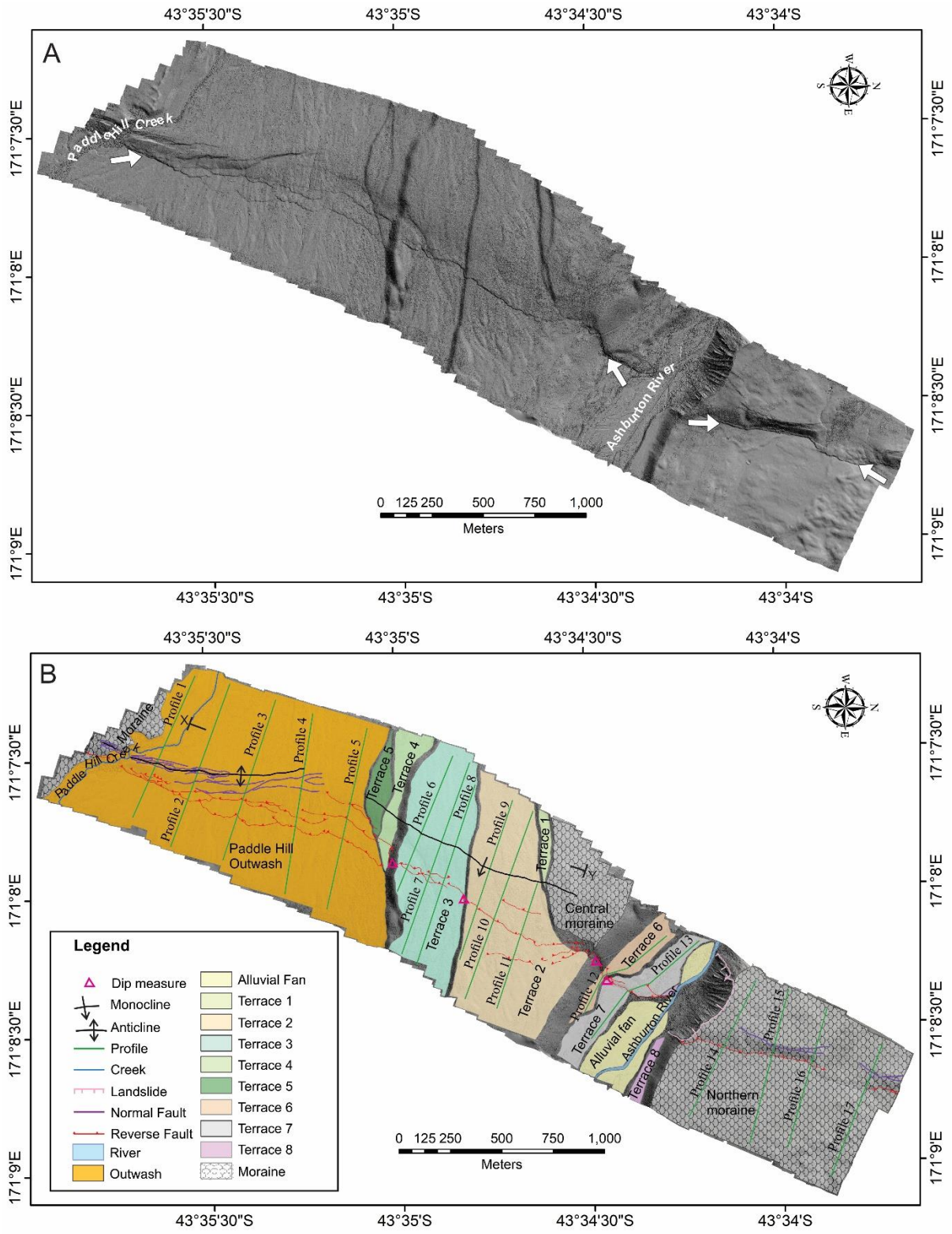

Figure 2-5. A) Hill shaded DSM of the Lake Heron area extending from Paddle Hill Creek in the southeast to 1 km northeast of the South Branch Ashburton River. White arrows represent fault scarps. The Lake Heron fault passes through the centre of the DSM, offsetting the surfaces. B) Geomorphic map of the Lake Heron fault area showing eight terrace levels (from oldest to youngest, Terrace 1 to Terrace 8), moraines, the Paddle Hill Outwash, alluvial fan (plain), faults and folds. Normal faults are represented by purple lines, while reverse faults are denoted by red lines with teeth. The axes of the anticline fold present in the south and monocline in the central parts run parallel to the Lake Heron fault. Seventeen

long profile lines perpendicular to the fault scarps are drawn. Thirteen profiles are further divided into 37 more small sub-profiles to calculate net slips. Fault dip measurement locations using indirect method are also shown by pink triangles. XY represents the section line. XY is the line of cross section presented in Figure 2-6.

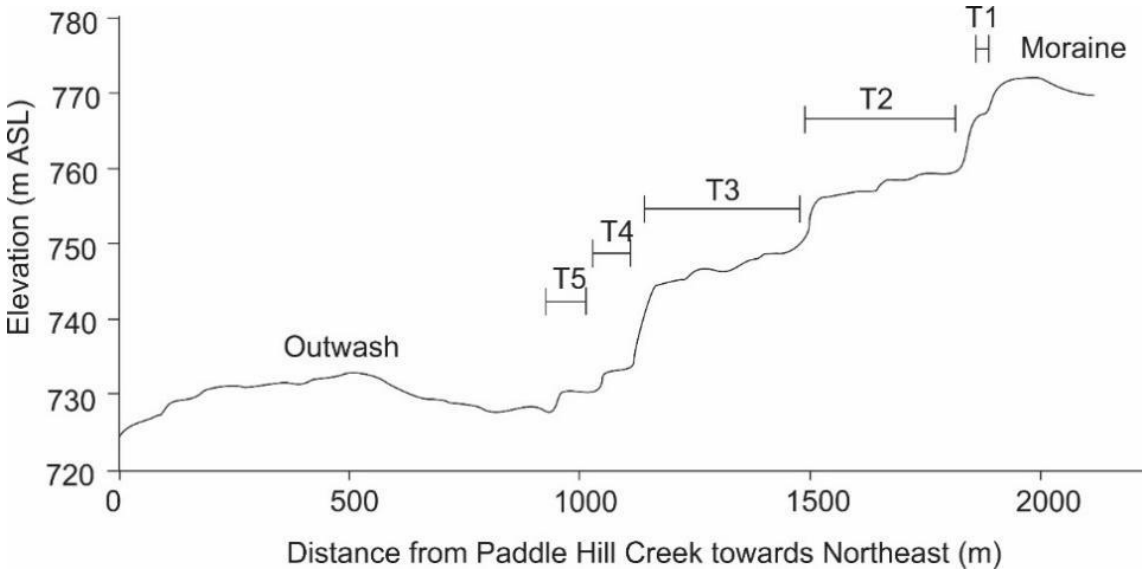

Figure 2-6. Section along XY in Fig. 2-5 showing different geomorphic surfaces at different altitudes. A height difference of around 45 m exists between the central moraine deposits (oldest deposits) and the Paddle Hill Outwash (youngest deposits).

Stratigraphy observed along the South Branch Ashburton River and Paddle Hill Creek shows that the various surfaces are mostly composed of mixed gravel and sand deposits with some loess cover. The left bank of the South Branch Ashburton River consists of steep bank exposures of poorly-bedded coarse sand and sub-rounded to sub-angular gravels, capped by a rocky B-horizon soil layer with aeolian input (Fig. 2-8A). In this area, the clasts of quartzofeldspathic sandstone range in size from 1 cm to 35 cm. The area north of the South Branch Ashburton River is out of the study area.

In the southern part of the study area, the Paddle Hill Outwash deposit consists mostly of gravel, with sands exposed on the banks of Paddle Hill Creek. The outcrop on the left bank of the Paddle Hill Creek contains unsorted gravels and coarse sands. Loess is not seen on the top of the section (Fig. 2-8B). The sands and gravels have Torlesse greywacke composition. The clast sizes typically range from less than 1 cm to 25 cm, though there was an outlier clast 50 cm in diameter on the surface of Paddle Hill Outwash in the study area, and clast sizes coarsen rapidly towards the rangefront.

OSL dating obtained from the coarse sandy layer of Paddle Hill Outwash fan, 120 cm below the surface, yielded an age of 24.3 ± 1.5 kyr (Appendix C). The age is way higher than that of Jacobson

(2015) and Barrell et al. (2011) (Table 2-3), and given the depositional environment I propose is most likely due to partial bleaching (Duller 1996). However, it is possible that the fan surface and terraces are older than previously supposed. Because exposures of the fan stratigraphy are rare, I carried out only one absolute dating in the whole study area and the age of the fan surface remains uncertain.

Figure 2-7. An outcrop of Torlesse greywacke overlain by river gravel on the right bank of the South Branch Ashburton River. Viewed towards the south.

A B

Figure 2-8. A) An outcrop on the left bank of the South Branch Ashburton River, showing sandy gravel deposit with loess input; B) Outcrop on the left bank of the Paddle Hill Creek fan shows sandy and gravelly layers, influenced by fluvial environment.

One landslide was identified near the fault zone on the erosional bank of the South Branch Ashburton River (Fig. 2-5B). It is unknown whether the landslide occurred as a single failure or multiple

failures through a combination of river and/or fault activity. The landslide material obscures the active fault scarp at the easternmost extent of the landslide.

Table 2-3: Age brackets of different geomorphic surfaces of the Lake Heron area.

Deposit	**Age brackets (Barrell et al., 2011)**
Alluvial plain	Holocene alluvial plain
T8	Holocene alluvial terrace
T7	Holocene alluvial terrace
T6	Late Otiran outwash
Paddle Hill Outwash	Late Otiran or younger outwash
T5	Late Otiran outwash
T4	Late Otiran outwash
T3	Late Otiran outwash
T2	Late Otiran outwash
T1	Late Otiran outwash

Surface slopes across the fault obtained from the profile lines were analysed to check the pattern of tilting or break points on the surfaces (Fig. 2-9). There is limited variation in slope across the different surfaces; the slopes of T2-T5 are nearly the same (e.g., T3 has a slope of 3.3^{o}) and show little variation. The Paddle Hill Outwash has the minimum slope of all surfaces at 2.2^{o}. There are no patterns of break points as on Ohau River terrace, South Island (Amos 2007)on these surfaces (Fig. 2-9).

There are not lateral displacements apparent in the terrace risers. Paleochannels in the different geomorphic surfaces in the hanging wall and foot wall were analysed to check the presence of more subtle lateral displacement on the fault or syntectonic effects on drainage pattern, terrace formation, and abandonment. Paleochannels in the different geomorphic surfaces show diverse flow directions. Flow lines in T2, T3 and the Paddle Hill Outwash, plotted in rose diagrams, show paleocurrent direction ranges from ENE to ESE directions. The active channel, Paddle Hill Creek, in the Paddle Hill Outwash flow towards the southeast, that has different flow direction from the paleochannels. Flow lines in these geomorphic surfaces are not laterally displaced by the fault showing the fault is purely dip slip (Fig. 2-10). There is no clear influence of faulting on channel orientation.

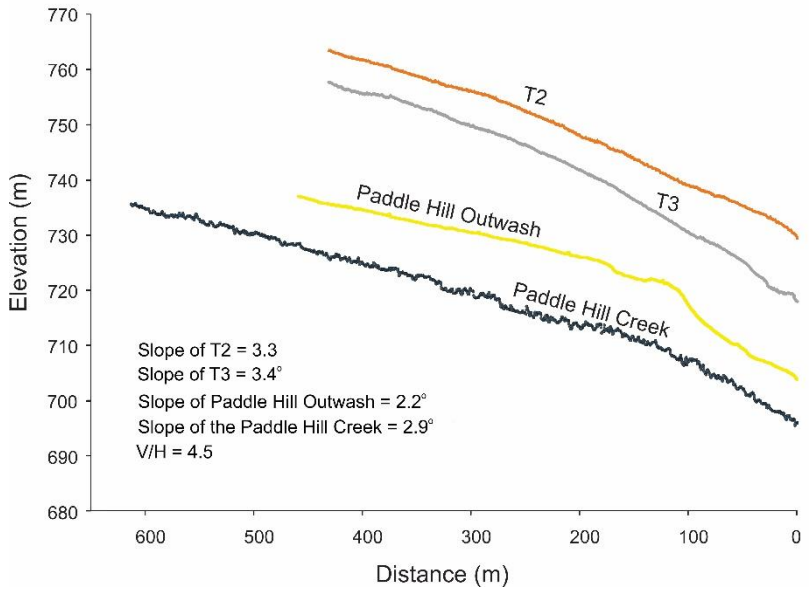

Figure 2-9. Slope of surfaces measured is on the hanging wall of the Lake Heron fault in the Lake Heron area. The profiles were drawn perpendicular to the fault zone and started from the southern fault scarp along each profile. The Paddle Hill Outwash shows minimum slope while terraces T2 has slightly lesser slope than T3. The ratio of vertical to horizontal scale of the plot is 4.5

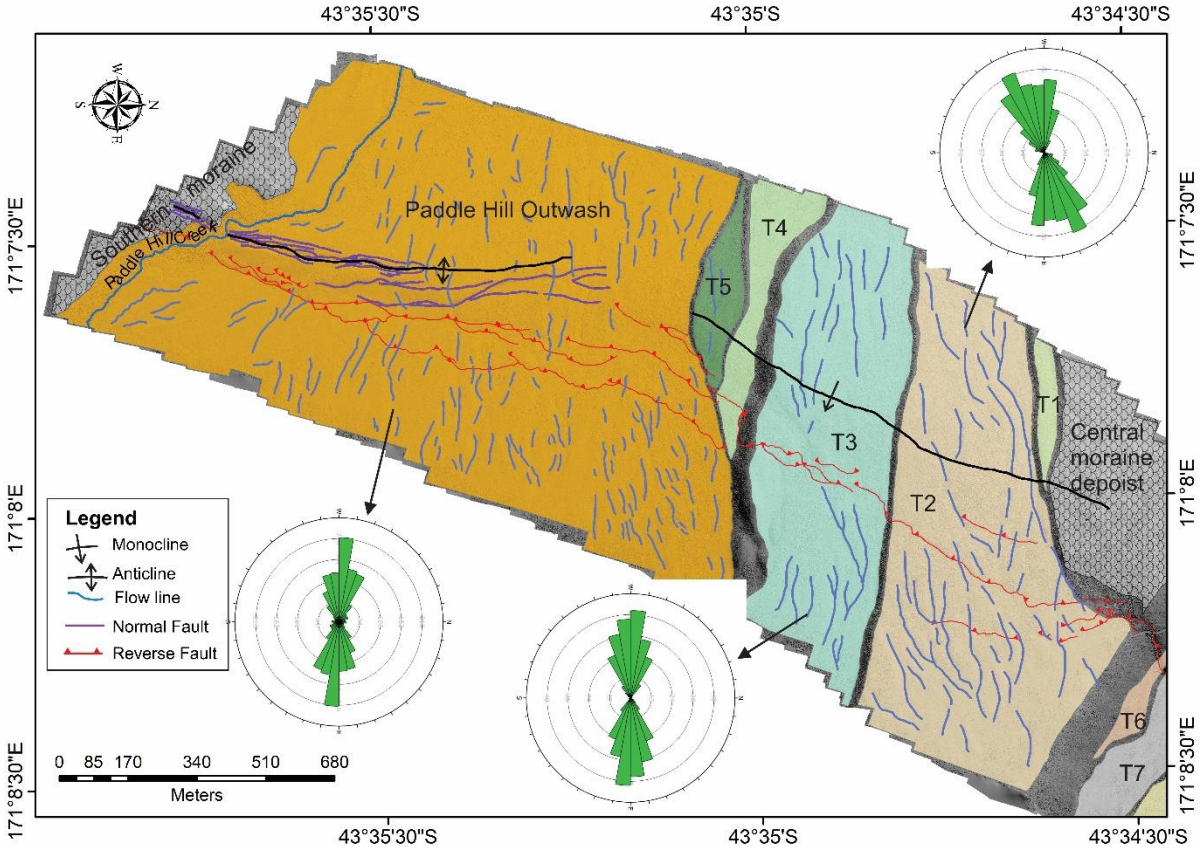

Figure 2-10. Rose diagrams prepared using flow lines from different geomorphic surfaces to determine paleocurrent directions. Paleo flow direction changes from ENE in T2 to ESE in the Paddle Hill Outwash.

The current flow direction of the Paddle Hill Creek is towards the southeast. Pure dip slip fault is revealed by the absence of lateral offset of paleochannels.

The sense of slip along the Lake Heron fault can be further refined through evaluating displacements of a moraine ridge in the north of the DSM area. The orientation of the moraine ridge suggests it is a terminal moraine formed during a southwest-oriented glacial advance. It is not laterally displaced; hence I have confirmed that the fault is likely purely dip slip (Fig. 2-11).

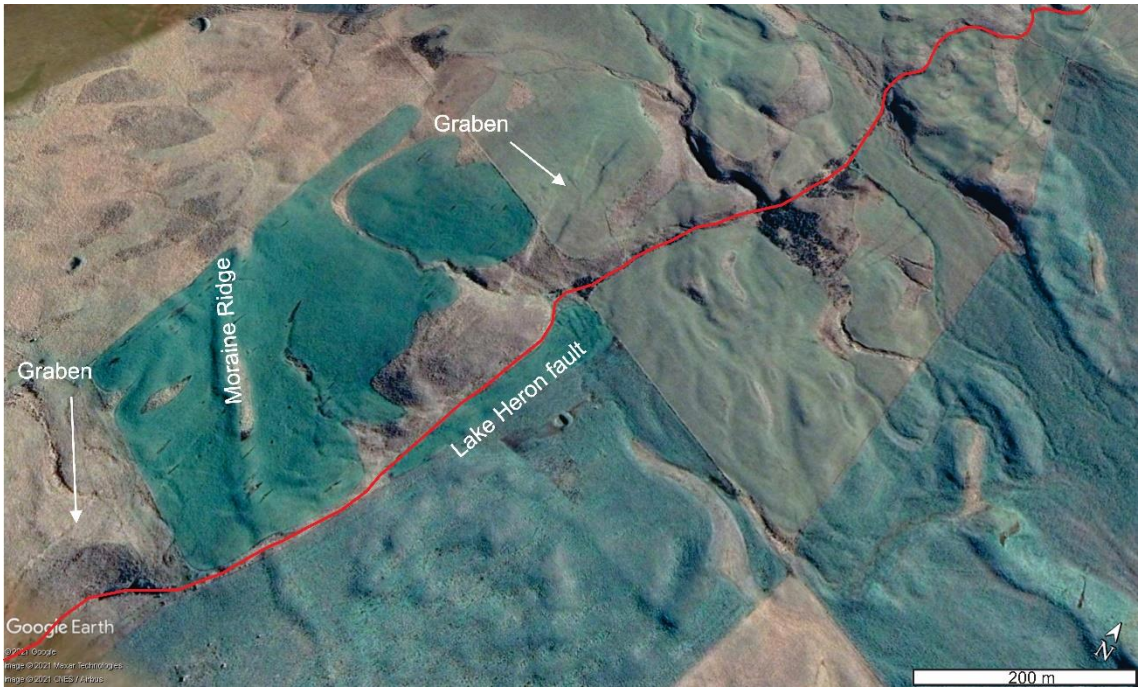

Figure 2-11. Moraine deposits are displaced by the Lake Heron fault. No lateral offset of the displaced moraine ridge is found at the southwest part of the image. Two crestal grabens are formed in the moraine deposits to the north of the South Branch Ashburton River. Grabens are in the hanging wall of the fault.

2.4.2 Fault mapping

The discrete faults in the Lake Heron area displace multiple terraces, moraines and outwash deposits. The individual, smaller-scale faults have a cumulative scarp height of around 20 m. Not all the fault scarps in the survey area are continuous, though there is one uninterrupted fault scarp. The average strike of the fault in the DSM survey area shows a direction of S25°W (Fig. 2-5B). Both normal and reverse fault scarps are present at the surface in the study area. Reverse faults, the dominant fault type in the study area, are distributed throughout. In contrast, normal faults are concentrated in the Paddle Hill Outwash, near the Paddle Hill Creek and in the complex glacial and periglacial landforms north of the South Branch Ashburton River (Fig. 2-5B). In these areas, synthetic and antithetic normal faults form crestal grabens (Fig. 2-11 and 2-12). Synthetic normal faults, confined in a few areas, dip towards the west, whereas antithetic normal faults dip towards the east.

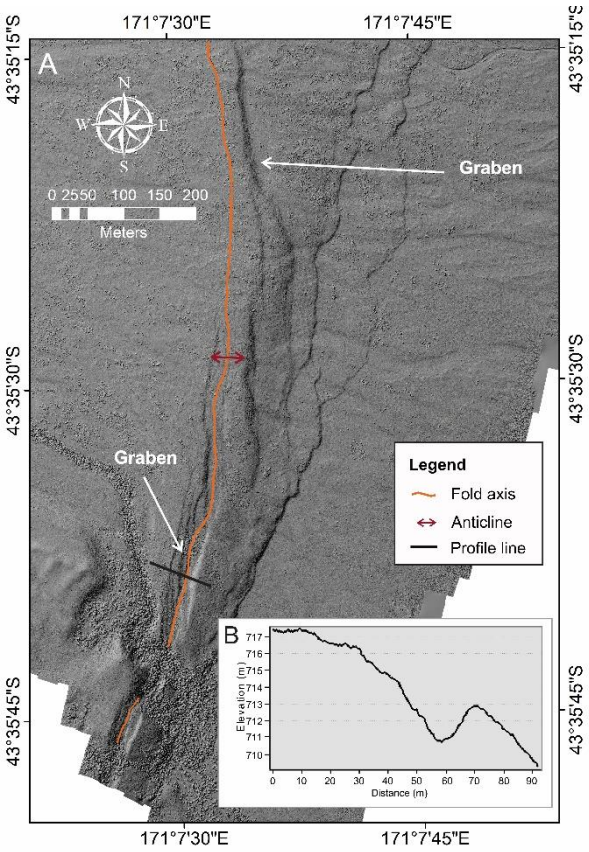

Figure 2-12. A) A graben formed in the hanging wall is incised by the Paddle Hill Creek. Another graben is present to the northeast and formed in the Paddle Hill Outwash. B) An elevation profile from the graben area shows subsidence of 2.5 m within the graben at the Paddle Hill Outwash.

Grabens identified in the area, oriented ~15° off of the strike of the fault, contain various amounts of subsidence. The most prominent graben in the southern part of the study area, with subsidence of 2.5 m, is in the Paddle Hill Outwash incised by the Paddle Hill Creek (Fig. 2-12). Another graben was identified just north of the most prominent graben with a shorter length, likely because antithetic normal faults are more prominent than synthetic normal faults in this location. Two grabens are situated to the north of the South Branch Ashburton River exhibiting subsidence of ~50 cm (Fig. 2-11).

The number of faults in the study area was measured along each profile within 200 m length of profile to show the concentration of faults. Total number of fault scarps within 200 m along the profile starting from the southernmost fault scarp towards the north is taken to include as many synthetic and antithetic faults as possible. The number of faults calculated along the existing profiles shows the greatest number of faults at the Paddle Hill outwash and lowest number of faults at T3 and T7 (Fig. 2-13).

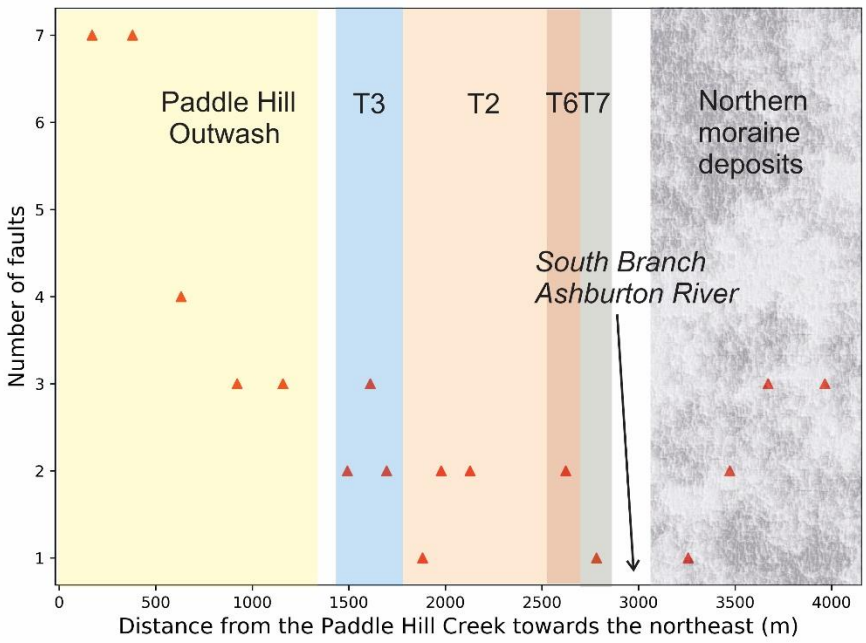

Figure 2-13. Number of faults within 200 m length along the profile in the study area. The starting point for the calculation is chosen from the southernmost fault along each profile. The largest number of faults was identified in the Paddle Hill Outwash.

Direct measurement of fault dips, aside from those previously identified in bedrock, was not possible. As the fault plane was not clearly identifiable in the field, I used the projection of traces across terrace risers to estimate the fault dip. I identified four steep terrace risers (T2/T3, T3/T4, T2/T6 and T6/T7) where it was possible to estimate dip from projection of the fault trace (Fig. 2-14). Resultant values range from 13.4° to 20° (Table 2-4).

The fault dip measured in the bedrock from the study area and surrounding region along the same fault shows a relatively high dip value (Stahl 2014; Jacobson 2015). A fault dip of 70° towards the west has been measured along the same fault in the Spider Lake Section (Jacobson, 2015), around 5 km west of the Paddle Hill Creek. In addition, Jacobson (2015) and Stahl (2014) measured an active fault plane, as well as secondary fractures at the bedrock exposure on the right bank of the South Branch Ashburton River and found a fault dip as 60°. This suggests that the fault plane refracted to lower angles (i.e. is anti-listric in the shallow subsurface) as it propagated through the Pleistocene and Holocene deposits.

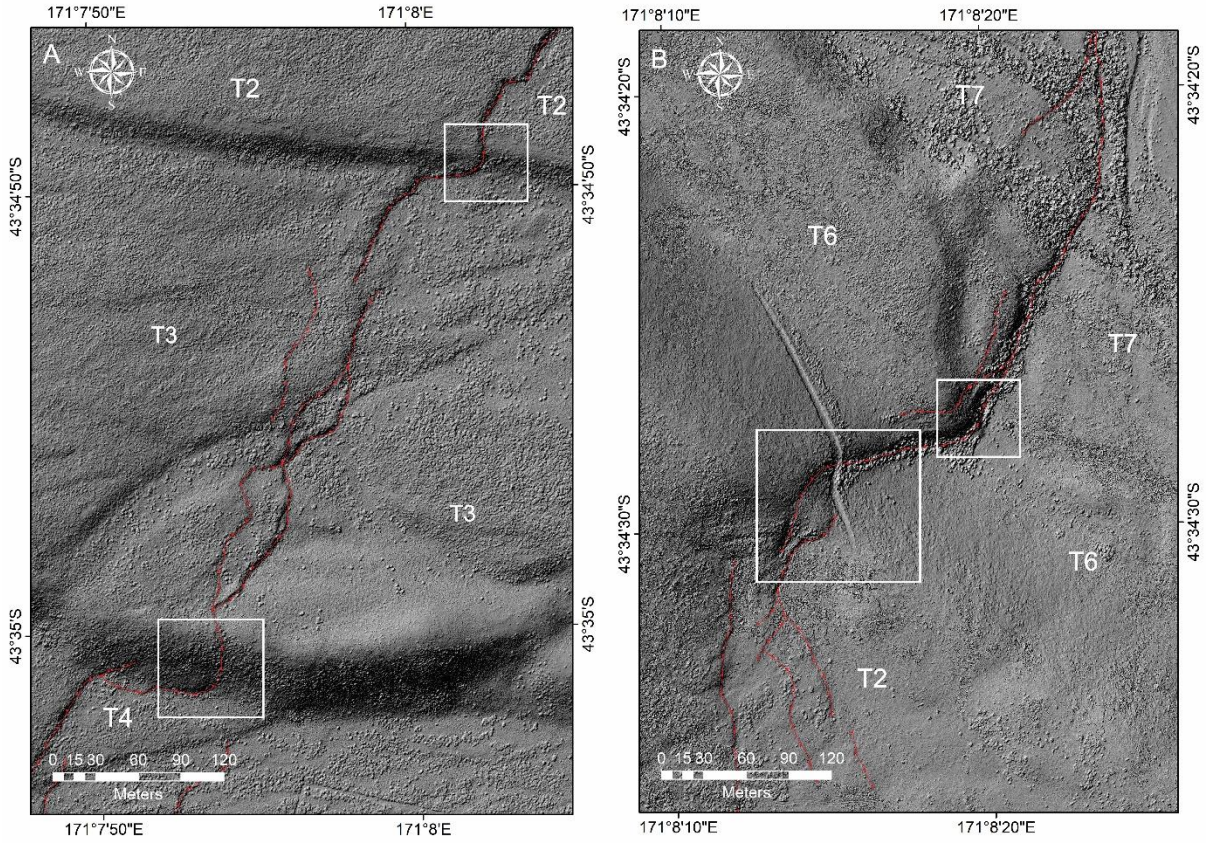

Figure 2-14. A) Location of terrace risers T3/T4 and T2/T3 and B) T2/T6 and T6/T7 indicated by the white rectangular boxes. The red lines indicate faults. From the calculation the fault dip ranges from 13.4^o to 20^o.

Table 2-4: Fault dip measured using indirect method at different locations.

Fault dip measurement location	**Fault dip**
T2/T3 riser	13.4^o
T3/T4 riser	17^o
T2/T6 riser	20^o
T6/T7 riser	15.6^o

2.4.3 Folds

DSM analysis and my mapping indicate that there are two folds in the hanging wall of the Lake Heron fault. The folds are roughly parallel to the strike of the fault zone (Fig. 2-5B). An asymmetrical fold is observed in the Paddle Hill Outwash with the fold axis running parallel to the fault zone,

following the graben in the hanging wall near the fault. A monocline identified in the central part of the study area has a steep forelimb and gentle back limb. The trace of the monocline is also parallel to the fault zone. There is a fault breakthrough (i.e., a fault scarp or series thereof) in the forelimb of the monocline (Fig. 2-5B).

2.4.4 Width of deformation zone

Deformation zone width is the amount of distortion measured across the fault scarp, consisting of both faulting and folding. Deformation zone width extents range from 65 m at T7 to around 396 m at T2. It is expected that the deformation width is greatest at the moraine deposits in the central part of the study area because it consists of the oldest (and perhaps thickest) deposit. However, an absolute deformation width cannot be calculated in that location, as the moraine deposits are not displaced across the fault. A deformation width of 167 m calculated along profile 1 passes through the graben near the Paddle Hill Creek. From observation, deformation in the higher elevation surface (e.g., T2 and T3) is greater than that of lower elevation surface (e.g., T7) in the Lake Heron area.

The deformation zone width and elevation in the study area shows a positive correlation (Fig. 2-15). The elevation is taken parallel to the strike of the fault in the hanging wall plotted against the deformation zone width. The graph shows high elevation areas are correlated with wider deformation zone than low elevation areas. Elevation is taken as a proxy for thickness of gravel deposits in the Lake Heron area. An assumption is made to estimate the thickness of gravel deposits in the area. It is assumed that the gravel deposits in the area is formed by cut-in-fill and the bedrock at the right bank of the South Branch Ashburton River follows same elevation in the study area. The gravel deposit thickness is estimated on the basis of the difference between the inferred bedrock surface elevation and surface profile elevation taken in the hanging wall parallel to the fault. The graph of deformation width zone plotted against gravel thickness replicates the former graph and shows wide deformation zone in the thick gravel deposits than in the area close to the bedrock (Fig. 2-15). ±10% error is estimated for the deformation zone width because slope line on the hanging wall is manually adjusted to make parallel to the slope line on footwall during calculation.

2.4.5 Fault displacements

Vertical separation and net slip of the fault were determined using 17 long profiles extracted from the DSM and two profiles obtained from the Maori Lake area, using Geo7x. Profiles 1 to 13 (Fig. 2-16), between the Paddle Hill Creek and South Branch Ashburton River, were divided into 37 smaller profiles to incorporate individual scarps to estimate net slip of those scarps. The southern boundary of the deformation zone is set at the southernmost fault scarp as no prominent folding was identified

in the downthrown side. A profile length of more than 700 m was obtained for each long profile line in order to include the whole deformation zone (Fig. 2-5).

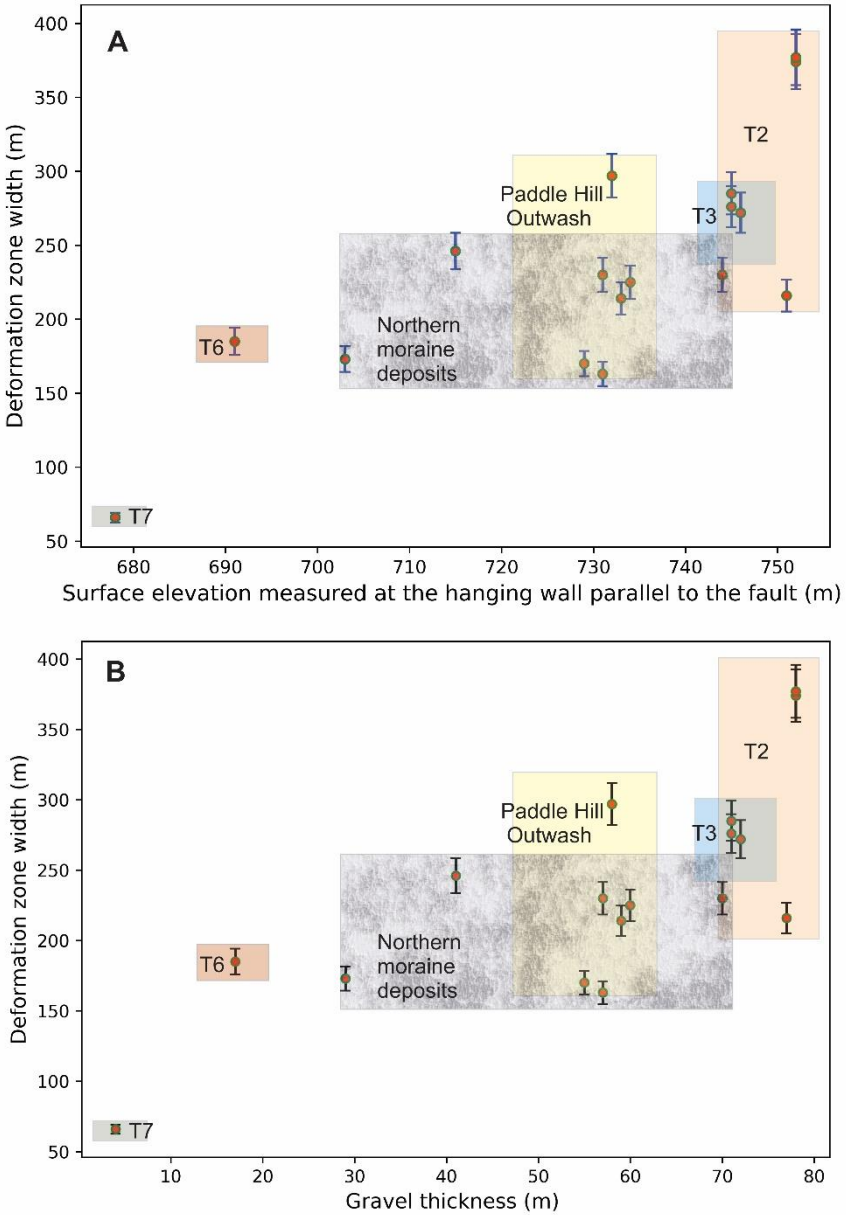

*Figure 2-15. A) Graph showing d*eformation width measured in the area along the seventeen profiles across the fault strike. The X-axis shows the elevation of surface measured at the hanging wall parallel to the fault. ±10% error is calculated for the deformation zone width. The graph shows the deformation width zone increases with the increasing elevation*. B) Plot of deformation zone width versus anticipated gravel thickness.* ±10% error is calculated for the deformation zone width. *Gravel thickness in the area is assumed on the basis of the acquired topographic profile parallel to the strike of the fault in the hanging wall assuming the deposits are cut-in-fill, and the bedrock follows same elevation in the study area. Coloured boxes show geomorphic surfaces.*

The results show that vertical separation across the fault ranged from 2 m to 32 m, with minimum and maximum values of the surfaces inferred to be the youngest and oldest, respectively.

(Fig. 2-17). Approximately 50% of the vertical deformation occurred within 30% of the deformation width. This result is similar to the finding of Jacobson (2015). Vertical deformation calculated around the fault scarp in the Paddle Hill Outwash, T6 and T7 is higher than that distributed in the hanging wall. In contrast, vertical deformation is lower around the scarp in T2 and T3 and remaining is distributed in the hanging wall. Hence, vertical separation varied at different profiles. In the Paddle Hill Outwash, the deformation zone consists of a fold and 4 to 7 fault scarps. From T2 to T5, the deformation zone consists of one monocline and contains 1 to 3 fault scarps. Vertical separation and net slip mostly follow similar trends (Fig. 2-17).

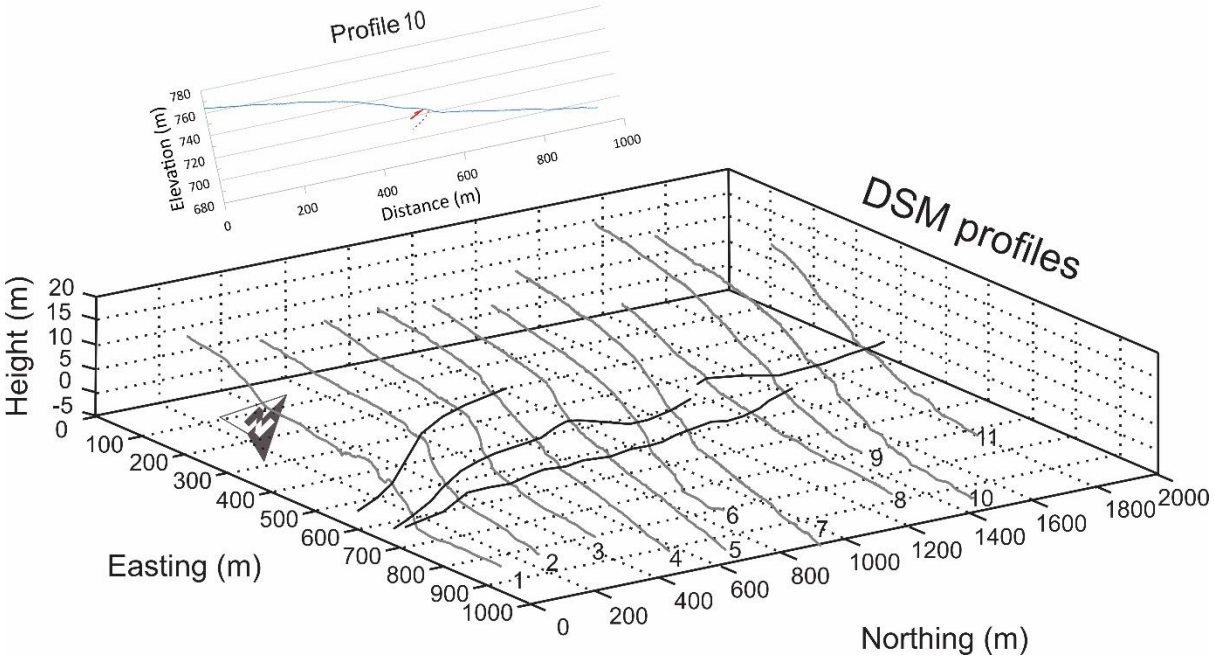

Figure 2-16. 3D perspective diagram showing profiles. Elevation profiles across the Lake Heron fault obtained from the DSM. Numbers 1 to 11 represents profile numbers. Profile1 to profile 5 are taken across the fault on the Paddle Hill Outwash, profile 6 to profile 8 on the T3 and profile 9 to profile 11 on the T2. Dark black lines are faults. Dark black lines represent fault scarps. The graph on the top of the 3D diagram shows the elevation profile of 10 obtained from T2, showing fault location. Easting and northing of the diagram are reference grids.

I propose a trapezoidal dip model with the fault dip of Min1, Min2, Max1 and Max2 to estimate errors based on the indirect fault dip measurement and inferred dip values (e.g., Jacobson 2015), and fault scarp orientation. Different fault dips were used to calculated net slip for different profiles. In the Lake Heron area, fault dip estimated at terraces and fans is shallower (13.4° to 20°) (Table 2-4) than measured fault dip at the bedrock (60° to 70°). Even the lowest fault dip estimated in the area is 13.4°, the minimum dip amount for the fault to calculate net slip is taken as 20° anticipating the anti-listric nature of the fault. The minimum fault dip is raised in terraces and fan during the net

slip calculation because denudation of the top of terrace riser and deposition at its base riser may lead to a shallower fault dip measurement at that particular location.

Trapezoidal fault position model with Min1, Min2, Max1 and Max2 were used to constrain the location of the fault 'breakout' on the scarp. Fault position was limited to the middle one-third part of the scarp with a highest probability of approximately 50% (between 44-55%) up the scarp (Table 2-5).

Table 2-5: Fault dip and position constraints used to calculate net slip.

Fault geometry along	**Dip Model**	**Dip Model Constraints**	**Position constraints**
Profile 1	Trapezoidal	35°; 40°; 50°; 55°	0.33; 0.44; 0.55; 0.66
Profile 2	Trapezoidal	30°; 35°; 45°; 50°	0.33; 0.44; 0.55; 0.66
Profile 3	Trapezoidal	30°; 35°; 45°; 50°	0.33; 0.44; 0.55; 0.66
Profile 4	Trapezoidal	25°; 30°; 40°; 45°	0.33; 0.44; 0.55; 0.66
Profile 5 to Profile 11	Trapezoidal	20°; 25°; 35°; 40°	0.33; 0.44; 0.55; 0.66
Profile 12	Trapezoidal	30°; 35°; 45°; 50°	0.33; 0.44; 0.55; 0.66
Profile 13	Trapezoidal	40°; 45°; 55 °; 60°	0.33; 0.44; 0.55; 0.66
Profile 14 to Profile 17	Trapezoidal	30°; 35°; 45°; 50°	0.33; 0.44; 0.55; 0.66

The average net slips determined from the 17 long profiles range from ~2 m at T7 to 43 m at T2 (Fig. 2-17) with associated uncertainties. The net slip calculated on the fault using long profiles varies from 0.5 m to 58 m at the 95% confidence interval (Appendix A). In addition, cumulative net slips obtained from 37 sub-profiles, using same fault dip constrains which were used in long profiles during calculation of net slips (Table 2-5), across individual scarps of the fault zone show considerably low slips. (Fig. 2-17 and 2-18). The average net slip of the individual scarp varied from 0.3 m to 3.5 m in the areas of Paddle Hill Outwash, T2 and T3. A discrepancy exists in the calculation of net slip from the cumulative sub-profiles and from the long profile which is attributable to folding (Fig. 2-18).

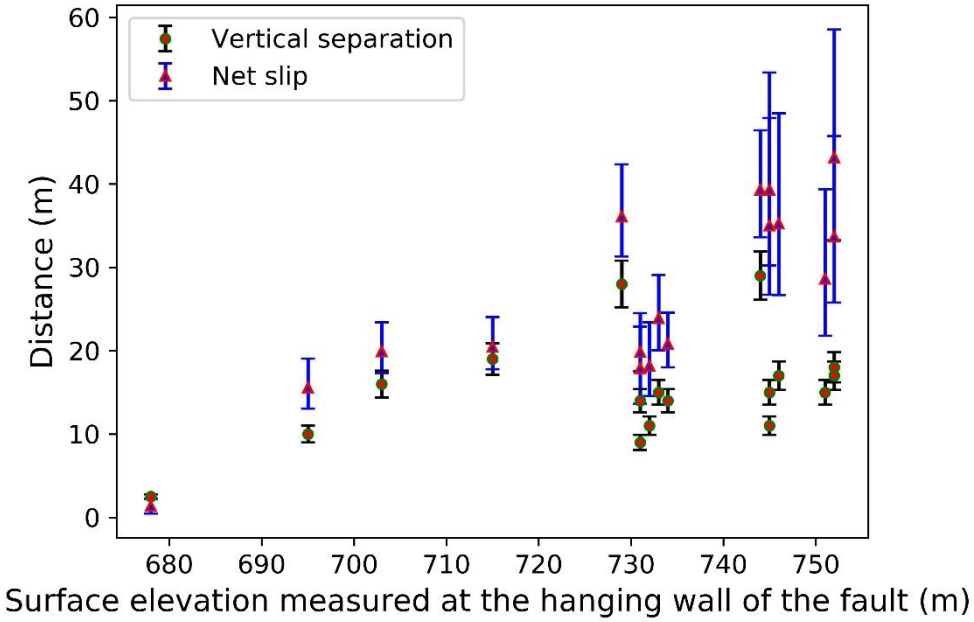

Figure 2-17. Vertical separation and net slips are also measured along the 17 profiles against the surface elevation measured from the mean sea level. Net slip is measured at the 95% confidence range while ±10% error is calculated for the vertical separation. The graph shows the higher vertical separation and net slip on the fault at higher elevation. Net slip values measured are more than vertical separation in the area. The discrepancy between two calculations is due to application of fault dip to calculate net slip but not in vertical separation. Lower angled fault produces more dip.

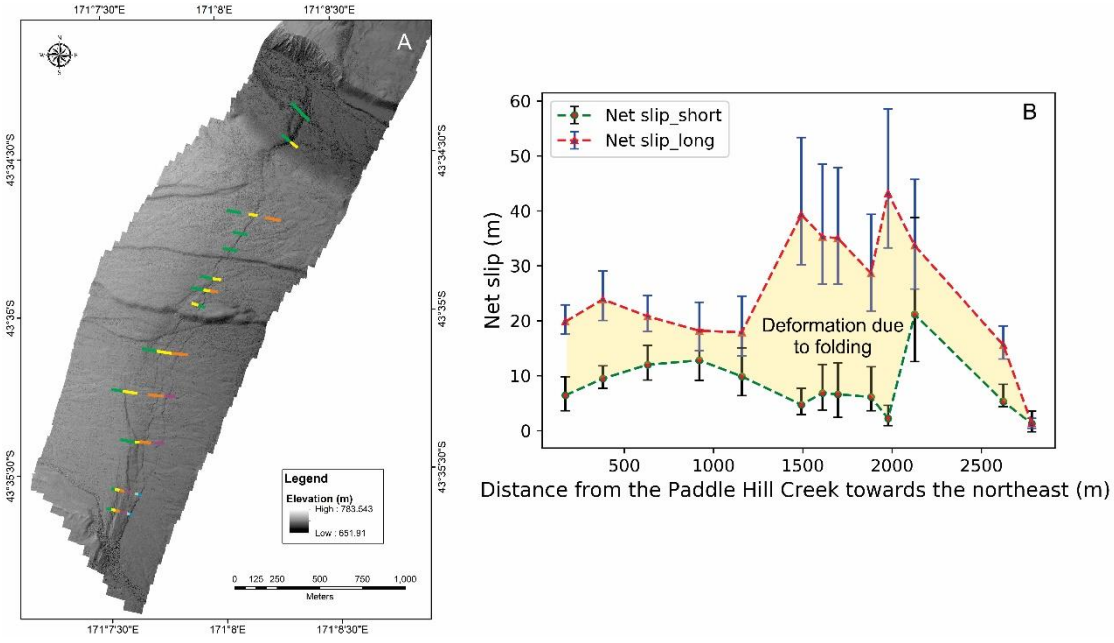

Figure 2-18. A) Map showing location of sub-profiles for net slip calculation. Each sub-profile is represented by different coloured short line. B) Comparison of net slips calculated from13 long profiles (Net slip_long) and cumulative net slips from 37 sub-profiles (Net slip_short). Discrepancy exists between two calculations.

The northeast striking Maori Lakes fault is present 1.7 km south of the Lake Heron fault and runs parallel to it (Fig. 2-1). The Maori Lakes fault passes across the South Branch Ashburton River but does not appear in the Paddle Hill Outwash plain. To the north of the South Branch Ashburton River, the Maori Lakes fault forms prominent scarps near Maori Lake (Fig. 2-19). The Maori Lakes fault displaces latest Late Otiran outwash and Late Otiran outwash deposits (Barrell et al. 2011) and the date of displaced surfaces has been assigned based on previous. studies (e.g., Suggate et al. 2005) The Maori Lakes fault has a net slip of around 9 m (when inferred a fault dip of around 35°, given there is no surface outcrop of the fault in the area). The Lake Heron fault and Maori Lakes fault both dip towards the west and It is probable that both faults merge at depth.

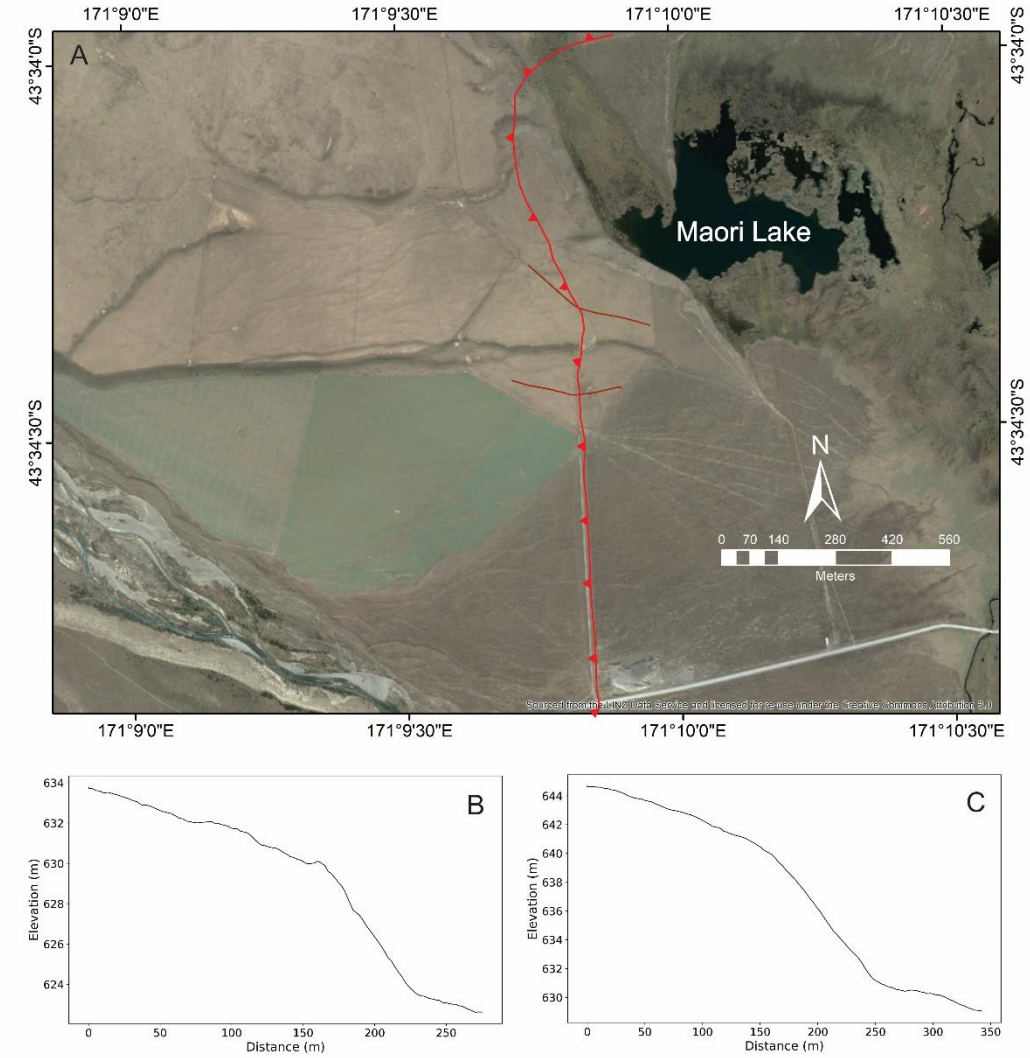

Figure 2-19. A) Location map showing two profile lines across the Maori Lakes fault near the Maori Lake. The South Branch Ashburton River in the southwest part of the map flows towards the south. B) Elevation profile (southern dark red line) across the Maori fault using the Geo7x. C) Elevation profile (northern dark red line) across the Maori fault.

2.4.6 Sub-surface structure

Detailed subsurface imaging of the Lake Heron area is lacking. However, a GPR survey conducted on the Lake Heron fault by Jacobson (2015) shows a low dipping fault splay to ~5 m depth. The extrapolation of this very shallow fault dip is not reliable enough to infer fault geometry at depth. To account for the lack of subsurface data, I projected surface data into the subsurface using the surveyed data and the geological map. The fault dip has been measured at the bedrock exposed in the survey area and ranges from 60^{o} to 70^{o} (Jacobson 2015), which differs from the measured fault dip of 13.4^{o} to 20^{o} at terrace risers on the gravel deposits. This discrepancy of fault dip in the bedrock and terrace riser is likely caused by the propagation of fault traces at low angles near the surface. Measurement of high-angle faults in the bedrock in surrounding areas (Stahl 2014; Jacobson 2015) is steeper than calculated in the gravel deposits. Thus, it appears that the fault may have an anti-listric geometry with the fault shallowing significantly as it nears the surface (Fig. 2-20), as has been proposed for other reverse faults and folds in New Zealand (Bull 2008).

2.4.7 Slip rate

The slip rate calculation on the Paddle Hill Outwash, T3 and T2 was carried out using ranges of net slips and two scenarios of ages of the displaced surfaces (Table 2-6). I used age constraints of the Paddle Hill outwash, T3 and T2 determined by Jacobson (2015) in scenario 1 and age limits of those deposits estimated by Barrell et al. (2011) in scenario 2 (Table 2-6). Jacobson (2015) has estimated ages of the Paddle Hill Outwash, T3 and T2 on the basis of relative dating method, calibrated Schmidt hammer rebound age dating (Table 2-6). In scenario 2, ages of geomorphic surfaces estimated on the basis of surface correlation of glacial advance in the south Island (Barrell et al. 2011).

Table 2-6: Minimum and maximum age adopted from Jacobson (2015) and Barrell et al. (2015) to calculate slip rates.

Geomorphic surface	**Age (years)**	
	Jacobson (2015) (Min-Max)	**Barrell et al. (2011) (Min-Max)**
Paddle Hill Outwash	9300-13100	11500-18000
T3	10200-19400	180000-30000
T2	12400-22100	180000-30000

Plot of net slip at the 95% confidence range versus constrained age (minimum to maximum) of geomorphic surfaces in two scenarios (Fig. 2-20) (Annex 3) using MCSST (Wolfe et al. 2020) shows the slip rate varies from 0.8 mm/year to 4.355 mm/year (Table 2-7) (Appendix A). The best slip rate

calculated for the Lake Heron fault ranges from 1.21 to 2.76 mm/year. Similarly, average horizontal shortening rate for the fault obtained using MCSST (Wolfe et al. 2020) ranges from 0.96 mm/year to 2.4 mm/year at the 95% confidence range.

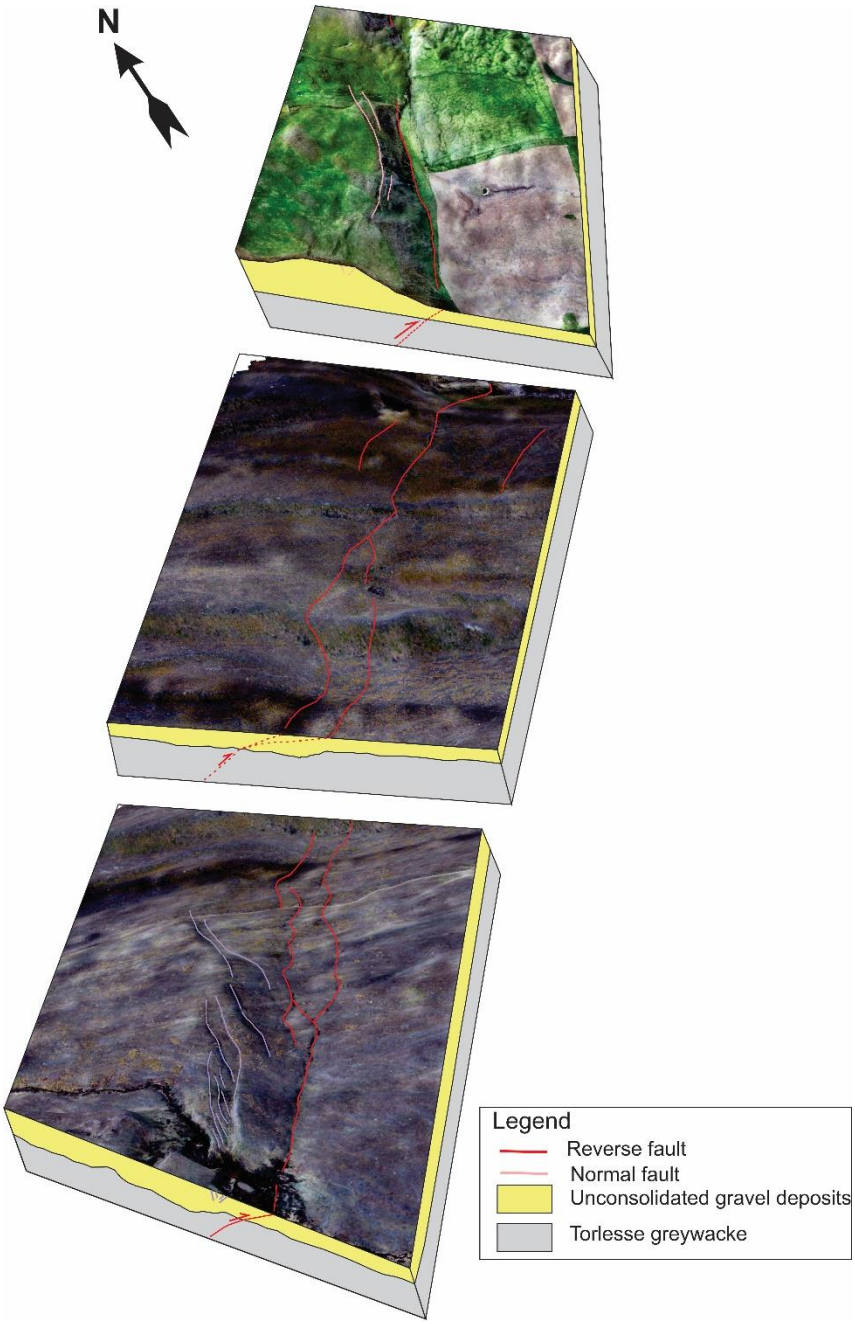

Figure 2-20. Block diagrams showing the possible subsurface structure of the Lake Hern area. UAV derived images are used for the surface of block diagram. The red arrow shows the relative block movement direction.

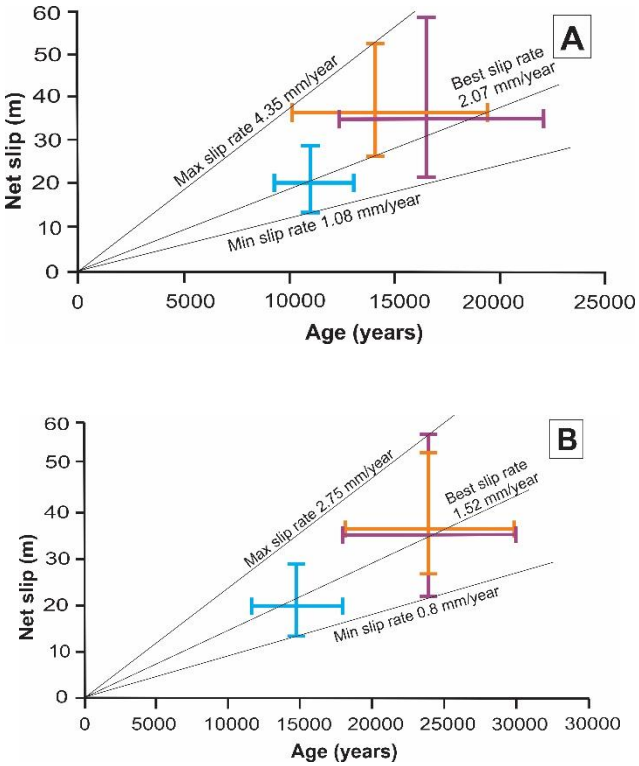

Figure 2-21. Plot of average net slip measured on the Lake Heron fault at Paddle Hill Outwash, T3 and T2 versus constrained age of displaced geomorphic surfaces. Net slip is calculated at the 95% confidence range. Minimum to maximum age range of the offset geomorphic surface is used. Blue, orange and purple lines represent the values related to the Paddle Hill outwash, T3 and T2 respectively. A) Age constraints in the graph are utilized from the values estimated by Jacobson (2015) who used calibrated Schmidt hammer rebound method to date different geomorphic surfaces. B) Age constraints estimated by Barrell et al. (2011) on the basis of geomorphic correlation is used in the plot of net slip versus age. Slope lines of min best and max slip rate are shown.

Table 2-7: Slip rate calculated for the Lake Heron fault at the 95% confidence range using net slip and two age scenarios.

Slip rate at	**Scenario 1: Using age of surfaces given by Jacobson (2015) (Min-Max)**	**Scenario 2: Using age of surfaces estimated by Barrell (2011) (Min-Max)**
Min	1.08 to 1.73 mm/year	0.80 to 1.22 mm/year
Max	2.25 to 4.35 mm/year	1.79 to 2.75 mm/year
Average	1.60 to 2.55 mm/year	1.21 to 1.84 mm/year

2.4.8 Fold modelling

Fold modelling was done to see if trishear fold replicate the style of deformation in the reverse fault system given the assumed thickness and fault geometries (Table 2-8). Deposit thickness is estimated assuming the deposits formed by cut-in-fill process cover the bedrock and that bedrock on

the right bank of South Branch Ashburton River deposits follows the same elevation. A series of strath terraces having a similar thickness of unconsolidated gravel deposits in the area is discarded as the bedrock outcrops on the bank of the South Branch Ashburton River is not exposed in the T2/T6, T2/T3 and T4/T5 risers. The thickness of gravels (depth to the bedrock) in the Paddle Hill Outwash, T3 and T2 areas area estimated ~58 m, 71 m and 78 m based on the assumption of cut-in-fill terraces.

Fold modelling was carried out using FaultFold version 7.2 software to reproduce monocline surfaces. Forward modelling was done assuming different thickness of gravel deposits in three geomorphic surfaces, Paddle Hill Outwash, T3 and T2. It is hard to model folding of cut-in-fill terraces that decrease in age and deposit thickness with elevation. Thus, modelling was done taking successive deposition of gravel deposits. Parameters like trishear angle (60^o) and propagation to slip ratio (P/S ratio, 1.5) are fixed because these values are widely used in modelling of fault-propagated-folds. Clockwise rotation of the model ~3^o was done to ensure that the model fit with the slope of the geomorphic surfaces. Different net slips obtained from the area using the Monte Carlo method (Thompson et al. 2002) (Table 2-5) were trialled to see the deformation style (Table 2-8). Slip on the single fault scarp during different events was taken to simplify the model.

Table 2-8: Table showing input parameters for the fault-fold model in the study area. These parameters resulted in similar topographic surfaces along different profiles. FaultFold version 7.2 was used for modelling.

Trishear angle	**P/S ratio**	**Net Slip (m)**	**Fault dip**	**Surface of model matches with profile no**
60	1.5	24	27^o	2
60	1.5	36	22^o	8
60	1.5	36	17^o	11

The model shows the analogous relationship between deformation zone width and thickness of unconsolidated deposits. Variations in materials and time of deposition across the fans and terraces reveals different degrees of deformation in the Lake Heron area. The study area consists mostly of coarse sandy gravel deposits with clasts of pebbles, cobbles and boulders of Torlesse derived rock materials. The timewise model shows the deformation zone width increases as depth to the bedrock increases. Deformation zone width also increases in the successive events even without consecutive deposition. Here the chronological position of the deposits is different for successive deposition maintaining assumed thickness in the model (Fig. 2-22); however, the deformation shown by the model with combined thickness represents actual deformation in the field (Fig. 2-23). Topographic

profiles P2, P8 and P11 generated on DSM mostly matches with the top surface of models a, b and c respectively (Fig. 2-23). Similar fashion of deformation formed by the reverse faulting is likely in the nearby areas consisting of unconsolidated deposits.

Using parameters identified in Table 2-5, the models mostly matched with the resultant topographic profiles (e.g., profiles 8 and 11). The modelling was also performed in profile 2 in the Paddle Hill Outwash. The resultant net slip obtained after matching with the topography was close to the net slip generated from long profiles calculated from the Monte Carlo method. Changing the propagation slip ratio only changes the position of fault tip during the events but it does not change the resultant topography. As the hanging wall and footwall of the modelled surface mostly matched with topographic surface profile but there was very small clashing in the graben area in profile 2 (Fig. 2-23a) and noticeable clashing in steep forelimb part of monocline in profile 11 (Fig. 2-23c).

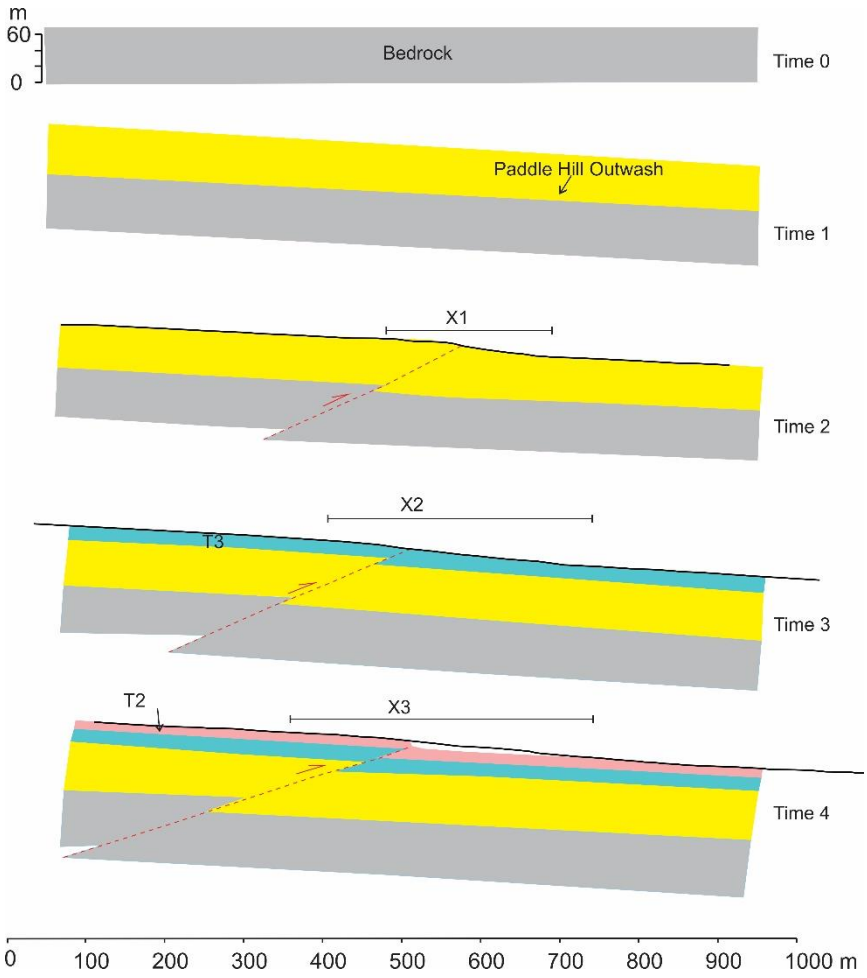

Figure 2-22. Models developed using software FaultFold version 7.2.0 shows the history of deformation in the Lake Heron area. Black lines on the top of the models represents topographic profiles: profile 2 on the Paddle Hill Outwash at time 2, profile 8 on T3 at time 3 and profile 11 on T2 at time 4. Progression of deformation is shown from the top to the bottom. Bedrock is formed in the time 0. Time 1 indicates tilting of bedrock and formation of Paddle Hill Outwash. Time 2 shows the deformation of the Paddle Hill Outwash, time 3 shows the deformation of T3 and time 4 shows the deformation of T2.

X1, X2 and X3 are deformation zone width. Thickness of T2 and T3 and stratigraphic positions in time 1 to time 4 does not match with the field as T2, T3 and Paddle Hill Outwash are cut-in- fill terraces and modelling was done on the successive deposition of gravel deposit. Assumed depth to the bedrock for the surfaces was maintained with constant propagation slip ration, trishear angle and net slip (Table 2-8) in the modelling.

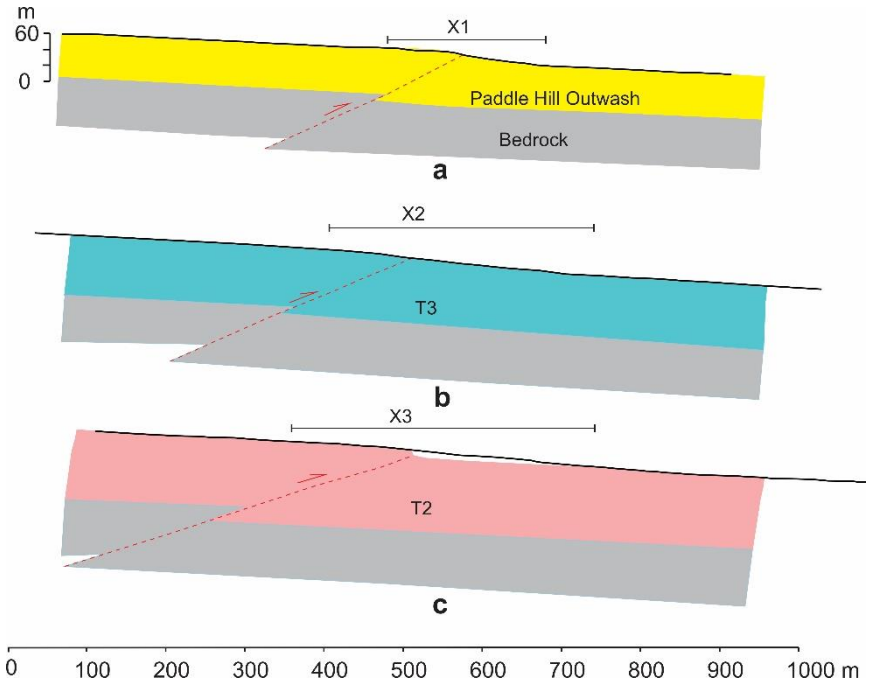

Figure 2-23. Model showing final deformation style on FaultFold software version 7.2 using gravel thickness, propagation-slip ratio, trishear angle, fault dip and net slip (Table 2-8). The figure shows the actual model of the deformation in three cut-in-fill terraces. Thickness of gravel deposits in different terraces, determined from the indirect method, is used in the model. Black lines on the top of the models represents topographic profiles: profile 2 on the Paddle Hill Outwash in figure a, profile 8 on T3 in figure b and profile 11 on T2 in figure c Model mostly matches with real topographic surfaces. X1, X2 and X3 represent deformation zone widths.

2.4.9 Summary of geomorphology and fault kinematics

A flight of terraces in the Lake Heron area is displaced by discrete normal and reverse faults trending NNE-SSW. The presence of normal faults in the compressive domain is explained by bending moment faults in a few crestal grabens. Number of faults is greatest in the Paddle Hill Outwash while there are fewer faults in the older terraces. The highest value of deformation width, 396 m in T2, is mostly in the hanging wall where there are fewer faults and is quite substantial for the region. Two asymmetrical folds and one monocline in the hanging wall run parallel to the Lake Heron fault, which shows the relationship between faulting and folding. Average net slips measured in the area using long profiles obtained from DSM range from ~2 m to 43 m and high values are obtained from the moraine deposit of the northern part, and T2 and T3 from the central part. The best slip rate for the fault varies from 1.21 mm/year to 2.76 mm/year at the 95% confidence interval based on two age

scenarios of offset surfaces. Models formed using FaultFold software matches with the deformation zone width at T3 and T2 surfaces.

2.5 Discussion

2.5.1 Surfaces ages of Lake Heron area

Previous age models have shown discrepant results, but generally agree that the top terrace (T2) is Last Glacial Maximum (LGM) and Paddle Creek Outwash is late glacial or post-glacial (Barrell et al. 2011). In this study I received a low-confidence OSL age for Paddle Hill Creek Outwash fan of 24.3±1.5 ka (Appendix C). In any of those age scenarios, both the geomorphology and the ages demonstrate that the terraces are likely to be a series glacial-sediment controlled cut-in-fill terraces. Because of this, and because of the fact that many examples of cut-in-fill terraces of this age around Canterbury, I infer that model applies to this site, which gives us more confidence in estimating gravel thicknesses.

2.5.2 Lithological control on deformation

There is a positive correlation between deformation zone width and thickness of unconsolidated deposit through which the fault must rupture (Fig. 2-15). These findings are consistent with global literature investigating the relationship between lithology, time of deposition, and deformation due to faulting. Lithology and fault geometry were identified as vital in controlling the occurrence of faults and inelastic deformation in the 2016 M_w 6.5 Central Italy earthquake (Ferrario et al. 2018). In the eastern California shear zone, splays of fewer faults, with narrow deformation, were found near the bedrock, while wide and more distributed deformation was associated with thick sediments (Milliner et al. 2015). Lithology and fault dip has been identified as the main controlling factors of deformation zone width (Bullock et al. 2014).In the thrust fault rupture caused by the 2005 M_w 7.6 Kashmir earthquake, Kaneda et al. (2008) identified the wide zone of deformation at the older terraces consisting of thick deposit and narrow zone of deformation at the younger terrace area having a thin layer of deposits. Similar patterns are found in the Lake Heron area. These kinds of features found in the Lake Heron area support the broad zone of deformation in a thick deposit. These results from different reverse fault systems elsewhere in the world (Kaneda et al. 2008; Milliner et al. 2015; Ferrario et al. 2018) generally suggest that wide deformation is commonly related to thick deposits of unconsolidated sediments.

2.5.3 Deformation width and folding percentage

The relative percentage of folding and faulting that make up the Lake Heron fault deformation zone varies in each surface (terrace, outwash, moraine and flood plain). The results from this study indicate that, generally, deformation is more distributed where folding accommodates more of the

offset (e.g., T2 and T3) (Fig. 2-24). There is a lower amount of folding present near Paddle Hill Creek, where the deformation zone is narrower. Here, faulting and folding appear to exist in an inverse relationship; a lower number of fault scarps are typically associated with a higher degree of fold-induced surface warping. In the survey area, deformation is mostly caused by folding. The folding percentage in T3 reaches up to 89%, which means that the fault scarp accounts for about 11% of the vertical deformation (Fig. 2-24). It is seen that the folding percentage and width of deformation zone are correlated with the thickness of unconsolidated deposits (Fig. 2-24). It is likely that wide deformation zones are likely in unconsolidated deposits where depth to the bedrock is higher in the South Island, New Zealand, and simple empirical equations could be developed based on this work that help guide fault setback distance, for example.

Vertical deformation is unevenly distributed in the study area. In the study area, around 50% of the vertical deformation occurs within 30% of the deformation zone width, confined to a narrow near-fault zone. This observation shows that half of the vertical deformation is distributed over a wider area. This finding is consistent with other faults in New Zealand. In areas consisting of loose and unconsolidated deposits, folding can occur alongside faulting but the accommodation of deformation by folding can vary depending on the thickness of the deposit and the geometry of the fault (Fig. 2-22 and 2-23). A similar process of folding and faulting, i.e., wide deformation in older terraces with more folding and narrow deformation with scarp height similar to slip in the younger terraces near the bedrock, is likely to take place in the terrace sequence deformed by the Klondyke fault (Barrell et al. 2009) near the Rangitata River in the mid-Canterbury region, 10 km west of the Lake Heron area.

A sand box model experiment carried out using homogeneous material shows folding of layers in the initial stage, then formation of a blind fault and ultimately permeation of the fault to the surface after applying continuous stress (Hughes et al. 2015). One model of deformation at the Lake Heron fault is one in which most of the slip occurred after formation of the entire terrace sequence, providing a relatively thin package of gravel on the Paddle Hill Creek fan through which the fault had to propagate (relatively small deformation zone width, high number of fault traces, low percentage of folding) and a relatively thick package of gravel under T2 (relatively wide deformation zone, single recently-emergent fault trace, high percentage of folding) (Fig. 2-23).

Gravel deposits in the older terraces have experienced a higher magnitude of deformation indicated by the net slip and width of the deformation zone. Deformation in the terraces is mostly absorbed by gravels deposits and voids present in the deposits, as was observed as in the 2015 Kashmir earthquake (Kaneda et al. 2008), 2016 Central Italy earthquake (Ferrario et al. 2018), 2014 Nagano earthquake (Ando et al. 2017) and 2008 Wenchuan earthquake (Wang et al. 2021). Wang et

al. (2021) found that in the 2008 Wenchuan earthquake, fault movement started at the bedrock, then scattered through unconsolidated deposits. This interpretation indicates that the fault deformation is absorbed in the near the surface deposit. A significant proportion of gravel deformation in the upthrown side of a fault is taken up by folding (Wang et al. 2021) supports our understanding of the Lake Heron area.

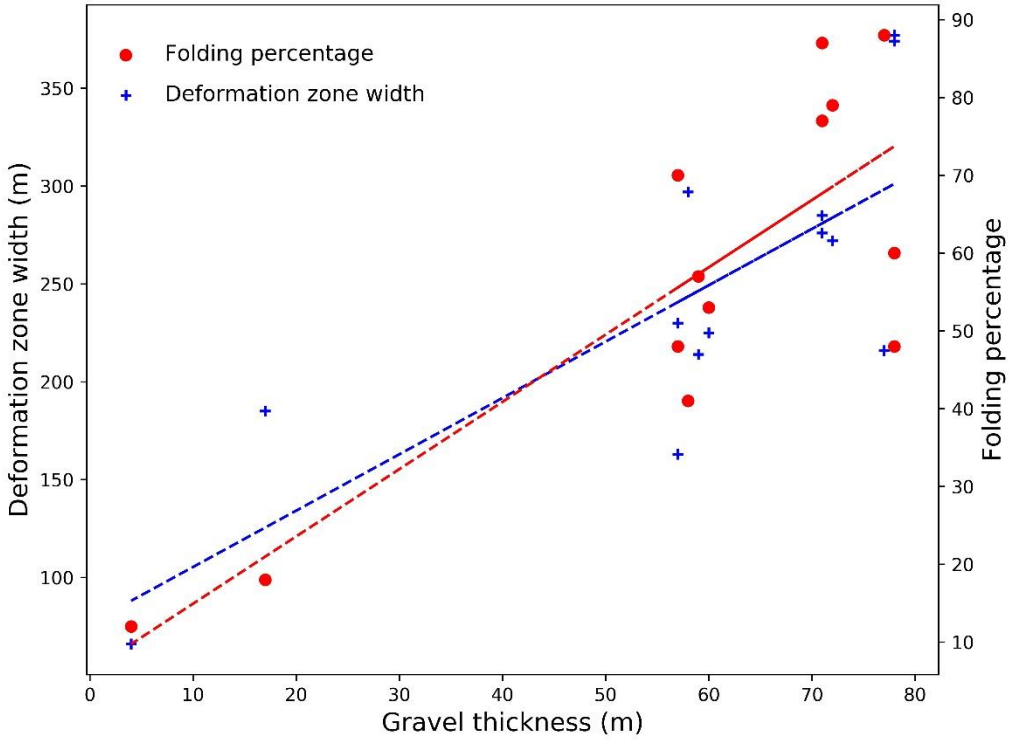

Figure 2-24. Deformation zone width and folding percentage from the Paddle Hill Outwash. T3 and T2 of the survey area show the positive correlation to gravel thickness.

2.5.4 Deformation history

Probable types of folding in the reverse/thrust fault zone have been proposed that show the relationship between faults and folds (Mitra 1990; Suppe et al. 1990; Erslev 1991; Allmendinger 1998; Champion et al. 2001; Lin et al. 2001; Gold et al. 2006; Brandes et al. 2010; Hughes et al. 2015; Johnson 2018). Brandes & Le Heron (2010) identified three main types of fault related folds: a) detachment folds, b) fault bend folds, and c) fault propagation folds. Deformation in the area consists of faulting and folding.

Probable deformation history is described based on fault scarp height, net slip, deformation zone width and inferred ages in the Lake Heron area. Terrace deposit T2 in Lake Heron area was transported by the Paddle Hill creek during the demise of LGM (Rother et al. 2014) was followed by the formation of T3, T4, T5 and the Paddle Hill outwash (Barrell et al. 2009; Barrell et al. 2011) (Fig. 2-5) as cut-in-fill terraces. Hence T2 and T3 are not expected to find below the Paddle Hill outwash. Most of the

deformation needs to occur after formation of T1 to T5 and Paddle Hill Creek because cumulative fault scarps in T2, T3 and Paddle Hill outwash are similar. If there were many rupture events before formation of Paddle Hill Outwash fan then there would be difference in scarp height in T2, T3 and Paddle Hill outwash. Though scarp height changes in single earthquake along the rupture (Kaneda et al. 2008) large changes in scarp height are not expected over the scale of the study area. T6 and T7 deposited after formation of Paddle Hill outwash have experienced less deformation, because the cumulative fault scarp height on T7 and T6 is way smaller than that of Paddle Hill outwash. Net slip obtained in T2 has experienced a higher number of earthquakes because net slip and deformation width zone calculated at T2 is higher than that of other surfaces in the area. Deformation derived from the mode also shows high deformation width zone in the thick gravel deposits (Fig. 2-22 and 2-23).

2.5.5 Slip and slip rate uncertainty

Slip and slip rate calculations are affected by various sources of epistemic and aleatory uncertainty. At a basic level, measuring slip can be complicated. Slip is confined to the fault plane at depth and is distributed through faulting and folding at the surface (Fig. 2-25). Cumulative slip summed across distributed traces at the surface is anticipated to be equal with slip at depth. However, inconsistency is observed between measurement of slips using the long profiles and the cumulative net slips using the individual sub-profiles (Fig. 2-18B). The difference is due to the omission of warped surfaces in between scarps during the calculation of cumulative slips using small profiles across the fault scarp (Fig. 2-18A). In addition, the northernmost sub-profile does not cover a large monoclinal part of the hanging wall which acts to reduce net slips. Therefore, folding of the surface accommodates the difference of net slips calculated by two different ways (Fig. 2-18) (Table 2-5).

The master fault does not outcrop in the study area hence dip is not directly measured. Estimation of dip based on indirect methods is associated with uncertainty and this ultimately affects the calculation of the slip rates of the fault. If the net slip was calculated from the low angle dip measured from the terrace risers, the median slip rate would be more than 2 mm/year in every measured location.

The calculated slip rate is affected by uncertainty related to surface ages. Schmidt hammer ages of clasts are affected by clast roundness, surface roughness and clast volume (Olsen et al. 2020) and the resulting uncertainty affects the slip rate for the fault. The ages of many adjacent terrace levels have not been differentiated and has been assigned the same age range based on inference of geomorphic surfaces (Barrell et al. 2011). This gives a wide range of similar slip rates for the fault at different terraces. Any of the scenarios of slip rate calculation could be appropriate for the fault.

The Maori Lakes fault and Lake Heron fault both dip towards the west and it is probable that the two meets at depth. The slip rate of Maori Lakes fault is expected to be around 0.5 mm/year (Barrell et al. 2009). When Maori Lakes fault's slip rate is added to that of the Lake Heron fault the slip rate is higher than 2 mm/year. Thus, this study refines the slip rate for the Lake Heron fault from previously estimated ~1 mm/year (Litchfield et al. 2013; Litchfield et al. 2014; Langridge et al. 2016).

2.5.6 Earthquake geology

Horizontal shortening rates obtained from the Lake Heron fault range from 0.64 to 3.99 mm/year with an average rate varying from 0.96 mm/year to 2.4 mm/year at the 95% confidence interval in two age scenarios. This is similar to the shortening rates of other South Canterbury reverse faults like the Ostler (Amos 2007), and Fox Peak and Forest Creek (Stahl 2014; Stahl et al. 2016) (Fig. 2-25). However, geodetic slip rate in those areas (2.5-7 mm/year) is around 2-3 times greater than the geological slip rate with as strike-slip component (Wallace et al. 2007) showing active folds or blind faults in the region accommodate remaining slip. The higher slip rate obtained from this study diminishes the gap between geological slip rate and geodetic slip rate across the fault in the region (Wallace et al. 2007).

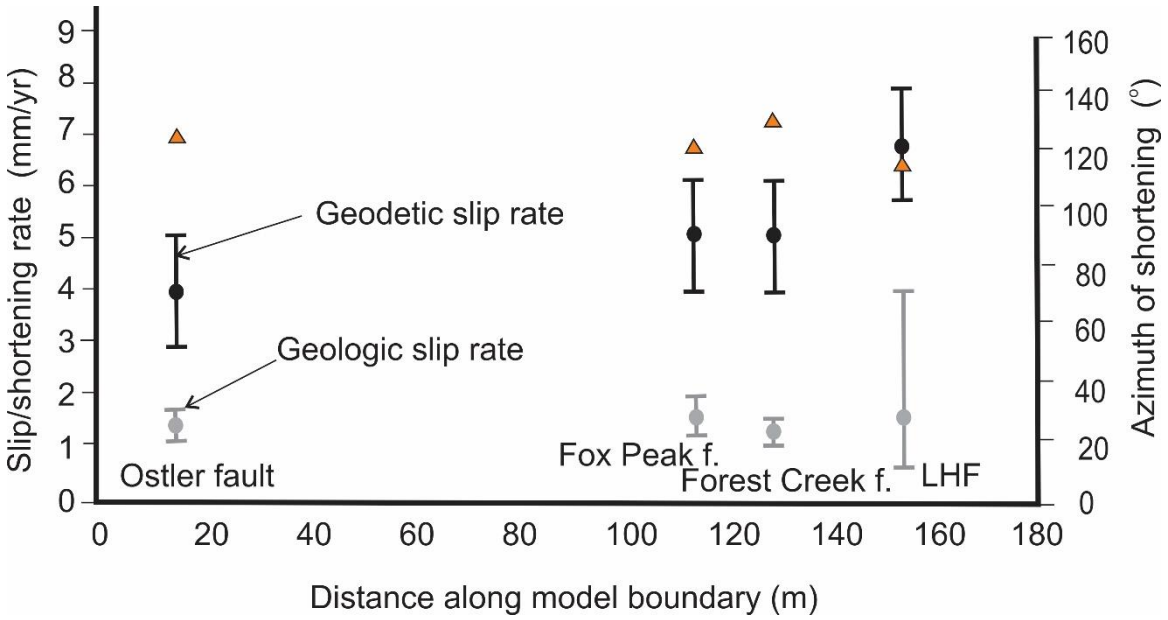

Figure 2-25. Discrepancy between shortening rate of the Ostler (Amos, 2007), Fox Peak (Stahl, 2014), Forest Creek (Stahl 2014) and Lake Heron fault, with geodetic slip rate (Wallace et al., 2007). Triangle in the graph indicates azimuth of regional shortening. measured right angle to the reverse fault. f represents a fault.

The number of events causing surface deformation in the area is important to understand the recurrence interval of such events. It is hard to estimate the exact number of events causing surface

deformation, given a lack of constraints on subsurface fault properties. Paleoseismic studies of the area were not possible, hence single event displacement is used as a proxy for estimating the number of past rupture events. Considering a scarp height of ~2 m to be indicative of at least one event, surfaces with cumulative scarp heights of 20 m measured on the Lake Heron fault could have experienced 8-10 events (e.g., T2). The cumulative scarp height of 12 m measured on the moraine ridge north of the South Branch Ashburton River might have experienced around 6-7 events.

2.5.7 Lake Heron fault deformation zone compared to established setback and avoidance measures for fault displacement hazard

Fault setback or fault avoidance zones, generally determined for fault displacement hazard, directly relates to the deformation zone width. The Lake Heron fault highlights how deformation zone widths vary with site properties. Below, I compare one measure of fault setback distances to my results for the Lake Heron fault.

Regulations regarding the proposed setback of active faults or safety distance have been implemented in different countries, including New Zealand, to mitigate surface rupture hazard. Fault setback distance is defined as the safety distance between buildings and the deformation zone along the principal slip zone. In addition, setback depends on a criticality factor, based on the International Building Code (IBC), building occupancy class, displacement, fault dip and maximum depth of footing of the building for normal faults (Christenson et al. 2003) (Fig. 2-26).

Downthrown side: $S = U\left[2D + \left(\frac{F}{tan\theta}\right)\right]$ ……*Equation 2.10*

Upthrown side: $S = U(2D)$ ……*Equation 1.11*

Where, S is the minimum setback distance

U is the critical factor, based on the IBC building occupancy class

D is the expected fault displacement per event

F is the maximum depth of footing of the building

θ is the dip of the fault

This formula of setback for the upthrown and downthrown side is used in the Lake Heron area, noting that the equations are developed for normal faults, and the dip direction for reverse faults will be opposite of Fig. 2-26. Therefore, values calculated to determine setback for upthrown and downthrown sides in the Lake Heron area are swapped in the equations. A setback distance of 8 m is determined for the downthrown side after taking 2 m of fault displacement per event. Setback distance varies from 8 m to 11 m in the upthrown side while taking general footing depth for

residential building as 1.5 m (for two storey residential house with dwelling greater than 10) (IBC Code) (Fig. 2-27), and the average displacement occurred on the Lake Heron fault is assumed as 2 m with a range of fault dip (Table 2-4). Even summing the setback distance of the upthrown side and downthrown side is far less than the identified width of deformation zone in the Lake Heron area (e.g., 396 m at T2). A plot of deformation percentage accommodated outside of estimated set back distance versus surface profiles shows 10% (in Paddle Hill outwash along profile 4) to 93% (in T2 along profile 10) deformation accommodated outside of calculated setback zone.

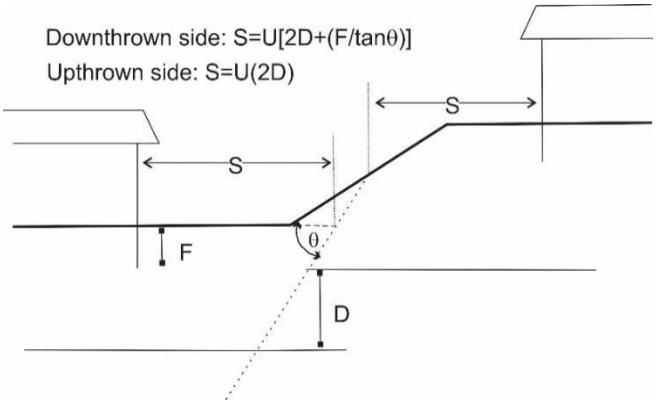

Figure 2-26. Schematic diagram showing the variables used to determine setback, where S is the minimum setback distance where buildings are not permitted, U is the critical factor based on the IBC building occupancy classes, D is the expected fault displacement per event, F is the maximum depth of footing of the building; and (ϑ) is the dip of fault in degrees (Christenson et al. 2003).

The NZ Ministry for the Environment has developed a risk-based approach to determine fault avoidance zones, based on three main criteria: recurrence interval, fault complexity, and building importance category (Kerr et al. 2003). Here, I look at fault complexity where faulting and folding with the buffer of +20 m is added to form the fault avoidance zone. This buffer zone is added to the extent of the entire deformation zone. Langridge and Ries (2014) proposed different values of uncertainty for different maps (e.g., LiDAR, image, Qmap etc.) to add to the buffer of +20 m for the fault avoidance zone. However, the problem is to measure the extent of deformation, which might be distributed over large areas that are not visualized in low-resolution imagery and DEMs of non-planar surfaces, and may change based on thickness of alluvial cover. Therefore, studies where the original geometries of markers are known using a high-resolution DEM/DSM are required to minimize the uncertainty related to determining a deformation zone, and empirical data from these studies can be applied elsewhere where markers are not available. In this study, fault avoidance zones calculated in the area are significantly wider than for most other faults in New Zealand.

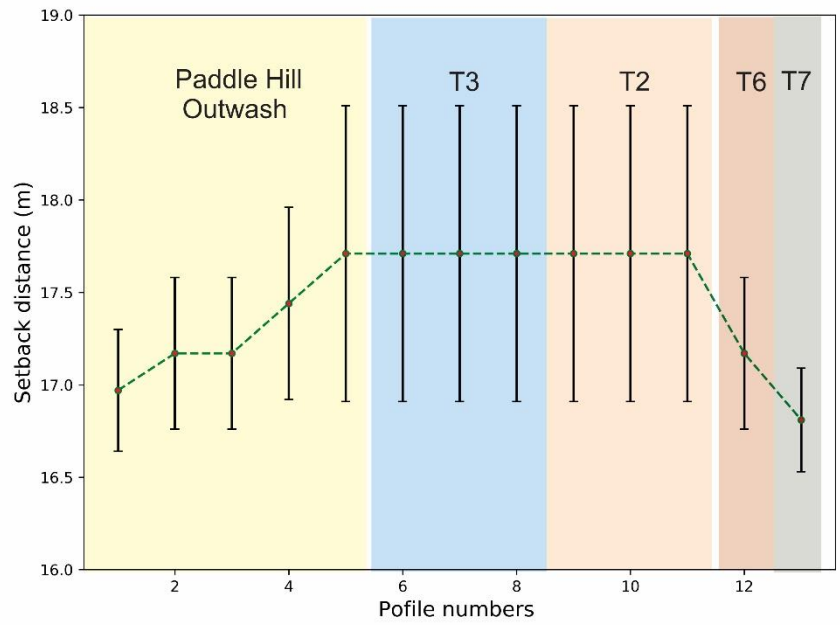

Figure 2-27. Plot of total setback distance calculated for the reverse fault at the location crossing the profile lines. An average displacement of 2 m, critical factor of 2 for residential buildings with more than 10 dwellings, maximum depth of footing of 1.5 m (Christenson et al. 2003) and minimum and maximum values of fault dip along each profile from Table 2-5 are used to calculate fault setback distance. The dashed line indicates the average setback distance. Variable setback distance is calculated at each fault location along the profile. 8 m setback distance is calculated at each profile location in the upthrown side.

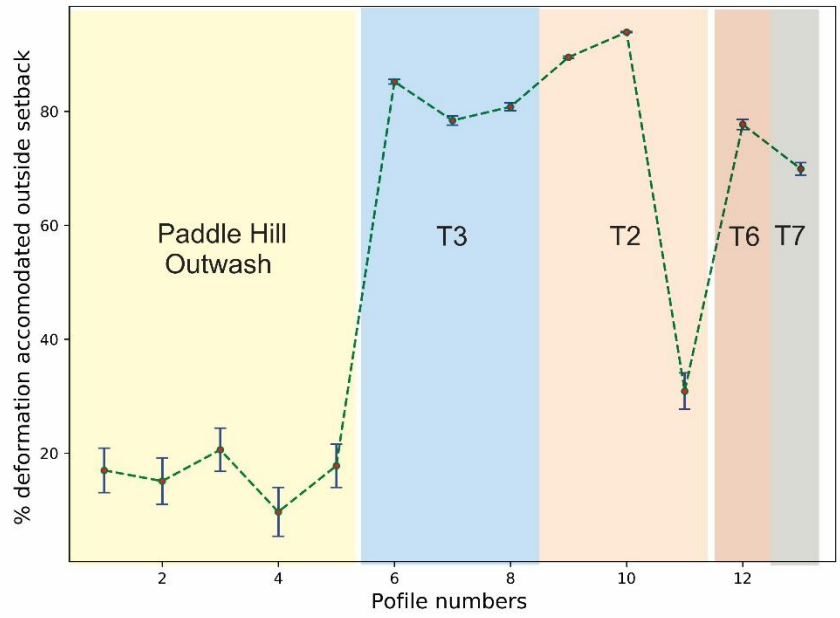

Figure 2-28: Percentage of deformation width accommodated outside setback distance at the crossing of profile lines in the Lake Heron area. Higher percentage of deformation width is accommodated outside of deformation width zone in T2 and T3.

2.6 Conclusion

Deformation associated with reverse faulting and folding in the hanging wall of the Lake Heron fault was analysed using remote sensing and field mapping within the area of the Paddle Hill Creek to c. 1 km north of the South Branch Ashburton River. The average net slip obtained from different locations across the deformation zone varies from 2 m in the youngest terrace to 58 m in T2. The best slip rate for the fault ranges from 1.2 to 2.7 mm/year based on two age scenarios. Eight to ten events causing surface deformation are expected on T2 and T3 comprising late Otiran deposits-based analysis of the compound scarp. Folding played an essential role in the deformation of the area and accounts for more than 50% of the total deformation. Displacement from folding is generally highest where the displacement measured from faulting is lowest, suggesting that folding and faulting are complementary deformation mechanisms in this region. The deformation width shows an inverse relationship with the number of faults but increases with the rise in folding percentage. Modelling and field data show that the thickness of overlying gravel plays an important role in the expression and width of earthquake deformation, which can vary over short distance along a fault.

2.7 References

Allmendinger RW 1998. Inverse and forward numerical modeling of trishear faultpropagation folds. Tectonics 17: 640-656.

Amos CB 2007. The geomorphic and structural evolution of the Ostler fault zone, New Zealand. Unpublished thesis, University of California, Santa Barbara. 191 p.

Ando R, Imanishi K, Panayotopoulos Y, Kobayashi T 2017. Dynamic rupture propagation on geometrically complex fault with along-strike variation of fault maturity: Insights from the 2014 Northern Nagano earthquake Crustal Dynamics: Unified Understanding of Geodynamics Processes at Different Time and Length Scales Yoshihisa Iio, Richard H. Sibson, Toru Takeshita, Takeshi Sagiya, Bunichiro Shibazaki and Junichi Nakajima. Earth, Planets and Space 69.

Barrell D, Strong D 2009. General distribution and characteristics of active faults and folds in the Ashburton District, mid-Canterbury. GNS Science Consultancy Report 2009/227. Environment Canterbury Report: 17.

Barrell DJA, Andersen BG, Denton GH 2011. Glacial geomorphology of the central South Island, New Zealand, GNS Science.

Beavan J, Tregoning P, Bevis M, Kato T, Meertens C 2002. Motion and rigidity of the Pacific Plate and implications for plate boundary deformation. Journal of Geophysical Research: Solid Earth 107: ETG 19-1 - 19-15.

Berryman K 1979. Active faulting and derived PHS directions in the South Island, New Zealand. Royal Society of New Zealand Bulletin 18: 29-34.

Boyer SJ, Pheasant DR 1974. Delimitation of weathering zones in the fiord area of eastern baffin Island, Canada. Bulletin of the Geological Society of America 85: 805-810.

Brandes C, Le Heron DP 2010. The glaciotectonic deformation of Quaternary sediments by fault-propagation folding. Proceedings of the Geologists' Association 121: 270-280.

Bull WB 2008. Tectonic Geomorphology of Mountains: A New Approach to Paleoseismology. 1-316 p.

Bullock RJ, De Paola N, Holdsworth RE, Trabucho-Alexandre J 2014. Lithological controls on the deformation mechanisms operating within carbonate-hosted faults during the seismic cycle. Journal of Structural Geology 58: 22-42.

Campbell JK, Nicol A, Howard ME 2003. Long-term changes to river regimes prior to late Holocene coseismic faulting, Canterbury, New Zealand. Journal of Geodynamics 36: 147-168.
Champion J, Mueller K, Tate A, Guccione M 2001. Geometry, numerical models and revised slip rate for the Reelfoot fault and trishear fault-propagation fold, New Madrid seismic zone. Engineering Geology 62: 31-49.
Christenson GE, Batatian LD, Nelson CV 2003. Guidelines for evaluating surface-fault-rupture hazards in Utah, Utah Geological Survey.
2007 Geology of the Aoraki area, Institute of Geological and Nuclear Sciences 1: 250000 Geological Map 15. Lower Hutt, New Zealand, GNS Science.
Cox SC, Stirling MW, Herman F, Gerstenberger M, Ristau J 2012. Potentially active faults in the rapidly eroding landscape adjacent to the Alpine Fault, central Southern Alps, New Zealand. Tectonics 31.
DeMets C, Gordon RG, Argus DF 2010. Geologically current plate motions. Geophysical Journal International 181: 1-80.
Duller G 1996. Recent developments in luminescence dating of Quaternary sediments. Progress in Physical Geography 20: 127-145.
Erslev EA 1991. Trishear fault-propagation folding. Geology 19: 617-620.
Ferrario MF, Livio F 2018. Characterizing the Distributed Faulting During the 30 October 2016, Central Italy Earthquake: A Reference for Fault Displacement Hazard Assessment. Tectonics 37: 1256-1273.
Gair HS 1967. The question of post-Rangitata Peneplantation in New Zealand.
Gold RD, Cowgill E, Wang XF, Chen XH 2006. Application of trishear fault-propagation folding to active reverse faults: Examples from the Dalong Fault, Gansu Province, NW China. Journal of Structural Geology 28: 200-219.
Hughes AN, Shaw JH 2015. Insights into the mechanics of fault-propagation folding styles. Bulletin of the Geological Society of America 127: 1752-1765.
Imbrie J 1984. The orbital theory of Pleistocene climate: support from a revised chronology of the marine d18O record. Milankovitch and climate. Proc. NATO workshop, Palisades, 1982. Vol. 1: 269-305.
Jacobson D 2015. Tectonic Geomorphology and Paleoseismology of theLake Heron Fault, New Zealand. Unpublished thesis, University of Canterbury, Christchurch, New Zealand. 130 p.
Johnson KM 2018. Growth of Fault-Cored Anticlines by Flexural Slip Folding: Analysis by Boundary Element Modeling. Journal of Geophysical Research: Solid Earth 123: 2426-2447.
Kaneda H, Nakata T, Tsutsumi Het al. 2008. Surface rupture of the 2005 Kashmir, Pakistan, earthquake and its active tectonic implications. Bulletin of the Seismological Society of America 98: 521-557.
Kerr J, Nathan S, Van Dissen R, Webb P, Brunsdon D, King A 2003. Planning for development of land on or close to active faults. Wellington: Ministry for the Environment.
King G, Vita-Finzi C 1981. Active folding in the Algerian earthquake of 10 October 1980. Nature 292: 22-26.
Langridge RM, Ries WF, Litchfield NJet al. 2016. The New Zealand Active Faults Database. New Zealand Journal of Geology and Geophysics 59: 86-96.
Lettis WR, Wells DL, Baldwin JN 1997. Empirical observations regarding reverse earthquakes, blind thrust faults, and quaternary deformation: Are blind thrust faults truly blind? Bulletin of the Seismological Society of America 87: 1171-1198.
Lin A, Ouchi T, Chen A, Maruyama T 2001. Co-seismic displacements, folding and shortening structures along the chelungpu surface rupture zone occurred during the 1999 Chi-Chi (Taiwan) earhtquake. Tectonophysics 330: 225-244.
Litchfield NJ, Van Dissen RJ, Sutherland Ret al. 2013. A model of active faulting in New Zealand: fault zone parameter descriptions. GNS Science. Pp. 120.

Litchfield NJ, Van Dissen R, Sutherland Ret al. 2014. A model of active faulting in New Zealand. New Zealand Journal of Geology and Geophysics 57: 32-56.
Mabin MCG 1980. The glacial sequences in the Rangitata and Ashburton valleys, South Island, New Zealand. Unpublished thesis, University of Canterbury, Christchurch. 238 p.
Mabin MCG 1984. Late pleistocene glacial sequence in the lake heron basin, mid canterbury. New Zealand Journal of Geology and Geophysics 27: 191-202.
Martinson DG, Pisias NG, Hays JD, Imbrie J, Moore Jr TC, Shackleton NJ 1987. Age dating and the orbital theory of the ice ages: Development of a high-resolution 0 to 300,000-year chronostratigraphy. Quaternary Research 27: 1-29.
Milliner CWD, Dolan JF, Hollingsworth J, Leprince S, Ayoub F, Sammis CG 2015. Quantifying near-field and off-fault deformation patterns of the 1992 M<inf>w</inf> 7.3 Landers earthquake. Geochemistry, Geophysics, Geosystems 16: 1577-1598.
Mitra S 1990. Fault-propagation folds: geometry, kinematic evolution, and hydrocarbon traps. American Association of Petroleum Geologists Bulletin 74: 921-945.
Molnar P 1994. Quaternary climate change and the formation of river terraces across growing anticlines on the north flank of the Tien Shan, China. Journal of Geology 102: 583-602.
Murray AS, Wintle AG 2000. Luminescence dating of quartz using an improved single-aliquot regenerative-dose protocol. Radiation Measurements 32: 57-73.
Murray AS, Wintle AG 2003. The single aliquot regenerative dose protocol: Potential for improvements in reliability. Radiation Measurements 37: 377-381.
Nicol A, Campbell JK 2001. The impact of episodic fault-related folding on late Holocene degradation terraces along Waipara River, New Zealand. New Zealand Journal of Geology and Geophysics 44: 145-156.
Norris RJ, Cooper AF 2001. Late Quaternary slip rates and slip partitioning on the Alpine Fault, New Zealand. Journal of Structural Geology 23: 507-520.
Oliver P, Keene H 1990. Sheet J36 BD and Part Sheet J35, Clearwater. Geological map of New Zealand 1: 000.
Olsen T, Borella J, Stahl T 2020. Clast transport history influences Schmidt hammer rebound values. Earth Surface Processes and Landforms 45: 1392-1400.
Pettinga J, Chamberlain C, Yetton M, Van Dissen R, Downes G 1998. Earthquake source identification and characterisation: stage 1 (Part A) earthquake hazard and risk assessment study. Canterbury Regional Council CRC: 121.
Pettinga JR, Yetton MD, Van Dissen RJ, Downes G 2001. Earthquake source identification and characterisation for the Canterbury region, South Island, New Zealand.
Philip H, Meghraoui M 1983. Structural analysis and interpretation of the surface deformations of the El Asnam Earthquake of October 10, 1980. Tectonics 2: 17-49.
Pugh JM 2008. The late quaternary environmental history of the Lake Heron Basin, Mid Canterbury, New Zealand. Unpublished thesis, University of Canterbury, Christchurch. 156 p.
Rockwell TK, Keller EA, Clark MN, Johnson DL 1984. Chronology and rates of faulting of Ventura River terraces, California. Geological Society of America Bulletin 95: 1466-1474.
Rother H, Fink D, Shulmeister J, Mifsud C, Evans M, Pugh J 2014. The early rise and late demise of New Zealand's last glacial maximum. Proceedings of the National Academy of Sciences 111: 11630-11635.
Schaefer JM, Putnam AE, Denton GHet al. 2015. The southern glacial maximum 65,000 years ago and its unfinished termination. Quaternary Science Reviews 114: 52-60.
Smith BW, Aitken MJ, Rhodes EJ 1986. Optical dating: Methodological aspects. Radiation Protection Dosimetry 17: 229-233.
Stahl T 2014. Active Tectonics and Geomorphology of the central South Island, New Zealand: Earthquake Hazards of Reverse Faults. Unpublished PhD thesis, Univeristy of Canterbury, Christchurch. 230 p.

Stahl T, Quigley M, Bebbington M 2016. Tectonic geomorphology of the Fox Peak and Forest Creek Faults, South Canterbury, New Zealand: slip rates, segmentation and earthquake magnitudes. New Zealand Journal of Geology and Geophysics 59: 568-591.

Stein RS, King GCP 1984. Seismic potential revealed by surface folding: 1983 Coalinga, California, earthquake. Science 224: 869-872.

Suggate R, Waight T 1999. Geology of the Kumara-Moana Area. Institute of Geological and Nuclear Sciences Map 24. IGNS Ltd, Lower Hutt, New Zealand.

Suggate RP 1990. Late pliocene and quaternary glaciations of New Zealand. Quaternary Science Reviews 9: 175-197.

Suggate RP, Almond PC 2005. The Last Glacial Maximum (LGM) in western South Island, New Zealand: Implications for the global LGM and MIS 2. Quaternary Science Reviews 24: 1923-1940.

Suppe J, Medwedeff DA 1990. Geometry and kinematics of fault-propagation folding. Eclogae Geologicae Helvetiae 83: 409-454.

Thompson SC, Weldon RJ, Rubin CM, Abdrakhmatov K, Molnar P, Berger GW 2002. Late Quaternary slip rates across the central Tien Shan, Kyrgyzstan, central Asia. Journal of Geophysical Research: Solid Earth 107: ETG 7-1-ETG 7-32.

Wallace LM, Beavan J, McCaffrey R, Berryman K, Denys P 2007. Balancing the plate motion budget in the South Island, New Zealand using GPS, geological and seismological datas. Geophysical Journal International 168: 332-352.

Wang H, Zhang Z, Ran Yet al. 2021. Quaternary Deposits Affect Coseismic Offset on Thrust Faults: Evidence from the 2008 Mw 7.9 Wenchuan, China, Earthquake. Seismological Research Letters.

Westoby MJ, Brasington J, Glasser NF, Hambrey MJ, Reynolds JM 2012. 'Structure-from-Motion' photogrammetry: A low-cost, effective tool for geoscience applications. Geomorphology 179: 300-314.

Wolfe FD, Stahl TA, Villamor P, Lukovic B 2020. Short communication: A semiautomated method for bulk fault slip analysis from topographic scarp profiles. Earth Surface Dynamics 8: 211-219.

Appendix A-Net slip and slip rate calculation

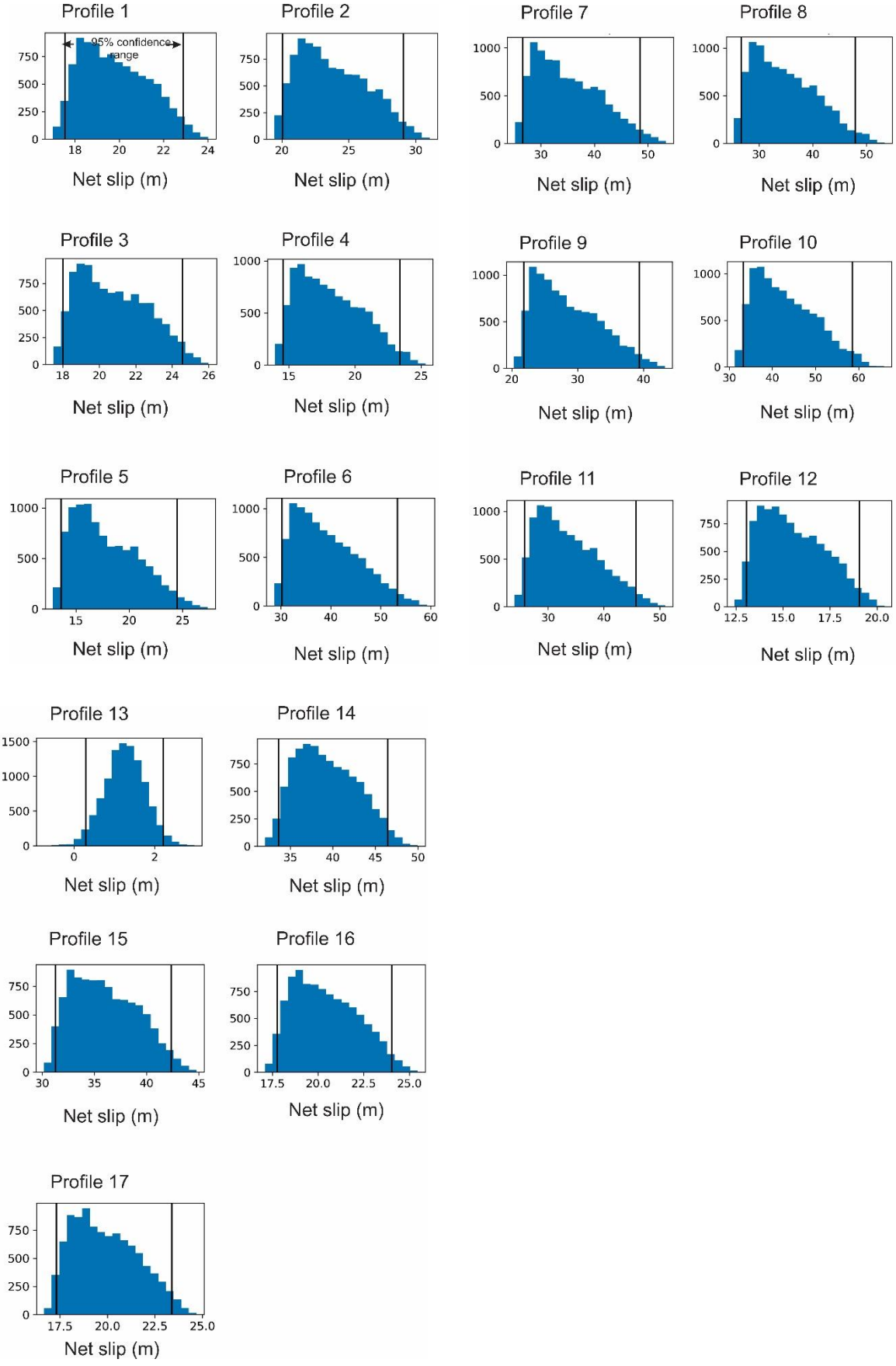

Figure 1. Slip calculated from the elevation profiles and fault plane geometry following the Monte Carlo method (Thompson et al., 2002) at the 95% confidence interval. Trapezoidal system fault dip angle was used in the calculation with dip model constraints of Min1, Min2, Max1 and Max2. Dip model constraints are different for each net slip calculation (Table 2-5) and position constraints of 0.33, 0.44, 0.55, and 0.66. Python code, MCSST (Wolfe et al. 2020) developed for the method is used to estimate slips.

Figure 2. Slip rate calculated using net slip obtained from topographic profiles and regional glacial advance age of the surfaces in the Lake Heron area. Python code, MCSST (Wolfe et al. 2020) developed for the method is used to estimate slips.

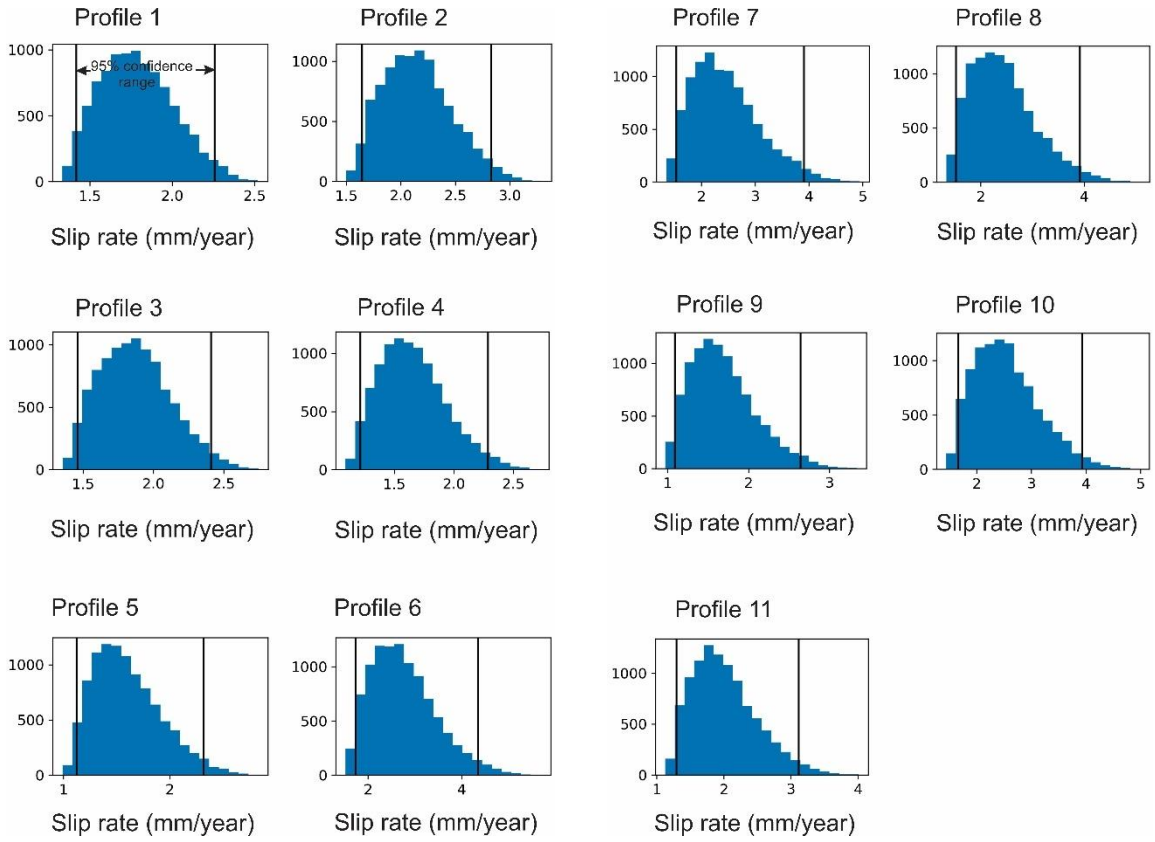

Figure 3. Slip rate calculated on the basis of net slip derived from topographic profiles and age of offset surfaces(Jacobson 2015) using python code, MCSST (Wolfe et al. 2020)

Appendix B- Probable moment magnitude (M_w) and average displacement

I estimated the magnitude of faulting events experienced in the area using scaling relationships between surface rupture length (SRL) and earthquake magnitude (Wells et. al. 1994; Stirling et al. 2008; Wesnousky 2008; Leonard 2010; Moss et al. 2011) (Table 2-6). Considering a surface rupture length of 36 km for the Lake Heron fault (Pettinga et al. 2001) and using established equations for determining moment magnitude of earthquakes (Table 2-B1), I determined a probable M_w of 6.7 to 7.0 for the Lake Heron fault (Table 2-B2).

Different earthquakes have different displacements, and it is hard to be sure about the average and maximum displacement from observation without paleoseismic trenches. The recent earthquake most probably had displacement values of ~2 m on the Lake Heron fault. Small displacement amounts present on the youngest surface (T7) is ~2 m and the frontal scarps on older terraces have similar height. This evidence justifies the average single event displacement of ~2 m. Taking the average displacement of this height, the probable magnitude will be M_w 7.7 (Table 2-7) for the Lake Heron fault using equation 2.7 (Table 2-6). This probable magnitude shows that the fault length might be longer than estimates of previous researchers (e.g., Pettinga et al. 2001).

Table 2-B1: Scaling relationships between M_w and surface rupture length (SRL), and between M_w and cumulative surface displacement (CSD).

Equation no.	Equation	Source data	Reference
Eq. 2.1:	$M_w = 1.52 \times \log(SRL) + 4.4$	Dip slip faults	Leonard (2010)
Eq. 2.2	$M_w = 1.22 \times \log(SRL) + 5.0$	Reverse faults	Wells and Coppersmith (1994)
Eq. 2.3	$M_w = 4.11 + 1.88\log L$	Reverse faults	Wesnousky (2008)
Eq. 2.4	$M_w = 4.18 + 2/3 \log W + 4 = 3 \log L$	Reverse faults	Stirling et al. (2008)
Eq. 2.5	$M_w = 2.00 \times \log(MeanCSD) + 6.55$	Dip slip faults	Leonard (2010)
Eq. 2.6	$M_w = 0.13 \times \log(MeanCSD) + 6.64$	Reverse faults	Wells and Coppersmith (1994)
Eq. 2.7	$M_w = 3.08 \times \log(MeanCSD) + 6.84$	Reverse faults	Moss and Ross (2011)
Eq. 2.8	$M_w = 0.44 \times \log(MaxCSD) + 6.52$	Reverse faults	Wells and Coppersmith (1994)
Eq. 2.9	$M_w = 1.96 \times \log(MaxCSD) + 6.27$	Reverse faults	Moss and Ross (2011)

W in the table denotes width (km) and L denotes surface rupture length (km).

Table 2-B2: M_w obtained using different equations. Average displacement is also calculated using the surface rupture length.

Authors	**M_w**	**Average displacement**	**Based on**
Leonard (2010)	6.76		Using surface rupture length
		0.99	Using surface rupture length
Wells and Coppersmith (1994)	6.89		Using surface rupture length
Moss and Ross (2011)	7.77		Using average displacement 2 m
	6.84		Using average displacement 1 m
	6.86		Using max displacement 2 m
Stirling et al. (2008)	7.04		Using surface rupture length
Wesnousky (2008)	7.04		Using surface rupture length

References

Leonard M 2010. Earthquake fault scaling: Self-consistent relating of rupture length, width, average displacement, and moment release. Bulletin of the Seismological Society of America 100: 1971-1988.

Moss RES, Ross ZE 2011. Probabilistic fault displacement hazard analysis for reverse faults. Bulletin of the Seismological Society of America 101: 1542-1553.

Stirling M, Gerstenberger M, Litchfield Net al. 2008. Seismic hazard of the Canterbury Region, New Zealand: New earthquake source model and methodology. Bulletin of the New Zealand Society for Earthquake Engineering 41: 51-67.

Wells DL, Coppersmith KJ 1994. New empirical relationships among magnitude, rupture length, rupture width, rupture area, and surface displacement. Bulletin - Seismological Society of America 84: 974-1002.

Wesnousky SG 2008. Displacement and geometrical characteristics of earthquake surface ruptures: Issues and implications for seismic-hazard analysis and the process of earthquake rupture. Bulletin of the Seismological Society of America 98: 1609-1632.

Appendix C-OSL dating report

Report No. 17/19

Luminescence Dating Technical Report

Luminescence Dating Laboratory
School of Geography, Environment and Earth Sciences
Victoria University of Wellington
Wellington
New Zealand

Reported by: Ms. Ningsheng Wang
Date of Issue: 05-11-2019
Contact: Room 414
Cotton Building
Victoria University of Wellington
Ph: (04) 463 6127

1. SUMMARY

One sample (Field code: PDH-1) was submitted for luminescence dating by Dr. Tim Stahl and Santosh Dhakal from the University of Canterbury. The laboratory code of the sample is WLL1409.

The fine grain (4-11μm) preparation technique was used. The blue luminescence was measured during infrared stimulation of fine grain feldspar. The luminescence age was determined by Single Aliquot Regenerative method (SAR). The dose rate was determined on the basis of gamma spectrometry measurements.

2. SAMPLE PREPARATION

The sample preparation consisted of two parts:

(i) Preparation for measurement of equivalent dose (equivalent to the paleodose)

(ii) Preparation for measurement of dose rate

Part 1: The Preparation for Measurement of Equivalent Dose (D_e)

1. Chemical Treatment

The sample had its outer surfaces removed. Of this removed outer scrapings, 100g was weighed and dried in an oven in preparation for gamma spectrometer analysis. A plastic cube was then filled with remaining scrapings in preparation for water content measuring.

"Fresh" sample material, that had outer surfaces removed earlier (unexposed light sample material), was treated in 10% HCl. This was carried out overnight until all carbonate was removed by the reaction. Following this treatment, the sample was further reacted overnight with 10% H_2O_2 in order to remove organic matter.

D_e was obtained by using SAR.

Single Aliquot Regenerative Method (SAR)

The Single Aliquot Regenerative Method (SAR) was used to determine the equivalent doses. This technique is described by Murray and Wintle (2000).

For the SAR method, a number of aliquots (disks) were subjected to a repetitive cycle of irradiation, preheating and measurement. Firstly, natural shining down curves was measured after preheating. Then shining down curves were measured for the next four or five cycles for different beta doses. Then from the variety of shining down curves, a luminescence growth curve (β induced luminescence versus added dose) was established. This was used to determine the equivalent dose (equivalent to the palaeodose). The measurement for the aliquots resulted in a variety of equivalent doses, so called dose distribution. D_e given in the report were used the arithmetic mean of the data.

In order to correct potential sensitivity changes from cycle to cycle, the luminescence response to a test dose was measured after preheat between cycles.

The blue luminescence of 12 aliquots of the sample were measured at 50^0C for 100s using a Riso TL-DA-20 reader with infrared diodes at 880nm used to deliver a stimulated beam. Blue luminescence centre about 410nm from feldspar was then detected by an EMI 9235QA photomultiplier fixed behind two filters consisting of a Schott BG39 and Kopp5-58. Beta irradiation were done on the Riso TL-DA-20 ^{90}Sr/Y β irradiator, calibrated against ^{60}Co gamma source, SFU, Vancouver, Canada with about 3% uncertainty. Preheat and cut heat temperature was 260 °C for 10 seconds.

Luminescence growth curve (β induced luminescence intensity versus added dose) was constructed by using the initial the first a few seconds of the shine down curves and subtracting the average of the last 20 seconds, along with the so-called late light which was thought to be a mixture of background and hardly bleachable

Water content was measured as weight of water divided by dry weight of the sample taking into account a 25% uncertainty.

(ii) ***Dose rate from cosmic rays***

Dose rate from cosmic rays were determined by the depth of sample below the surface along with its longitude, latitude and altitude, convention formula and factors published by Prescott, J.R. & Hutton, J.T. (1994).

4. RESULTS

Table 1 Cosmic dose rates

Table 2 Water contents, radionuclide contents

Table 3 a- Values, equivalent doses, dose rates and luminescence ages

Table 1: Cosmic Dose Rates

Laboratory Code	Depth Below the Surface(m)	Cosmic Dose Rate (Gy/ka)	Field Code
WLL1409	1.2	0.2015±0.0101	PDH-1

Table 2: Water Contents, Radionuclide Contents

Laboratory Code	Water Content (%)	U(ppm) from ^{234}Th	U(ppm) from ^{226}Ra, ^{214}Pb, ^{214} Bi	U(ppm) from ^{210}Pb	Th(ppm) From ^{208}Tl ^{212} Pb ^{228} Ac	K(%)	Field Code
WLL1409	7.8	3.07±0.30	2.56±0.14	2.34±0.21	10.41±0.12	2.04±0.04	PDH-1

Table 3: a-Values, Equivalent Doses, Dose Rates and Luminescence Ages

Laboratory Code	a-Values	D_e(Gy)	Dose Rate(Gy/ka)	**Luminescence Age(ka)**	Field Code
WLL1409	0.06±0.03	4.17±0.25	101.45±0.76	**24.3±1.5**	PDH-1

*a-value was estimated.

CONTENTS

The next step involved 200ml CBD* solution being added to the sample for 12 hours to remove iron oxide coatings. Note, after every chemical treatment procedure distilled water was used to wash the sample several times.

*CBD solution: 71g sodium citrate, 8.5 g sodium bicarbonate, and 2g sodium dithionate per litre of distilled water

2. Fine Grain Technique (4-11μm)

After chemical treatment, calgon solution (1g sodium hexametaphosphate per litre distilled water) was added to make thick slurry. This slurry was placed into an ultrasonic bath and mechanically agitated for an hour. The sample was then placed into a 1L measuring cylinder, filled with a certain amount of distilled water to separate out the 4-11μm grains according to Stokes' Law.

The 4-11μm grains were then rinsed with ethanol and acetone and a suspension of these grains were then deposited evenly onto 70 aluminium disks.

Part 2: The Preparation of Measurement of Dose Rate

The dry, ground and homogenised sample material were weighed and sealed in air tight perspex containers and stored for at least four weeks. This storage time minimizes the loss of the short lived noble gas ^{222} Rn and allows ^{226}Ra to reach equilibrium with its daughters ^{214} Pb and ^{214} Bi.

3. MEASUREMENTS

Luminescence age was determined by two factors: the equivalent dose (D_e) and the dose rate.

> Equivalent dose: obtained from the lab equivalents to the paleodose absorbed by samples during the burial time in the natural environment since their last exposure to the light.
> Dose rate: amount dose received by the sample each year.

Part 1: Determination of Equivalent Dose (D_e)

components. Interpolation of this growth curve to the dose axis was yielded the equivalent dose D_e which was used as a paleodose. The measurements of 12 aliquots obtained 12 D_e's, the D_e's were accepted within 10% recycling ratio. D_e used for the age determination was used the arithmetic means of the data. A dose recovery test and a zero dose were checked no anomalies. No fading tendency was observed.

a-value

a-value is measured by comparing the luminescence induced by alpha irradiation with that induced by beta or gamma irradiation. The a-value was for dose rate calculation. For this study, a- value was estimated.

Part 2: Determination of Dose Rate

Dose rate consisted of two parts.
(i) Dose rate from sample's burial environment
(ii) Dose rate from cosmic rays.

(i) *Dose rate from burial environment*

Dose rate from sample's burial environment was determined by radionuclide contents of ^{238}U, ^{232}Th and ^{40}K, a-value and water content.

Determination of Contents of U, Th and K by Gamma spectrometry

Gamma rays produced from sample material was counted for a minimum time of 24 hours by a high resolution and broad energy gamma spectrometer. The spectra were then analysed using GENIE2000 software. The contents of U, Th and K were obtained by comparison with standard samples. The dose rate calculation was based on the activity concentration of the nuclides ^{40} K, ^{208}Tl, ^{212}Pb, ^{228} Ac, ^{214} Bi, ^{214}Pb, ^{226} Ra, using dose rate conversion factors published by Guérin, G., Mercier, N., Adamiec, G. 2011.

Measurement of Water Contents

3 Tectonic geomorphology of the Torlesse fault, mid-Canterbury, New Zealand

Abstract

The Porters Pass – Amberley Fault Zone located in the mid-Canterbury region of the South Island, New Zealand, has been identified as one of the main sources of regional seismic hazard to the city of Christchurch. Despite this significant hazard, virtually no information about the fault's active 31 km-long backthrust, the Torlesse fault, is on record. In this study, I used field mapping, surveying (Global Positioning System and Structure-from-Motion photogrammetry), and luminescence and radiocarbon dating to characterise the rupture history of the Torlesse fault and determine if it is a distinct source of seismic activity. I measured horizontal and vertical displacements ranging from 3 to 15 m and 0.5 to 5 m, respectively, across offset terraces and stream channels assumed to be younger than the Last Glacial Maximum. Time-integrated slip rates on strike-slip traces may vary from c. 0.3 to 0.9 mm/year, but better age control is required to confirm these numbers. Net slips range from c. 2.82 to 6.96 m and slip rates varying from c. 0.17 to 0.43 mm/year at the 95% confidence interval were estimated on two dip-slip faults at the Porter River terrace, previously used to estimate the slip rate of the entire fault but here identified as likely flexural slip faults formed within underlying bedding. Positive flower structure model in the Torlesse Range supported by structural and kinematic data of the Torlesse and other faults (e.g., Porters Pass fault) in the range shows the probability of multi-fault ruptures in the region.

3.1 Introduction

Multi-fault ruptures have been observed in various large-magnitude earthquake events, such as the 2016 M_w 7.8 Kaikōura earthquake in New Zealand (Litchfield et al., 2018; Nicol et al., 2018), the 1992 M_w 7.3 Landers earthquake in California (Hart et al. 1993), and the 2002 M_w 7.9 Denali earthquake in Alaska (Schwartz et al. 2012). Clustering and synchronization of earthquake events across faults have also been recognized in the Iceland seismic zone, the central Nevada seismic belt, and the eastern California shear zone (Dolan et al. 2007; Oskin et al. 2007; Scholz et al. 2010; Zinke et al. 2019). The complex and sometimes unpredicted fault rupture patterns that occur in such events are significant because they highlight gaps in current understandings of seismic hazard and fault source parameters for complex rupture events.

Secondary faults, like backthrusts, are common at mountain fronts in contractional regions (Butler et al. 2020) and, when proximal to primary faults with high- or medium-slip rates, are significant for recognizing the kinematics of wider fault systems that may promote multi-fault ruptures during large earthquakes. Secondary fault ruptures have been documented in numerous earthquakes (e.g., Lavine et al. 2003; Fukuyama 2015; Lin et al. 2017; Baize et al. 2019; Ross et al. 2019) however, most of such studies have concentrated on the much larger and more prominent primary fault systems. Understanding the kinematics and connectivity of primary and secondary faults on local or regional scales may indicate possible interactions between them, thus providing an opportunity to better understand the drivers of multi-fault ruptures.

The Torlesse fault, in the mid-Canterbury region of New Zealand, is an oblique backthrust of the higher-slip-rate Porters Pass fault (Fig. 3-1) that provides an opportunity for gaining insight into the interaction between secondary and primary faults. The Torlesse fault has been mapped as a 31 km long reverse fault with a slip rate of less than 1 mm/year (Pettinga et al. 2001; Forsyth et al. 2008; Litchfield et al. 2013), while the neighbouring Porters Pass fault has a slip rate of 3-5 mm/year (Cowan 1992; Pettinga et al. 2001; Howard et al. 2005). The Torlesse fault, along with the Porters Pass fault, thus poses a potential seismic hazard to both the rural area of Castle Hill and urban area of Christchurch (Fig. 3-1). Better characterisation of the fault is needed to understand its relationship, and potential rupture connectivity, to the Porters Pass fault.

In this chapter, I apply field mapping, surveying (Global Positioning System (GPS) and Structure-from-Motion (SfM) photogrammetry), and luminescence and radiocarbon dating to characterise the surface deformation history of the Torlesse fault. High-resolution Digital Surface Models (DSMs) developed using SfM were used to calculate the slip and slip rates of the faults. I propose a revised structural model for the fault based on my measurements and mapping, which provides a structural and kinematic context for potential multi-fault earthquakes in the region. There

is currently very limited information related to the Torlesse fault in the NZAFD (https://data.gns.cri.nz/af/), (Langridge et al. 2016).The detailed investigation of the Torlesse fault presented here is also an important fundamental contribution to the New Zealand Active Fault Database (NZAFD), which documents the location of active faults as well as their characteristics throughout the country.

3.2 Geologic Background

3.2.1 Regional active tectonics

The South Island of New Zealand straddles the Australian and Pacific Plates, which converge obliquely at a rate of c. 30-50 mm/year (Wallace et al. 2007; DeMets et al. 2010). The Alpine fault, one of the fastest moving faults with a slip rate of around 25 mm/year (Pettinga et al., 2001; Beavan et al., 2002), transfers plate motion from the Puysegur subduction zone in the south to the Hikurangi subduction zone in the north (Fig. 3-1). The Torlesse fault and other faults in northwest Nelson, Canterbury, Marlborough, and Otago accommodate the remaining components of oblique continental collision in the South Island.

The central South Island falls in a zone of dextral transpression comprising a range of fault orientations and kinematics (Pettinga et al. 2001; Litchfield et al. 2014). The major faults with surface expression strike NNE-SSW and are dextral to dextral reverse. Slip rates of active faults in the central South Island range from <1 mm/year (e.g., the Greendale fault) to more than 20 mm/year (e.g., the Alpine and Hope faults). The characteristics of many low to medium slip rate faults in the area are still unknown (Pettinga et al. 2001; Litchfield et al. 2014; Langridge et al. 2016).

3.2.2 Regional geology and geomorphology

The Torlesse Range consists of Rakaia Terrain Torlesse Greywacke, comprising Permian to late Triassic feldspathic sandstone and mudstone (Gage 1958). Cretaceous to Tertiary rocks are present in the structural depression of the Castle Hill Basin (Gage 1958). Tuff and limestone deposits of the Thomas Formation are well-expressed as a series of strike ridges in the basin (Gage 1970; Bradshaw 1975; Forsyth et al. 2008) (Fig. 3-2). The Torlesse fault passes through the Rakaia Terrain at the rangefront and Late Pleistocene to Quaternary sediments overlying Cretaceous to Tertiary rocks in the basin. Quaternary units in the basin primarily consist of locally-sourced (rangefront-derived) Torlesse sediments.

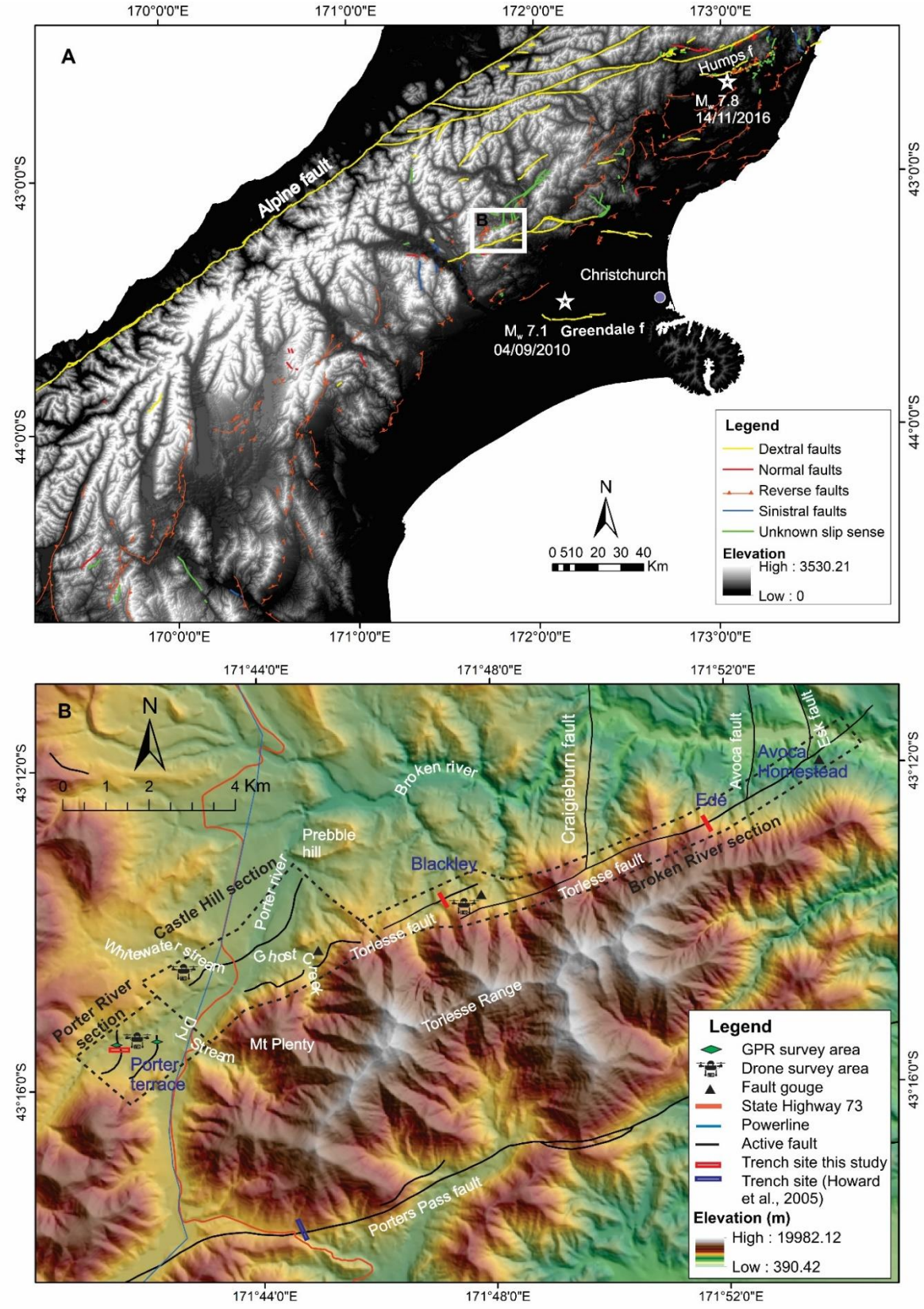

Figure 3-1.A) Location map of the study area shown in the box on a 25 m Digital Elevation Model (DEM). The letter "f" following fault names in the figure denotes "fault". B) Location map of the Torlesse fault and surrounding faults in a hill-shaded 8-m DEM (https://data.linz.govt.nz/layer/51768-nz-8m-digital-elevation-model-2012). The Craigieburn, Avoca and Esk faults connect with the Torlesse

fault to the northeast. Active fault traces provided by GNS Science, available at https://data.gns.cri.nz/af/, (Langridge et al. 2016). The Torlesse fault zone is divided into three sections: the Broken River section from the Broken River to the Blackley Stream area, the Castle Hill section from Blackley Stream area to the Whitewater terrace; and the Porter River section from the junction of the Porter River and Dry Stream to the south of the lime quarry near the Porter Ski road. Different methods used in the study are shown in the map. Drone surveys were conducted in three areas to develop high-resolution digital surface models of significant sites. Crush zones with fault gouges and cataclasites were mapped in three outcrops. A Ground Penetrating Radar (GPR) survey was carried out in two nearby locations in the Porter Terrace. Three trenches were excavated across the fault. One previous trench site dug across the Porters Pass fault (Howard et al. 2005) is also given in the map (see detail in Chapter 4).

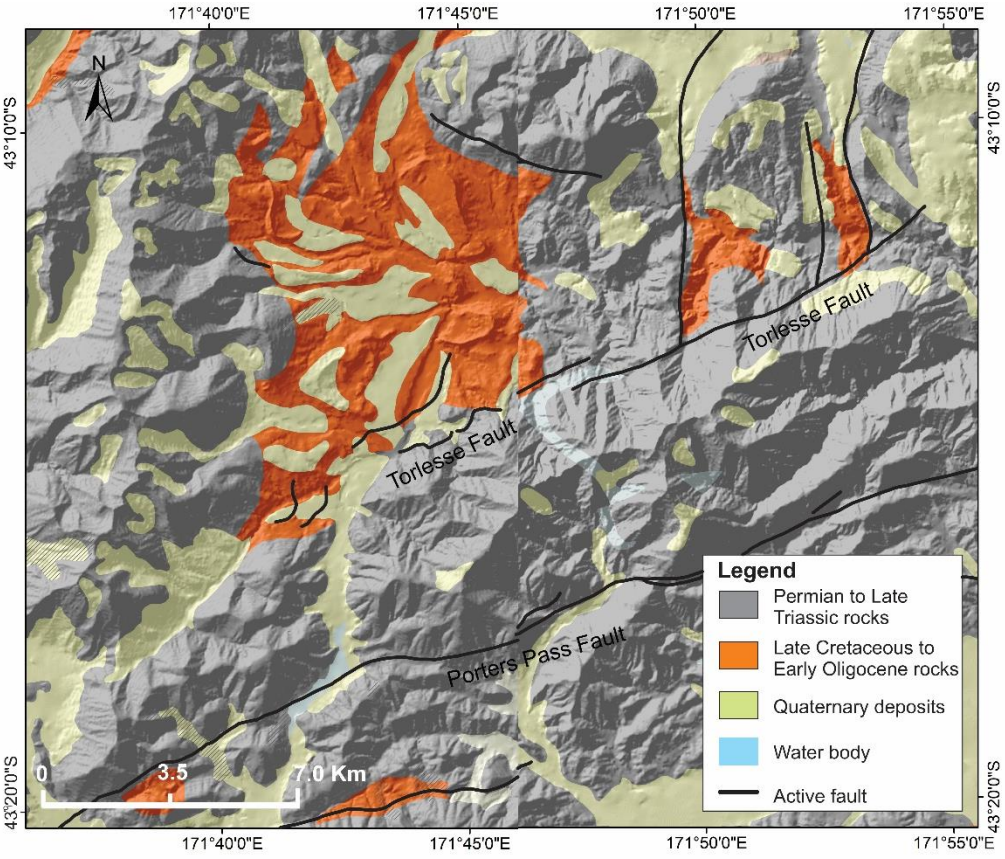

Figure 3-2. Simplified regional geological map of the study area. Most of the area consists of Permian to late Triassic (Triassic) rocks. Late Cretaceous to Early Oligocene rocks are concentrated in the basin, and Quaternary deposits are present in the valley slope and basin. Active faults (red lines) are from the active fault database of New Zealand (https://data.gns.cri.nz/af/) (Langridge et al. 2016). Solid red lines represent definite active faults. Modified after Cox and Barrell, 2007; Forsyth et al., 2008.

Landform age correlations in the Castle Hill basin are heavily reliant on mapping of glacial and glaciofluvial deposits. Evidence of several Pleistocene glacial advances has been identified in the Castle Hill basin (Gage 1958; Ricker et al. 1993). Glacial advances ~60-74 ka (Marine Isotope Stage (MIS) 4) were extensive and are well-preserved in the South Island (Fitzsimons 1997). Various terraces of glaciofluvial origin associated with such glacial activity have been identified in the Castle Hill basin (Breed 1960; Barrell et al. 2011) (Fig.3-3). Unit names, their MIS correlations, and 'absolute' age

controls are listed in Table 3-1. Much of the Torlesse Rangefront is either unmapped, or contains Quaternary deposits below existing map resolutions (Fig. 3.3).

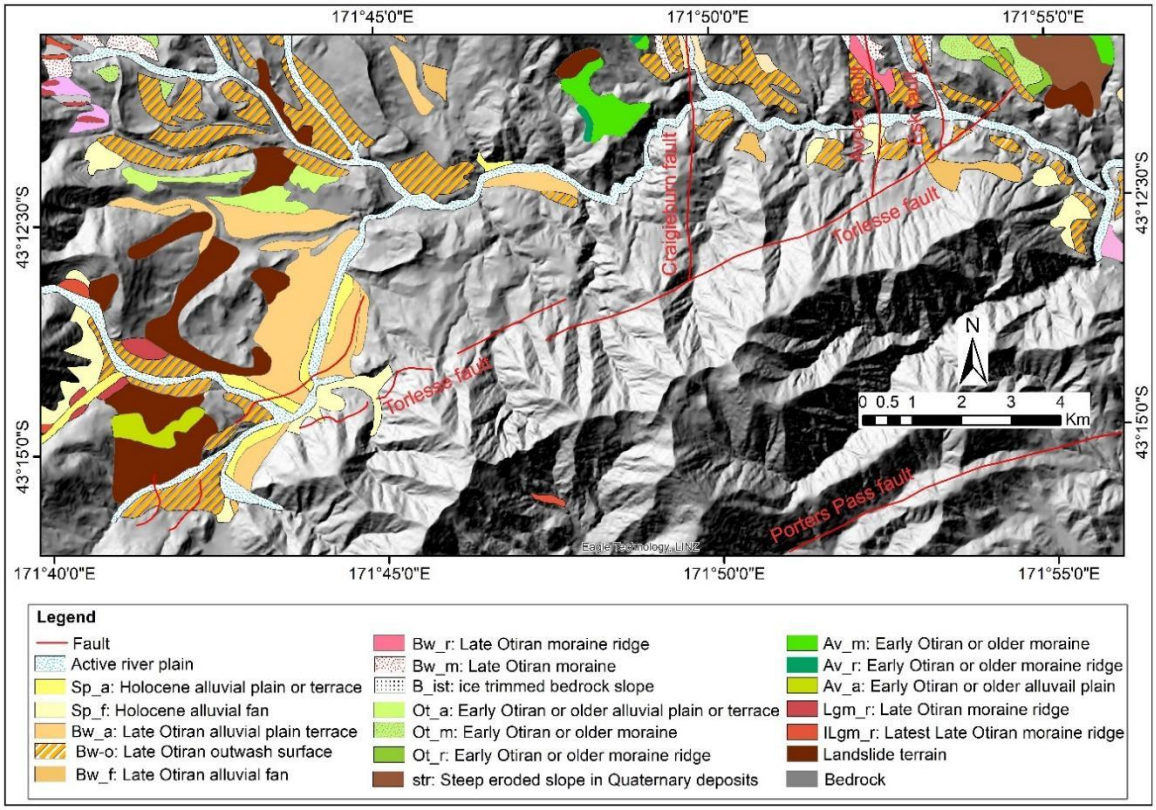

Figure 3-3. Simplified geomorphological map of the study area. Modified after Barrell et al. (2011).

Table 3-1: Correlation of mid to late Quaternary glaciation and interglaciation in New Zealand with Marine Isotope Stage (MIS) (Barrell et al. 2011).

Glaciation		Interglaciation		MIS Stage	Approximate age (years ago)	Waimakariri catchment (Gage, 1958)	
						Glacial Advance	Formation
			Aranui	1	0 - 11,700		Springston
Late-glacial				2	11,700-14,500		
Otiran	Late Otiran			3	14,500 ~19,000 ~21,500-28,000 ~45,000	Poulter Blackwater	St Bernard Burham
	Early Otiran			3 4	~45,000 ~65,000 ~74,000	Otarama	Windwhistle

3.2.3 Previous work on the Torlesse fault

Preliminary investigations of the Torlesse fault have identified the fault as an east-northeast trending, 31 km long reverse-slip fault (Pettinga et al. 1998; Pettinga et al. 2001). Pettinga et al. (1998; 2001) determined a maximum possible moment magnitude (M_w) of 6.7 and a recurrence interval of more than 2,000 years based on the fault length. Litchfield et al. (2013) assigned a slip rate ranging from 0.25 to 0.75 mm/year to the Torlesse fault. Barrell et al. (2013) estimated a slip rate of 0.3 mm/year for the Torlesse fault based on a 5-m-high scarp at the Porter River terrace (Fig. 3-1). These studies, based on aerial photographs, limited fieldwork, and inferred ages of displaced surfaces, provide preliminary estimates for the potential surface rupture history, lengths, and magnitudes of the Torlesse fault.

3.3 Methods

The main objectives of this study were to map traces of the Torlesse fault, measure horizontal and vertical offsets, and estimate slip rates to better understand the Torlesse fault. A variety of surveying and geochronological approaches were utilised to document deformation across various types of terrain, including the rugged slopes of the Torlesse Range and gentle slopes of Castle Hill Basin. Different field methods were used to study the geometry, offsets and slip rates of fault scarps (Fig. 3-2). Each of these methods is detailed below.

3.3.1 Mapping

Field and remote mapping was carried out in the study area to produce geomorphic maps and analyse surface deformation. I used an 8 m DEM, historical aerial photographs, and Google Earth images for mapping. High-resolution DSMs developed from drone images (see sections below) were used to trace geomorphic features like terrace treads, risers, fault scarps and channels. Geomorphic mapping was carried out on a scale of 1:500 in the DSM survey areas.

3.3.2 Surveying

The majority of surveying was accomplished using Unmanned Aerial Vehicle (UAV) drone flights. A handheld Trimble Geo7x Global Navigation Satellite System (GNSS) unit was used for both mapping and conducting scarp profiles where UAV flights were not feasible. Vertical and horizontal GPS positions were differentially corrected to get precise locations of points and lines. Vertical precisions of the data following differential correction were on the order of 10-15 cm.

3.3.2.1 Photogrammetric DSMs

I created high-resolution DSMs and orthmosaics using the SfM photogrammetry technique (Westoby et al. 2012) over the Torlesse fault at the Blackley, Whitewater, and the Porter River terrace sites (Fig. 3-1B). A UAV was flown 100-125 m above the ground over the sites (Table 3-2). All surveys

were scaled and positioned using Geo7x-surveyed ground control points (GCPs) located throughout the surveyed extents.

Table 3-2: Details of UAV surveys in the study areas.

Place	Area (Km^2)	No of images captured	Flying height (m above the ground)	No. of GCPs
Blackley area	0.39	465	109	9
Whitewater terrace	1.1	1087	108	13
Porter terrace	1.21	948	123	18

An image overlap of 60-80% with fixed zoom photography was used for the image capture setting in order to generate the DSMs with a resolution of around 10 cm. The heights of the UAV surveys were planned in order to maintain a ground sample distance of about 3 cm/pixel. DSMs and orthomosaics were built in Agisoft Metashape Professional.

3.3.3 Offset measurements/calculations

Offset measurements across fault scarps were acquired using profiles generated from the DSMs and Geo7x surveys. Vertical and horizontal separations of offset geomorphic features (e.g., streams, spurs, terrace treads and risers) were measured. The MATLAB-based toolbox Lateral Displacement Calculator (LaDiCaoz) (Zielke and Arrowsmith, 2012) was used to evaluate both horizontal and vertical offsets for laterally displaced channels, spur, and terrace risers. I applied LaDiCaoz to the DSMs, which worked acceptably, though the toolbox was mainly developed for estimating lateral and vertical offsets in lidar-derived DEM data. Linear geomorphic features (e.g., channels, thalwegs, terrace risers, spurs) from the hanging wall and the footwall were projected onto the fault scarp to calculate the horizontal and vertical slips.

Calculations performed with LaDiCaoz depend on comparing pre-earthquake and post-earthquake linear geomorphic features. Resultant estimates may have large uncertainties. Careful placing of fault and projection lines as well as careful inspection of back-slipped topography are fundamental aspects of reducing uncertainties from the LaDiCaoz method. Back slipped topography ensures the computed offset values as close as possible to the actual amount.

Vertical and horizontal offsets of geomorphic features in forested and remote areas were estimated manually using tape and compass. Where no horizontal component of slip was observed, dip-slips on faults (e.g. from the Porter River terrace) were estimated following a Monte Carlo simulation method (Thompson et al. 2002) using the tool Monte Carlo Slip Statistics Toolkits (MCSST)

(Wolfe et al. 2020) at the 95% confidence range (Fig. 2-4). Different input parameters like slopes of surfaces, fault dip, and fault position were used in the dip-slip calculation (Fig. 2-4).

3.3.4 Slip rate calculation

Slip rates were calculated using the cumulative slip and constrained ages of the displaced geomorphic features (streams, spurs, terrace treads, risers etc.) in the region. Both vertical and horizontal slip rates were estimated for faults with strike-slip and dip-slip components. Slip rates of the dip-slip faults (e.g., from the Porter River terrace) were estimated at the 95% confidence range following the Monte Carlo method (Thompson et al. 2002) using MCSST (Wolfe et al. 2020) (Fig. 2-4).

3.4 Results

Mapping revealed distinct geomorphic sections within the Torlesse fault zone, defined by kinematics and interpreted relationships to the structure of the overall basin. The main Torlesse fault, which was traced from Broken River in the north to the Porter River in the south (Fig. 3-1B) passes through the bedrock of the Torlesse Range. It displaces spurs, debris fans and fluvial terraces. Fault traces also traverse the basin, displacing terraces and hillslopes. Based on variations in surface expression and position in the landscape, I divided the Torlesse fault into three sections (from NE to SW): (1) Broken River section (2) Castle Hill section and (3) Porter River section. Here, I provide field observations for the entirety of the Torlesse fault zone, identify features in the landscape that constrain possible age of faulting, and present calculations of slip and slip rate for the different sections of the fault. Finally, I summarise the findings from each section to present the general characteristics of the Torlesse fault zone.

3.4.1 Field observations

3.4.1.1 Broken River Section

The Broken River section of the Torlesse Fault extends from Broken River in the north to the Blackley Steam area in the south (Fig. 3-4). In this section, the average scarp height is c. 3 m and is associated with a depression along the uphill-facing fault scarp. Faults were observed in outcrop at landslide source areas near the Avoca Homestead and Blackley Stream. Fault gouge within shear zones was also observed at the junction of the Esk fault and Torlesse fault near Avoca Homestead and in the northern vicinity of the Blackley Stream. This fault section is further divided into four subsections, each described in detail below.

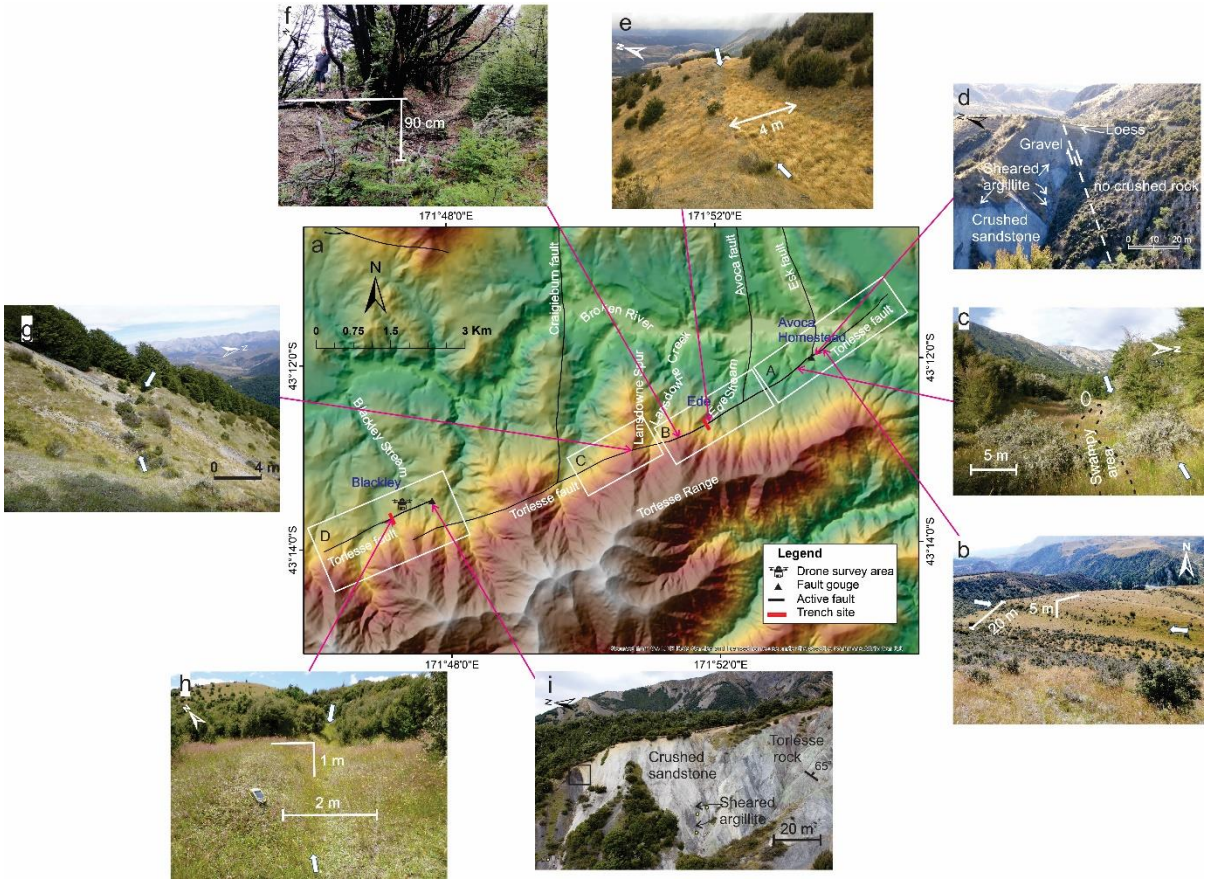

Figure 3-4. a) Location map of the Broken River section of the Torlesse Fault, with photos of the field area. Locations of photos along the fault are indicated by blank extent lines. A) Avoca Homestead area. B) Ede area C) Lansdowne Spur area. C) Blackley Stream area. b) Fault scarp with a wide depression (20 m) and scarp height of 5 m located to the south east of the Avoca Homestead. Here, terrace deposits are crosscut by the fault. Arrows show fault scarps. c) Fault scarp depression consisting of sparse vegetation. A man in the white circle shows the scale. There is a swamp in the middle part of the photo, with matagouri bushes in foreground and pine trees on either side. Arrows show fault scarps. Viewed to the west. d). The Torlesse fault passes through the landsliding area near the Avoca Homestead. It is the section view of Fig. 3-1b. The white dashed line shows the tentative orientation of the fault (dip amount around 70^o) based on the boundary between the crushed rock zone and the uncrushed bedrock. Sheared argillite and some fault gouge zones and crushed sandstone are underlying gravel deposits. Viewed towards the east. e) The Torlesse fault scarp along a spur at an elevation of 928 m above sea level. The white tent in the figure shows the scale. The white arrows represent the fault scarp. The width of the depression ranges from 2.5 m to 5 m. Viewed towards the east. f) Fault scarp 100 m west of the previous location (Fig. 3-4e). The scarp height is estimated visually around 90 cm. Depression formed in the downthrown side ranges from 3 to 5 m and consists of sparse vegetation. g) Uphill facing fault scarp on the Lansdowne spur. White arrows show the fault scarp. Height of scarp ranges from 0.4 m to 1.1 m in the area. Aspects of upthrown and downthrown sides perpendicular to the fault scarp are different. i) Sheared argillite, sandstones and gouge zones to the north of the Blackley Stream. Small circles with yellow fill show the fault plane and striae measurement locations. Strike and dip of the bed is shown towards middle right. Full-sized versions of Fig. 3-4b to 3-4i are provided in Appendix A.

3.4.1.1.1 Avoca Homestead area

Near the Avoca Homestead, the Torlesse fault manifests as a N50^{o}E trending, uphill facing scarp with a 5 to 20 m wide depression on the downthrown side. The maximum height of the fault

scarp, located to the southeast of the Avoca Homestead, measures approximately 5 m (Fig. 3-4b). The minimum measurable scarp height, located near the farm track south of the homestead, is around 1 m. A sparsely vegetated swamp exists along the 200 m long depression formed on the downthrown side of the scarp (Fig. 3-4c). Surface expressions of the Torlesse fault cease north of Broken River.

In the Avoca Homestead area, the fault scarp cross-cuts a terrace surface, which is composed of gravels underlain by Torlesse greywacke and capped by loess. This terrace is assumed to be late Otiran in age (Barrell et al., 2011). The fault is also clearly identified in an area exposed by landslides adjacent to the uphill facing scarp near the Avoca Homestead (Fig. 3-4d).

Additional, though subtler, expressions of the fault were observed near the uphill facing scarp. A small reverse fault striking N65°W with a vertical separation of 35 cm was identified in a 60 cm thick loess deposit near the uphill facing scarp (Fig. 3-4d). This fault, which has only a small offset, is interpreted as secondary to the overall normal sense of dip-slip displacement. There are no geomorphic constraints on horizontal displacements at this scarp.

A crush zone around 150 m wide was identified in the landslide area beneath ~18 m thick gravel deposits. The slip surfaces are formed parallel to, or within, sandstone and argillite beds of the Torlesse greywacke and have variable degrees of gouge thickness and development (Fig. 3-4d). The thickness of the fault gouge zones ranges from 1 cm to a few cm (Fig. 3-5). The attitude of the bedding planes measured in the area is N45°E/75° SE. The linked Bingham fault plane solution of striae from the faults processed in FaultKin software version 8.1 shows primarily northwest dipping sinistral sense of slip (Fig. 3-6) because measured striae are from the junction of the Torlesse fault and Esk fault (Fig. 3-1).

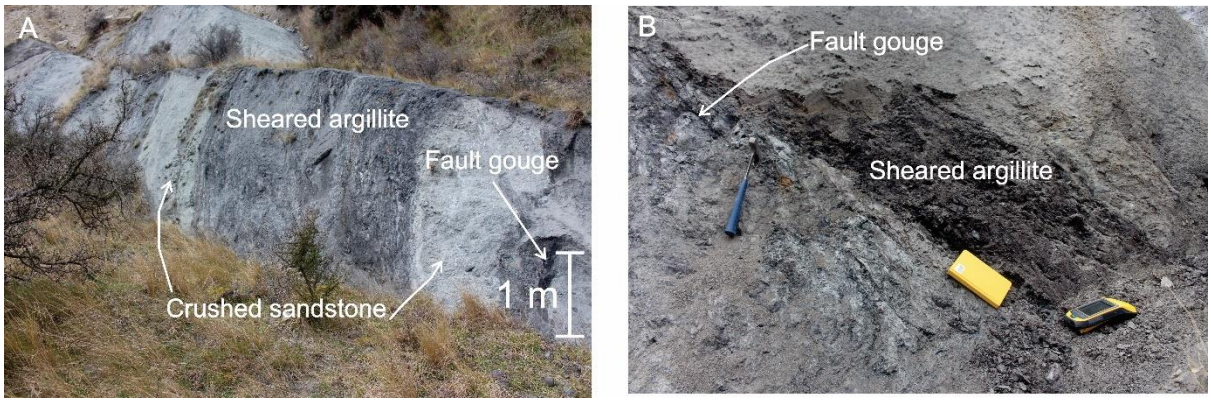

Figure 3-5. A) Sheared argillite and crushed sandstone in the landslide areas near the Avoca Homestead. Fault gouge zones in the area ranges from 1 cm to few cm in width. B) Sheared argillite and fault gouge zones.

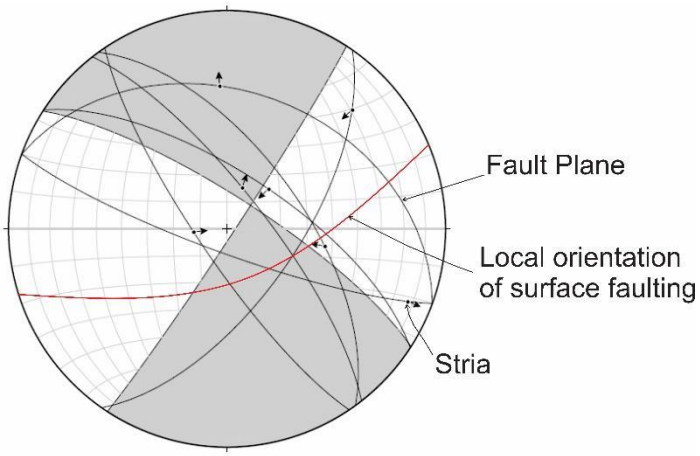

Figure 3-6. An equal area projection of seven sets of fault planes and striae measured from the fault gouge zones in the landslide near the Avoca Homestead. Arrows from the striae show the hanging walls slip directions. The striae were measured from the junction of the Torlesse fault and Esk fault which is not well denoted in outcrop. The linked Bingham fault plane solution was processed using FaultKin software version 8.1. It shows dominant slip as a northwest dipping sinistral faults which is resulted due to measurement at the junction. The dip of the surface faulting is estimated (~70^o) by tracing fault scarp downwards following the boundary between crush rock and uncrushed rock at the landslide near the Avoca Homestead (Fig. 3-4d). Striae measurement location is at the junction between the Torlesse and Esk faults, and NW predominant strikes of fault planes containing striae are obtained from NW striking Esk fault.

3.4.1.1.2 Ede Stream area

Approximately 2.5 km to the southwest of the Avoca area, a fault scarp is traceable from the left bank of the Ede Stream to the drainage divide of Lansdowne Creek (Fig. 3-4a and 3-7). The area is characterised by sparse vegetation and dead trees, most of which were found along the fault scarp on the left bank of Ede Stream. The maximum height of the uphill facing fault scarp in this section is 1.2 m, measured on the left bank of Ede Stream (Fig. 3-4e). A depression ranging in width from 2.5 to 5 m is present along the downthrown side of the fault on the north-facing slope, where an abandoned channel is displaced dextrally. Stands of thin vegetation are present in the depression (Fig. 3-4f). The height of the scarp in this area is approximately 90 cm.

A single measurement of a bedrock fault comes from an expression in the Ede Stream area. The main fault scarp is around 50 m from the sandstone containing striae located on the left bank of the Ede Stream. The main fault scarp is obscured by the debris deposit on the channel, however, the fault location is determined by the depression formed adjacent to the fault scarp on either side of the stream. The plane containing striae is sub parallel to the bedding plane, but the confidence level on striae is low since gouges or crushed rock were not identified in this area. Rather the striae identified in the sandstone is assumed to be on the fault plane. A stria measured in the fault plane in the sandstone bed shows the dextral slip sense (Fig. 3-8). The attitude of the bedding plane measured in the sandstone is N70^{o}E/70^{o}SE.

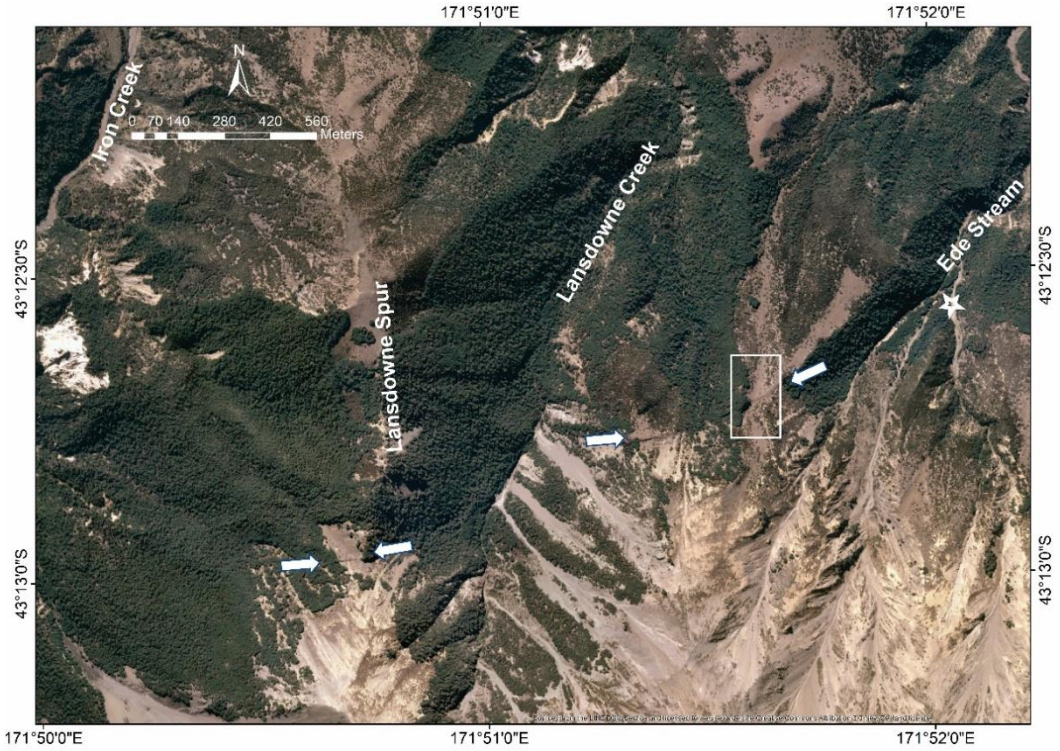

Figure 3-7. Google Earth image showing faults scarps at the Ede Stream area and Lansdowne Spur. The white arrows show the fault scarp near the Ede Stream and at the Lansdowne Spur. The rectangular white box shows the DSM developed area from the GPS points which were collected using Geo7x. Location of sandstone containing stria is denoted by a white star.

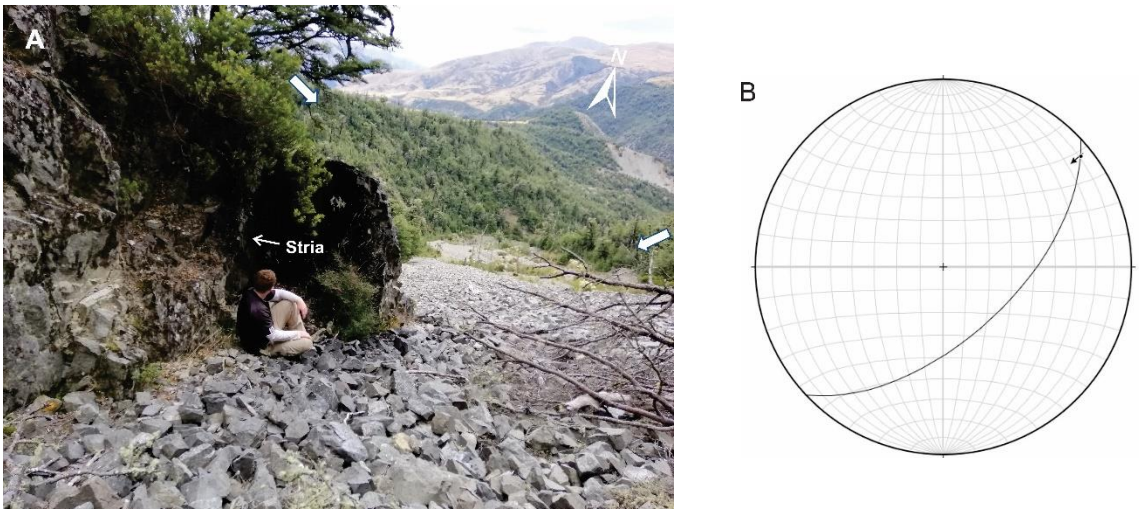

Figure 3-8. A) Location of stria measurement in the sandstone bed at the Ede Steam area. Fault plane consisting stria is sub parallel to bedding at the location. Thick arrows represent fault scarp. B) An equal area projection of the fault and striation measured at the Ede Stream area. An arrow showing the movement direction of the hanging wall.

3.4.1.1.3 Lansdowne Spur

No traces were identified across the steep topography in the transition from the Ede Stream area to the Lansdowne Spur area, where they are potentially obscured by scree deposits. A 0.4 to 1.1

m high uphill facing scarp was observed near Lansdowne Spur at an elevation of 1200 m (Fig. 3-4g). Here, the fault scarp is continuously traceable for ~200 m. A 2-4 m wide depression with thin vegetation has formed on the downthrown side (Fig. 3-4g). Colluvium and scree consisting of angular fragments of Torlesse greywacke were identified in the area along the fault scarp. Scree deposits that span the upthrown and downthrown fault blocks are displaced by the fault, disconnected by the uphill facing fault scarp. Evidence of a similar grade of weathering in the scree on both blocks suggests that the deposit was once continuous and has experienced displacement due to a potentially very recent surface rupture. Lateral offset was evident in Lansdowne spur, and in the uphill facing scarp, where measurements of hillslope aspect taken above and below the scarp varied (Fig. 3-4g).

3.4.1.1.4 Blackley Stream area

Approximately 6.5 km southwest of the Ede Stream area, in the Blackley Stream area, the Torlesse fault is identifiable as a fault scarp displacing spurs and a debris fan. Due to vegetation and steep topography, the observations presented here mostly come from analysis of the SfM DSM of the area (Fig. 3-9).

A fault scarp displaces a debris fan and two ancillary faults offset spurs near Blackley Stream. A c. 20 m thick debris fan deposit is found on the right bank of the Blackley Stream, which is transected by the Torlesse fault ~45 m above Blackley Stream. The height of the fault scarp ranges from 40 cm to 1 m and the width of the depression formed by the faults ranges from 1.5 m to 3 m (Fig. 3-4h). The ancillary faults, located 300 m apart, display lateral offset and form a step over. The faults on the northwest face of the Torlesse Range manifest as uphill facing scarps (Fig. 3-4a).

Two small abandoned channels were identified in the debris fan deposit. The channels, with paleaoflow towards the north, are located about 20 m away from each other and are laterally offset (Fig. 3-10). The easternmost channel shows truncation adjacent to the fault scarp to the north, which suggests the formation of a new channel in the upthrown side after faulting, along with abandonment of the previous channel.

I observed crush zones roughly 200 m wide in a tributary of Blackley Stream. Crushed sandstone and sheared argillite with fault gouges were identified in the area. The thickness of the argillite zone reached up to 10 m (Fig. 3-4i and 3-11). Striae measured on fault planes (Fig. 3-12) revealed a mixture of east-striking dextral faulting and dip slip faulting (Fig. 3-13).

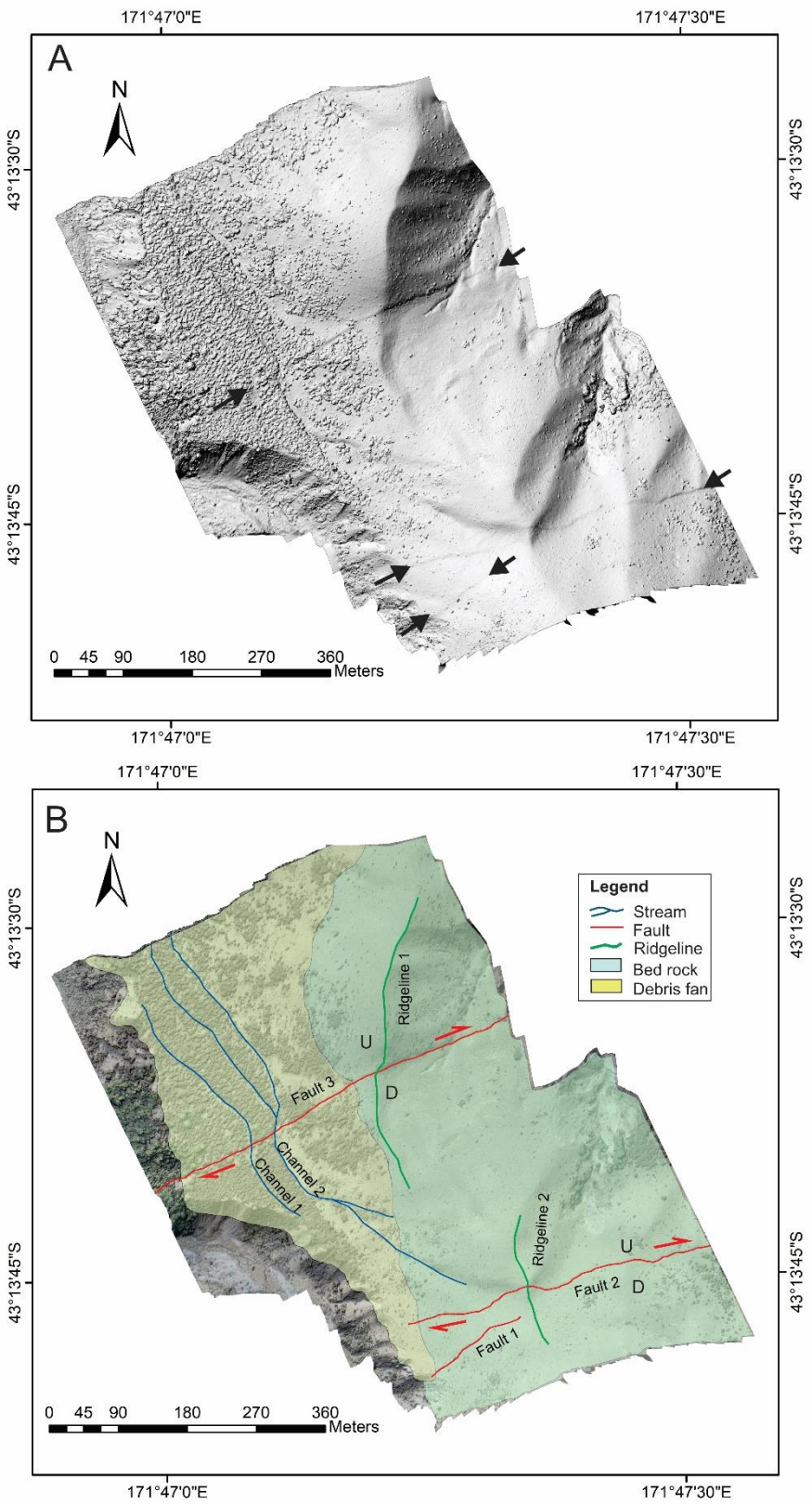

Figure 3-9. A) DSM of the area near the Blackley Stream. Black arrows in the DSM show three fault scarps and yellow rectangle indicates trench location (see detail in Chapter 4). B) Geomorphic layer overlain on the DSM of the Blackley area. Debris fan and bedrock both are displaced by faults. U in the figure represents upthrown side while D represents downthrown side.

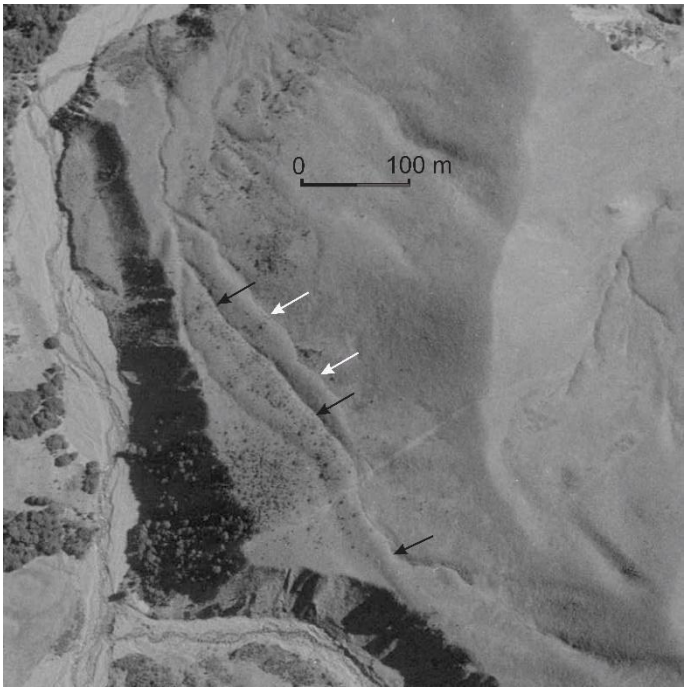

Figure 3-10. Aerial image taken in 1948 showing the offset streams at the debris fan deposit near the Blackley Stream. One stream towards east is beheaded. Black arrow shows the younger abandoned channel white arrows denote older abandoned channel. Aerial photo provided by Land Information New Zealand (LINZ) CC-By 3.0, available at http://retrolens.nz.

Figure 3-11. Zoom of rectangular area of Fig. 3-4f. The crushed zone consists of dark grey coloured sheared argillite and light grey coloured crushed sandstone in the Blackley area. A Niwashi in the centre of the photo shows the scale. The boundary between the two types of rocks is sub vertical.

Figure 3-12. Crushed zone near the tributary of Blackley stream area showing striae (oriented in the direction of pencil) in the fault gouge. Location of the cataclasite zone is in the bottom left corner of Fig. 3-4i.

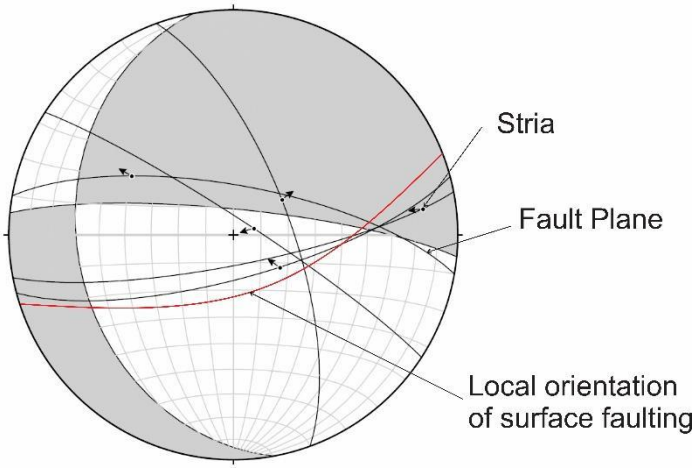

Figure 3-13. Fault plane solution of data obtained from fault gouge and cataclasites. Three faults in the area orient along west and two along east. The linked Bingham fault plane solution shows the strike-slip fault with some dip-slip (reverse) component.

3.4.1.2 Castle Hill Section

The Castle Hill section ranges from south of Blackley Stream to the southwest of Whitewater Stream (Fig. 3-1). This section consists of two fault traces: the main fault, which passes through the rangefront, and a splay that passes through the basin (Fig. 3-14a). The main fault is in the Ghost Creek area and displaces colluvium at the northern face of Mt. Plenty. The average scarp height observed in this area is ~0.6 m and the average width of the depression formed by the scarp is ~3 m, measured at the south end of Ghost Creek. An outcrop of fault rocks, consisting of crushed sandstone and sheared argillite, is present along the fault trace north of Ghost Creek. A splay of the main fault displaces

terraces along Whitewater Stream and terraces near the Ghost Creek. Fault scarps on the terraces have an average height of ~0.8 m, while the width of the depression formed by the scarp varies from less than 1 m to 4 m.

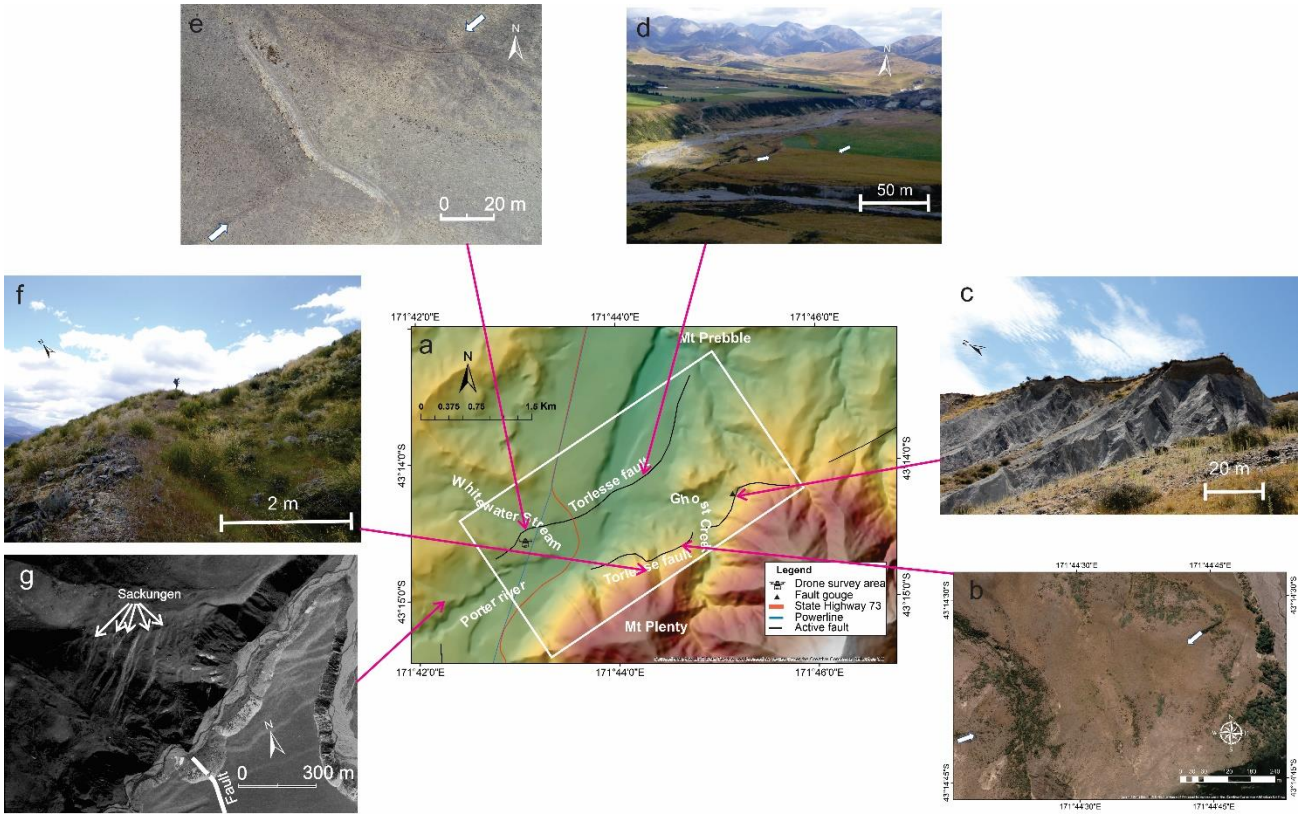

Figure 3-14. a) Map showing the Castle Hill section of the study area represented by rectangular box. b) Google Earth image showing an uphill facing scarp located to the south of the Ghost Creek. c) Crush zone in the Torlesse bedrock north of the Ghost Creek. d) Fault scarp on the terrace near the junction of the Ghost Creek and the Porter River. e) Fault scarp on the terrace in the Whitewater area. f) An uphill facing scarp formed at the western slope of Mt. Plenty with depression of 1.2 m is identified as Sackung. g) Sackungen formed on the northern slope of the Porter River valley. Many sackungen running parallel to each other are confined on the spur. The scarp height of sackungen range from less than 0.5 m to around 3 m in the area. Aerial photo no. 2759/36 taken in 1959, provided by LINZ CC-By 3.0, available at http://retrolens.nz. White thick arrows in the figures indicate fault scarps. Full-sized versions of Fig. 3-14b to 3-14g are provided in Appendix B.

3.4.1.2.1 Ghost Creek area

The Ghost Creek Area of the Castle Hill Section extends along the base of Mount Plenty to the valley north of Ghost Creek (Fig. 3-14a). A prominent 0.5 m to 1.0 m fault scarp is present at the rangefront to the south of Ghost Creek. The width of the depression formed on the downthrown side of the fault ranges from 2 to 3 m (Fig. 3-14b).

Recent fault activity is evident from the displacement of debris features that span the fault. A debris fan and a colluvial deposit are both laterally offset (Fig. 3-14b). Additionally, fault rocks were found in a landslide near Ghost Creek (Fig. 3-14c). The fault rocks consist of crushed sandstone,

sheared argillite, gouge, and breccia (Fig. 3-15). The linked Bingham fault plane solutions carried out on striae measured in the fault gouges show the main slip type of the fault is dextral normal (Fig. 3-16).

Figure 3-15.Fault gouge zone (dark unit) to the north of the Ghost Creek where striae were measured (below the hammer). Grey unit is crushed sandstone.

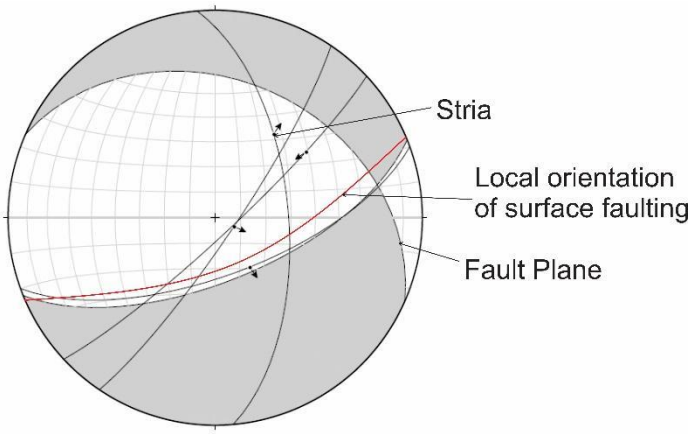

Figure 3-16. Linked Bingham fault plane solution of fault planes and striae from fault cataclasites/gouge zone north of the Ghost Creek indicates dextral normal faulting. Dip of the surface faulting is estimated from the orientation of fault trace on the topography.

3.4.1.2.2 Whitewater Stream area

The Whitewater Stream area of the Castle Hill section ranges from Prebble Hill in the north to Whitewater Stream in the south (Fig. 3-14a). The area consists of terrace and fan surfaces displaced by the Torlesse fault (Fig. 3-17). The average height of the scarp formed by the fault is approximately 80 cm. The depression formed by the fault scarp ranges in width from less than 1 m to 4 m and the primary sense of slip of the fault is interpreted to be strike-slip (discussed more below).

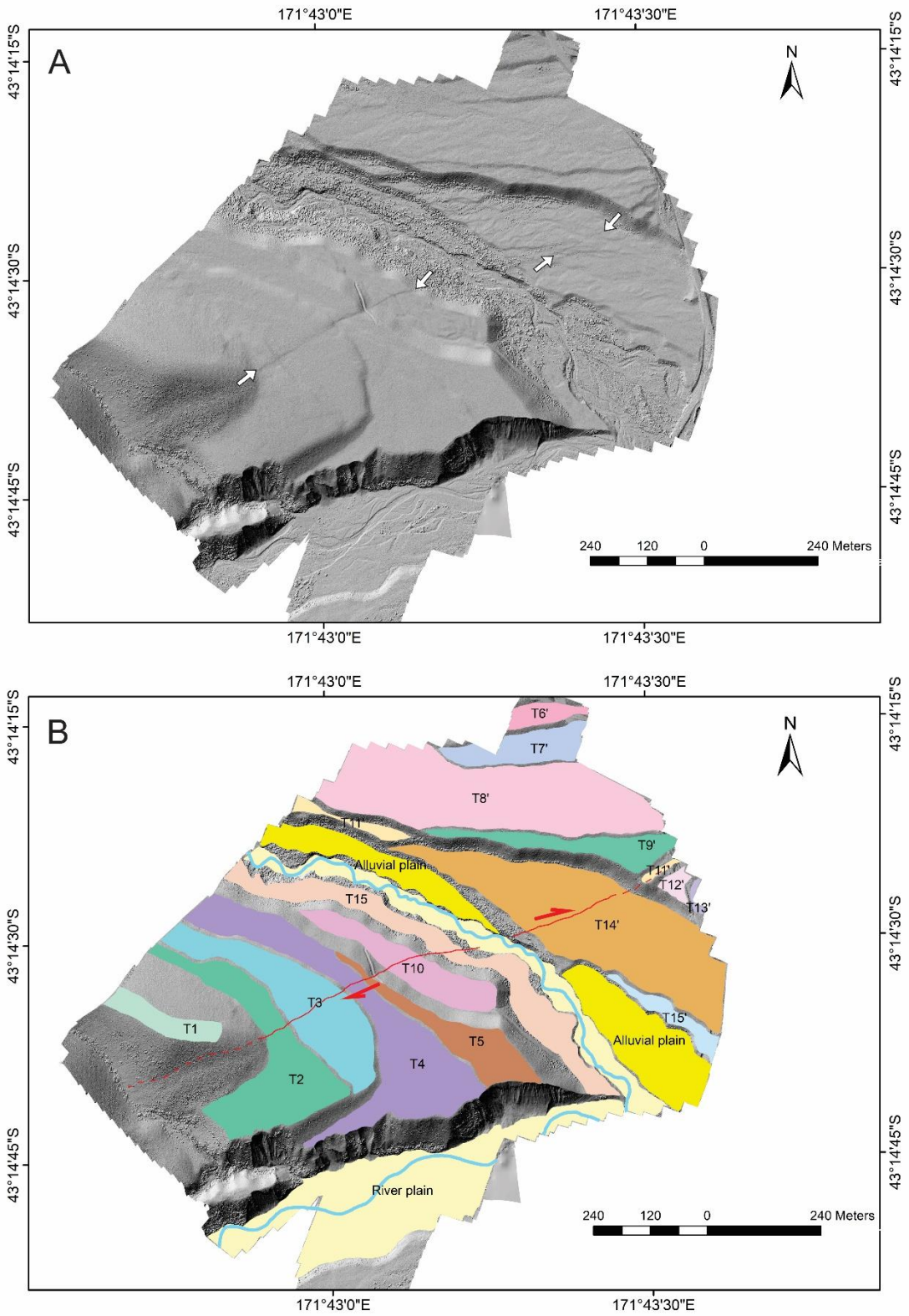

Figure 3-17. A) DSM of the Whitewater Stream terrace, where the fault indicated by the red line offsets the flight of terraces. White arrow shows the fault scarp while the red arrows represent sense of slip. B) Geomorphic map of the Whitewater Stream area. Terraces are labelled from T1 to T15' from older to younger. River plain is the youngest deposit followed by alluvial plain. Terraces to the north of the stream are named according to the elevation measured perpendicular to the stream in both terraces.

In the Whitewater Stream terraces, the scarp height ranges from 60 cm to 1.2 m. The width of the depression formed by the fault ranges from around 50 cm to 4 m (Fig. 3-14d). The fault scarp, which was not identified in the young alluvial plain (T14') of the Whitewater Stream in the field is apparent on the DSM (Fig. 3-17). The fault becomes obscure between State Highway 73 and the Porter River near Ghost Creek. The dip of the fault is estimated as sub vertical from the orientation of fault across the terrace risers (Fig. 3-14a and 3-17).

After crossing the Porter River near its junction with Ghost Creek, the fault passes through the terrace and dies out near bedrock at Prebble Hill (Fig. 3-14e and 3-18). Displacement in the bedrock at Prebble Hill is not apparent. In some places in the field, it is difficult to identify the fault scarp due to obstruction by vegetation and a small channel flowing parallel to the fault scarp (Fig. 3-18A).

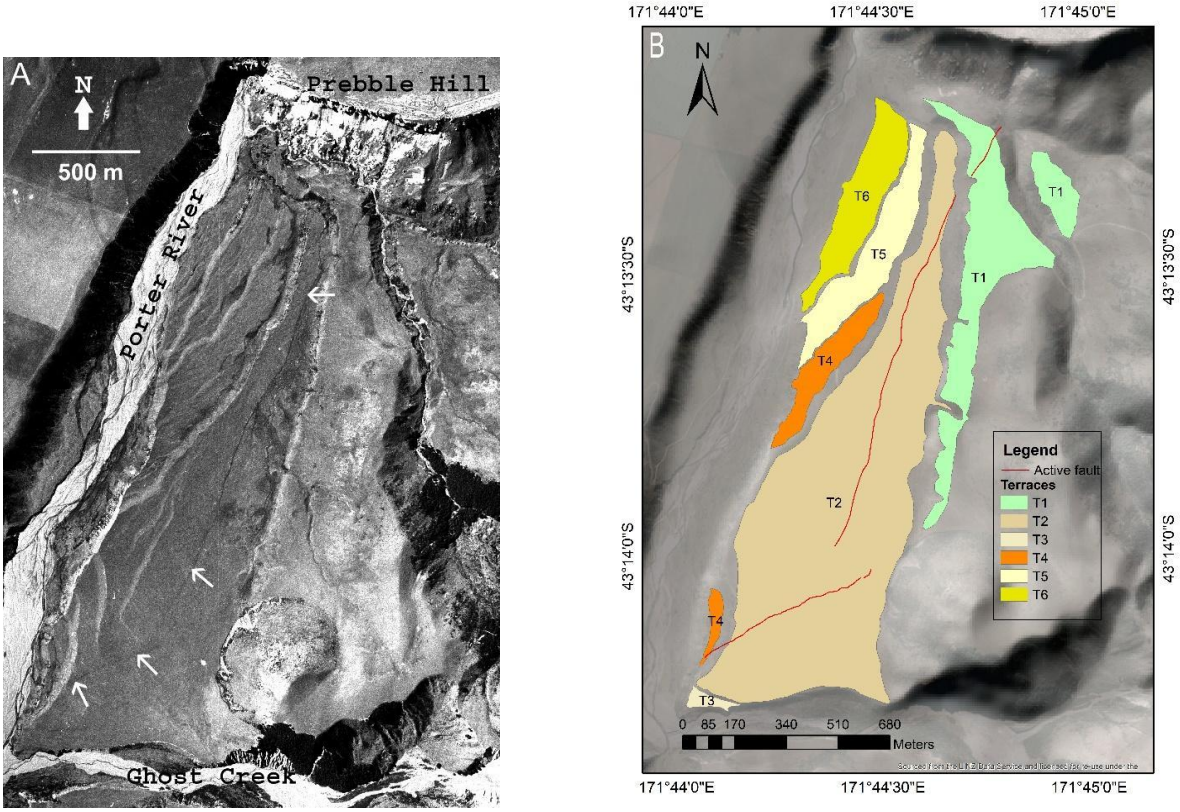

Figure 3-18. A) Fault scarps near Prebble Hill shown in the 1948 historical aerial photo no. 1685/17. White arrows show locations of fault scarps. Aerial photo provided by LINZ CC-By 3.0, available at http://retrolens.nz. B) Geomorphic map of the terrace near the junction of the Ghost Creek and the Porter River. The red line represents the active fault surveyed from the Geo7x GPS unit.

3.4.1.2.3 Additional fault-related features in the Castle Hill section

There are a number of other uphill facing scarps present along the Castle Hill section of the Torlesse fault. I mapped two uphill facing scarps on the northern slope of Mt. Plenty at elevations of ~560 m and ~542 m (Fig. 3-19). The heights of the scarps range from 0.5 to 1.5 m (Fig. 3-14e) and the lengths of the scarps are less than 200 m. These scarps run roughly parallel to the topography and the

vertical distance between the upper and lower scarps is 18 m. The main Torlesse fault passes around 120 m below the lower scarp (Fig. 3-14a and 3-19). These two higher-elevation scarps are tentatively interpreted as sackungen as they trend roughly parallel to the topography and their displacement-to-length ratio is high (McCalpin 2009).

The south facing slope to the west of Whitewater Stream and on the left bank of the Porter River consists of many uphill facing depressions roughly parallel to the topography (Fig. 3-14g). In this area, the scarp heights range from 0.5 m to 3.0 m, and the longest lineament found in the area is 412 m. These scarps are also tentatively interpreted as sackungen, though it is recognised that they might be formed by combination of gravitational and tectonic (i.e. fault-related) causes.

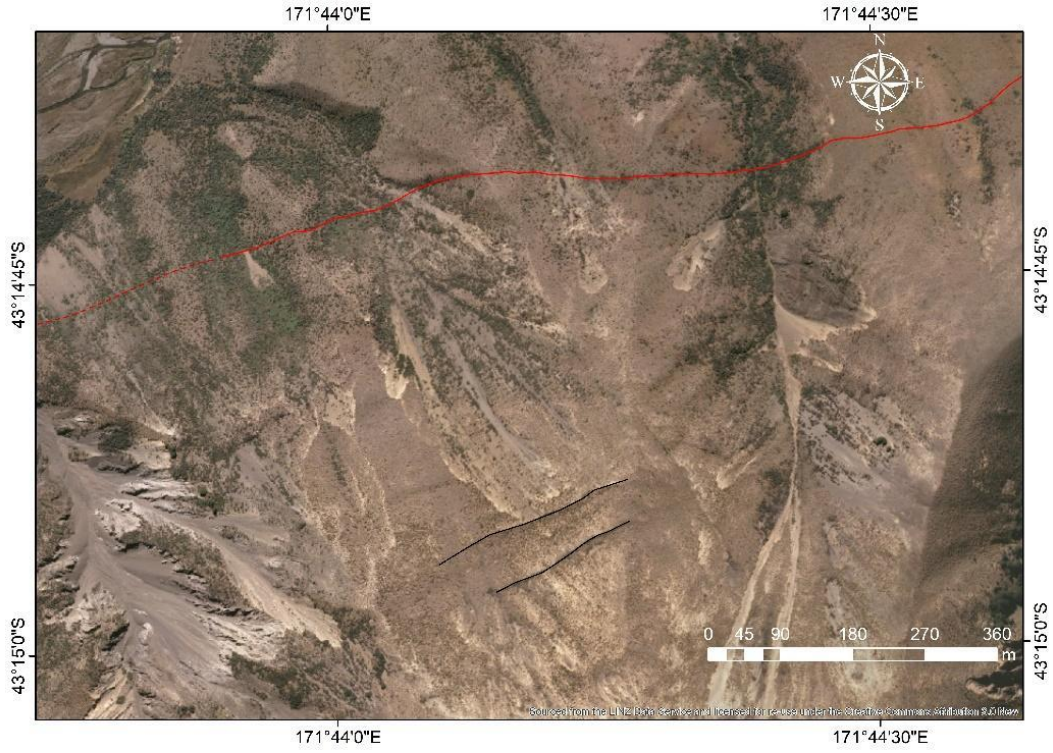

Figure 3-19. Google Earth image showing two sackungen (represented by black lines) and the Torlesse fault (indicated by red line). Solid red line shows confirmed fault (based on my mapping) while the dashed red line in the western part represents inferred fault (based on active fault database). Viewed towards the north.

3.4.1.3 Porter River section

The Porter River section extends from the junction of the Porter River and the Dry Stream in the north to the limestone quarry area (near the Porter ski road) in the south (Fig. 3-20a). Two oppositely-facing fault scarps, trending north-south and located 800 m apart, displace multiple terraces along the Porter River. The average height of the fault scarp in the area is around 3 m (Fig. 3-20). The main Torlesse fault is not identified in the Porter River section; however, it is probable that

the fault passes through upstream of the Porter River to the Coleridge Pass as this topography favours the fault.

The eastern fault displaces multiple terraces (T3, T4, and T5) (Fig. 3-20b and 3-21). Small alluvial fans on the Porter terrace (T3 and T4) have been formed by the stream flowing from the northern slope of the hill (Fig. 3-21). Small landslide scars are present within the old landslide terrain in the northern slope of the Porter River valley. Mining activity has taken place in Thomas Formation limestone. The eastern fault, with an upthrown block on the east was traced clearly from the Porter River to the small channel in the terrace (T3). The fault scarp location was determined by measuring topographic profiles across the surface in the southern part of the area (Fig. 3-22). Surface profiles (1 and 2) show the topographic breakage along the channel with the eastern side going up. The eastern fault side also bends towards the west, following the channel. Profiles across the surface show the eastern side has moved higher relative to the western side (Fig. 3-22). The fault scarp and the southern valley slope of Porter River indicate the fault dip is high angle.

The western fault dips at a low angle as the fault scarp bends toward the west in the limestone area (Fig. 3-20b). In the southern slope of the Porter River valley, a limestone bed near the fault scarp dips at 35^{o} and the bed is not displaced at an angle by the fault. I thus interpret the fault to be subparallel to bedding. There is a surface warping in the hanging wall of the western fault in the Porter terrace (Fig. 3-20d and 3-22).

These dip-slip faults are identified as secondary faults because their alignment is different from the main Torlesse fault, and they are sub-parallel to bedding in Tertiary rocks. These dip-slip faults are interpreted as flexural-slip-faults formed due to ‘shallow folding’ of the Tertiary sequence at Porter River. Another fault scarp is present to the east of T2, south of the eastern fault (Fig. 3-21). The real sense of slip is unknown and is presumed to be strike-slip as it is oriented in the N68^{o}E direction.

A recent flood-scoured exposure of a major, dextral-reverse fault in Torlesse greywacke basement, located in the upstream reach of Porter River (Fig. 3-23) (west of the western fault in Fig. 3-21) (T. Stahl, Personal Communication, January 14, 2022) supports the Torlesse fault passing parallel to the Porter River in the area. It also supports the inferred fault trace located on Qmap (Cox et al. 2007) and the previously estimated length of the Torlesse fault as being c. 31 km. Data obtained from striae measurement from the fault at this location shows strike-slip faulting with reverse slip component (Fig. 3-24). Fault scarp has not been identified on the Holocene surface hence local orientation of faulting in not included in the stereographic plot (Fig. 3-24).

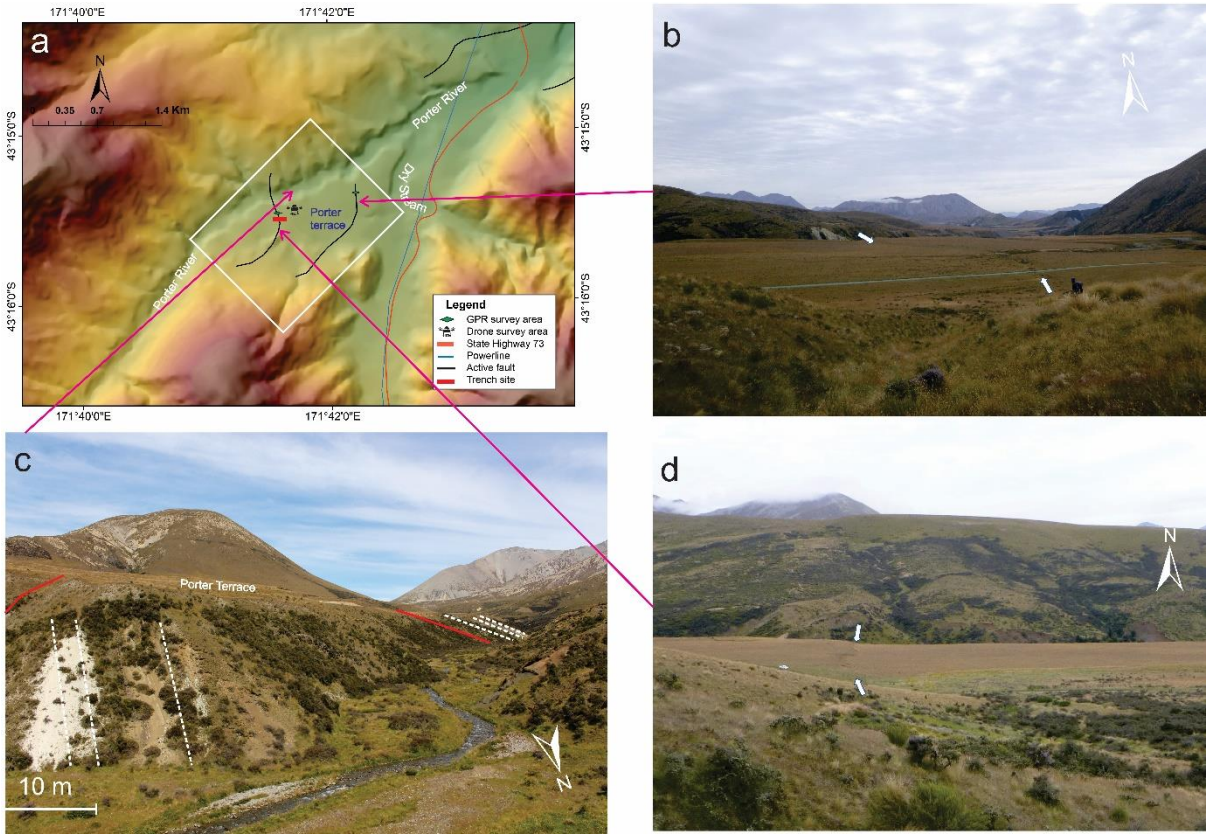

Figure 3-20. a) A white rectangular box represents the Porter River section of the study area. b) Terrace displaced by the eastern fault. c) Bedding shown on the southern slope of the Porter valley near the faults. Red line indicates fault while white dash line represents the bedding plane. d) Western fault displacing the terrace. White arrows in the figures indicate fault scarps. Zoom view of Fig. 3-20b, to 3-20d are given in Appendix C.

There is some evidence that faults in the Porter terrace are flexural slip faults. The fault planes are inferred to be parallel to the local bedding dip. The western fault coincides with the contact between indurated limestone and underlying weak tuff and the dip of the fault in a paleoseismic trench (Chapter 4) is parallel to the bedding (Fig. 3-20c). Fault gouge observed parallel to the tuff bed across the Porter River (Lombardi et al. 2020) also supports that the western fault is parallel to the bedding. The slip histories of these faults are probably related to folding in the Tertiary units and/or faulting on surrounding structures, including the bedrock fault found further upstream. Bedding parallel faults are formed due to flexural-slip faulting and the faulting is associated with the flexural slip folding (Burbank et al. 2011). The eastern fault also coincides with the contact between quartzose sandstone and tuff and is inferred to be parallel to the bedding –bedding planes in the eastern fault area dip at 70° and the fault dip is also determined to be approximately 70° based on GPR (see detail in Chapter 4).

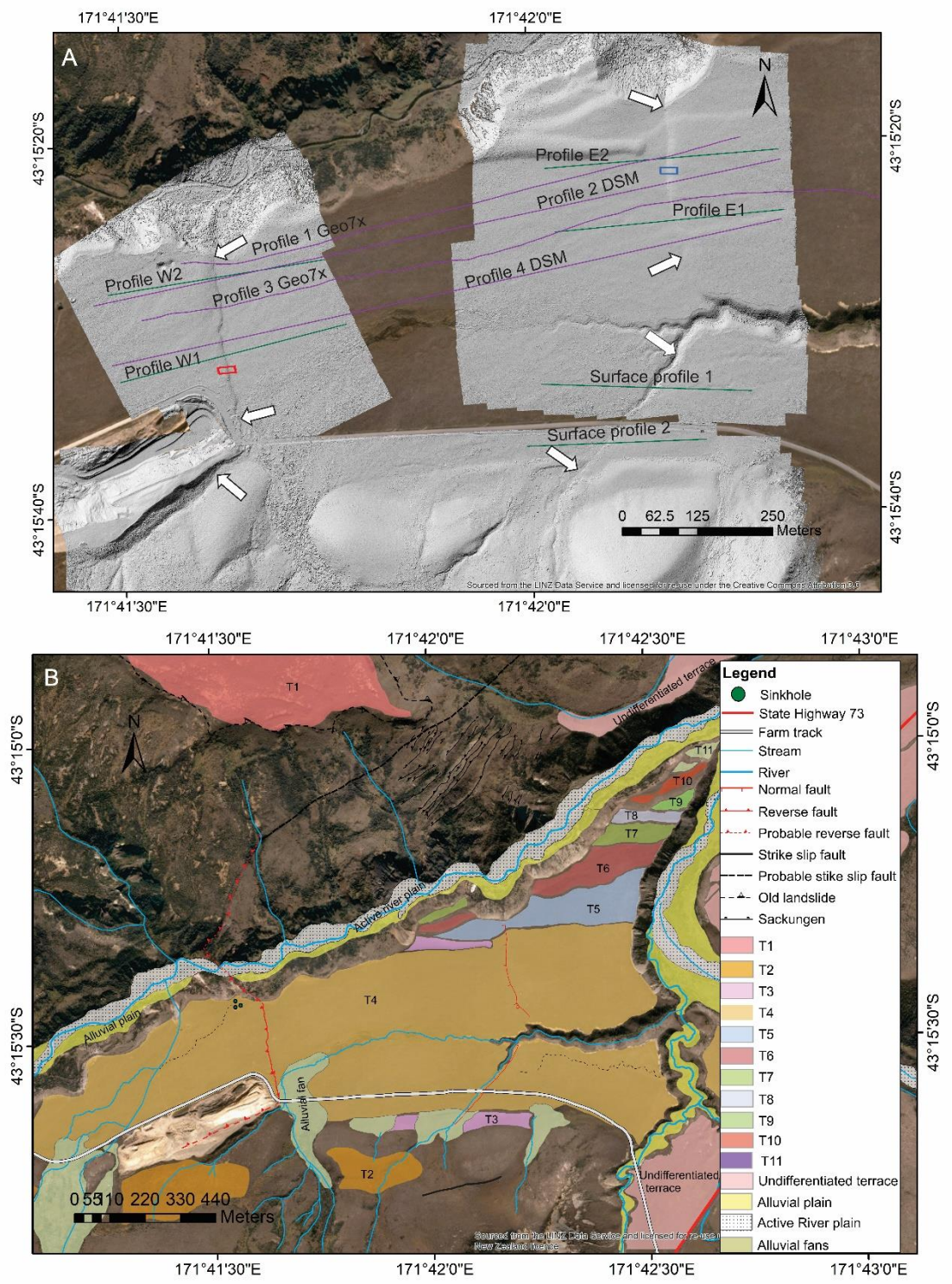

Figure 3-21. A) DSM of the Porter terrace over the Environmental System Research Institute (ESRI) base map. White arrows indicate the locations of fault scarps. Different profiles are drawn to locate fault scarp, to calculate net slip and to measure the surface warping. Purple lines obtained across the terrace are used to show the fault scarps and fold. Two surface profiles across the channel in the eastern part are used to delineate fault. Small profiles across the faults are used for net slip analysis. Blue rectangular box shows GPR survey area while the red rectangular area displays trenching area (see detail in Chapter 4). B) Geomorphic map of the Porter terrace area near Porter ski road. Multiple levels of terraces are displaced by faults in the area. Terraces are labelled from T1 to T11, from older to younger.

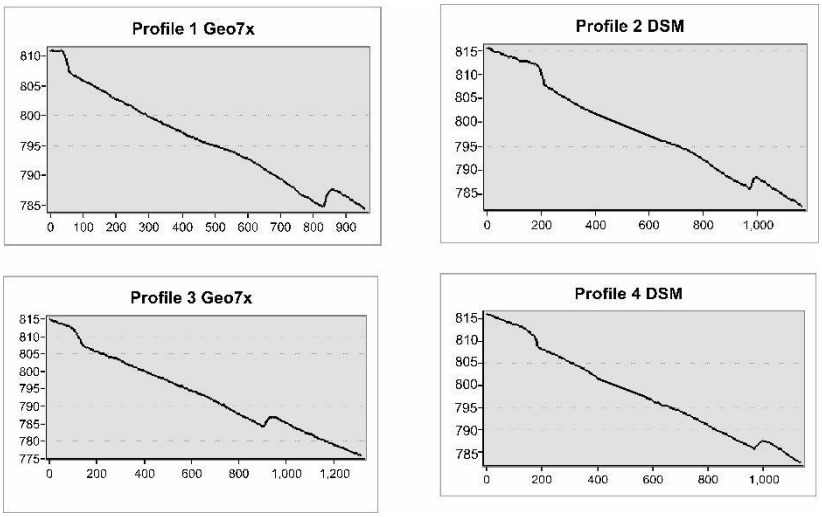

Figure 3-22.Profiles across the fault scarps in the Porter River terrace area. Two fault scarps near the two ends of the profiles are clear. Surface warping is identified about 300 m towards west from the eastern fault along each profile.

Figure 3-23. Brecciated greywacke with gouge zone identified in the upstream of the Porter River. Five striae have been measured from the gouge zone.

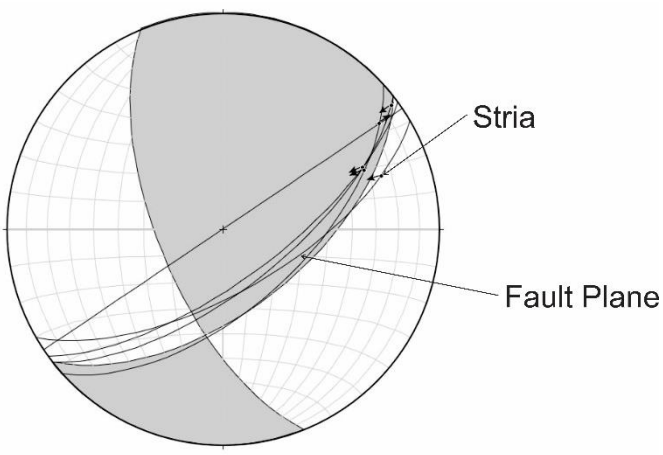

Figure 3-24. Fault plane solution of data obtained from gouge zone in upstream of the Porter River. All five faults measured in the area orient along east. The linked Bingham fault plane solution shows the strike-slip fault with dip-slip (reverse) component.

3.4.2 Regional age correlations and constraints

Numerous features across the landscape help to loosely constrain the timing of faulting. In the Avoca Area, the fault scarp crosscuts a terrace surface assumed to be late Otiran in age (Barrell et al., 2011) (Table 3-3). In the Ede area, the inferred age for the alluvial deposits emplaced by the abandoned channel is around 18,000 years (post-LGM), suggesting that fault rupture along this section of the Torlesse fault would also be post-LGM. In the Lansdowne area, the absolute age of scree displacement is not available; however, it is inferred as having occurred within a recent time as the scarp looks youthful, the scree is virtually unweathered, and the depression formed on the downthrown side consists of sparse vegetation. This location is 1.4 km from the Ede area where a very young age of faulting was identified (see detail in Chapter 4).

The inferred age of surfaces from the Whitewater Stream terrace are known. Barrell et al. (2011, 2013) attributed the Whitewater terraces (T2 to T4) as Late Otiran Outwash deposits and the young alluvial plain (T14) as the Holocene fluvial plain. For this study, the ages of the terraces T2 to T4 of the Whitewater area are inferred to be around 18,000 years. The ages of terrace deposits T9' to T15' cross cut by a splay of the Torlesse fault in the Whitewater area are inferred as post Late Otiran (Table 3-3). Alluvial plains in the area, where no displacement was observed, are attributed to the Holocene time period.

Some absolute age constraints exist from paleoseismic trenching, and these samples are discussed in detail in Chapter 5. An absolute age of the debris fan in the Blackley area was obtained from radiocarbon dating of a silty layer 60 cm below the surface in the Blackley trench. The calibrated age of the layer is 15,670-15,220 cal BP based on the radiocarbon dating of carbonaceous silts. An Optically Stimulated Luminescence (OSL)-determined age of the Porter River terrace (T4) suggests

16.4±0.9 ka, from the Single Aliquot Regeneration (SAR) method of sample collected from the sandy gravel deposit in the Porter terrace (see detail in Chapter 4). The age of displaced T3 and T5 can be inferred as late Otiran based on the stratigraphic position of terraces and the height of risers.

In summary, most of the gravel deposits displaced by the main Torlesse fault, splay and secondary faults in the study area belong to the late Otiran based on absolute dating and inferred age correlations from previous works (e.g., Barrell et al. 2011). Some features are inferred to be post-Otiran or Holocene in age.

Table 3-3:Correlation of geomorphic surfaces of Avoca, Blackley Whitewater and Porter terraces in the study area with glacial advances of Barrell et al. (2011).

MIS Stage	Glaciation	Approximate age(years ago)	Porter Terraces	White-water	Blackley	Avoca
1		0 - 11,700	Alluvial plain	Alluvial plain		
2	Late-glacial	11,700-14,500		T9'-T15'		
	Late Otiran	14,500 ~19,000	T4 T5	T6'-T8' T4 T5 T6	Debris F.	Fluvial T.
3		~21,500-28,000	T3	T2,T3		
		~45,000	T2	T1		
	Early Otiran	~45,000	T1			
4		~65,000 ~74,000				

Note: F following Debris in the Table denotes "fan" and T preceding numbers and following Fluvial denotes "Terrace". Each terrace numbers are taken from the corresponding areas.

3.4.3 Slip calculations

3.4.3.1 Broken River Section

3.4.3.1.1 Avoca Area

Measurements of vertical displacements from five elevation profiles and a measurement of fault dip (70^{o}) were used to estimate vertical slip along the Torlesse fault near Avoca. I used MCSST(Wolfe et al. 2020) to calculate slip and slip rate for the scarps. Around 5.3 m of dip-slip and 5 m of vertical slip is estimated for the fault near the Avoca Homestead (Fig. 3-14b). At the site, no features were identified to measure horizontal offset. Using the measurements of vertical displacement and an age constraint provided by a ~18,000 year old alluvial fan deposit in the area (Barrell et al. 2011), I estimate a dip-slip rate of 0.29 mm/year for the Torlesse fault at this site. It is important to note that this rate likely represents a minimum possibility for the total fault slip rate. The ratio of horizontal to vertical is around 2.5 in the Ede stream area (see section below) therefore the strike-slip rate at Avoca Homestead is loosely estimated to be 0.725 mm/year.

3.4.3.1.2 Ede Stream Area

Displacement in the Ede Stream area was measured on the dGPS-derived DSM generated for the area (Fig. 3-25). Average horizontal displacements of 10 m with a range of 8 to 12 m were determined for the Ede area. Similarly, a vertical displacement of 4 m with a range of 3 to 5 m was calculated for the same area (Fig. 3-26). Single event vertical displacement in the area, informed by displacement associated with the penultimate event in the area, is estimated to be a minimum of 50 cm (see detail in Chapter 4). The age of the displaced surface is loosely estimated as a "post glacial", i.e. ~18000 years. Therefore, loose estimation of dextral slip rate at Ede stream area ranges from 0.45 to 0.67 mm/year whereas horizontal slip rate at this place ranges from 0.17 to 0.28 mm/year.

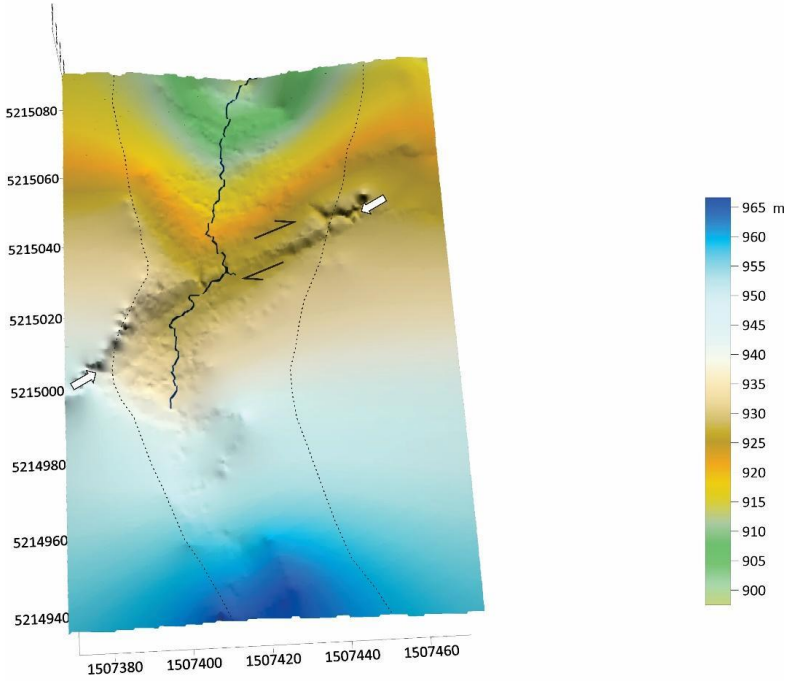

Figure 3-25. DSM of the Torlesse fault area generated by the Geo7x survey for the slip calculation purpose. Around 200 GPS points from the displaced channel were used to build DSM and that DSM was used in LaDiCaoz to calculate displacements. The dark blue line represents the thalweg while black dash lines show channel margins. The white arrows represent the fault location while the black arrow indicates the sense of slip.

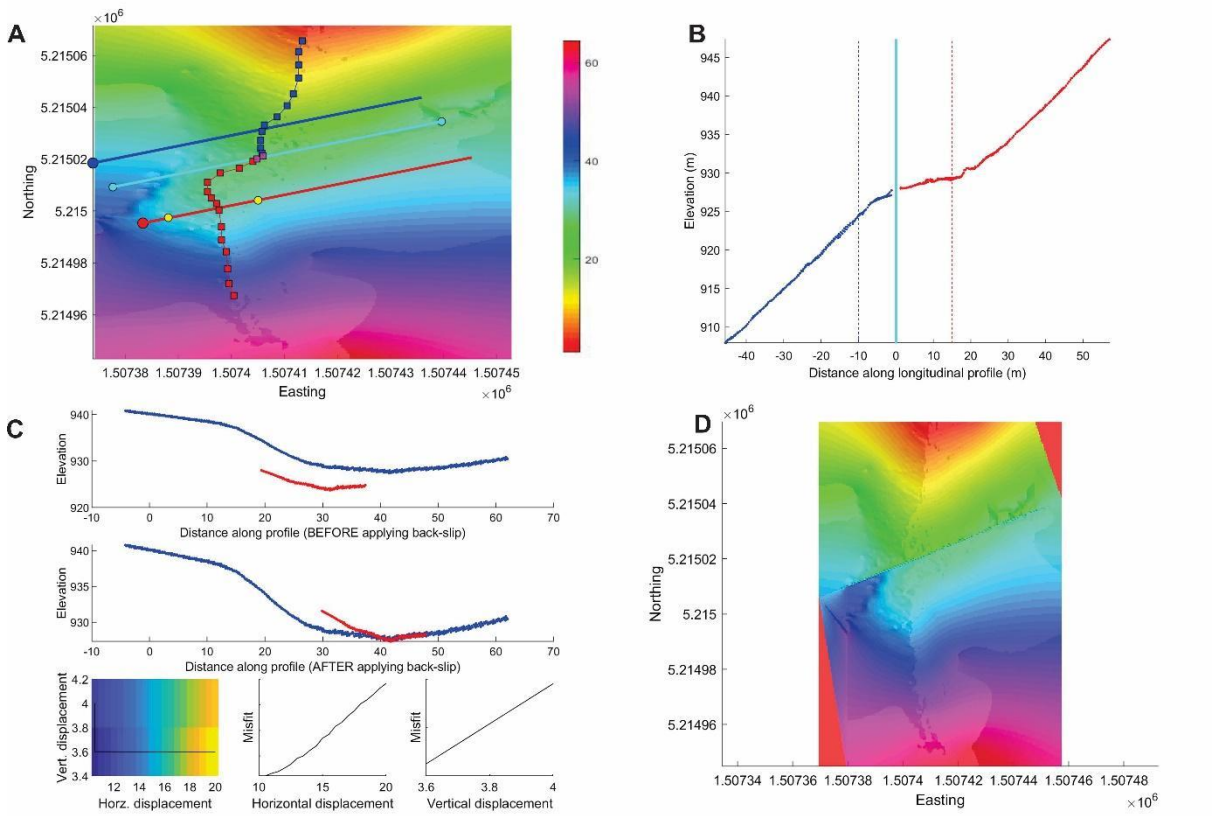

Figure 3-26. Horizontal and vertical displacement estimated using LaDiCaoz method. A) Base map with profile lines. Blue lines represent profile along the hanging wall while the red lines indicated the profile along the footwall. Colour bar represent height of the DSM in meter. B) Longitudinal profiles are the plot of elevation versus distance from the hanging wall and footwall, lines are projected up to the fault scarp. C)) Cross correlation curve, small segment of profile matched with long profile parallel to the fault scarp. Profiles across the valley parallel to the fault do not match exactly after applying back slip because the valleys in the downside and upside of the fault do not have symmetrical shape in DSM and uncertainties are associated due to development of DSM from randomly collected GPS points. To offset the channel by horizontal displacement of 10 m, there should be vertical displacement of 3.6 m and D) Back-slipped base map.

4.4.3.1.3 Lansdowne Spur

A horizontal slip of about 3 m was obtained from measuring displaced scree in the Lansdowne Spur area by measuring offset scree using tape on upthrown and downthrown block. I also measured displacement at Lansdowne Spur where I found right lateral displacement of around 3 m. While these tape and compass measurements were associated with a high degree of uncertainty, the spur and scree offsets provide possible evidence for a single event displacement along the main trace of the Torlesse fault.

4.4.3.1.4 Blackley Stream area

Two displaced channels from the debris fan deposit and ridgelines in the Blackley Stream area were used to calculate horizontal displacements (Table 3-4). The horizontal displacements in Channel 1, Channel 2 and Ridgeline 1 vary from 6 to 15 m and the vertical displacements in the same features

range from 0.8 m to 3.0 m (Table 3-4). The horizontal slip calculation on Fault 2 at Ridgeline 2 is around 4 m (Fig. 3-17).

The horizontal slip rate for the Torlesse fault calculated in the Blackley area using the above range of displacement and constrained age of the displaced debris surface (see detail in Chapter 4) ranges from 0.39 mm/year to 0.98 mm/year. Similarly, a vertical slip rate of 0.03 mm/year to 0.19 mm/year is estimated for Fault 1. Here, the ages of the deposits on the downthrown side of the fault are younger than those on the upthrown side, hence the vertical slip rate calculated in the area represents a minimum possible value.

Table 3-4: Displacements measured from the offsets features at the Blackley area.

Displaced geomorphic feature	Method used to calculate displacement	Horizontal displacement (best, range) in m	Vertical displacement (best, range) in m
Channel 1	LaDiCaoz	8, 6-12	1.2, 0.8-2.4
Channel 2	LaDiCaoz	9, 8-15	2, 1.0-3.0
Ridgeline 1	Projection of lines on fault scarp	14, 13-15	2, 1.5-2.5
Ridgeline 2	LaDiCaoz	4, 3-7	1, 0.8-1.2

3.4.3.2 Castle Hill Section

3.4.3.2.1 Ghost Creek Area

One displaced spur to the southwest of the Castle Hill Creek was used to calculate displacements in this area (Fig.3-14b). The dextral displacement is clearly visible on the surface from where a dextral displacement of 5±2 m and vertical displacement of 0.6±0.3 m was estimated at this location using a tape measure. The linked Bingham fault plane solution shows the kinematic indicator from the north of the Ghost Creek area is consistent with a dextral faulting (Fig. 3-16).

3.4.3.2.2 Whitewater Stream area

I measured horizontal and vertical displacement of the Whitewater terrace using LaDiCaoz (Zielke et al. 2012). Horizontal displacement in the Whitewater terrace varies from 3 to 14 m and the vertical displacement varies from 1.0 m to 3.0 m (Fig. 3-27) (Table 3-5). The result shows low horizontal slip towards the T2/T3 riser and higher values towards the T4/T5 riser, which is abnormal when upper terraces are assigned as older terraces. The vertical separation data shows considerable variability along strike.

Considerable epistemic uncertainty exists with the slip calculation of the fault at Whitewater terrace. The abnormal displacement pattern might be due to (1) fault attenuation, 2) formation of T2 after the formation of T4 to T10 in the area, or 3) apparent strike-slip caused by erosion rather than faulting. Regarding (1), the fault is not identifiable west of T2, suggesting that the fault likely dies out in this region. Hence, the low slip value calculated at T2/T3 is likely due at least in part to the termination of the fault trace. Regarding (2), it is possible that the glacio-fluvial deposit transported from north western mountain during 12000 to 11000 years (glacial advance) forms T1 and T2 after T4, T5 and T10. Regarding (3), it is possible that the mapped dextral offsets on lower terraces are formed by erosion rather than progressive faulting. I consider this less likely than (1) and (2), but it is worth noting that slip rates from the Whitewater terraces should be attributed a lower degree of confidence than other sites.

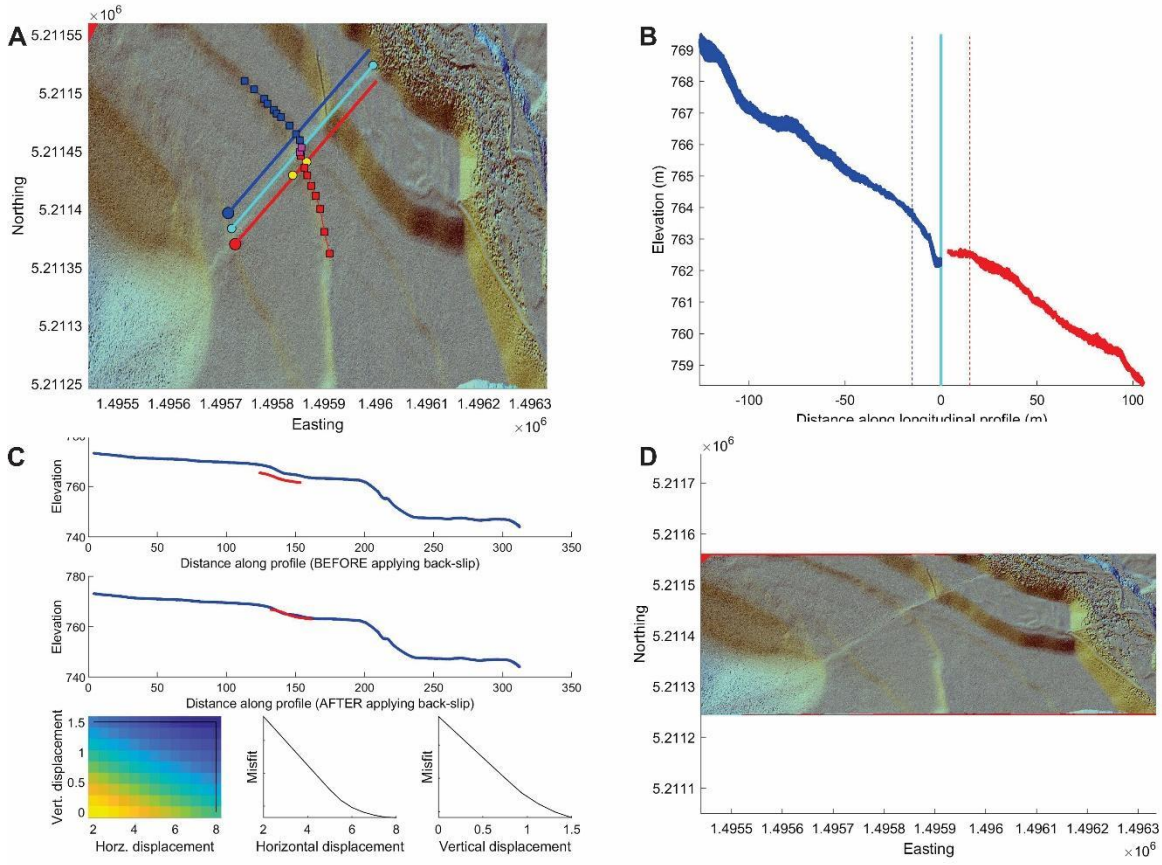

Figure 3-27. Figure showing example of horizontal and vertical slips calculated using LaDiCaoz in T3/T4. A) Base map with profile lines B) longitudinal profiles C)) Cross correlation curve; D) Back-slipped base map.

Table 3-5:Displacements measured from the offsets features at the Whitewater Stream terrace.

Displaced geomorphic feature	Method used to calculate displacement	Horizontal displacement (best, range) in m	Vertical displacement (best, range) in m
Base of T2/T3	LaDiCaoz	4, 3-7	0.8, 0.6-2.0
Base of T3/T4	LaDiCaoz	6, 5-10	2, 1.0-3.0
Base of T4/T5	LaDiCaoz	13, 8-14	2, 1.0-2.0
Base of T5/T10	LaDiCaoz	12, 6-12	1.5, 1.0-2.5

3.4.3.3 Porter River Section

I estimated slip and slip rates from both faults in the Porter River terrace using MCSST (Wolfe et al., 2020). Horizontal displacement in this area was not identified. Four profiles perpendicular to the fault scarps were collected— two from the western fault scarp and two from the eastern fault scarp (Fig. 3-21). Following (Stahl et al. 2016), a 'trapezoidal' probability distribution was assigned to the fault dip in the analysis tool to calculate net slip (Table 3-5). The range of fault dips for the western fault were estimated from stratigraphy and the trench (see detail in Chapter 4). Fault dip for the eastern fault was inferred after GPR survey across the eastern fault (see detail in Chapter 4) and mapping in the river (Lombardi et al. 2020).

The median net slips calculated for the western fault ranges from 3.36 to 5.31 m and that of the eastern fault ranges from 3.30 to 4.76 m (Fig. 3-28). Age of T3 determined from OSL is 16.4±0.9 ka (see detail in Chapter 4). The median slip rate calculated for the western fault ranges from 0.21 to 0.32, while the slip rate for the eastern fault varies from 0.20 to 0.29 mm/year (Fig. 3-29).

Table 3-6: Estimation of fault dip distribution in the Porter terrace area

Fault	Dip model	Fault dip constraints Min1, Min2, Max1, Max2	Fault position on scarp (Trapezoidal distribution) Min1, Min2, Max1, Max2
Western fault	Trapezoidal	30°, 45°, 55°, 70°	0.33,0.45, 0.55, 0.66
Eastern fault	Trapezoidal	60°, 75°, 85°,90°	0.33,0.45, 0.55, 0.66

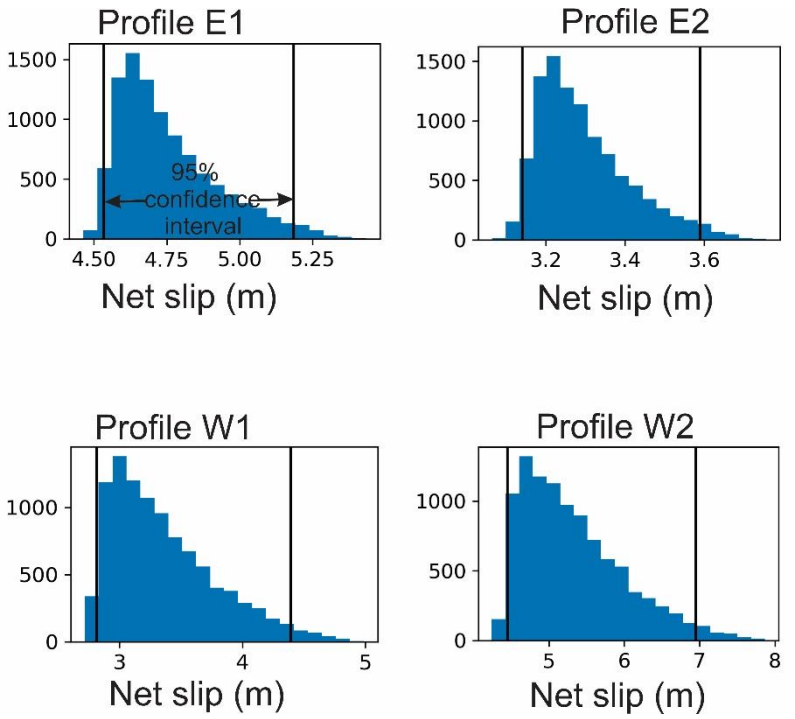

Figure 3-28. Net slips calculated on the eastern and western faults on the Porter River terrace using MCSST (Wolfe et al. 2020). Profiles E1 and E2 are taken across the eastern fault while profiles W1 and W2 across the western fault (Fig. 3-21A).

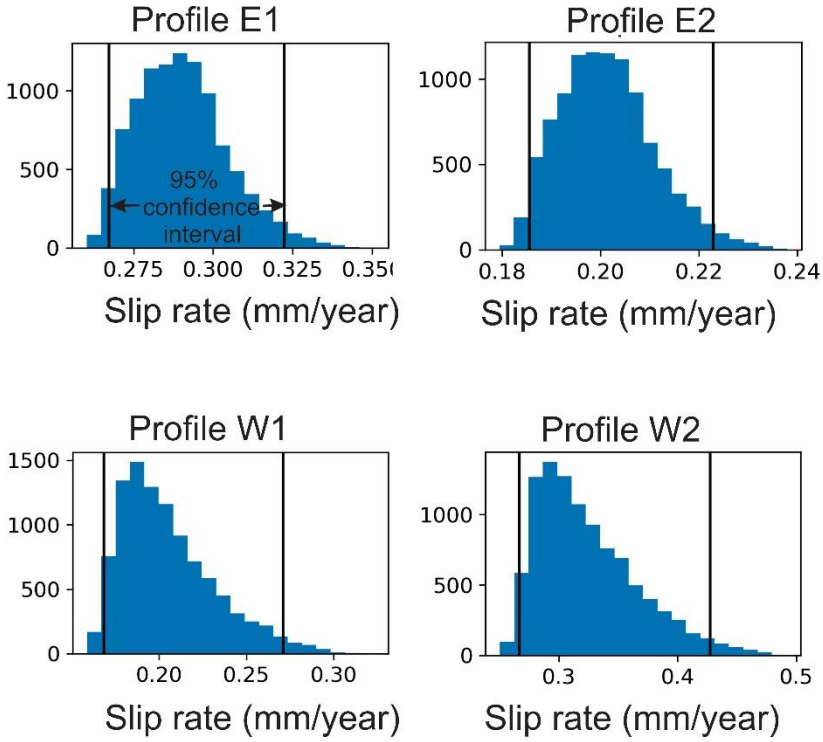

Figure 3-29. Slip rates calculated for the eastern and western faults in the Porter River terrace using the MCSST (Wolfe et al. 2020). Profiles E1 and E2 are taken across the eastern fault while profiles W1 and W2 across the western fault (Fig. 3-21A).

3.4.4 Summary of observations and interpretations from mapping, age, slip and slip rate calculation

Sections of the main Torlesse fault in the rangefront predominantly manifest as uphill facing scarps with a predominantly dextral sense of motion. Measurements of slip from limited locations along the main Torlesse fault demonstrate that horizontal slip along the fault ranges from 3 m to 15 m since ~18,000 years ago. Dip-slip likely ranges from ~0.5 m to 5.5 m in the area with associated uncertainties. Linked Bingham fault plane solutions of striae measured in the fault gouges of crush zones in the rangefront show mainly a NE striking dextral sense of slip except at Avoca where it shows strongly NW striking sinistral due to the Torlesse fault's interaction with the Esk fault. The main Torlesse fault is oriented approximately parallel to the bedding throughout the area.

Fault traces in the basin have more uncertain slip estimates. Horizontal slip in the Whitewater terrace varies from 3 m to 14 m, but is associated with some epistemic uncertainty regarding the timing and nature of displacements. Net slip of the secondary faults in the Porter terrace vary from 2.82 m to 6.96 m for the western fault and 3.14 to 5.18 m for the eastern fault at the 95% confidence range, but the relationship of these interpreted flexural-slip faults to slip on the underlying 'master' fault is unclear.

The absolute ages of the surface were measured in the Blackley area and in the Porter River terrace and used to calculate time-integrated slip rates. The radiocarbon age of the displaced surface at the Blackley area ranges from 15,670 to 15,220 cal. years BP while the OSL age of the Porter terrace (T3) ranges from 17,300 to 15,500 yr BP (see detail in Chapter 4).

Correlation of surfaces within the study area based on absolute and inferred ages shows the deposits belonging to different periods are offset by the fault.

A horizontal slip rate of 0.39 mm/year to 0.98 mm/year is proposed for the main Torlesse fault. A dip-slip rate of 0.17 to 0.43 mm/year is calculated for the western fault while a dip-slip rate of 0.19 to 0.32 mm/year is obtained for the eastern fault in the Porters terrace at the 95% confidence range. For hazard purposes, the net slip rate is best approximated by an estimate of between ~0.5-1 mm/year.

3.5 Discussion

3.5.1 Overview of geomorphic expression and relation to deeper structure of the Torlesse fault

Topographic expression of the Torlesse fault is intermittent along the rangefront. For example, in the steep slopes of Lansdowne Stream and Iron Creek, the fault scarp is not visible presumably due to more intense erosion and scree deposition. There is also variation of the fault scarp height and depression width associated with the uphill facing scarps from site to site. A relatively high (~5 m high)

fault scarp with a wider depression (~25 m) in the Avoca area (Fig. 3-4b) compared to a subtler expression in the Ghost Creek area (Fig. 3-14b) illustrates the range of this variability. The variability in surface expression has several possible explanations. Surface rupture might not occur across all sections at once and some sections that get displaced in one event may not move in others (Nicol et al. 2019), resulting in scarp height variations. Displacement may also be enhanced or subdued by gravity and the interplay of strike-slip displacement with topography in 3D. Depressions and gravitational collapse structures form due to minor extension during each earthquake (Little et al. 2018) and the various sizes of those collapse structures formed in different events may be responsible for different geomorphic expressions of fault. Vertical displacement can appear larger or smaller based on horizontal slip sense and how the fault intersects topography (Mackenzie et al. 2017).

Transfer of slip onto the Esk fault and complex structural relationships at the junction of the faults may also influence the geomorphic expression (i.e. wider depression and higher fault scarp) in the Avoca Homestead area. The sinistral slip sense at the junction of the Torlesse fault and Esk fault (Fig. 3-6) and dextral slip sense in other locations (Fig.3-13 and 3-16) of Torlesse may cause block rotations at the junction of these faults forming wide and high scarps. Sometimes short rupture length faults produce high vertical displacement and this displacement varies at different locations as on the Papatea fault in the 2016 M_W 7.8 Kaikōura earthquake (Diederichs et al. 2019). Diederichs et al. (2019) claims a localised space problem imposed by neighbouring fault within the major stepover lead to large uplift. Some combination of all of these factors could be at play.

The main Torlesse fault manifests as an uphill facing scarp with a dominant slip sense of strike-slip with a minor dip-slip (normal) component. While reverse fault scarps typically develop in transpressive settings, range-bounding, uphill-facing scarps in mid-slope positions are common throughout the hillslopes of Canterbury (e.g., Pettinga et al. 2001; Eusden et al. 2005; Howard et al. 2005). The Porters Pass fault also manifests as an uphill facing scarp on the other side of the Torlesse Range (Cowan 1992; Howard et al. 2005) and the Esk fault, which intersects the Torlesse fault near Avoca, also presents as an uphill facing scarp for much of its mapped length (Noble 2011). In all cases, even if the fault scarp displays normal sense, the master faults at depth are believed to accommodate contraction and have a component of reverse slip at depth. This is also supported by a number of striae showing reverse sense in the crush rock in the upstream of Porter River (T. Stahl, Personal communication, January 14, 2022) (Fig. 3-24 and Appendix D), Ghost and Blackley area (Fig. 3-13 and 3-16).

The formation of uphill facing scarps along hillslopes in zones of regional transpression has been associated with several factors. Topographic loading (gravity loading) on a vertical fault causing the bending of fault towards the basin (Noble 2011; Stahl et al. 2016)) (Fig.3-30), and formation of

collapsed thrust wedge in a negative flower structure on the hillslope (Eusden et al. 2000, 2005) likely contribute to forming these uphill facing scarps. Stress conditions vary in different fault systems, and the local stress field may be different from the regional stress (Holt et al. 2013), which can also lead to the formation of uphill facing scarps in compression . Another important factor is a variation of fault geometry (Lunina et al. 2008); the fault having near-vertical fault dip can rotate slightly perpendicular to the strike to create sometimes normal and sometimes reverse fault scarps. Thus, the formation of dextral normal faults in the Torlesse Range is not unusual.

The crush zones and gouges in the rangefront of the study area suggest there may be a wider deformation zone in the Torlesse terrain beneath the Torlesse fault scarp at other locations. The width of the shear zones ranges from ~150 m in the Avoca Homestead area to ~300 m in the Ghost Creek area. All shear zones are within the Torlesse supergroup rocks (Fig. 3-4d, 3-4i, 3-14c and 3-23). Shear zones of similar properties (i.e. tens of meters) have been identified in other areas within the Torlesse terrain. The Kaiwara fault and shear zone within the Torlesse terrain ranges in width from 40 to 200 m (Kellahan 1998), indicating that gouge zones are common in the brittle rock of Torlesse rocks. In almost all of the study area, the Torlesse fault behaves as a bedding parallel fault (Fig. 3-31).

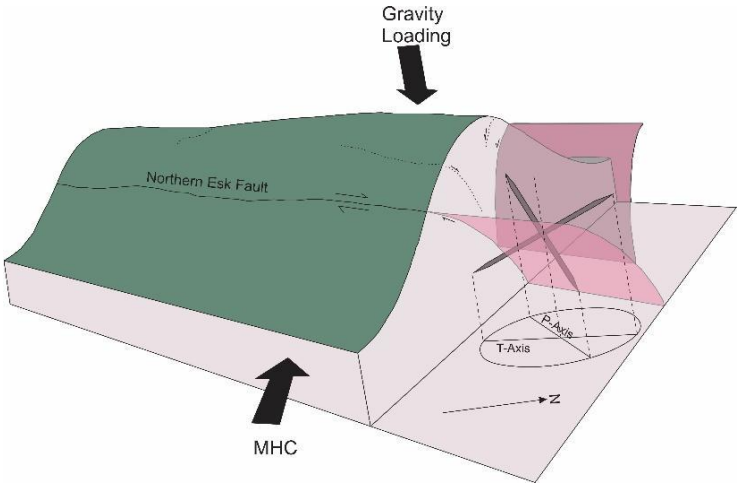

Figure 3-30. Model showing the topographic effect of gravity loading on strike-slip fault. Modified after Noble (2011). MHC in the figure stands for maximum horizontal compression and the axis of MHC is orienting northwest.

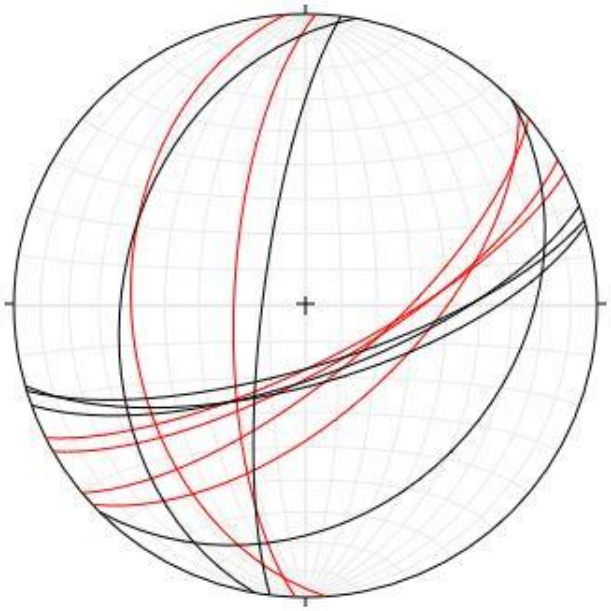

Figure 3-31, Stereonet plot (equal area projection) of beddings (represented by black lines) and fault planes (represented by red lines) measured in Avoca, Ede, Blackley, Ghost and Porter terrace area. Strike of fault plane is taken as local orientation of fault scarp at the particular location and dip estimation is based on rupture orientation on topography and other techniques including trenching (see detail in Chapter 4). N-S orienting faults are measured in the Porter terrace area.

3.5.2 Interaction with other faults in the area

Many faults north of the Torlesse Range are connected with the main Torlesse fault (Fig. 3-1B and 3-4a). Understanding the relationship between different types of faults in the region is vital for identifying deformation in the transpressive environment. The Esk, Avoca and Craigieburn faults connect with the Torlesse fault as splays to the north (Pettinga et al. 2001; Litchfield et al. 2014; Langridge et al. 2016) (Fig. 3-1B and 3-4a). The surface trace of the Torlesse fault dies out north of the Broken River area and there is a high chance that slip is transferred from the main fault to other faults (e.g., Esk fault, Avoca fault) in this area. The Avoca fault terminates within a few kilometres from its junction with the Torlesse fault, and the Craigieburn fault also passes through the area (Langridge et al. 2016), but there is very limited information available regarding these faults. There is a similarity of slip rates among the Torlesse and Esk faults, 0.5 to 0.9 mm/year (Litchfield et al. 2014). The net slip rate on the Esk fault has been identified as 0.5 mm/year (Litchfield et al. 2013) and lateral slip rate has been found as 0.8 mm/year (Noble 2011). These similar slip rates connected faults are accommodating slips in the area.

The relationship between faults within the Torlesse fault zone is complex. The main fault and the traces in the basin orient sub-parallel to each other. Generally, fault splays in strike-slip systems form acute angles (Scholz et al. 2010). The fault system within the basin exhibits such acute-angled

geometry, suggesting the subsidiary faults in the basin are splays of the main Torlesse fault. At the Porter terrace, two secondary faults oriented perpendicularly to the strike-slip faults dip in the same direction. A cross sectional view in the Porter terrace area based on geological section can generate flexural-slip faulting with two distinct dip-slip faults dipping towards one direction (Fig. 3-32). The model is similar to the Lake Grassmere area, South Island (Kaneko et al. 2015) where mudstone and sandstone beds slip past each other in the middle part of the area and the main dip-slip faults bound the region from the two sides. It is likely that dip slip faults on Porter terrace connect with the strike-slip fault extending from the Whitewater terrace towards the upstream of Porter River. However, the lack of a visible connection between the dip-slip faults and the strike-slip faults in the study area limits the interpretation of the geometry and connectivity of the faults. The southern extent of the Torlesse fault passes through upstream of the Porter River (T. Stahl, Personal Communication, January 14, 2022) towards Coleridge Pass may connect and transfer slip to the Porters Pass fault (Fig. 3-1B and 3-33 (Barrell 2013)). However, fault scarps in the Coleridge Pass area are not apparent.

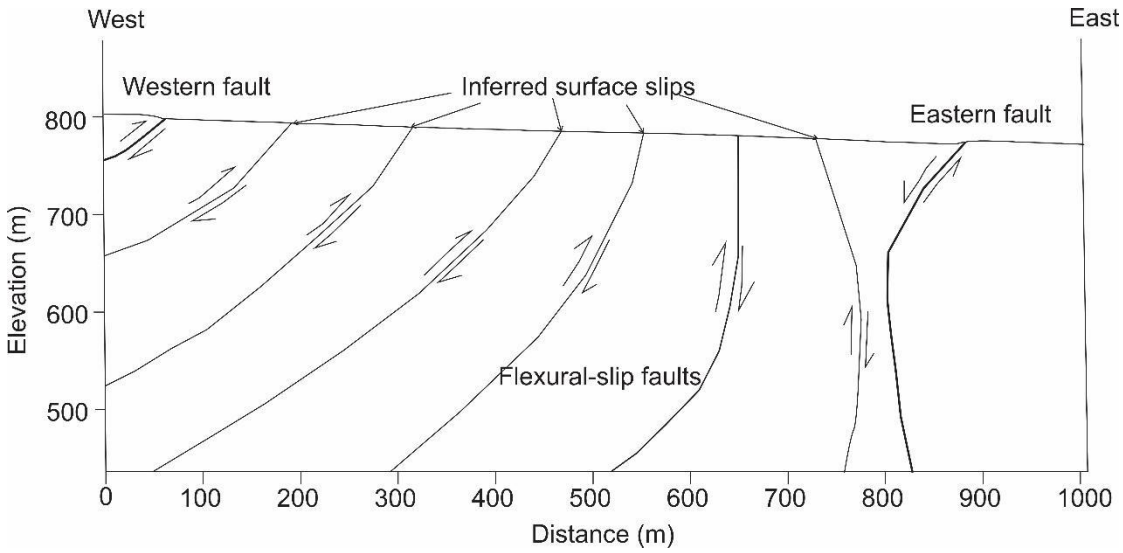

Figure 3-32. Flexural slip faults in the Porter River terrace. Faults in the western and eastern are prominent however surface slips in the middle part are inferred based on the topographic profile (Fig. 3-22). Topographic profile is obtained from Geo7x. Modified after Kaneko et al. (2015).

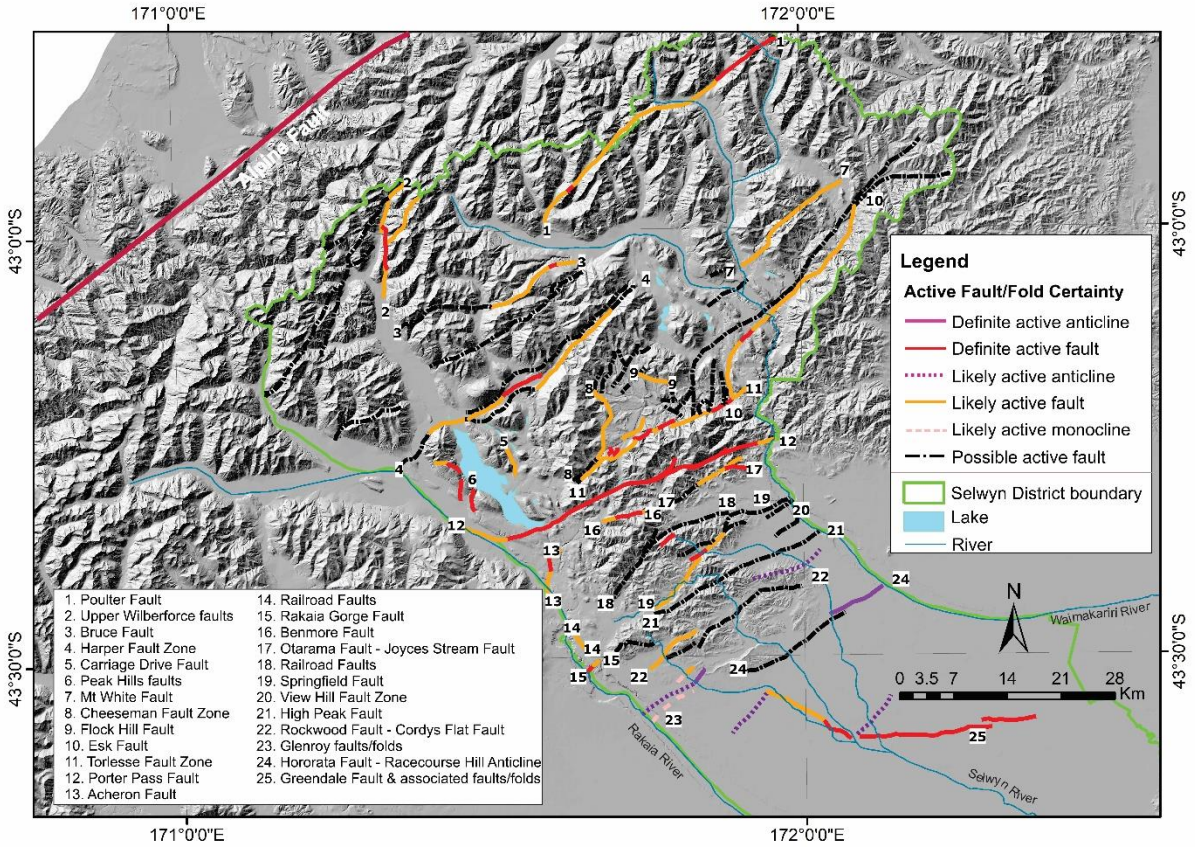

Figure 3-33. Ongoing deformation in the region (Selwyn District, North Canterbury) with the formation of folds and many NE-SW trending faults. Axis of folds are also orienting in NE-SW directions. Likely and possible active faults are orienting in different directions and shows the probability of connection among faults and folds. Modified after Barrell (2013).

3.5.3 Positive Flower Structure Model for the Torlesse Range

The Torlesse fault dips steeply to the southeast and thus must meet the west-dipping Porters Pass fault at depth (Howard et al. 2005; Cox et al. 2007; Forsyth et al. 2008). I propose that the kinematic and structural relationships observed in this study and those on the Porters Pass fault are best explained by the Torlesse Range being the long-term geomorphic expression of a positive flower structure (Harding 1985; Sylvester 1988) situated between the two primary fault zones (Fig. 3-1B and 3-4a). Positive flower structures are defined by the presence of convex upward parallel reverse or thrust faults fanning out from a single sub-vertical, predominantly strike-slip fault at depth (Sylvester 1988). Evidence supporting this proposed structure includes the presence of four nearly parallel oblique dextral faults in the Torlesse Range with steep dip (Fig. 3-34A). The macro structure formed by the faults is a 'positive flower' structure, but the uphill facing scarps are just local 'negative flowers'. A model from Nankai, Japan (Tsuji et al. 2014) is modified to show the three-dimensional schematic of the area (Fig. 3-34B).

The structure model might exhibit slip partitioning between the rangefront traces I measured in the field. Rupture on the Torlesse fault along with other linked faults in strike direction (e.g., Esk

fault) or in dip direction (Porters Pass fault) displaying slip partitioning may occur. It is possible that there is a potential 'blind' thrust at the base and that 'blind' fault might come to the surface in the future events, e.g., Hope fault (Eusden et al. 2000, 2005), Fox Peak fault (Stahl et al. 2016). Kinematics of fault traces may work as dip-slip in one event and strike-slip in another event as in Jordan thrust (Howell et al. 2020). Similarly, bimodal slip on a single fault in individual event (Barnhart et al. 2015) is also possible. In summary, slip partitioning might occur in various ways in multi-fault ruptures among the fault traces of regional 'flower' model.

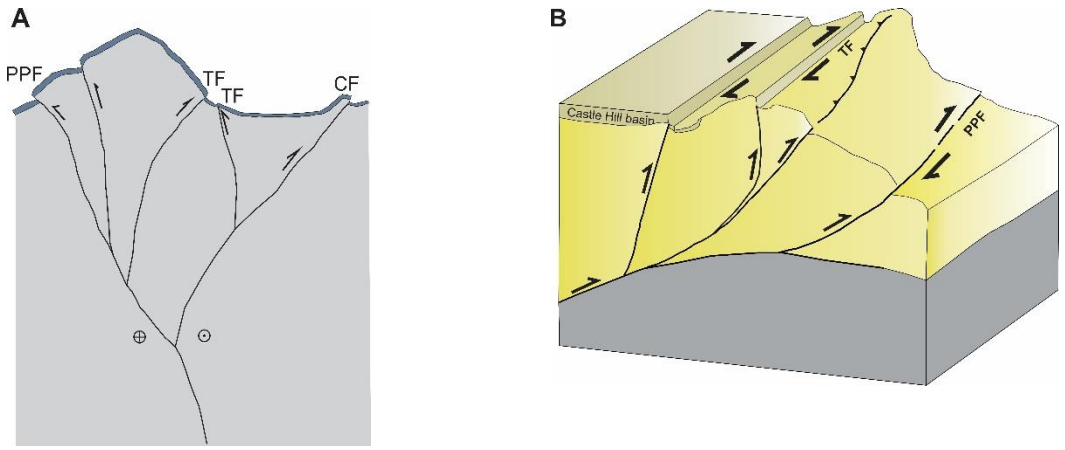

Figure 3-34. A) A flower structure model in cross section view from the limited geological data obtained from the geological map. The fault without name is the inferred dextral reverse fault. PPF: Porters Pass fault; TF: Torlesse fault, CF: Cheeseman fault. B) Model adapted from (Tsuji et al., 2014) to show the geometry of faults in the Torlesse Range with. Torlesse fault and the Porters Pass fault are in two sides of the range.

3.5.4 Surface fault rupture and seismic hazard context

The results of this study influence seismic hazard along and around the Torlesse fault. Fault displacement hazard in the study area is vital as the fault crosses State Highway 73, Coleridge Otira transmission line, and, potentially, the Trans Alpine railway track near its northern end. The probable horizontal single event displacement of ~3 m estimated from the Lansdowne spur and probable vertical single event displacement of 50 cm estimated from the Ede area for the Torlesse fault could damage infrastructure in a future surface faulting event. Moment magnitude calculated using average displacement of 3 m in empirical scaling laws (Wells et al. 1994) results in an estimated M_W 7.3 to 7.5. Using the proposed single event displacement of 3 m, a surface rupture length of 81 km to 117 km is obtained using empirical equations (Wells et al. 1994). This surface rupture length is significantly longer than the measured fault trace (~31 km) in the field. This discrepancy might be due to recent co-rupture of other faults (e.g., Esk or Porters Pass faults) in the last event (e.g., Hamling et al. 2017; Langridge et al. 2018) forming larger surface rupture length.

This study provides a structural and kinematic context for assessing co-rupture likelihoods of adjacent faults. Similarities in slip rates and kinematics with the Esk fault, which is hard-linked to the Torlesse, means that there is a non-zero probability of larger magnitude earthquakes cascading onto one from the other. The inferred positive flower structure relationship with the Porters Pass fault (Fig. 3-34) also provides a pathway for ruptures to cascade onto both faults from a master fault at depth– though the difference in slip rates means that this likely does not happen in every event.

3.6 Conclusion

This chapter aimed to document, analyse and develop the physical characteristics and rupture potential of the Torlesse fault and adjacent faults. The major findings of this chapter are:

1) The northeast-striking fault in the western slope of the Torlesse Range exhibits dextral displacement with some dip component and manifests as an uphill facing scarp over the entire length. The main Torlesse fault is parallel to the bedding throughout the area, and slip surfaces and fault gouge are observed to form within argillite beds in particular, demonstrating the influence of basement rock on, at the very least, the position of faulting in the landscape. Fault plane solutions using fault strike, dip and slip from the fault gouges of crush zones in the rangefront show a dextral sense of slip consistent with regional transpression.
2) Horizontal slip on the main fault ranges from 3 to 15 m and vertical slip ranges from 0.8 to 3.0 m at the Blackley area. Geologically-derived horizontal slip rates for the strike-slip fault calculated on the main Torlesse fault in the Blackley area varies from 0.39 to 0.98 mm/year. An overall best estimate of the net slip rate lies between c. 0.5-1 mm/year since approximately the LGM.
3) Probable horizontal single event displacement is around 3 m measured from the offset of the Lansdowne Spur, and the probable vertical single event displacement is around 50 cm, measured from the Ede area, though both values are uncertain.
4) Secondary faults in the Porter River terrace are bedding parallel flexural-slip dip-slip faults with reverse and normal sense of slip, formed by the folding of beds. Net slip varies from 2.82 m to 6.96 m for the western fault and 3.14 to 5.18 m for the eastern fault at the 95% confidence range. Similarly, slip rate for the western fault varies from 0.17 to 0.43 mm/year while slip rate for the eastern fault ranges from 0.19 to 0.32 mm/year at the 95% confidence range. While these are similar to values derived for the main Torlesse fault, and the faults may accumulate slip in Torlesse fault earthquakes (see Chapter 4), the slip rates are not directly representative of those for the Torlesse fault.

5) Based on these findings, I propose that the Torlesse fault may rupture with faults linked along-strike (e.g. Esk) or down-dip (i.e. Porters Pass) in multi-fault earthquakes. Providing structural, kinematic, and neotectonic frameworks for fault systems as presented in this study may help to refine multi-fault rupture scenarios elsewhere.

3.7 References

Baize S, Nurminen F, Sarmiento Aet al. 2019. A Worldwide and Unified Database of Surface Ruptures (SURE) for Fault Displacement Hazard Analyses. Seismological Research Letters 91: 499-520.

Barnhart WD, Briggs RW, Reitman NG, Gold RD, Hayes GP 2015. Evidence for slip partitioning and bimodal slip behavior on a single fault: Surface slip characteristics of the 2013 Mw7.7 Balochistan, Pakistan earthquake. Earth and Planetary Science Letters 420: 1-11.

Barrell DJA 2013. General distribution and characteristics of active faults and folds in the Selwyn District, North Canterbury. GNS Science. Pp. 53.

Barrell DJA, Andersen BG, Denton GH 2011. Glacial geomorphology of the central South Island, New Zealand, GNS Science.

Bradshaw J 1975. The folds at Castle Hill (Canterbury) and their bearing on Kaikouran deformation style in the Canterbury Basin. Journal of the Royal Society of New Zealand 5: 209-217.

Breed WJ 1960. River Terraces and Other Geomorphic Features, Castle Hill Basin, Canterbury, New Zealand.

Burbank DW, Anderson RS 2011. Tectonic geomorphology, John Wiley & Sons.

Butler RWH, Bond CE, Cooper MA, Watkins H 2020. Fold–thrust structures – Where have all the buckles gone? Geological Society Special Publication. Pp. 21-44.

Cowan HA 1992. Structure, seismicity and tectonics of the Porter's Pass-Amberley fault zone, North Canterbury, New Zealand.

2007 Geology of the Aoraki area, Institute of Geological and Nuclear Sciences 1: 250000 Geological Map 15. Lower Hutt, New Zealand, GNS Science.

DeMets C, Gordon RG, Argus DF 2010. Geologically current plate motions. Geophysical Journal International 181: 1-80.

Diederichs A, Nissen EK, Lajoie LJet al. 2019. Unusual kinematics of the Papatea fault (2016 Kaikōura earthquake) suggest anelastic rupture. Science Advances 5: eaax5703.

Dolan JF, Bowman DD, Sammis CG 2007. Long-range and long-term fault interactions in Southern California. Geology 35: 855-858.

Eusden JD, Pettinga JR, Campbell JK 2000. Structural evolution and landscape development of a collapsed transpressive duplex on the Hope Fault, North Canterbury, New Zealand. New Zealand Journal of Geology and Geophysics 43: 391-404.

Eusden JD, Pettinga JR, Campbell JK 2005. Structural collapse of a transpressive hanging-wall fault wedge, charwell region of the hope fault, South Island, New Zealand. New Zealand Journal of Geology and Geophysics 48: 295-309.

Fitzsimons SJ 1997. Late-glacial and Early Holocene glacier activity in the Southern Alps, New Zealand. Quaternary International 38-39: 69-76.

Forsyth PJ, Barrell DJA, Jongens R 2008. Geology of the Christchurch area. Institute of Geological and Nuclear Sciences 1:250,000 Geological Map. Pp. 1-76.

Fukuyama E 2015. Dynamic faulting on a conjugate fault system detected by near-fault tilt measurements. Earth, Planets and Space 67: 38.

Gage M 1958. Late Pleistocene glaciations of the Waimakariri Valley, Canterbury, New Zealand. New Zealand journal of geology and geophysics 1: 123-155.

Gage M 1970. Late cretaceous and tertiary rocks of broken river, canterbury. New Zealand Journal of Geology and Geophysics 13: 507-536.

Hamling IJ, Hreinsdóttir S, Clark Ket al. 2017. Complex multifault rupture during the 2016 M<inf>w</inf> 7.8 Kaikōura earthquake, New Zealand. Science 356.

Harding TP 1985. Seismic characteristics and identification of negative flower structures, positive flower structures, and positive structural inversion. AAPG Bulletin 69: 582-600.
Hart EW, Bryant WA, Treiman JA 1993. Surface faulting associated with the June 1992 Landers earthquake, California. Calif. Geol 46: 10-16.
Holt RA, Savage MK, Townend J, Syracuse EM, Thurber CH 2013. Crustal stress and fault strength in the Canterbury Plains, New Zealand. Earth and Planetary Science Letters 383: 173-181.
Howard M, Nicol A, Campbell J, Pettinga JR 2005. Holocene paleoearthquakes on the strike-slip porters pass fault, Canterbury, New Zealand. New Zealand Journal of Geology and Geophysics 48: 59-74.
Howell A, Nissen E, Stahl Tet al. 2020. Three-Dimensional Surface Displacements During the 2016 MW 7.8 Kaikōura Earthquake (New Zealand) From Photogrammetry-Derived Point Clouds. Journal of Geophysical Research: Solid Earth 125: e2019JB018739.
Jacobson D 2015. Tectonic Geomorphology and Paleoseismology of theLake Heron Fault, New Zealand. Unpublished thesis, University of Canterbury, Christchurch, New Zealand. 130 p.
Kaneko Y, Hamling IJ, Van Dissen RJ, Motagh M, Samsonov SV 2015. InSAR imaging of displacement on flexural-slip faults triggered by the 2013 Mw 6.6 Lake Grassmere earthquake, central New Zealand. Geophysical Research Letters 42: 781-788.
Kellahan H 1998. Stratigraphy and structure of the Cheviot-Kaiwara Area, North Canterbury. Unpublished thesis, Univeristy of Canterbury, Christchurch.
Langridge RM, Rowland J, Villamor Pet al. 2018. Coseismic Rupture and Preliminary Slip Estimates for the Papatea Fault and Its Role in the 2016 Mw 7.8 Kaikōura, New Zealand, Earthquake. Bulletin of the Seismological Society of America 108: 1596-1622.
Langridge RM, Ries WF, Litchfield NJet al. 2016. The New Zealand Active Faults Database. New Zealand Journal of Geology and Geophysics 59: 86-96.
Lavine A, Gardner JN, Reneau SL 2003. Total station geologic mapping: an innovative approach to analyzing surface-faulting hazards. Engineering Geology 70: 71-91.
Lin A, Chiba T 2017. Coseismic conjugate faulting structures produced by the 2016 Mw 7.1 Kumamoto earthquake, Japan. Journal of Structural Geology 99: 20-30.
Litchfield NJ, Van Dissen RJ, Sutherland Ret al. 2013. A model of active faulting in New Zealand: fault zone parameter descriptions. GNS Science. Pp. 120.
Litchfield NJ, Van Dissen R, Sutherland Ret al. 2014. A model of active faulting in New Zealand. New Zealand Journal of Geology and Geophysics 57: 32-56.
Little TA, Van Dissen R, Kearse J, Norton K, Benson A, Wang N 2018. Kekerengu Fault, New Zealand: Timing and Size of Late Holocene Surface Ruptures. Bulletin of the Seismological Society of America 108: 1556-1572.
Lombardi C, Amadon W 2020. A study of the fault activity and straitgraphy of the Porter river valley in relation to the Torlesse fault. Frontiers Abroad.
Lunina OV, Gladkov AS, Novikov IS, Agatova AR, Vysotskii EM, Emanov AA 2008. Geometry of the fault zone of the 2003 Ms = 7.5 Chuya earthquake and associated stress fields, Gorny Altai. Tectonophysics 453: 276-294.
Mackenzie D, Elliott A 2017. Untangling tectonic slip from the potentially misleading effects of landform geometry. Geosphere 13: 1310-1328.
McCalpin JP 2009. Paleoseismology, Academic press.
Nicol A, Walsh J, Childs C, Manzocchi T 2019. The growth of faults. Understanding Faults: Detecting, Dating, and Modeling. Pp. 221-255.
Noble DP 2011. Tectonic geomorphology and paleoseismicity of the Northern Esk Fault, North Canterbury, New Zealand. Unpublished thesis, University of Canterbury, Christchurch. 169 p.
Oskin M, Perg L, Blumentritt D, Mukhopadhyay S, Iriondo A 2007. Slip rate of the Calico fault: Implications for geologic versus geodetic rate discrepancy in the Eastern California Shear Zone. Journal of Geophysical Research: Solid Earth 112.

Pettinga JR, Yetton MD, Van Dissen RJ, Downes G 2001. Earthquake source identification and characterisation for the Canterbury region, South Island, New Zealand.

Pettinga JR, Chamberlain CG, Yetton MD, Van Dissen RJ, Downes G 1998. Earthquake source identification and characterisation: stage 1 (Part A) earthquake hazard and risk assessment study. Canterbury Regional Council CRC: 121.

Ricker KE, Chinn TJ, McSaveney MJ 1993. A late Quaternary moraine sequence dated by rock weathering rinds, Craigieburn Range, New Zealand. Canadian Journal of Earth Sciences 30: 1861-1869.

Ross ZE, Idini B, Jia Zet al. 2019. Hierarchical interlocked orthogonal faulting in the 2019 Ridgecrest earthquake sequence. Science 366: 346-351.

Scholz CH, Ando R, Shaw BE 2010. The mechanics of first order splay faulting: The strike-slip case. Journal of Structural Geology 32: 118-126.

Schwartz DP, Haeussler PJ, Seitz GG, Dawson TE 2012. Why the 2002 Denali fault rupture propagated onto the Totschunda fault: Implications for fault branching and seismic hazards. Journal of Geophysical Research B: Solid Earth 117.

Stahl T, Quigley M, Bebbington M 2016. Tectonic geomorphology of the Fox Peak and Forest Creek Faults, South Canterbury, New Zealand: slip rates, segmentation and earthquake magnitudes. New Zealand Journal of Geology and Geophysics 59: 568-591.

Sylvester AG 1988. Strike-slip faults. Geological Society of America Bulletin 100: 1666-1703.

Thompson SC, Weldon RJ, Rubin CM, Abdrakhmatov K, Molnar P, Berger GW 2002. Late Quaternary slip rates across the central Tien Shan, Kyrgyzstan, central Asia. Journal of Geophysical Research: Solid Earth 107: ETG 7-1-ETG 7-32.

Tsuji T, Ashi J, Ikeda Y 2014. Strike-slip motion of a mega-splay fault system in the Nankai oblique subduction zone. Earth, Planets and Space 66.

Wallace LM, Beavan J, McCaffrey R, Berryman K, Denys P 2007. Balancing the plate motion budget in the South Island, New Zealand using GPS, geological and seismological datas. Geophysical Journal International 168: 332-352.

Wells DL, Coppersmith KJ 1994. New empirical relationships among magnitude, rupture length, rupture width, rupture area, and surface displacement. Bulletin - Seismological Society of America 84: 974-1002.

Westoby MJ, Brasington J, Glasser NF, Hambrey MJ, Reynolds JM 2012. 'Structure-from-Motion' photogrammetry: A low-cost, effective tool for geoscience applications. Geomorphology 179: 300-314.

Wolfe FD, Stahl TA, Villamor P, Lukovic B 2020. Short communication: A semiautomated method for bulk fault slip analysis from topographic scarp profiles. Earth Surface Dynamics 8: 211-219.

Zielke O, Arrowsmith JR 2012. LaDiCaoz and LiDARimager-MATLAB GUIs for LiDAR data handling and lateral displacement measurement. Geosphere 8: 206-221.

Zinke R, Dolan JF, Rhodes EJet al. 2019. Multimillennial Incremental Slip Rate Variability of the Clarence Fault at the Tophouse Road Site, Marlborough Fault System, New Zealand. Geophysical Research Letters 46: 717-725.

Appendix A – Zoom view of Fig. 3-4b to 3-4i

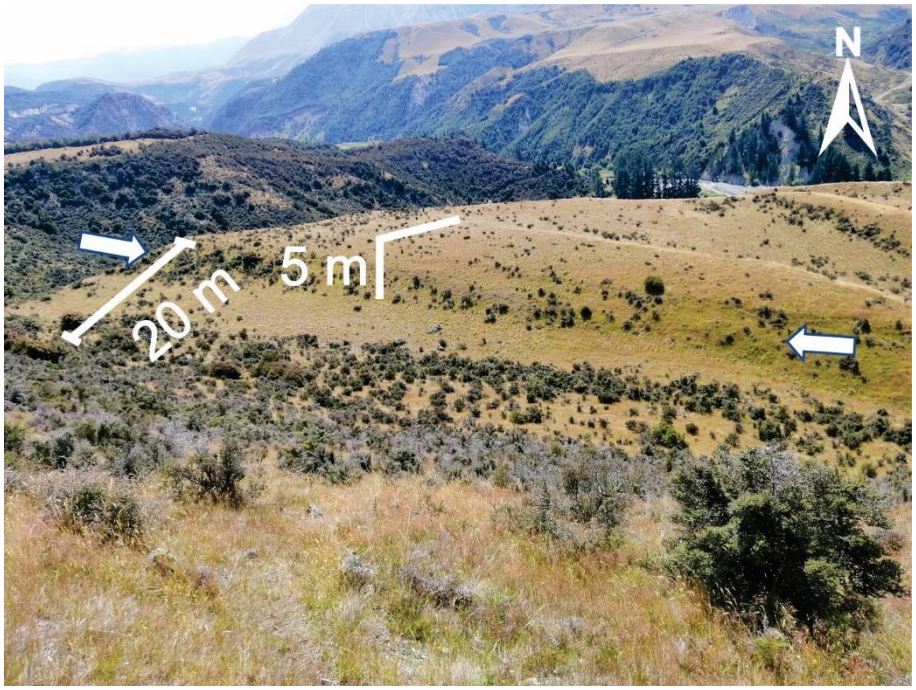

Figure 1: Full-sized version of Fig.3-4b.

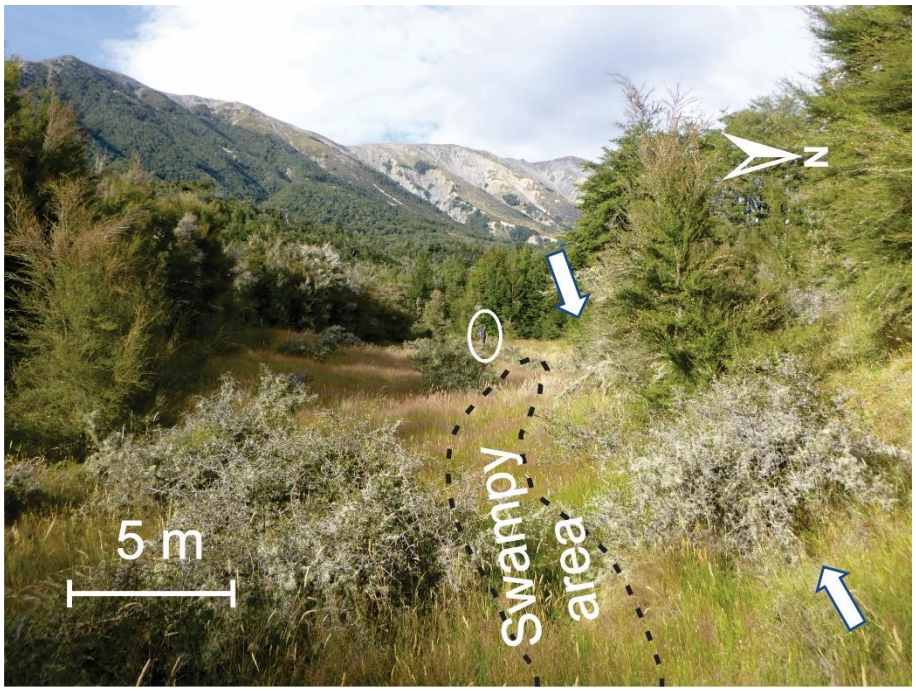

Figure 2: Full-sized version of Fig.3-4c.

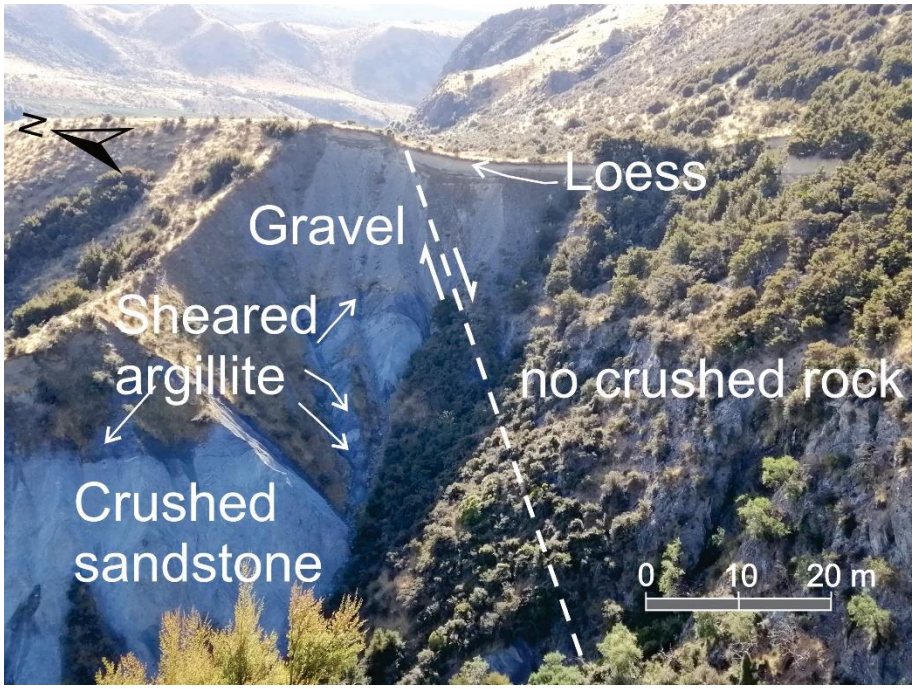

Figure 3. Full-sized version of Fig. 3-4d.

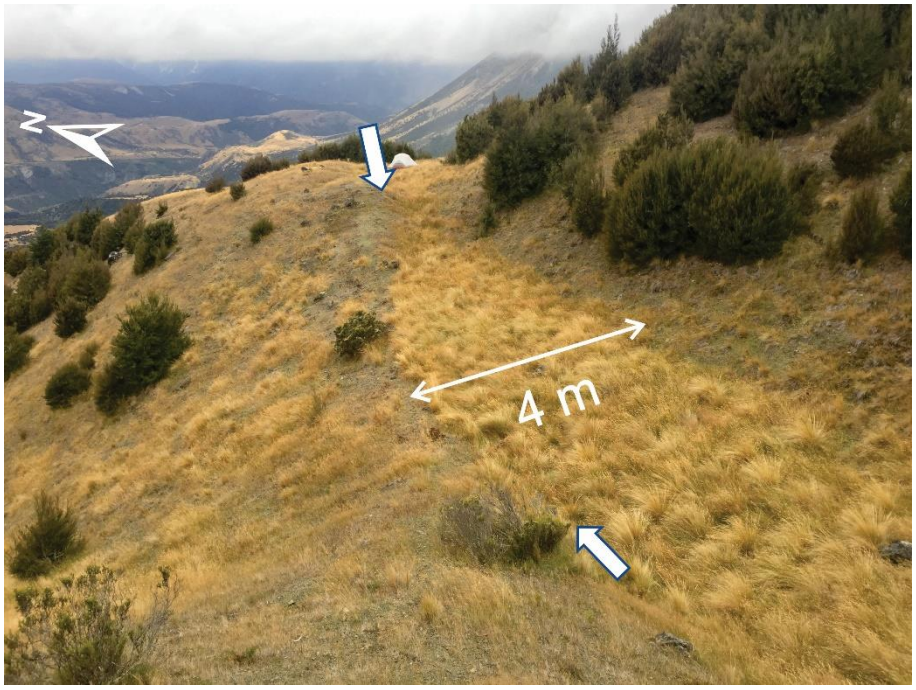

Figure 4. Full-sized version of Fig. 3-4e.

Figure 5 Full-sized version of Fig. 3-4f.

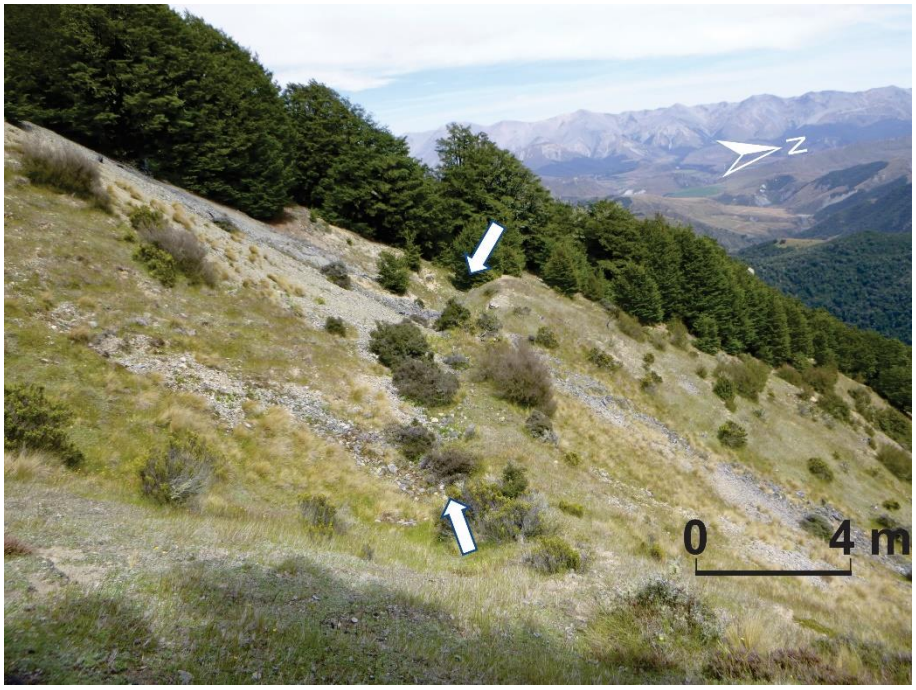

Figure 6. Full-sized version of Fig. 3-4g.

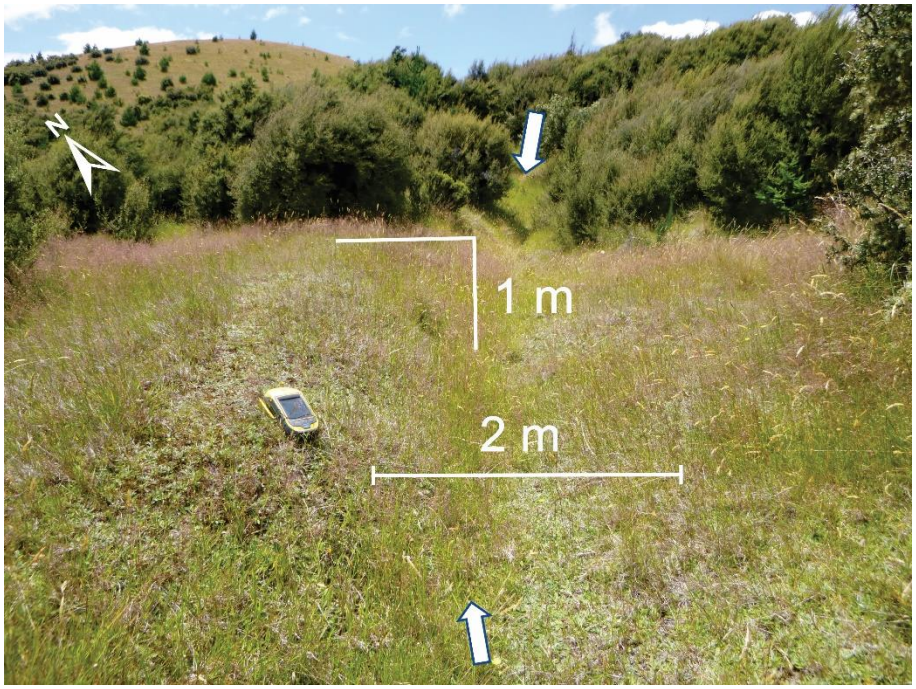

Figure 7. Full-sized version of Fig. 3-4h.

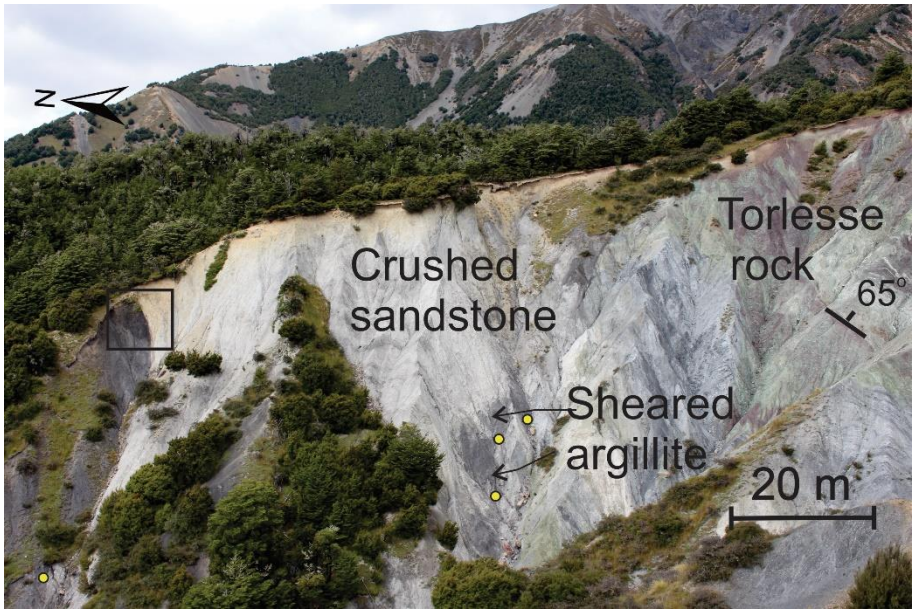

Figure 8. Full-sized version of Fig. 3-4i. Small yellow cirecles represent locations of striae measrurement.

Appendix B – Full-sized version of Fig 3-14b to 3-14g

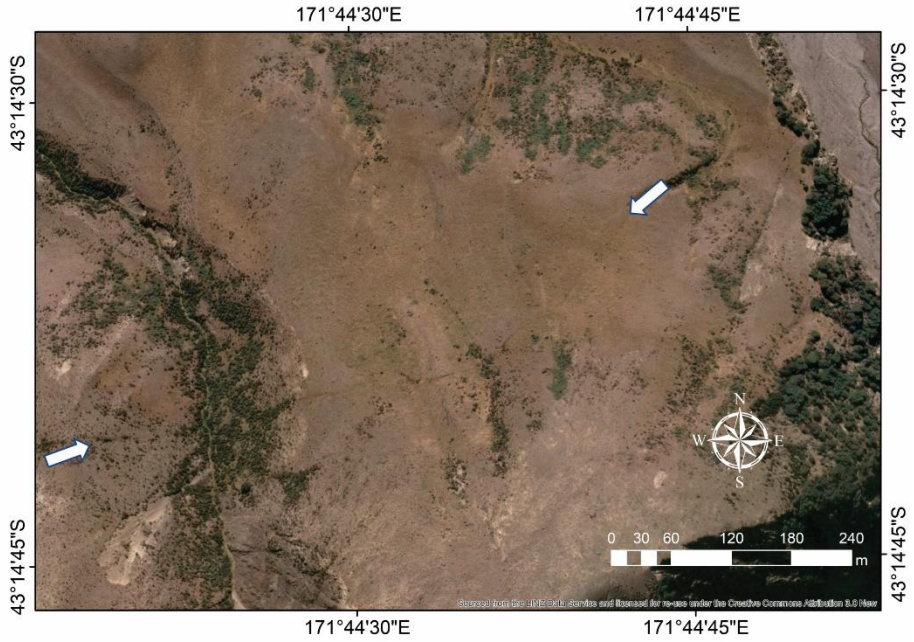

Figure 9. Full-sized version of Fig. 3-14b.

Figure 10. Full-sized version of Fig. 3-14c.

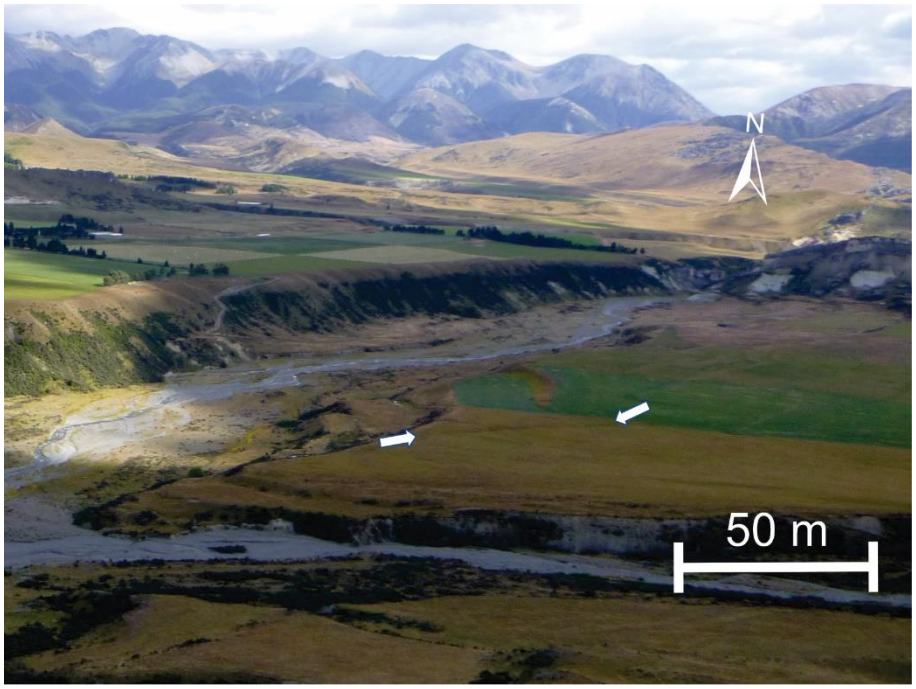

Figure 11. Full-sized version of Fig. 3-14d.

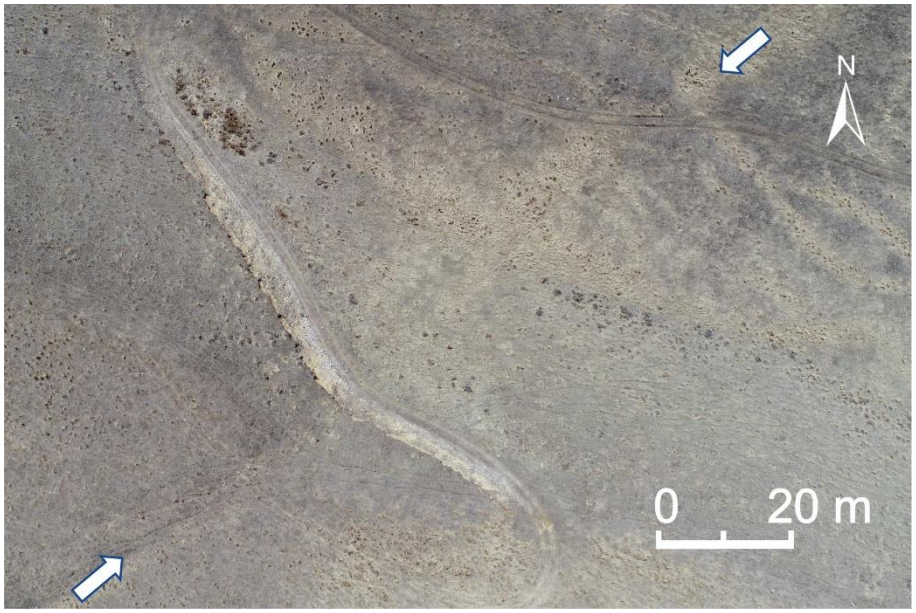

Figure 12. Full-sized version of Fig. 3-14e.

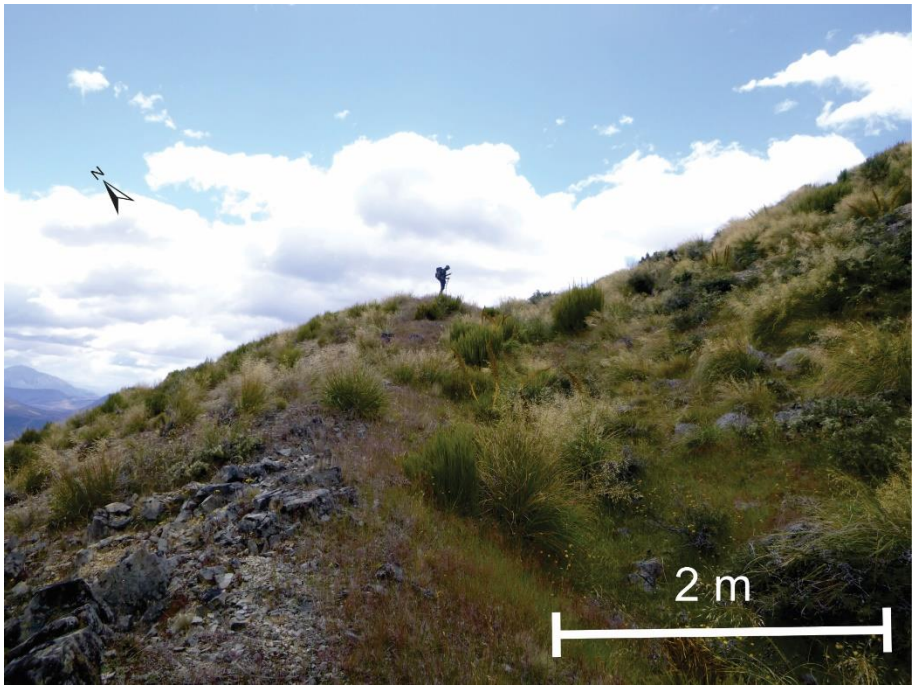

Figure 13. Full-sized version of Fig. 3-14f.

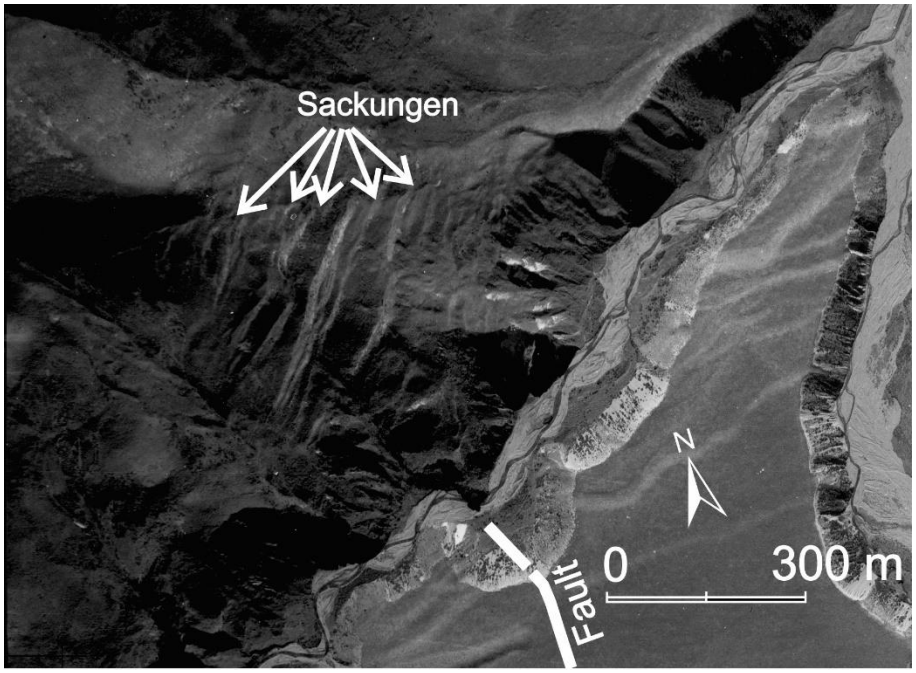

Figure 14. Full-sized version of Fig. 3-14g.

Appendix C – Full-sized version of Fig 3-20b to 3-20d

Figure 15. Full-sized version of Fig. 3-20b.

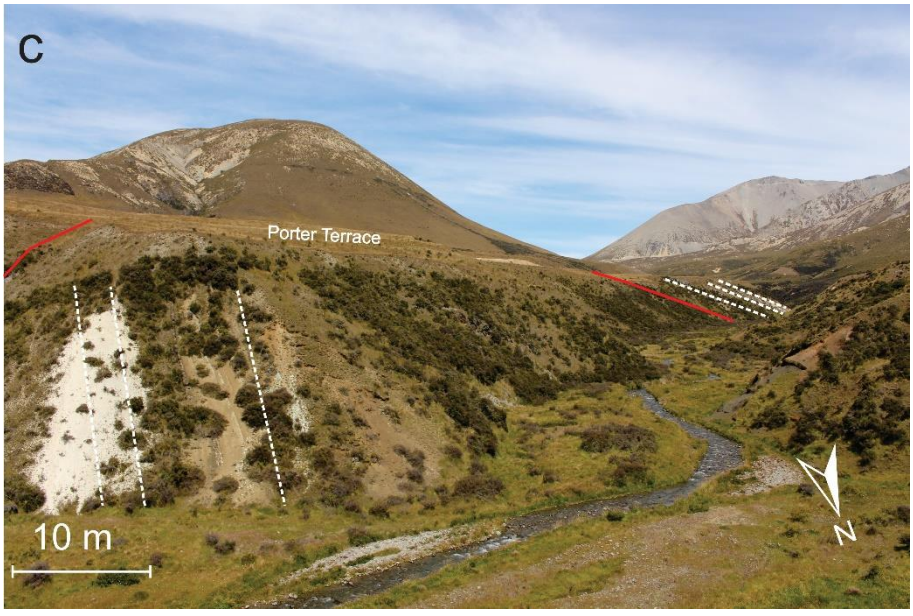

Figure 16. Full-sized version of Fig. 3-20c.

Figure 17. Full-sized version of Fig. 3-20d

Appendix D – Linked Bingham fault plane solutions of striae

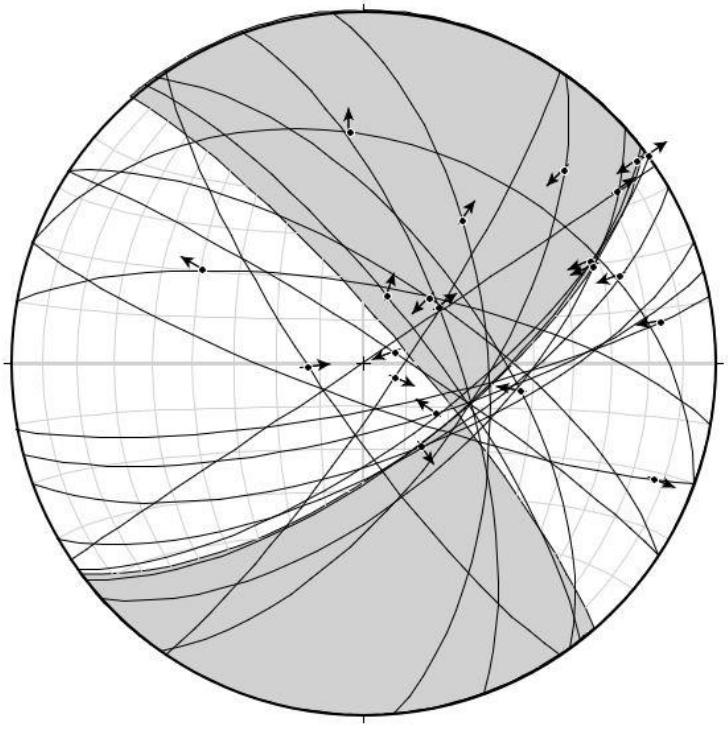

Figure 18. Fault plane solution of striae measuredin crush rock at four different location (Avoca, Blackley, Ghost and Upstream of Porter River (T. Stahl, Personal communication, January 14, 2022) used after from of. The linked Bingham fault plane solutions shows the sense of slip as the dextal fault with some reverse component.

4 Paleoseismology of the Torlesse fault, mid-Canterbury, New Zealand

Abstract

The 31-km-long Torlesse fault in the Torlesse Range, South Island has been identified as an active fault capable of producing a ~M 7 earthquake. The fault poses a potential seismic hazard to transport networks, other infrastructure, and to Christchurch, but paleoseismic studies on the fault are lacking. I used field mapping, surveying (Global Positioning System and Structure-from-Motion photogrammetry), trenching, and luminescence and radiocarbon dating to characterise the Torlesse fault's paleoseismicity. There is evidence for three surface rupturing events from three different trenches: evidence for events between 282 and 54, between 2856 and 535, and around 5000 calibration years before present at the 95% confidence range. Newly modelled ages from the Porters Pass fault and the ages presented in this study demonstrate that timing of two earthquake events recorded in the Torlesse fault overlaps with the timing of events in the Porters Pass fault, which 'rules in' multi-fault ruptures in the region. However, modelled ages from these faults shows that the Torlesse fault may operate as a distinct seismic source in some events, raising questions about how ruptures branch at depth to the surface beneath the Torlesse Range.

4.1 Introduction

Earthquakes that involve more than one fault, like the 2016 Mw 7.8 Kaikōura earthquake (Hamling et al., 2017; Litchfield et al., 2018; Nicol et al., 2018), tend to have larger magnitudes that single fault ruptures. Forecasting multi-fault rupture scenarios is one of the key challenges in modern seismic hazard (Field et al. 2017; Shaw et al. 2022). Paleoseismic data can help to define fault relationships and the frequency of joint earthquake ruptures for fault systems (Duross et al. 2016; Rodriguez Padilla et al. 2021) , but records for adjacent faults are often difficult to synthesise due to epistemic and aleatory uncertainties in event timing, slip rates, and underlying structural relationships. More data and refined earthquake chronologies can help establish whether structurally linked faults or fault segments act as distinct seismic sources and helps to define model scenarios for possible multi-fault ruptures.

The Torlesse fault in the mid-Canterbury runs parallel to the higher slip rate Porters Pass fault (Fig. 4-1). While at least six earthquake events have been recorded in the Porters Pass fault (Cowan 1992; Howard et al. 2005) there is no paleoseismic data on the Torlesse fault. Thus, paleoseismic study of the Torlesse fault is required to examine the fault as a distinct seismic source and to understand the rupture connectivity to the Porters Pass fault.

In this chapter, I used field mapping, surveying (Global Positioning System (GPS) and Structure-from-Motion (SfM) photogrammetry), trenching, luminescence dating and radiocarbon dating to characterise the surface deformation history of the Torlesse fault. High-resolution Digital Surface Models (DSMs) developed using SfM were used for the slip calculation of faults. I compared modelled ages of events from the Porters Pass fault with the new ages in this study to test the hypothesis that the Torlesse fault is a distinct seismic source from the Porters Pass fault.

4.2 Methods

4.2.1 Mapping and Surveying

Geological background including regional active tectonics, regional geology and geomorphology, and previous works on the Torlesse fault is described in Chapter 3. Mapping was carried out in the Torlesse Range in order to produce geomorphic maps. An 8 m Digital Elevation Model (DEM) and high-resolution DSMs were used to trace geomorphic features and to locate the paleoseismic trenches (Chapter 3). The majority of the surveying was conducted using drone flights. A hand held Geo7x was used for mapping and conducting scarp profiles where UAV flights were note possible (Chapter 3).

4.2.2 Subsurface investigation

4.2.2.1 Trenching

Three trenches across fault scarps were excavated in the Ede area, the Blackley area and the Porter River terrace in order to calculate single event displacements and constrain the ages of faulting. Two hand-dug trenches and one backhoe-dug trench were excavated in the study area. Gridding and flagging were done on the trench walls to delineate important features of the trenches while logging was done in the field in order to identify stratigraphic sequences. From these trenches, samples were taken for luminescence and radiocarbon age dating to constrain the age of units.

In the backhoe-dug trench, SfM was run using the photos of trench walls in order to produce orthomosaics of the walls. 230 photos of southern trench wall and 251 photos of the northern trench wall were used to develop orthophotos. Six GPSs-surveyed Ground Control Point (GCP)s were placed on each trench walls to orient the photo and maintain the scale.

4.2.2.2 Ground Penetrating Radar (GPR) survey

A GPR survey was conducted at the Porter terraces to constrain subsurface (and sub-trench) fault dips at the trench site and at another trace. Common Offset Profile (COP) and Common Mid-Point (CMP) surveys were conducted using a pulseEKKO Pro GPR system with two 100 MHz antennas. CMP method was used to obtain velocities of the subsurface materials while the COP was used to obtain the structure.

The CMP profiles were acquired by stepping out the antennas 20 cm each time from a central point increasing to 10 m. There was a 40 cm net increase in transmitter-receiver separation in each reading. The CMP profiles were then analysed to produce the velocities for the surveyed ground. The CMP profiles were extracted from the downthrown side of the fault near the trench in the Porter River terrace (Fig. 3-1B and 3-21).

To carry out the COP survey, the distance between the transmitter and receiver in the system was set at 1 m. A time window of 200 nano seconds and pulsar voltage of 1000 volts was used in the survey. COP surveys were carried out perpendicular to the fault scarp; 13 survey lines with a fixed spacing of 1 m were generated across the eastern fault of Porter River terrace (Fig. 3-1B and 3-21). The elevation profile of each survey line was taken with the help of Geo7x GPS unit to check the GPR profile distance and to reduce the collective error associated with positioning.

Two GPR survey lines were used as ground truths adjacent to a paleoseismic trench (section below) across the western fault of the Porter River terrace. The fault dip was estimated by analysing

the topography corrected individual GPR survey line and comparing with validated GPR trace across the western fault.

4.2.3 Geochronology

4.2.3.1 Optically Stimulated Luminescence (OSL) dating

OSL dating was carried out to constrain the burial ages of various units. Samples for luminescence dating were collected from coarse sand layers by hammering four metal tubes into the trench walls. Two metal tube of length 25 cm and diameter 2.5 cm, and two metal tubes of length 25 cm and diameter 5 cm were used. When the tubes were full after penetrating in the sand/silt, tubes were taken out along with filled samples and capped with caps protected by duct tape. Calculation of the luminescence dose rate and moisture content from the sediment obtained within ~25 cm radius of each tube was performed in the laboratory.

Moisture content of the dose rate samples collected within the 25 cm radius of inserted OSL tubes was measured using a mass difference calculation after dying in an oven for five days at 60^{o}C. Homogenisation of the samples collected within the 25 cm radius of each sample tube during excavation were also carried out in the same laboratory.

Four OSL tubes were opened in the luminescence laboratory at Middlebury College, Vermont, USA. Sediment ~5 cm at the both ends of each tube was rejected and only the sediment from the central part of the tube was treated for dating. Purification of quartz from the central part of each tube was done in the laboratory. 9.8 mm aluminium discs were used to mount quartz grains and small portions (20-50 grains) from each quartz sample were analysed applying Single Aliquot Regenerative method (SAR) method on a Daybreak 2200 reader (Murray et al. 2000, 2003). Standard laboratory procedures were followed during the analysis.

High-resolution gamma spectrometry was used to calculate the dose rate and it was calculated from sediment dug around each OSL tube Then, the in situ dose rate was determined using standard conversion parameters (Adamiec et al. 1998) and the dose rate and age calculator (DRAC) (Durcan et al. 2015).

Distribution of apparent ages were found from multiple aliquot analysis and these distribution were used to calculate sediment's burial age (Duller 2008; Arnold et al. 2009). R-package 'Luminescence' was used to analyse age distribution, uncertainties and to plot age estimation (Galbraith et al. 1999; Thomsen et al. 2003; Galbraith 2005; Thomsen et al. 2007; Arnold et al. 2009; Kreutzer et al. 2012). Sample age was determined by dividing the equivalent dose rate by mean dose rate:

4.2.3.2 Radiocarbon dating

Radiocarbon dating was performed to constrain the age of events that occurred in the area. Visible macro-charcoal samples in trench units were targeted and taken out using a knife and scraper. Well round macro-charcoal was discarded to avoid redeposited samples. Therefore, angular macro-charcoals were examined to infer that they were syndepositional samples. In areas that lacked visible charcoal fragments, bulk samples were also taken for micro-charcoal analysis. In the lab, I identified micro-charcoal fragments under a microscope and sent these fragments for separation and age dating. Radiocarbon dating was performed in the Radiocarbon Dating Laboratory, University of Waikato using the Accelerator Mass Spectrometry (AMS). In the lab, samples cleaning and chemical pre-treatment were done. Samples were washed with hot HCl and hot NaOH and then rinsed multiple times. The insoluble fraction was filtered, rinsed and dried. In the AMS technique, the ^{14}C content is directly measured comparative to the ^{12}C and ^{13}C.

4.2.3.3 OxCal Model

OxCal (Ramsey 2001, 2017) is tool of estimating event ages and their uncertainties. This model follows Bayesian statistics in which all available age constraints are integrated. Calibrated radiocarbon ages are expressed as probability distributions and these asymmetrical distributions area are squeezed adding chronological information (e.g., stratigraphic order, timing of recent and historic events). The model reweights the overlapping age distributions and allows calculation of events that are constrained only with bounding ages.

The radiocarbon and luminescence dates were calibrated and modelled in OxCal 4.4 using the Southern Hemisphere Calibration (SHCal) (Hogg et al. 2013). Ages from the past events obtained from the Porters Pass fault were also modelled in OxCal.

4.3 Results

4.3.1 Paleoseismology of the Torlesse fault zone

4.3.1.1 Ede Stream Trench

I hand-excavated a 1.4 m and 70 cm deep trench perpendicular to the uphill facing fault scarp in the abandoned channel near Ede Stream (Fig. 3-1B and 3-7). An alluvial deposit filled by the abandoned channel in the depression formed by fault scarp is present on the northern slope of the Torlesse Range at Ede area (Chapter 3). This location was selected for trenching to maximise the potential for trapping datable material (slope wash and organic detritus) against the scarp; the trench location was difficult to reach and it took 3.5 hours to reach there from the Avoca Homestead each day.

I identified four stratigraphic units within the trench. At the base of the southeast wall, a reddish orange sandy gravel (Unit 1) was found. The unit was clast supported and the size of the clasts varied from ~2 cm to greater than 20 cm with angular in shape. The thickness of this sandy gravel unit was more than 50 cm. Above this unit was carbonaceous material composed of small charcoal fragments within a dark brownish grey matrix of clayey silt (Unit 2). Sporadic angular gravel clasts of greywacke ranging in size from 2-5 cm were distinguished in Unit 2. Warping of clayey silt layer (Unit 2) was observed (Unit 2) and the material was similar to modern A Horizon. Unit 3 consisted of light greyish brown clayey silt interbedded with, light orange fine mottling sands (Unit 3) was over Unit 2. The thickness of those fine sand layers was less than 1 cm while the thickness of the whole Unit 3 was 50 cm. At the top of the trench, ~9 cm thick modern A-Horizon was present consisting of carbonaceous brown silt (Unit 4) (Fig. 4-1 and 4-2) (Table 4-1).

Figure 4-1. Southeast trench wall from the Ede basin. Radiocarbon samples were taken from Unit 3 and the middle part of Unit 1

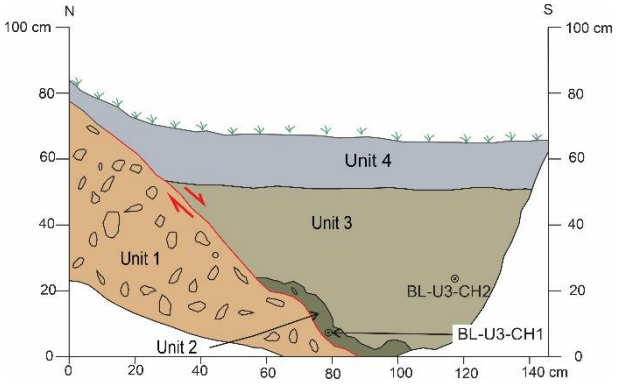

Figure 4-2. Trench wall shows different lithological units and the fault.

Table 4-1: Unit description of the Ede trench

Unit name	**Deposit/horizon**	**Colour**	**Texture**	**Notes**
Unit 1	Colluvium	Brownish grey	Gravel	Sub angular clasts
Unit 2	Swampy material	Greenish grey	Carbonaceous silt with clasts of gravel, charcoal fragments	Limited extent, Buried clay and angular gravel
Unit 3	Infilling material	Reddish brown	Silt interbeds with fine sand	Massive structure
Unit 4	A horizon	Dark grey	Silt	Modern soil

The paleoearthquake at this site is recognised based on stratigraphic relations and offset recorded by sedimentary units in the fault zone. The sequence of deposition starts with the deposition of gravel (Unit 1) on the northern slope of the Torlesse Range in Ede area. The first faulting event occurred forming depression on the downthrown side. An A-horizon comprising carbonaceous silt, charcoal fragments and gravel clasts formed on the downthrown side of the scarp (Unit 2). Then another faulting event occurred which deformed the carbonaceous silt (Unit 2) and increased the size of depression on the downthrown side hanging wall. The event horizon in the trench is defined by the contact between Unit 2 and Unit 3. Warping of Unit 2 also occurred in that event. Pebbles of Unit 1 near the shearing zone were rotated parallel to the fault surface. After this second surface rupture, slope wash material (silt and fine sand) (Unit 3) infilled the depression from the surrounding topography. Another layer of new soil (Unit 4) developed within the infilling material at the top. One distinct event is recognized based on the trench stratigraphy though a penultimate event is inferred to have created the space for Unit 2 to form (Fig. 4-1 and 4-2).

I interpret the fault plane to form the contact between gravel deposits of Unit 1 and silt deposits of Unit 3 and Unit 2. The strike and dip of the fault plane measured in the trench were N64^{o}E and 51^{o} respectively. The exact displacement of horizons in the trench was not recognized due to the limitation of the trench size. However, rough estimate of 50 cm vertical displacement was calculated from the 50 cm silt and fine sand (Unit 3) accumulated in the hanging wall of the fault (Fig. 4-2). This 50 cm of average displacement is taken to match the surface rupture length of 31 km (Pettinga et al. 2001) using surface rupture length displacement equation (Wells et al. 1994) though it is recognised that displacmeent is primarily strike-slip at this site (Chapter 3).

Samples were collected from Unit 2 and Unit 3 to date those units and to constrain the age of faulting because the event of faulting occurred between the formation of carbonaceous silt (Unit 2) and deposition of infilling material (Unit 3). Macroscopic charcoal fragments were collected from the base of Unit 2 and middle part of Unit 3 for radiocarbon analysis and those samples were analysed on an AMS at the Radiometric Dating Laboratory, University of Waikato, Hamilton, New Zealand. In addition, the dates were modelled in the OxCal (Ramsey 2017) using SHCal 13 atmospheric curve (Hogg et al. 2013). An age of 215±70 cal BP is obtained for the carbonaceous silt (Unit 2) and an age of 136±138 cal BP (1σ) is calculated for infilling material (Unit 3) (See appendix for full information regarding the distributions and confidence intervals). The time of faulting in the trench is young as constrained by young ages of units 2 and 3. This paleoearthquake occurred at 168±114 cal BP from the modelled age of layers of the Ede trench at the 95% confidence range using SHCAL13 atmospheric curve (Hogg et al. 2013) (Fig. 4-3), and may therefore be historical or immediately pre-European colonisation.

Limited data on paleoseismic events is found in surrounding area of Ede. Two earthquake events both within 12,000 cal. years BP have been identified on the nearby fault (Esk fault) which joins to the Torlesse fault near the Avoca Homestead of Ede area (Noble 2011).

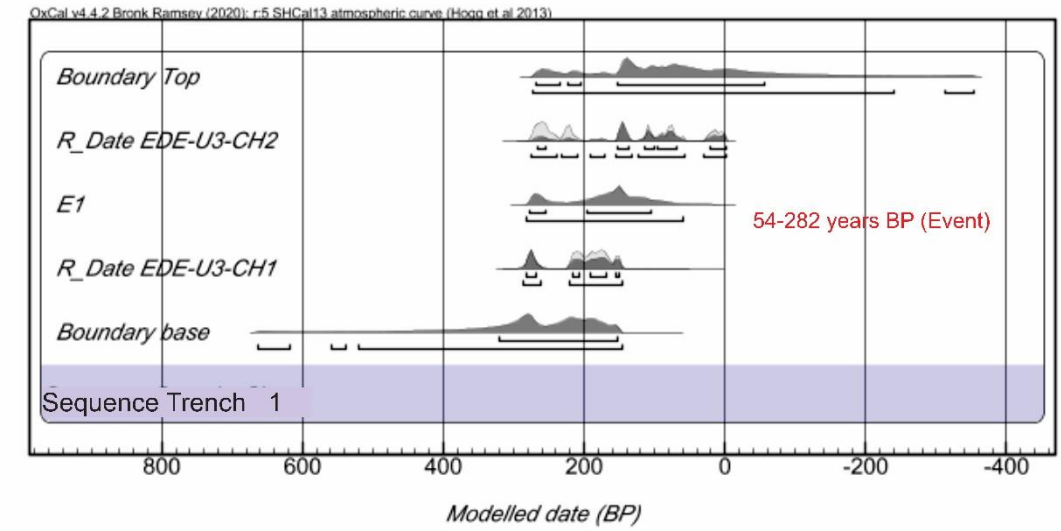

Figure 4-3. OxCal age models for the stratigraphic sequence in the Ede trench based on SHCAL13 atmospheric curve (Hogg et al. 2013). Probability density functions of event ages are modelled at the 95% confidence range. Ages are mentioned in calibrated years before present. Boundary top and boundary base are automatically generated by OxCal.

4.3.1.2 Broken River section: Blackley Stream area

In the Blackley area, a trench was dug perpendicular to the uphill facing fault scarp near the displaced channel (Fig. 3-4a, 3-4h, 3-9 and 3-10). As with the Ede trench site, the Blackley trench location was chosen in a depression adjacent to the fault scarp to get trapped datable material. The trench was dug mostly in the hanging wall near the 0.8 m high fault scarp. The trench was oriented in the direction of N10^{o}W with dimensions of 1.8 m in length, 85 cm in width and 75 cm in depth (Fig. 4-4). The trench location was accessible via a two-hour tramp from the junction of Porter River and Broken River.

Seven stratigraphic layers consisting of various materials were identified in the trench (Fig. 4-4 and 4-5). At the base, tightly packed sub-angular to sub-rounded yellowish-brown gravel with coarse sands were found (Unit 1). The deposit was dry and moderately weathered with sub horizontal bedding. Clast composition was greywacke and clasts varied in size from a few cm to 20 cm. The overlying deposit consisted of laminated silver grey to yellowish brown clayey silt and fine sand (Unit 2). Pebbles less than 1.5 cm were distributed in the unit with some iron leaching. A large cobble of size 17 cm was located at the bottom of Unit 2. I identified a thin layer of carbonaceous silt at the top part of Unit 2. Above this was the light brownish brown tightly packed and poorly graded silty gravel (Unit

3). In Unit 3, sub-angular to sub-rounded clast ranging in size from 1 to 4 cm of weathered greywacke were identified. This unit was overlain by loosely packed, poorly graded, yellowish brown silty gravel with sand and clay (Unit 4). Moreover, brownish grey clayey silt with few traces of peat was found above Unit 4. This unit was mostly homogeneous, assigned as Unit 5, and was stiff with manganese nodule mottled in places and consisted of pebbles of size 1 to 3 cm and rootlets. Unit 6, deposit overlying Unit 5, contained moist dark grey mottled clayey silt. Silt was carbonaceous and consisted of traces of peat and charcoals (Fig. 4-6). This unit became thicker towards southeast and the contact with the underlying deposit was gradual. A-horizon (Unit 7) mantled the scarp across the length of the trench with little variation in thickness (Fig. 4-4 and 4-5) (Table 4-2).

Figure 4-4. The north wall of the trench from the Blackley area. The upper unit consists of black carbonaceous rich deposit. Grids were made every 50 cm.

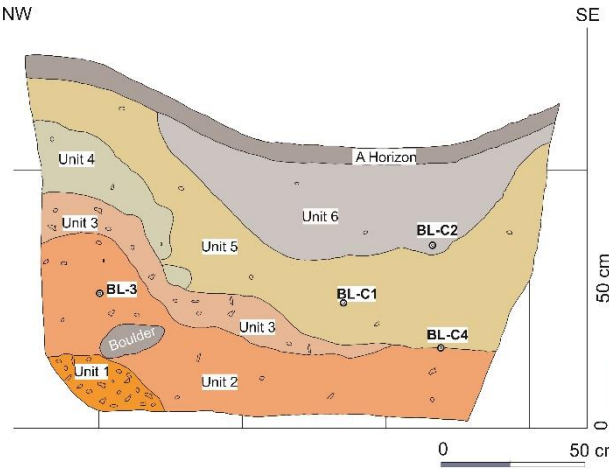

Figure 4-5. The northern trench wall from the Blackley area showing different units. The lower gravelly unit on the left side of the diagram is taken to be the footwall of the fault.

Table 4-2: Unit description of the Blackley trench

Unit name	Deposit/horizon	Colour (Munsell colour system)	Texture	Notes
1	Debris fan deposit	5 YR 5/6	Cobbles, silt	
2	Fluvial deposit	5 Y 7/1 and 10 YR 8/6	Gravelly silt	
3	Slope outwash	5 YR 7/4	Sandy silt	Gravitational

4	Colluvial wedge?	10 YR 8/1	Silt	Collapse of footwall,
5	Fluvial deposit	10 YR 8/6	Silt	
6	Swamp deposit	N 5	Carbonaceous silt	
7	A horizon	Dark grey	Silt, organic rich	

The fault plane was not identified in the trench even though the trench was dug across the fault scarp. However folded layers (presumably above the fault tip) were identified in the trench. Because the trench was dug using hand tools and the trench size was restricted by the Department of Conservation, a deeper trench was not possible here. Thus, in lieu of additional information, I interpret the trench structure to be a sag basin due to right lateral strike-slip fault, the western slope of the Torlesse Range and water entered in the basin through channel 2 (Fig. 3-4).

In detail, the sequence of deposition starts with the debris fan deposit (Unit 1). It is probable that the first faulting event (for which there is evidence in this trench) occurred after deposition of Unit 1 (Howard et al. 2005) Deposition of fine brownish to greenish grey coloured silt with gravel occurred above the debris fan deposit (Unit 2). Gravelly sand (Unit 3) was deposited in the form of slope outwash from the surrounding area. Another event occurred and was followed by the deposition of sandy gravel (Unit 4) forming a wedge shape tapering towards east. I interpret Unit 4 to be a colluvial wedge shaped deposit formed by the collapse of scarp. Next, fine silts (Unit 5) and some clasts of gravel deposited above the wedge deposit (Unit 4). The tilting of layers (Unit 1 to 4) and folding of brownish grey silt layer (Unit 5) was caused due to a definite faulting event. Then deposition of black carbonaceous silt (Unit 6) occurred above Unit 5. Finally, an A horizon (Unit 7) developed within grey silt (Unit 5) and black carbonaceous silt (Unit 6) at the top.

Samples from the middle part of Unit 2 and lower part of the Unit 5 were obtained from the trench to constrain the age of a probable faulting event. The calibrated age of Unit 2 is obtained as 15,445±225 cal BP (Appendix A) and the base of Unit 5 (top of Unit 2) is 10,000±225 cal BP (Appendix A). This first event therefore likely occurred between those two dates and may have resulted in the deposition of Unit 3, but this interpretation is highly uncertain and therefore not modelled in Fig. 4-7. Radiocarbon ages of Unit 5 and Unit 6 (which is undeformed) from the Blackley trench are respectively 2,955±105 cal BP (Appendix A) and 515±25 cal BP (Appendix A) at the 95% confidence range. These provide bounding ages for Unit 4, which is interpreted as representing scarp collapse and therefore a second event. Thus, a definite event causing faulting in the trench is found between 2,856 and 535 cal

BP from the modelled age of layers in the OxCal 4.4 (Ramsey 2017) in SHCal 13 (Hogg et al. 2013) (Fig. 4-7).

Figure 4-6. Charcoal location at the southeast trench wall in the Blackley trench.

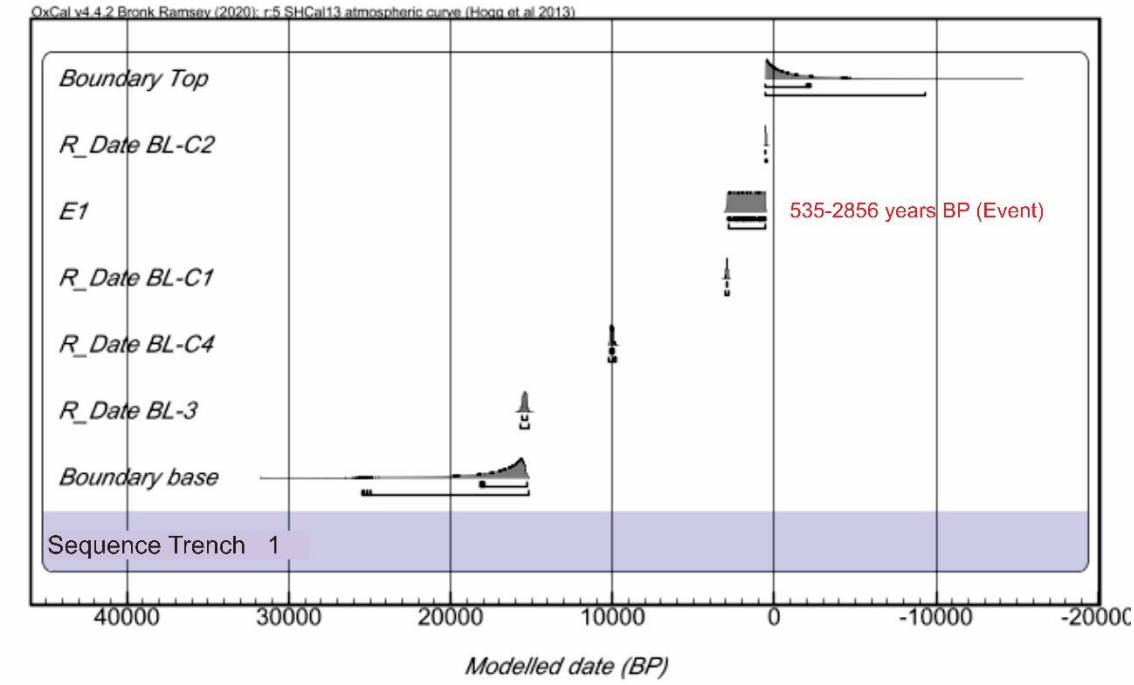

Figure 4-7. OxCal age models (Bronk Ramsey et al. 2020) for the stratigraphic sequence in the Blackley trench based on SHCAL 13 atmospheric curve (Hogg et al. 2013). Probability density functions of event ages are modelled at the 95% confidence range.

In summary, in the trench of the Blackley Stream area (Fig. 4-4 and 4-5), one certain and two probable records of faulting were identified.

4.3.1.3 Porter River Terrace

A trench 16 m long, 5 m wide and 5 m deep was dug across the reverse fault at the Porter River terrace near the lime quarry, Porter Ski road using the 14-tonne digger. This reverse fault is interpreted to be a flexural slip fault formed due to folding associated with the Torlesse fault. I hypothesised therefore that the timing of events on these faults would record events on the main Torlesse fault. The trench location (Fig. 4-8) was selected to constrain paleoearthquakes by dating materials from the stratigraphic units and to measure the displacements.

Figure 4-8. Location of the trench across the fault scarp in the Porter River terrace. Four orange flags shown by the white circles represent outer boundary of the trench.

The sequence of deposits in the trench showed six main stratigraphic units (Fig. 4-9 to 4-12) (Table 4-3). Unit 1, the oldest unit in the trench consisted of a matrix supported gravel. Clasts in the unit contained Torlesse Greywacke derived materials and mostly of sandstone and mudstone with maximum clast size of 35 cm diameter. Next Unit 2 with the similar composition as Unit 1 rested above the matrix supported gravel. Unit 2 consisted of coarse sandy gravels with sub-angular to sub-rounded shape and gravel size was less than 25 cm. In this unit, horizontal bedding in the patchy coarse sand and fine pebble layers were conspicuous. Unit 3 consisted of finning upward sequence of silt, sand and gravel was identified above Unit 2. A layer consisting mostly of silt and fine sand with pebble and cobble (Unit4) was found above Unit 2 and Unit 3. This Unit 4 was wedge shaped with tapered towards the east. Unit 5 also consisted of silt, fine sand and gravel as Unit 4 found above Unit 4. However, the proportion of pebble and gravel in Unit 5 was more than that of Unit 4. Both units 4 and 5 tapered to the north while the spread of Unit 4 was large. At the top of the trench, dark grey carbonaceous silt with pebbles and cobbles were identified (Fig. 4-9 to 4-12). In the southern trench wall, all six units similar to the northern wall deposits were also identified (Fig. 4-9 to 4-12). In addition, fissure fill

deposits (Unit F) were also observed in the hanging wall in the southern trench wall. (Fig. 4-11 4-12 and 4-13). Single event displacement in the trench was estimated on the basis of wedge thickness and scarp height (McCalpin 2009) due to the problem of tracing particular depositional layers in the footwall and the hanging wall. A single event displacement of around 2 m was estimated for the western fault in the Porter terrace.

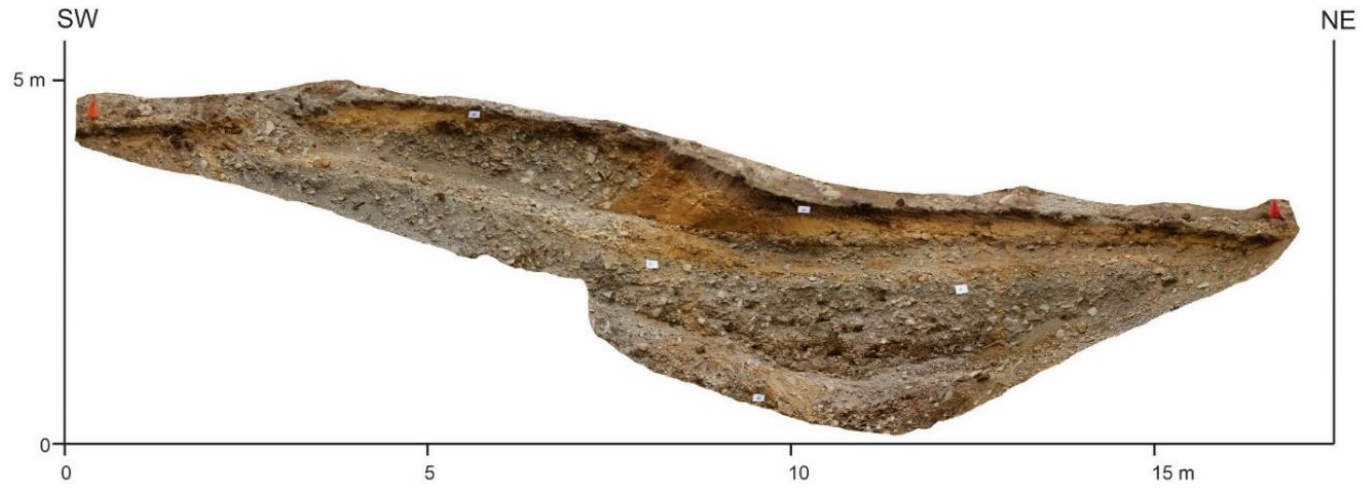

Figure 4-9. Photomosaic of the northwest trench wall from the Porter River terrace. Wedge shape deposit containing fines is at the middle part of the while gravel deposits are dominant in other parts.

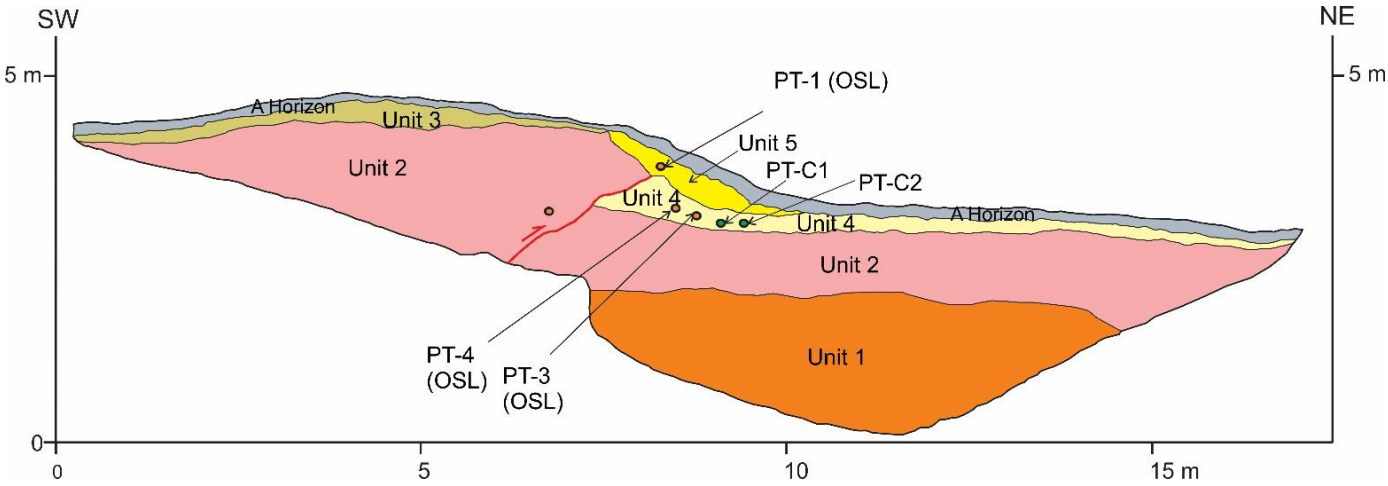

Figure 4-10. Trench log of the northwest wall showing samples collected for dating. Unit 1 is matrix supported gravel deposit, Unit 2 is sandy gravel deposit, Unit 3 is deposit consisting of gravel to silt, Unit 4 and Unit 5 are wedge shaped deposits consisting of fine sand and silt with pebble and cobbles, and Unit 6 is carbonaceous silt. PTC1 and PTC2 are radiocarbon sampling locations, whereas PT1, PT3 and PT4 are OSL sampling locations.

Figure 4-11. Photo mosaic of the southeast trench wall. Wedge shaped deposit can be seen on the upper middle part of the photo. Lower part consists of gravel deposits.

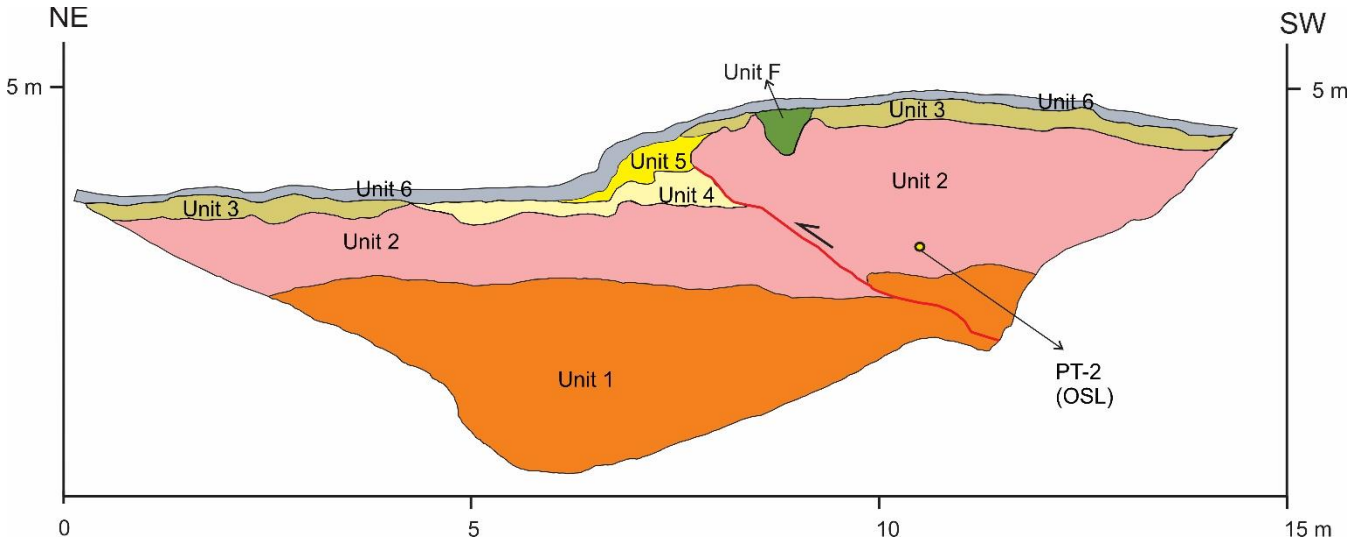

Figure 4-12. Trench log of the southeast wall showing samples collected for dating. Unit 1 is matrix supported gravel deposit, Unit 2 is sandy gravel deposit, Unit 3 is deposit consisting of gravel to silt, Unit 4 and Unit 5 are wedge shaped deposit consisting of fine sand and silt with pebble and cobbles, and Unit 6 is carbonaceous silt.PT2 is OSL sampling location.

Table 4-3: Unit description of the Porter terrace trench

Unit name	Deposit/horizon	Colour	Texture	Notes
1	Debris flow gravel	Brownish grey	Sandy Gravel	Matrix supported
2	Fluvial sandy gravel	Brownish grey	Sandy Gravel	Clast supported

3	B horizon	Reddish brown	Sandy silt	
4	Colluvial wedge	Reddish brown	Silt with pebbles and cobbles	Compact
5	Colluvial wedge	Reddish brown	Silt with pebbles and cobbles	Relatively loose
6	A horizon	Dark grey		
F	Fissure fill	Brownish-grey	Sandy gravel	

The trench showed the moderately dipping fault plane with two wedge shape deposits of silt and fine sand and cobble in the footwall. In both trench walls, the fault plane was represented by the clast fabric where gravels were rotated parallel to the shear zone. The strike of fault measured from the trench walls was measured to be N5°E–S5°W. It was found that the western fault dipped at 40° towards the west displacing gravel deposits. The fault maintained this dip up the base of the trench (Fig. 4-9 to 4-12). Coarse sand and pebble layers of Unit 2 were folded in the hanging wall but the phenomenon was not identified in the footwall. Folding of coarse sand layers of Unit 2 from the top to the bottom can be well seen in patches in the hanging wall near the shear zone (Fig. 4-13).

The sequence of deposition in the trench site starts with the deposition of debris flow gravel deposit (Unit 1). Deposition of fluvial gravel (Unit 2) took place above the debris flow gravel. Both are related to the initial formation of the terrace landform which is displaced by the fault. A B horizon (Unit 3) started to form in the top part of Unit 2. The first faulting event occurred with the displacement of surface and collapse of hanging wall. Because of the predominance of fine material in Unit 4, I infer that loess deposited on the collapsed material (i.e. against the newly formed scarp). Another faulting event occurred, displacing Unit 2 over Unit 4, and forming another colluvial wedge (Unit 5). The two wedges formed in short time since there is no deposition of other layers in between wedges. A fissure formed at the top of the hanging wall during second event due to extension and overlying material filled in the crack. The fissure developed in the second events because no other deposition was found between fissure deposits and A Horizon at the top. Finally, development of the modern A Horizon within Unit 4 and Unit 5 at the top took place.

Two radiocarbon and three OSL samples collected from the trench were dated to limit the ages of faulting. Radiocarbon samples (charcoal fragments) were dated at the University of Waikato, Hamilton, New Zealand while OSL samples were dated at the Middlebury College, Vermont USA. To limit the maximum age of events in the trench, OSL samples from fluvial sandy gravel (Unit 2 were dated. An OSL age of 16.4±0.9 kyr is obtained for the fluvial deposit (Unit 2) using IEU (internal external

consistency criteria) age model (Thomsen et al. 2003; Thomsen et al. 2007)(Table 4-4). IEU was used because it recognizes lowest normal-dose population, which have been well-bleached during deposition.

Figure 4-13. Folded sand layers in the southern trench wall just right of the fault plane (represented by red nailed ribbons). Fissure fill deposit consisting of weathered material is in the hanging wall.

OSL samples PT1 and PT4 were collected from the lower colluvial wedge (Unit 4) (Fig. 4-10). Ages of 5.1±0.2 kyr and 4.9±0.2 kyr respectively were obtained from OSL dating using the SAR method (Table 4-4). All ages were computed using SAR method in R Luminescence package (Kreutzer et al. 2012). Internal External Consistency criteria is taken as the preferred age model. Charcoal samples (PT-C1 and PT-C2) were collected from the middle part of the lower wedge (Unit 4) for radiocarbon dating (Fig. 4-10). Ages of 9860±120 cal BP and 9350±40 cal BP are obtained from radiocarbon dating of these samples (Appendix A). Thus, there is a discrepancy of radiocarbon dates and OSL dates of samples from the lower wedge. (Table 4-4) (Fig. 4-9 and 4-10). One OSL sample from the upper wedge (Unit 5) was dated and the age for the deposit was found to be 4.7±0.1 kyr (Table 4-4).

Colluvial wedges generally are deposited at the time or soon after the faulting. Direct dating of earthquake events using OSL dating of fault-scarp colluvium has been performed (Yanchou et al. 2002; Fattahi et al. 2007; Porat et al. 2009), hence I used OSL dates for timing of formation of colluvial wedge and timing of fault displacement. The main reason of discrepancy between OSL ages and radiocarbon ages of the same unit is inferred to be due to recycling of material used for radiocarbon

ages. These older radiocarbon ages are produced due to the mixing of old reworked charcoal fragments (Grimm et al. 2009). Sometimes samples can be contaminated by older material and can give a wrong age for the deposit (Bird et al. 2014). The age obtained from the OSL dating of unit containing eolian sediment works better than age obtained from the radiocarbon dating of carbon samples from that unit (Lee et al. 2011) because an old carbon problem can be excluded.

Table 4-4: Sample and age results from the OSL dating

Sample	**Material dated**	**Depth from surface (cm)**	**Grain Size (um)**	**H2O (%)**	**DR Gy/kyr**	**2σ Gy/kyr**	**MAM3 (ka)**	**2σ (ka)**	**IEU (ka)**	**2σ (ka)**	**CAM (ka)**	**2σ (ka)**
PT1	Silt	80	150-250	0.36	3.60	0.09	4.5	0.2	**4.9**	**0.2**	5.1	0.2
PT2	Coarse sand	155	80-250	0.05	3.99	0.12	14.9	1.6	**16.4**	**0.9**	22.4	2.1
PT3	Silt	60	150-250	0.18	3.60	0.09	4.0	0.2	**4.7**	**0.2**	4.7	0.1
PT4	Silt	78	150-250	0.36	3.53	0.09	3.7	0.3	**4.9**	**0.2**	4.9	0.2

Note: All ages computed using RLum package. All resulted ages are years before 2020. IEU is the preferred age model, DR is dose rate, σ is standard deviation, MAM is minimum age model, IEU is internal-external consistency criteria and CAM is central age model

The modelled OSL ages in OxCal (Bronk Ramsey et al. 2020) shows the timing of event 1 with wide range of time (15,833 years to 4,980 years) between deposition of fluvial sandy gravel and the colluvial wedge (Fig. 4-14). However, the colluvial wedge generally gives the timing of faulting hence the faulting age should be towards minimum value of the range, i.e., around 5,000 years BP. The second event is more constrained by the dating of two successive colluvial wedges. Though the modelled age shows range of 5,139-4,334 years BP, the timing of faulting is likely around 4,600 years BP.

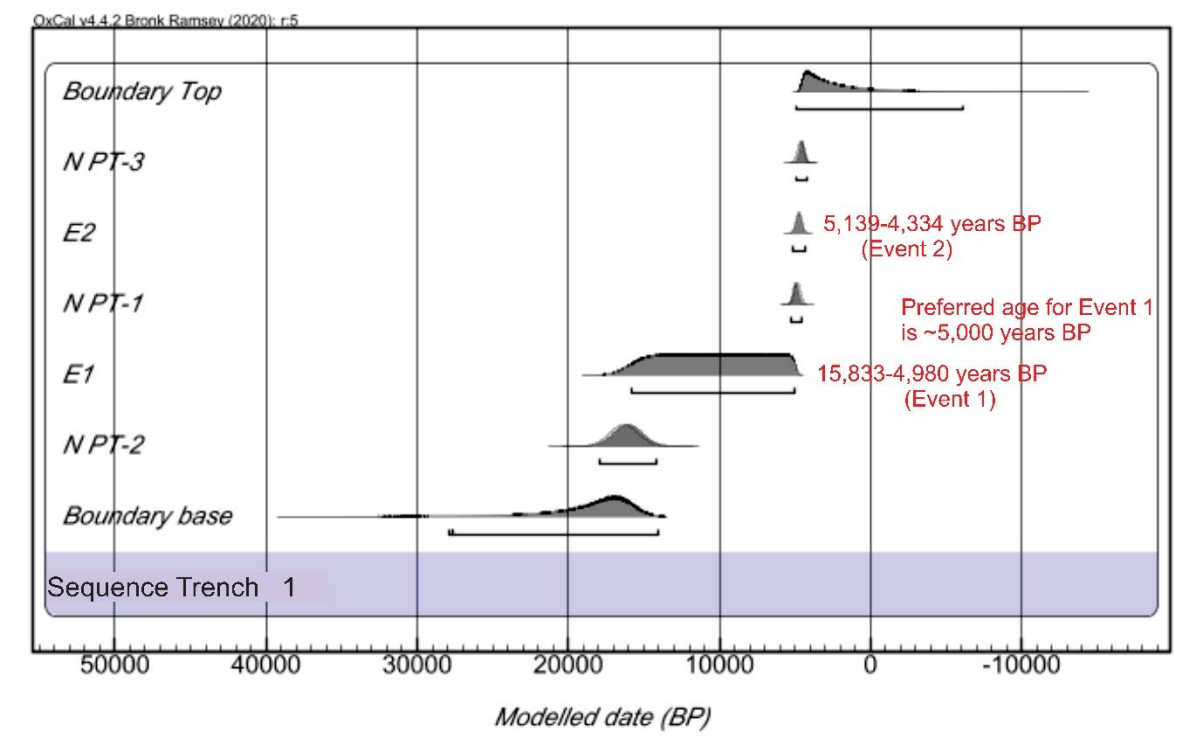

Figure 4-14. OxCal age models for the stratigraphic sequence in the Porter trench. Probability density functions of event ages are modelled at the 95% confidence range. Preferred age of Event 1 is around 5,000 as faulting should be towards minimum age of the range.

4.3.1.4 Summary of paleoseismic data and event chronologies

Three paleoseismic trenches were excavated in the Torlesse fault zone: two in the rangefront and one in the basin. All show clear indication of deformation caused by faulting. One young timing of faulting is identified in the Ede trench with the age ranges between 282 to 54 cal BP at 95% confidence range. One definitive event between 2,856 to 535 cal BP is calculated in the Blackley trench site with two probable older events. Clear colluvial wedges consisting of gravel and loess deposits in the Porter trench shows two definite events around 5,000 years and 4,600 years. Radiocarbon dating of the colluvial wedge in the Porter trench is excluded due to the contrast with OSL ages and inference of reworked carbon. From the study, at least three events occurred on the Torlesse fault or within the fault zone in the Holocene.

4.4 Discussion

4.4.1 Paleoseismic history

Paleoseismic study is carried out to identify event in the past, to constrain age of event and to correlate event with a historical earthquake. Three trenches dug at different geomorphic surfaces on the Torlesse fault zone recorded four events in the Torlesse fault zone. Event ages differed from site to site. (Ramsey 2001, 2017)

Event ages may differ for a few reasons. The recent paleoseismic record at Ede stream area might not represent a surface faulting event. For example, minor vertical displacement could have occurred on the Torlesse fault induced from shaking of somewhere else (Fig.4-1 and 4-2). (Cowan 1992; Howard et al. 2005)That said, the fault scarp in most of the main Torlesse fault looks fresh. The lateral scree displacement in the Lansdowne spur would probably be related to very recent faulting (Chapter 3). Hence, the event recorded in the Ede trench was more likely formed by faulting on the main Torlesse fault.

It is a common observation that events recorded in one part of a fault are not recorded in other parts. Preservation of events in the trench directly relates to the quickly burial of sediments before destruction of events by weathering or erosion (McCalpin 2009). The possibility of missing events in the steep slopes of the Torlesse Range remains as events are modified or removed by surficial processes (McCalpin 2009).

4.4.2 Synthesis of paleoseismic data for the Torlesse and Porters Pass Faults

Paleoseismological records show that many events occurred at different times rupturing different faults in the region (Cowan 1992; Howard et al. 2005; Noble 2011). At least six earthquake events causing deformation have been identified in the Porters Pass fault within 9,000 years (Howard et al. 2005) (Fig. 4-15). These prehistoric earthquakes have been estimated using radiocarbon dating of disrupted stratigraphic layers in the trench, but without performing statistical analysis of radiocarbon dates, hence the event age estimates are medium confidence. At least three earthquakes occurred within 5,300 years have been identified in the Torlesse fault zone after modelling in OxCal (Hogg et al. 2013). Similarly, three earthquake events (two events around 700 years ago and one event around 10,000 years ago have been recognized from Lake Coleridge area (Lee et al. 2009).

I modelled ages of Porters Pass fault events and events on the Esk fault to compare to the timing of events presented in this study. The plot of the probability density of earthquake events of modelled data of the Porters Pass trench (Fig. 4-15), Torlesse trenches (Fig. 4-3, 4-7 and 4-14) and Esk trench carried out using the OxCal in the southern hemisphere calibration display overlapping event ages in the Porters Pass-Torlesse seismic zone (Fig. 4-15 and 4-16). Recalculated ages show a wide range of overlapping event ages in the Blackley section and the Northern Esk section (Fig. 4-16).

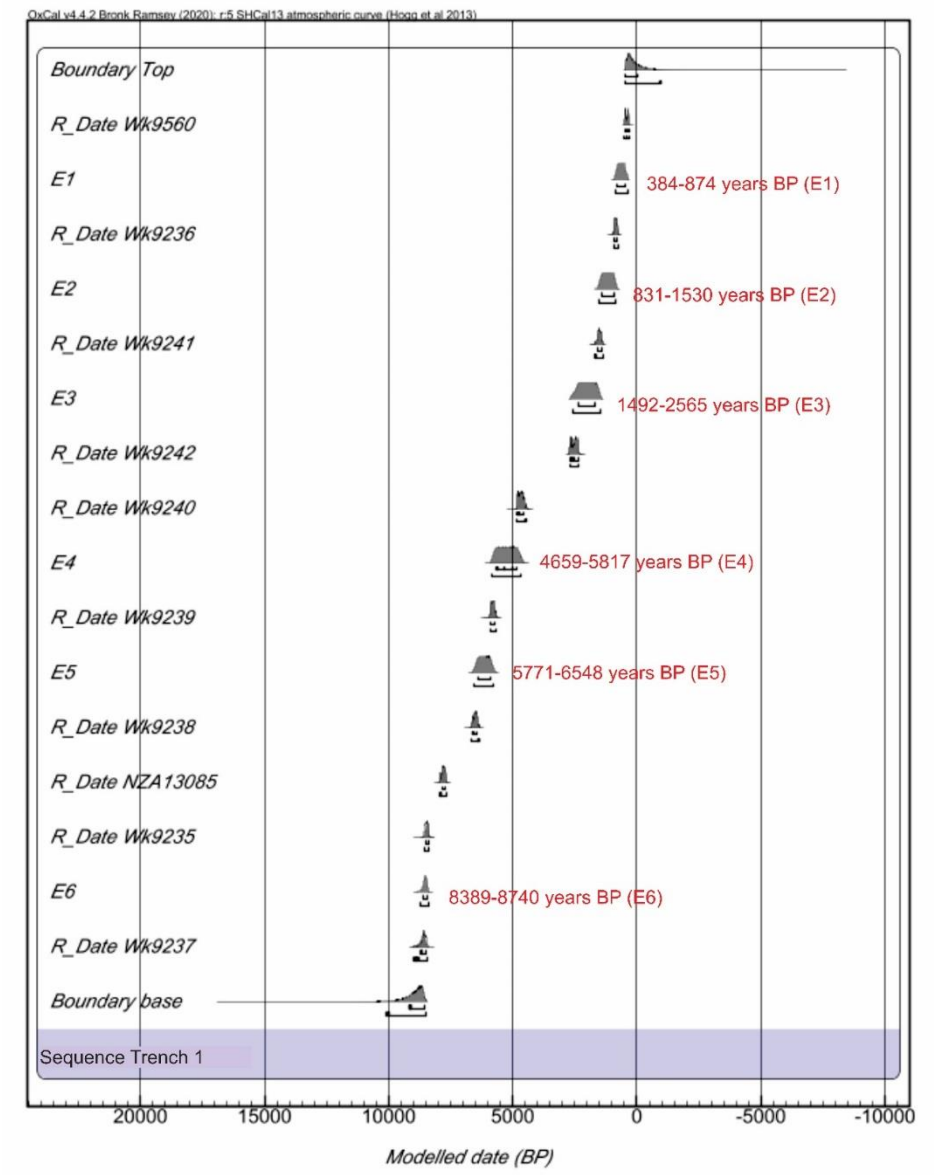

Figure 4-15. OxCal age models for the stratigraphic sequence in the Porters Pass trench (Howard et al. 2005) based on SHCAL13 atmospheric curve (Hogg et al. 2013). Probability density functions of event ages are modelled with the 95% confidence range.

While it is not possible to claim anything with certainty due to the errors associated with age dating, two interesting results emerge from this analysis:

(1) There is significant overlap in event timings between the penultimate and antepenultimate events on the Torlesse fault with events dated on the Porters Pass fault.

(2) There is no correlative Porters Pass fault event for the most recent event on the Torlesse fault.

For (1), it is of course tempting to guess that structurally linked faults at depth could rupture concurrently and I assume that this is possible. Alternatively, this could just indicate events (2856 years to 535 years and 5,100 years to 4,500 years) that are closely spaced but separate surface rupturing events.

For (2), the youngest event on the Torlesse fault is not recorded historically and this may be due to the event before the European settlement (1840 AD) in the region. From the analysis, there is no record of events on the Porters Pass fault at a similar time, revealing that the Torlesse fault could operate as a distinct seismic source regardless of its structural link with the Porters Pass fault (Fig. 4-16).

My preferred model is one in which large fault ruptures nucleate at depth on a master fault under the Torlesse Range and propagate to the surface on either (or both) of the Torlesse and Porters Pass faults. Interaction between strike-slip faults has been identified (Peacock 1991) hence there is interaction between the Porters Pass fault and the Torlesse fault. Multi-fault ruptures on the Porters Pass fault and Torlesse fault or ruptures on either of these faults may propagate to the surface.

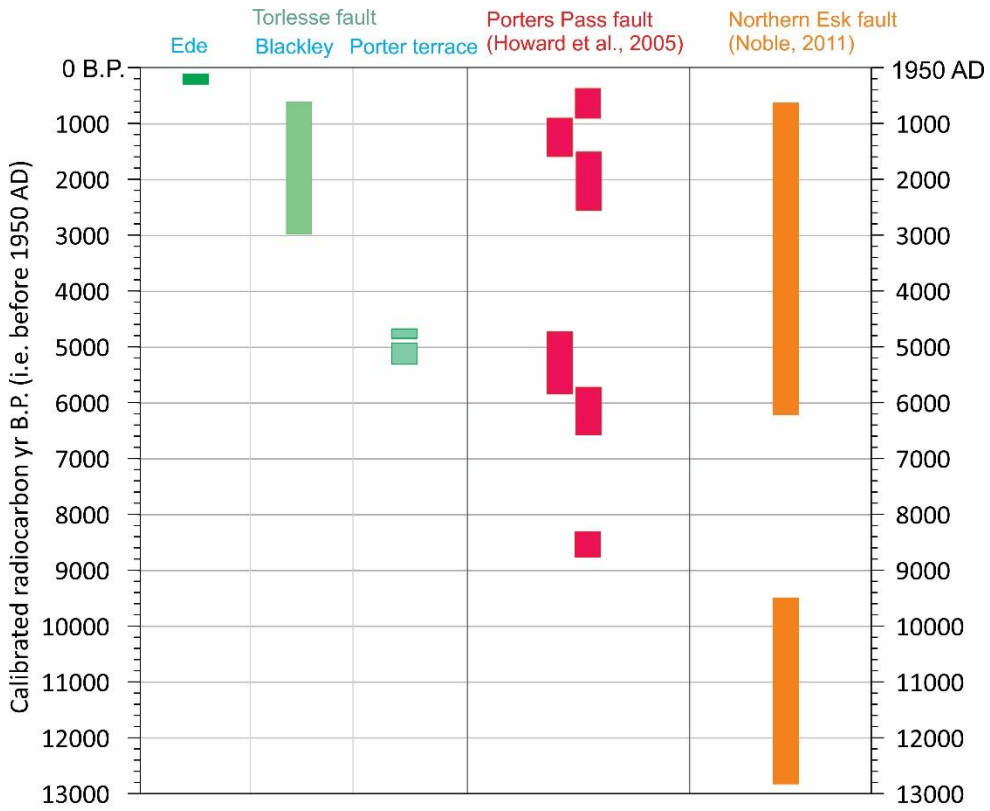

Figure 4-16. Space-time plot of late Holocene earthquake ruptures inferred from the paleoseismic data from Porters Pass fault (Howard et al. 2005), Northern Esk fault(Noble 2011) and the Torlesse fault. Time ranges shown in the green colour belong to the Torlesse fault. Age of events dated from the Ede area, the Blackley area and the Porter River terrace show at least three events.

Multi-fault ruptures during large earthquake events occurred in different places as in the 2016 Mw 7.6 Kaikōura earthquake (Hamling et al. 2017; Litchfield et al. 2018; Nicol et al. 2018), and in the 1992 Mw 7.3 Landers earthquake, California (Hart et al. 1993). The Torlesse fault runs parallel to the reverse dextral Porters Pass fault (Cowan 1992; Howard et al. 2005) and is believed to physically linked in depth as the back thrust of the Porters Pass fault (Fig. 3-34). In my preferred model, ruptures initiate at depth below the PPAFZ-Torlesse junction and can then propagate up dip onto one or both faults.

4.4.3 Magnitude scenarios: 1) segmented Torlesse 2) full Torlesse 3) Torlesse and Porters Pass

The probable magnitude of the earthquake producing surface rupture in the area is one of the most important earthquake source parameters. Using empirical relationships, the magnitude of the earthquake causing the rupture can be calculated (e.g., Wells et al. 1994). As only two hand-dug trenches with a depth of less than 1.3 m have been excavated in the main Torlesse fault, limitations exist with the paleoseismic and kinematics data. Measurement of cumulative displacement obtained from displaced spur shows 15 m at the Blackley area. Horizontal displacement of 3 m measured from the displaced scree of the Lansdowne spur could be used as the single event displacement with high uncertainty (Chapter 3). Using this single event displacement as average displacement for the fault zone, the Blackley area could experience at least four events after the LGM. However, the displacement in every event is not the same. Using this displacement in magnitude scaling equation (Wells et al. 1994), Mw of the Torlesse fault having the average displacement of 3 m is resulted in a range of 7.3 to 7.5.

Three magnitude scenarios are calculated based on ruptures on 1) segmented Torlesse fault 2) full Torlesse fault and 3) Torlesse and Porters Pass faults.

Regarding 1), it is possible that the earthquake produces surface rupture of around 25 km on the Torlesse fault. This length is taken on the basis of assumption that different rupture of different segment during events is normal. Using this rupture length in the empirical equations (Wells et al. 1994; Stirling et al. 2008; Wesnousky 2008; Leonard 2010; Yen et al. 2011; Stirling et al. 2013), M_w of 6.5 to 6.8 is calculated (Fig. 4-17).

Regarding scenario 2), If the rupture length is taken as 31 km (Pettinga et al., 2001), summing the definite rupture length and the probable fault length, then the M_w using equations (Wells et al. 1994; Stirling et al. 2008; Wesnousky 2008; Leonard 2010; Yen et al. 2011; Stirling et al. 2013) ranges from 6.7 to 6.9 .Magnitude estimated from the average displacement is higher than that of calculated using definite rupture length hence either rupture length of the Torlesse fault is longer than 31 km or the average single event displacement is lower than 3 m. Hence, the displacement of Lansdowne spur could be maximum single event displacement.

Regarding scenario 3), the probable magnitude may be more when the Torlesse fault and Porters Pass fault rupture concurrently. The length of surface rupture in multi-fault ruptures will be more than rupture length of single fault system. Rupture length of 40 km for the Porters Pass fault and 100 km for Porters Pass to Amberly Fault Zone have been estimated (Cowan 1992; Howard et al. 2005). Howard et al. (2005) estimated a fault length of 46 km for Porters Pass fault after conducting paleoseismic studies there. Hence, the total length is expected to be at least 77 km in joint ruptures and it is possible that the distribution of ruptures could be in the different faults. I used scaling relationships (Wells et al. 1994; Stirling et al. 2008; Wesnousky 2008; Leonard 2010; Yen et al. 2011; Stirling et al. 2013) to calculate M_w for the faulting event assuming 77 km rupture lengths. Calculated M_w for this rupture length ranges from 7.2 to 7.4 (Fig. 4-17). From the above calculation, M_w 7.2 to 7.4 is plausible in the area where there is a rupture length of around 77 km in the Torlesse Range. Multi-fault ruptures with the M_w ranges from 7.4 to 7.8 is expected if whole Torlesse fault and the Porters Pass-Amberly Fault Zone are ruptured with length of 130 km.

In summary, M_w (6.5 to 7.4) calculated using three rupture length scenarios in the Torlesse Range pose risk to the rural and urban areas of mid-Canterbury.

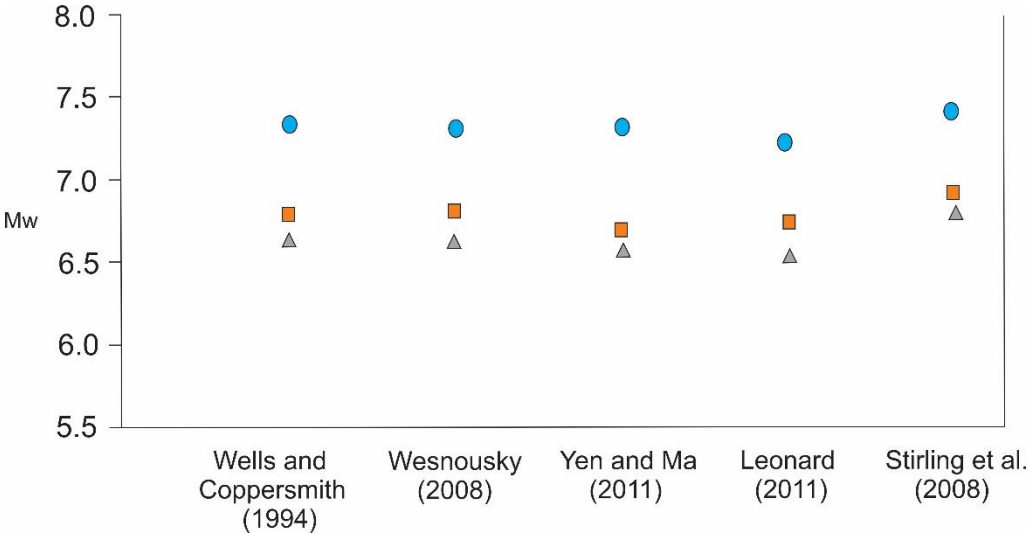

Figure 4-17. M_w of the Torlesse fault and the Porters Pass fault taking three scenarios. Scenario,1) segmented rupture of 25 km on the Torlesse fault, scenario 2) full ruptre (31 km) of Torlesse fault and scenario 3), joint ruputre of 77 km on Torlesse and Porters Pass faults using equations of different authors. Blue solid dot is probable M_w when rupture length is 77 km, orage square is probable M_w when rupture length is 31 km and grey dot is probable M_w when rupture length is 25 km.

4.5 Conclusion

Stratigraphic evidence logged in the trenches indicate the evidence of paleoearthquakes on the Torlesse fault:

- At least three ages of events (between 282 and 54 years BP, between 2856 and 535 years BP and around 5000 years BP) are dated for the Torlesse fault, of which two events shows similar timing with the ages of events for the Porters Pass fault. This shows the possibility of joint rupture on the Torlesse fault and the Porters Pass fault. One event recorded in the Torlesse trench, around 282-54 years before present, is unrecorded in the Porters Pass fault hence the Torlesse fault could be a distinct seismic source.
- I present a model whereby ruptures can propagate to the surface via either or both of the Torlesse and Porters Pass faults from a master fault at depth. The surface rupture length-scaling-derived magnitudes for these scenarios are 6.5 to 7.4.

4.6 References

Adamiec G, Aitken MJ 1998. Dose-rate conversion factors: update. Ancient tL 16: 37-50.

Arnold LJ, Roberts RG 2009. Stochastic modelling of multi-grain equivalent dose (De) distributions: Implications for OSL dating of sediment mixtures. Quaternary Geochronology 4: 204-230.

Bird MI, Levchenko V, Ascough PLet al. 2014. The efficiency of charcoal decontamination for radiocarbon dating by three pre-treatments - ABOX, ABA and hypy. Quaternary Geochronology 22: 25-32.

Bronk Ramsey C, Heaton TJ, Schlolaut Get al. 2020. Reanalysis of the Atmospheric Radiocarbon Calibration Record from Lake Suigetsu, Japan. Radiocarbon 62: 989-999.

Cowan HA 1992. Structure, seismicity and tectonics of the Porter's Pass-Amberley fault zone, North Canterbury, New Zealand.

Duller GA 2008. Luminescence Dating: guidelines on using luminescence dating in archaeology.

Durcan JA, King GE, Duller GA 2015. DRAC: Dose Rate and Age Calculator for trapped charge dating. Quaternary Geochronology 28: 54-61.

Duross CB, Personius SF, Crone AJet al. 2016. Fault segmentation: New concepts from the Wasatch Fault Zone, Utah, USA. Journal of Geophysical Research: Solid Earth 121: 1131-1157.

Fattahi M, Walker RT 2007. Luminescence dating of the last earthquake of the Sabzevar thrust fault, NE Iran. Quaternary Geochronology 2: 284-289.

Field EH, Jordan TH, Page MTet al. 2017. A Synoptic view of the third uniform California earthquake rupture forecast (UCERF3). Seismological Research Letters 88: 1259-1267.

Galbraith RF 2005. Statistics for fission track analysis. 1-219 p.

Galbraith RF, Roberts RG, Laslett GM, Yoshida H, Olley JM 1999. Optical dating of single and multiple grains of quartz from Jinmium rock shelter, northern Australia: Part I, experimental design and statistical models. Archaeometry 41: 339-364.

Grimm EC, Maher Jr LJ, Nelson DM 2009. The magnitude of error in conventional bulk-sediment radiocarbon dates from central North America. Quaternary Research 72: 301-308.

Hamling IJ, Hreinsdóttir S, Clark Ket al. 2017. Complex multifault rupture during the 2016 M<inf>w</inf> 7.8 Kaikōura earthquake, New Zealand. Science 356.

Hart EW, Bryant WA, Treiman JA 1993. Surface faulting associated with the June 1992 Landers earthquake, California. Calif. Geol 46: 10-16.

Hogg AG, Hua Q, Blackwell PGet al. 2013. Shcal13 Southern Hemisphere calibration, 0-50,000 years cal BP. Radiocarbon 55: 1889-1903.

Howard M, Nicol A, Campbell J, Pettinga JR 2005. Holocene paleoearthquakes on the strike-slip porters pass fault, Canterbury, New Zealand. New Zealand Journal of Geology and Geophysics 48: 59-74.

Kreutzer S, Schmidt C, Fuchs MC, Dietze M, Fischer M, Fuchs M 2012. Introducing an R package for luminescence dating analysis. Ancient TL 30: 1-8.

Lee J, Davies T, Bell D 2009. Successive Holocene rock avalanches at Lake Coleridge, Canterbury, New Zealand. Landslides 6: 287-297.

Lee MK, Lee YI, Lim HS, Lee JI, Choi JH, Yoon HI 2011. Comparison of radiocarbon and OSL dating methods for a Late Quaternary sediment core from Lake Ulaan, Mongolia. Journal of Paleolimnology 45: 127-135.

Leonard M 2010. Earthquake fault scaling: Self-consistent relating of rupture length, width, average displacement, and moment release. Bulletin of the Seismological Society of America 100: 1971-1988.

Litchfield NJ, Villamor P, Dissen RJVet al. 2018. Surface rupture of multiple crustal faults in the 2016 M w 7.8 Kaikōura, New Zealand, earthquake. Bulletin of the Seismological Society of America 108: 1496-1520.

McCalpin JP 2009. Paleoseismology, Academic press.

Murray AS, Wintle AG 2000. Luminescence dating of quartz using an improved single-aliquot regenerative-dose protocol. Radiation Measurements 32: 57-73.

Murray AS, Wintle AG 2003. The single aliquot regenerative dose protocol: Potential for improvements in reliability. Radiation Measurements 37: 377-381.

Nicol A, Khajavi N, Pettinga JRet al. 2018. Preliminary Geometry, Displacement, and Kinematics of Fault Ruptures in the Epicentral Region of the 2016 Mw 7.8 Kaikōura, New Zealand, Earthquake. Bulletin of the Seismological Society of America 108: 1521-1539.

Noble DP 2011. Tectonic geomorphology and paleoseismicity of the Northern Esk Fault, North Canterbury, New Zealand. Unpublished thesis, University of Canterbury, Christchurch. 169 p.

Peacock DCP 1991. Displacements and segment linkage in strike-slip fault zones. Journal of Structural Geology 13: 1025-1035.

Pettinga JR, Yetton MD, Van Dissen RJ, Downes G 2001. Earthquake source identification and characterisation for the Canterbury region, South Island, New Zealand.

Porat N, Duller GAT, Amit R, Zilberman E, Enzel Y 2009. Recent faulting in the southern Arava, Dead Sea Transform: Evidence from single grain luminescence dating. Quaternary International 199: 34-44.

Ramsey CB 2001. Development of the radiocarbon calibration program. Radiocarbon 43: 355-363.

Ramsey CB 2017. Methods for Summarizing Radiocarbon Datasets. Radiocarbon 59: 1809-1833.

Rodriguez Padilla AM, Oskin ME, Rockwell TK, Delusina I, Singleton DM 2021. Joint earthquake ruptures of the San Andreas and San Jacinto faults, California, USA. Geology 50: 387-391.

Shaw BE, Fry B, Nicol A, Howell A, Gerstenberger M 2022. An Earthquake Simulator for New Zealand. Bulletin of the Seismological Society of America 112: 763-778.

Stirling M, Goded T, Berryman K, Litchfield N 2013. Selection of earthquake scaling relationships for seismic-hazard analysis. Bulletin of the Seismological Society of America 103: 2993-3011.

Stirling M, Gerstenberger M, Litchfield Net al. 2008. Seismic hazard of the Canterbury Region, New Zealand: New earthquake source model and methodology. Bulletin of the New Zealand Society for Earthquake Engineering 41: 51-67.

Thomsen KJ, Murray AS, Bøtter-Jensen L, Kinahan J 2007. Determination of burial dose in incompletely bleached fluvial samples using single grains of quartz. Radiation Measurements 42: 370-379.

Thomsen KJ, Jain M, Bøtter-Jensen L, Murray AS, Jungner H 2003. Variation with depth of dose distributions in single grains of quartz extracted from an irradiated concrete block. Radiation Measurements 37: 315-321.

Wells DL, Coppersmith KJ 1994. New empirical relationships among magnitude, rupture length, rupture width, rupture area, and surface displacement. Bulletin - Seismological Society of America 84: 974-1002.

Wesnousky SG 2008. Displacement and geometrical characteristics of earthquake surface ruptures: Issues and implications for seismic-hazard analysis and the process of earthquake rupture. Bulletin of the Seismological Society of America 98: 1609-1632.

Yanchou L, Prescott JR, Hua Z, Jie C, Lanying W 2002. Optical dating of colluvial deposits from Xiyangfang, China, and the relation to palaeo-earthquake events. Quaternary Science Reviews 21: 1087-1097.

Yen YT, Ma KF 2011. Source-Scaling relationship for M 4.6-8.9 earthquakes, specifically for earthquakes in the Collision Zone of Taiwan. Bulletin of the Seismological Society of America 101: 464-481.

Appendix A: Accelerator Mass Spectrometry results

THE UNIVERSITY OF WAIKATO
Te Whare Wānanga o Waikato

Private Bag 3105
Hamilton,
New Zealand.
Ph +64 7 838 4278
email c14@waikato.ac.nz

Friday, 5 July 2019

Radiocarbon Dating Laboratory

Report on Radiocarbon Age Determination for Wk- 49540

Submitter	S Dhakal
Submitter's Code	EDE-U3-CH1
Site & Location	Torlesse Fault, New Zealand
Sample Material	Charcoal
Physical Pretreatment	Sample cleaned.
Chemical Pretreatment	Sample washed in hot HCl, rinsed and treated with multiple hot NaOH washes. The NaOH insoluble fraction was treated with hot HCl, filtered, rinsed and dried.

$D^{14}C$	-25.8 ± 1.9 ‰
$F^{14}C$%	97.4 ± 0.2 %
Result	**210 ± 15 BP**

(AMS measurement)

Comments

Please note: The Carbon-13 stable isotope value ($\delta^{13}C$) was measured on prepared graphite using the AMS spectrometer. The radiocarbon date has therefore been corrected for isotopic fractionation. However the AMS-measured $\delta^{13}C$ value can differ from the $\delta^{13}C$ of the original material and it is therefore not shown.

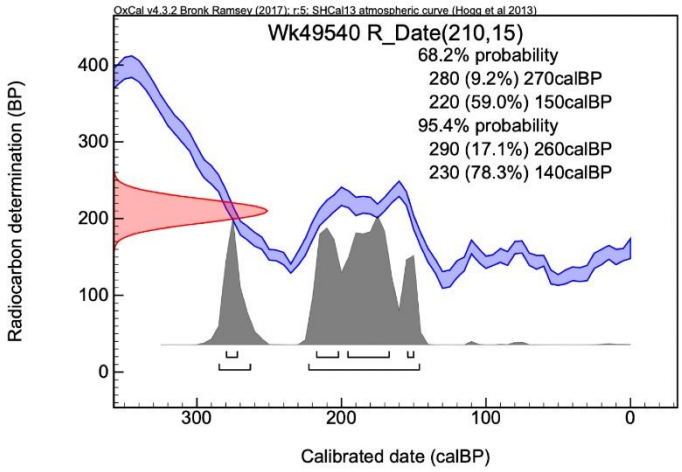

- Explanation of the calibrated Oxcal plots can be found at the Oxford Radiocarbon Accelerator Unit's calibration web pages (http://c14.arch.ox.ac.uk/embed.php?File=explanation.php)
- Result is *Conventional Age or Percent Modern Carbon (pMC)* following Stuiver and Polach, 1977, Radiocarbon 19, 355-363. This is based on the Libby half-life of 5568 yr with correction for isotopic fractionation applied. This age is normally quoted in publications and must include the appropriate error term and Wk number.
- Quoted errors are 1 standard deviation due to counting statistics multiplied by an experimentally determined Laboratory Error Multiplier.
- The isotopic fractionation, $\delta^{13}C$, is expressed as ‰ wrt PDB and is measured on sample CO_2.
- $F^{14}C$% is also known as *Percent Modern Carbon (pMC)*.

Figure 1: Radiocarbon result and calibrations of sample (EDE-U3-CH1) from the Ede trench.

THE UNIVERSITY OF WAIKATO
Te Whare Wānanga o Waikato

Private Bag 3105
Hamilton,
New Zealand.
Ph +64 7 838 4278
email c14@waikato.ac.nz

Friday, 5 July 2019

Radiocarbon Dating Laboratory

Report on Radiocarbon Age Determination for Wk- 49541

Submitter	S Dhakal
Submitter's Code	EDE-U3-CH2
Site & Location	Torlesse Fault, New Zealand
Sample Material	Charcoal
Physical Pretreatment	Sample cleaned.
Chemical Pretreatment	Sample washed in hot HCl, rinsed and treated with multiple hot NaOH washes. The NaOH insoluble fraction was treated with hot HCl, filtered, rinsed and dried.

$D^{14}C$	-21.6 ±	2.0 ‰
$F^{14}C$%	97.8 ±	0.2 %
Result	**175 ± 16 BP**	

(AMS measurement)

Comments

Please note: The Carbon-13 stable isotope value ($\delta^{13}C$) was measured on prepared graphite using the AMS spectrometer. The radiocarbon date has therefore been corrected for isotopic fractionation. However the AMS-measured $\delta^{13}C$ value can differ from the $\delta^{13}C$ of the original material and it is therefore not shown.

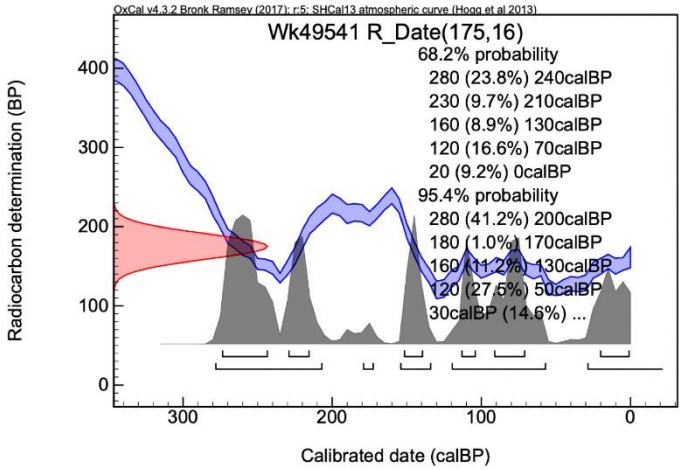

- Explanation of the calibrated Oxcal plots can be found at the Oxford Radiocarbon Accelerator Unit's calibration web pages (http://c14.arch.ox.ac.uk/embed.php?File=explanation.php)
- Result is *Conventional Age or Percent Modern Carbon (pMC)* following Stuiver and Polach, 1977, Radiocarbon 19, 355-363. This is based on the Libby half-life of 5568 yr with correction for isotopic fractionation applied. This age is normally quoted in publications and must include the appropriate error term and Wk number.
- Quoted errors are 1 standard deviation due to counting statistics multiplied by an experimentally determined Laboratory Error Multiplier.
- The isotopic fractionation, $\delta^{13}C$, is expressed as ‰ wrt PDB and is measured on sample CO_2.
- $F^{14}C$% is also known as *Percent Modern Carbon (pMC)*.

Figure 2: Radiocarbon result and calibrations of sample (EDE-U3-CH2) from the Ede trench.

THE UNIVERSITY OF WAIKATO
Te Whare Wānanga o Waikato

Private Bag 3105
Hamilton,
New Zealand.
Ph +64 7 838 4278
email c14@waikato.ac.nz

Wednesday, 15 April 2020

Radiocarbon Dating Laboratory

Report on Radiocarbon Age Determination for Wk- 51106

Submitter	S Dhakal
Submitter's Code	BL-3
Site & Location	Torlesse Fault, near Blackley Stream, New Zealand
Sample Material	carbonaceous silts
Physical Pretreatment	Visible contaminants removed.
Chemical Pretreatment	Sample washed in hot HCl, rinsed and treated with multiple hot NaOH washes. The NaOH insoluble fraction was treated with hot HCl, filtered, rinsed and dried.

$D^{14}C$	-800.8 ± 1.1 ‰
$F^{14}C$%	19.9 ± 0.1 %
Result	**12,961 ± 46 BP**

(AMS measurement)

Comments

Please note: The Carbon-13 stable isotope value ($\delta^{13}C$) was measured on prepared graphite using the AMS spectrometer. The radiocarbon date has therefore been corrected for isotopic fractionation. However the AMS-measured $\delta^{13}C$ value can differ from the $\delta^{13}C$ of the original material and it is therefore not shown.

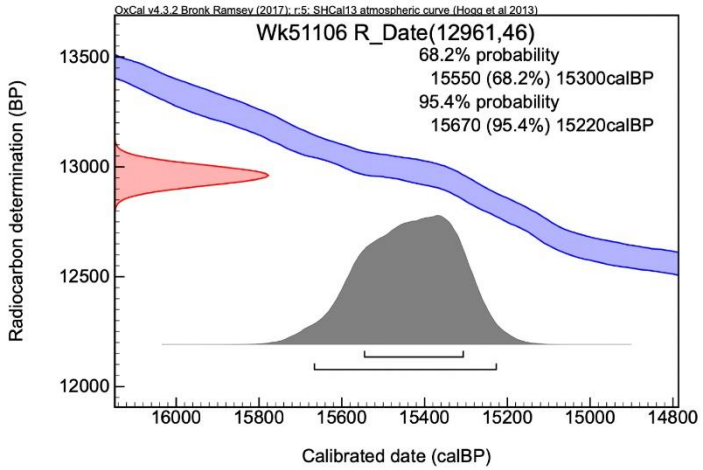

- Explanation of the calibrated Oxcal plots can be found at the Oxford Radiocarbon Accelerator Unit's calibration web pages (http://c14.arch.ox.ac.uk/embed.php?File=explanation.php)
- Result is *Conventional Age or Percent Modern Carbon (pMC)* following Stuiver and Polach, 1977, Radiocarbon 19, 355-363. This is based on the Libby half-life of 5568 yr with correction for isotopic fractionation applied. This age is normally quoted in publications and must include the appropriate error term and Wk number.
- Quoted errors are 1 standard deviation due to counting statistics multiplied by an experimentally determined Laboratory Error Multiplier.
- The isotopic fractionation, $\delta^{13}C$, is expressed as ‰ wrt PDB and is measured on sample CO_2.
- $F^{14}C$% is also known as *Percent Modern Carbon (pMC)*.

Figure 3: Radiocarbon result and calibrations of sample (BL-3) from the Blackley trench

Figure 4: Radiocarbon result and calibrations of sample (BL-C4) from the Blackley trench.

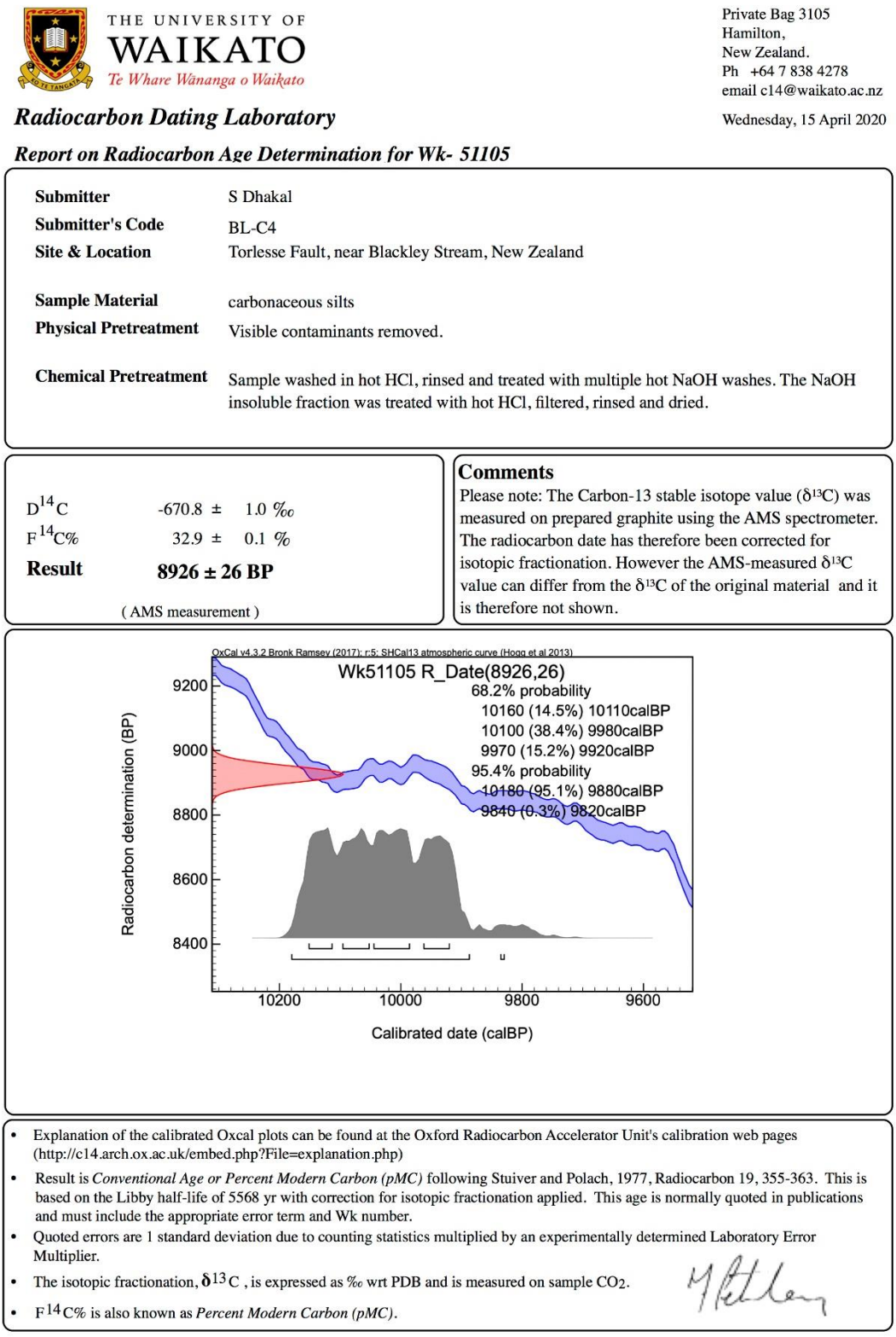

THE UNIVERSITY OF WAIKATO
Te Whare Wānanga o Waikato

Private Bag 3105
Hamilton,
New Zealand.
Ph +64 7 838 4278
email c14@waikato.ac.nz

Wednesday, 15 April 2020

Radiocarbon Dating Laboratory

Report on Radiocarbon Age Determination for Wk- 51105

Submitter	S Dhakal
Submitter's Code	BL-C4
Site & Location	Torlesse Fault, near Blackley Stream, New Zealand
Sample Material	carbonaceous silts
Physical Pretreatment	Visible contaminants removed.
Chemical Pretreatment	Sample washed in hot HCl, rinsed and treated with multiple hot NaOH washes. The NaOH insoluble fraction was treated with hot HCl, filtered, rinsed and dried.

$D^{14}C$	-670.8 ± 1.0 ‰
$F^{14}C$%	32.9 ± 0.1 %
Result	**8926 ± 26 BP**

(AMS measurement)

Comments

Please note: The Carbon-13 stable isotope value ($\delta^{13}C$) was measured on prepared graphite using the AMS spectrometer. The radiocarbon date has therefore been corrected for isotopic fractionation. However the AMS-measured $\delta^{13}C$ value can differ from the $\delta^{13}C$ of the original material and it is therefore not shown.

- Explanation of the calibrated Oxcal plots can be found at the Oxford Radiocarbon Accelerator Unit's calibration web pages (http://c14.arch.ox.ac.uk/embed.php?File=explanation.php)
- Result is *Conventional Age or Percent Modern Carbon (pMC)* following Stuiver and Polach, 1977, Radiocarbon 19, 355-363. This is based on the Libby half-life of 5568 yr with correction for isotopic fractionation applied. This age is normally quoted in publications and must include the appropriate error term and Wk number.
- Quoted errors are 1 standard deviation due to counting statistics multiplied by an experimentally determined Laboratory Error Multiplier.
- The isotopic fractionation, $\delta^{13}C$, is expressed as ‰ wrt PDB and is measured on sample CO_2.
- $F^{14}C$% is also known as *Percent Modern Carbon (pMC)*.

Figure 4: Radiocarbon result and calibrations of sample (BL-C4) from the Blackley trench

THE UNIVERSITY OF WAIKATO
Te Whare Wānanga o Waikato

Private Bag 3105
Hamilton,
New Zealand.
Ph +64 7 838 4278
email c14@waikato.ac.nz

Wednesday, 15 April 2020

Radiocarbon Dating Laboratory

Report on Radiocarbon Age Determination for Wk- 51103

Submitter	S Dhakal
Submitter's Code	BL-C1
Site & Location	Torlesse Fault, near Blackley Stream, New Zealand
Sample Material	River silts
Physical Pretreatment	Visible contaminants removed.
Chemical Pretreatment	Sample washed in hot HCl, rinsed and treated with multiple hot NaOH washes. The NaOH insoluble fraction was treated with hot HCl, filtered, rinsed and dried.

$D^{14}C$	-300.3 ± 2.0 ‰
$F^{14}C$%	70.0 ± 0.2 %
Result	**2869 ± 24 BP**

(AMS measurement)

Comments

Please note: The Carbon-13 stable isotope value ($\delta^{13}C$) was measured on prepared graphite using the AMS spectrometer. The radiocarbon date has therefore been corrected for isotopic fractionation. However the AMS-measured $\delta^{13}C$ value can differ from the $\delta^{13}C$ of the original material and it is therefore not shown.

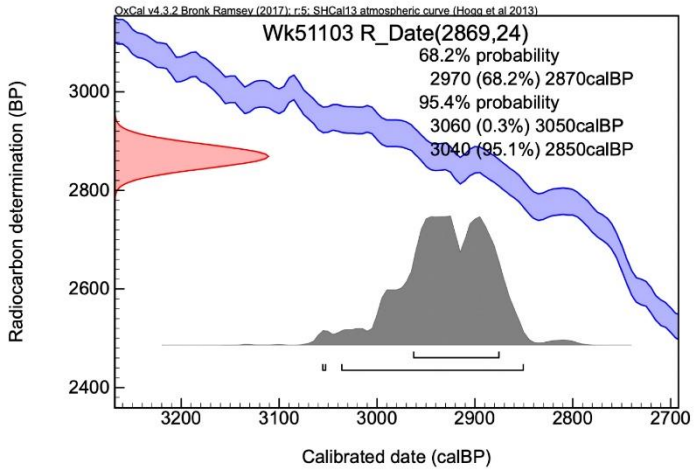

- Explanation of the calibrated Oxcal plots can be found at the Oxford Radiocarbon Accelerator Unit's calibration web pages (http://c14.arch.ox.ac.uk/embed.php?File=explanation.php)
- Result is *Conventional Age or Percent Modern Carbon (pMC)* following Stuiver and Polach, 1977, Radiocarbon 19, 355-363. This is based on the Libby half-life of 5568 yr with correction for isotopic fractionation applied. This age is normally quoted in publications and must include the appropriate error term and Wk number.
- Quoted errors are 1 standard deviation due to counting statistics multiplied by an experimentally determined Laboratory Error Multiplier.
- The isotopic fractionation, $\delta^{13}C$, is expressed as ‰ wrt PDB and is measured on sample CO_2.
- $F^{14}C$% is also known as *Percent Modern Carbon (pMC)*.

Figure 5: Radiocarbon result and calibrations of sample (BL-C1) from the Blackley trench.

THE UNIVERSITY OF WAIKATO
Te Whare Wānanga o Waikato

Private Bag 3105
Hamilton,
New Zealand.
Ph +64 7 838 4278
email c14@waikato.ac.nz

Wednesday, 15 April 2020

Radiocarbon Dating Laboratory

Report on Radiocarbon Age Determination for Wk- 51104

Submitter	S Dhakal
Submitter's Code	BL-C2
Site & Location	Torlesse Fault, near Blackley Stream, New Zealand
Sample Material	charcoal
Physical Pretreatment	Sample cleaned.
Chemical Pretreatment	Sample washed in hot HCl, rinsed and treated with multiple hot NaOH washes. The NaOH insoluble fraction was treated with hot HCl, filtered, rinsed and dried.

$D^{14}C$	-61.6 ± 2.8 ‰
$F^{14}C$%	93.8 ± 0.3 %
Result	**511 ± 24 BP**

(AMS measurement)

Comments

Please note: The Carbon-13 stable isotope value ($\delta^{13}C$) was measured on prepared graphite using the AMS spectrometer. The radiocarbon date has therefore been corrected for isotopic fractionation. However the AMS-measured $\delta^{13}C$ value can differ from the $\delta^{13}C$ of the original material and it is therefore not shown.

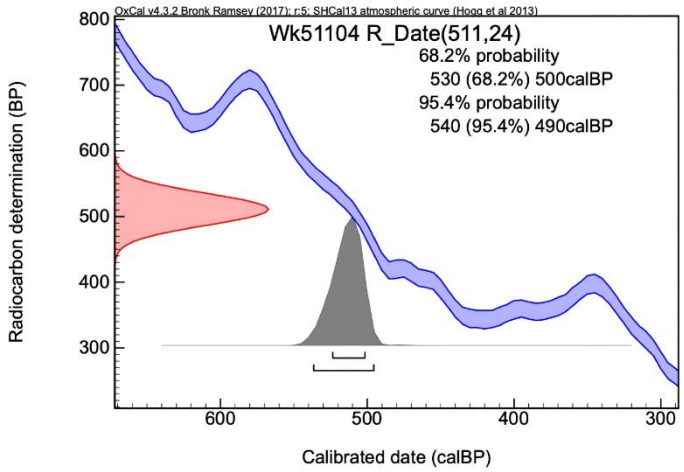

- Explanation of the calibrated Oxcal plots can be found at the Oxford Radiocarbon Accelerator Unit's calibration web pages (http://c14.arch.ox.ac.uk/embed.php?File=explanation.php)
- Result is *Conventional Age or Percent Modern Carbon (pMC)* following Stuiver and Polach, 1977, Radiocarbon 19, 355-363. This is based on the Libby half-life of 5568 yr with correction for isotopic fractionation applied. This age is normally quoted in publications and must include the appropriate error term and Wk number.
- Quoted errors are 1 standard deviation due to counting statistics multiplied by an experimentally determined Laboratory Error Multiplier.
- The isotopic fractionation, $\delta^{13}C$, is expressed as ‰ wrt PDB and is measured on sample CO_2.
- $F^{14}C$% is also known as *Percent Modern Carbon (pMC)*.

Figure 6: Radiocarbon result and calibrations of sample (BL-C2) from the Blackley trench.

THE UNIVERSITY OF WAIKATO
Te Whare Wānanga o Waikato

Private Bag 3105
Hamilton,
New Zealand.
Ph +64 7 838 4278
email c14@waikato.ac.nz

Wednesday, 8 July 2020

Radiocarbon Dating Laboratory

Report on Radiocarbon Age Determination for Wk- 51317

Submitter	S Dhakal
Submitter's Code	PT-C1
Site & Location	Torlesse Fault, Porter River Terrace (Near Porter Ski Field), New Zealand
Sample Material	Charcoal
Physical Pretreatment	Sample cleaned.
Chemical Pretreatment	Sample washed in hot HCl, rinsed and treated with multiple hot NaOH washes. The NaOH insoluble fraction was treated with hot HCl, filtered, rinsed and dried.

$D^{14}C$	-669.0 ± 0.8 ‰
$F^{14}C\%$	33.1 ± 0.1 %
Result	**8881 ± 19 BP**

(AMS measurement)

Comments

Please note: The Carbon-13 stable isotope value ($\delta^{13}C$) was measured on prepared graphite using the AMS spectrometer. The radiocarbon date has therefore been corrected for isotopic fractionation. However the AMS-measured $\delta^{13}C$ value can differ from the $\delta^{13}C$ of the original material and it is therefore not shown.

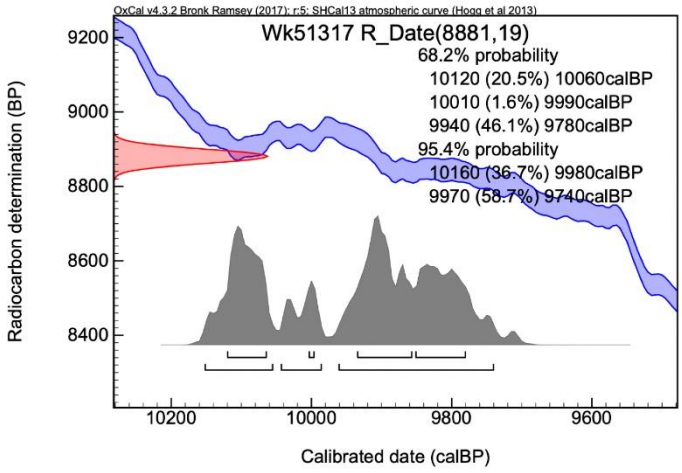

- Explanation of the calibrated Oxcal plots can be found at the Oxford Radiocarbon Accelerator Unit's calibration web pages (http://c14.arch.ox.ac.uk/embed.php?File=explanation.php)
- Result is *Conventional Age or Percent Modern Carbon (pMC)* following Stuiver and Polach, 1977, Radiocarbon 19, 355-363. This is based on the Libby half-life of 5568 yr with correction for isotopic fractionation applied. This age is normally quoted in publications and must include the appropriate error term and Wk number.
- Quoted errors are 1 standard deviation due to counting statistics multiplied by an experimentally determined Laboratory Error Multiplier.
- The isotopic fractionation, $\delta^{13}C$, is expressed as ‰ wrt PDB and is measured on sample CO_2.
- $F^{14}C\%$ is also known as *Percent Modern Carbon (pMC)*.

Figure 7: Radiocarbon result and calibrations of sample (PT-C1) from Unit 4 of the Porter trench.

THE UNIVERSITY OF WAIKATO
Te Whare Wānanga o Waikato

Private Bag 3105
Hamilton,
New Zealand.
Ph +64 7 838 4278
email c14@waikato.ac.nz

Wednesday, 8 July 2020

Radiocarbon Dating Laboratory

Report on Radiocarbon Age Determination for Wk- 51318

Submitter	S Dhakal
Submitter's Code	PT-C2
Site & Location	Torlesse Fault, Porter River Terrace (Near Porter Ski Field), New Zealand
Sample Material	Charcoal
Physical Pretreatment	Sample cleaned.
Chemical Pretreatment	Sample washed in hot HCl, rinsed and treated with multiple hot NaOH washes. The NaOH insoluble fraction was treated with hot HCl, filtered, rinsed and dried.

$D^{14}C$	-650.5 ± 0.9 ‰
$F^{14}C$%	34.9 ± 0.1 %
Result	**8446 ± 20 BP**

(AMS measurement)

Comments

Please note: The Carbon-13 stable isotope value ($\delta^{13}C$) was measured on prepared graphite using the AMS spectrometer. The radiocarbon date has therefore been corrected for isotopic fractionation. However the AMS-measured $\delta^{13}C$ value can differ from the $\delta^{13}C$ of the original material and it is therefore not shown.

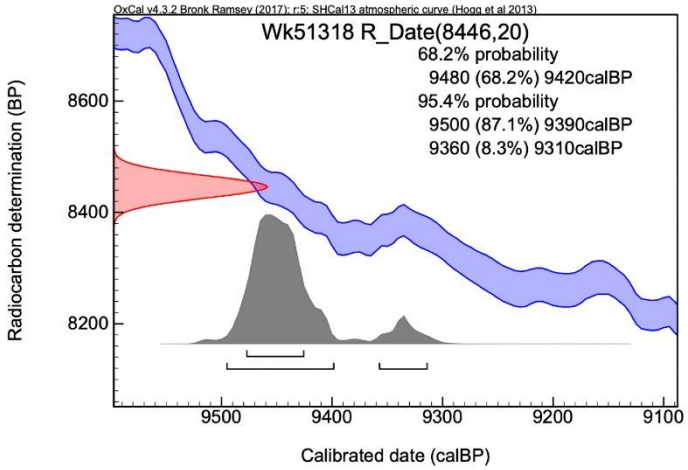

- Explanation of the calibrated Oxcal plots can be found at the Oxford Radiocarbon Accelerator Unit's calibration web pages (http://c14.arch.ox.ac.uk/embed.php?File=explanation.php)
- Result is *Conventional Age or Percent Modern Carbon (pMC)* following Stuiver and Polach, 1977, Radiocarbon 19, 355-363. This is based on the Libby half-life of 5568 yr with correction for isotopic fractionation applied. This age is normally quoted in publications and must include the appropriate error term and Wk number.
- Quoted errors are 1 standard deviation due to counting statistics multiplied by an experimentally determined Laboratory Error Multiplier.
- The isotopic fractionation, $\delta^{13}C$, is expressed as ‰ wrt PDB and is measured on sample CO_2.
- $F^{14}C$% is also known as *Percent Modern Carbon (pMC)*.

Figure 8: Radiocarbon result and calibrations of sample (PT-C2) from Unit 4 of the Porter trench

Appendix B: GPR survey

A GPR survey was conducted to estimate the dip to calculate displacements of the eastern fault in the Porter River terrace. In addition, the GPR survey was carried out in the western fault area, near the trench, to validate the GPR trace with the trench wall. From the CMP analysis, a velocity of 0.1m/ns was estimated for the gravel deposits in the area. This velocity was used to migrate profiles during the analysis. The fault dip was determined visualizing the disruption of reflectors.

The GPR survey was carried out mainly on the gravel deposit hence the reflectors obtained from the upthrown and downthrown sides in the terrace are undulated. Noises produced from the boulders are significant. Rock underlying fluvial gravel and belongs to Tertiary rocks is not identified in the GPR trace and interpreted the gravel deposit is more than 10 m at the GPR survey area.

The GPR trace obtained from the survey across the western Fault scarp was matched with the trench wall (Fig. 4-9). Disruption of reflectors in the colluvial wedges and fault plane were analysed from the trench area (Fig. 9 and 10). Similar trend of disruption of reflectors from the eastern fault scarp was examined to identify the fault.

By analysing 13 GPR traces obtained from the eastern fault area and two GPR traces from the western area, it is revealed that the eastern fault is normal. A fault plane dipping at an angle of around 70^{o} towards the west is estimated from the GPR traces of the eastern fault scarp (Fig 11) based on the interruption of reflectors in the upper 2 m. Reflectors are not so clear to display the fault line in each profile; however, placing normal fault in the images looks more accurate to represent a sense of slip for displaced reflectors. Displacement of reflectors on the upper part of the hanging wall can be inferred from the GPR trace (Fig. 11). The dip is also supported by the dip of beds in the fault area where high angle beds are observed. Lombardi et al. (2020) have also shown the dip of the eastern fault as 70^{o} based on the stratigraphic study in the Porter River section.

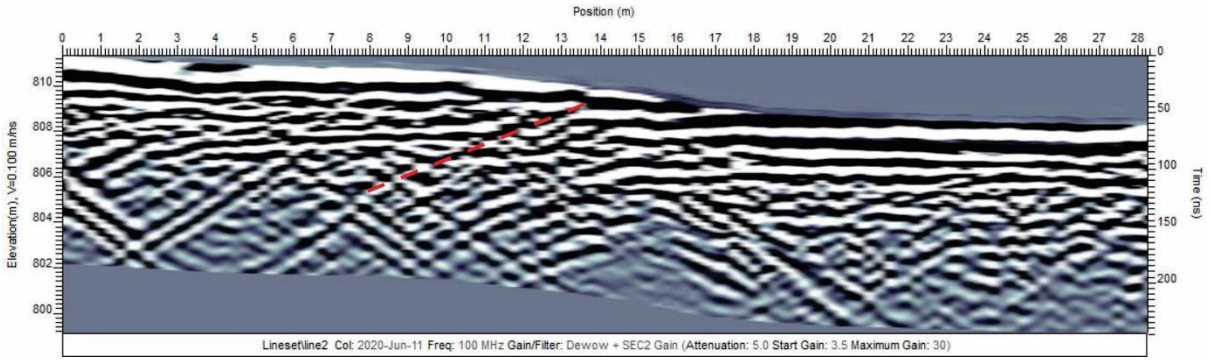

Figure 9: The GPR trace across the western fault in the Porter River terrace. The fault line (red line) is positioned after validating the subsurface reflectors with the trench wall. The dip of the fault measured from the trench is 40^{o}.

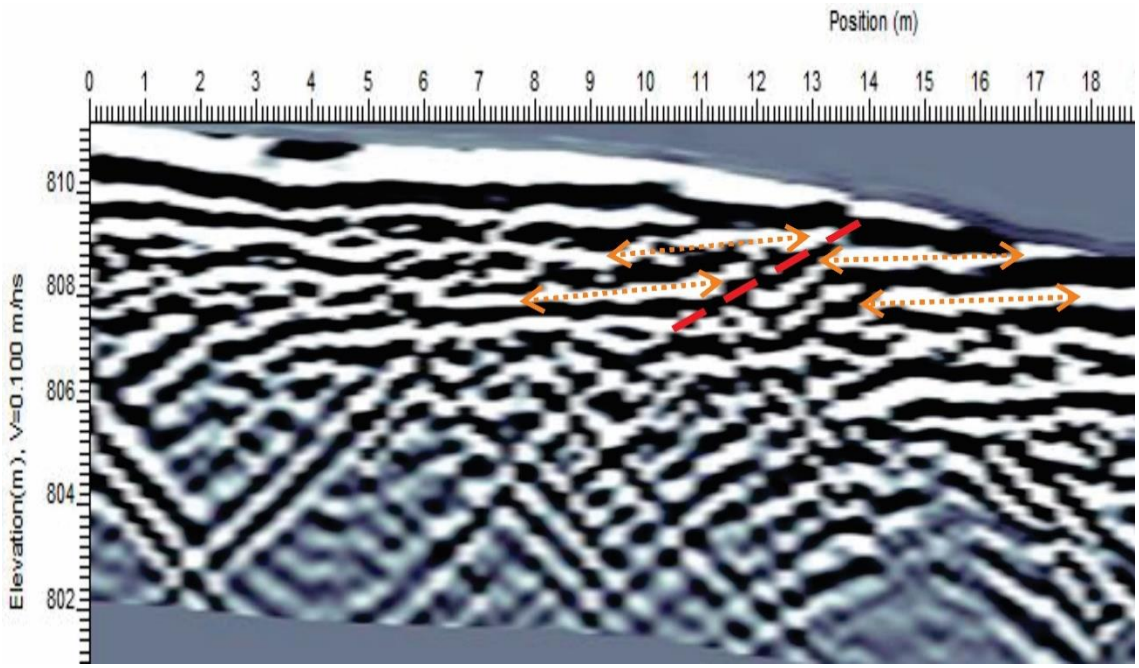

Figure 10: Zoom view of part of figure 4-62. The fault plane (dash red line) interpreted from the offset reflectors (indicated by brown line with arrow at the ends). The GPR trace was matched with ground reality (trench across the Western Fault.

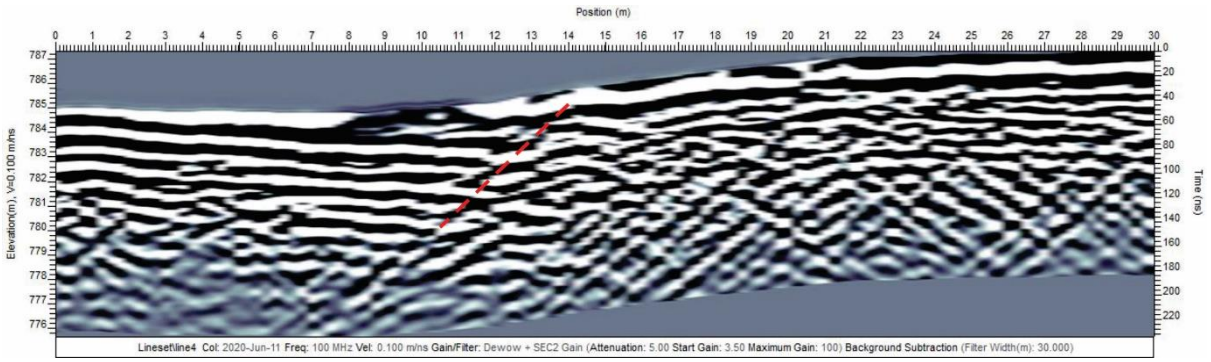

Figure 11: The fault position is shown in the GPR trace across the eastern fault. From the topography and the subsurface reflectors, and identifying features from western trench and the GPR trace, the fault (red line) in the eastern fault is identified as a normal type. The fault plane is measured at around 70^{o} (Lombardi et al. 2020)

References

Lombardi C, Amadon W 2020. A study of the fault activity and straitgraphy of the Porter river valley in relation to the Torlesse fault. Frontiers Abroad.

5 Synthesis and Conclusions

This chapter provides a synthesis of findings, recalls the research question, and shows how objectives have been met. General conclusions, implications, and future research questions are shown.

The main aims of this thesis are to improve knowledge on the surface expression, displacement, slip rates, magnitudes, and recurrence for the Lake Heron and Torlesse faults. I also assess co-rupture likelihood of faults in the Torlesse Range, mid-Canterbury. The goal was met by addressing five specific questions

1. What are the controls on fault deformation zone width?
2. What is the structure of the Lake Heron fault?
3. How can faulted geomorphic features and their displacements and surface age?
4. Are paleoseismic slip rates consistent? How does slip rate change with boarder scale fault structure?
5. Is there variation in the slip rate along the strike of fault? How does the slip rate vary in different segments of the Torlesse Fault?
6. Are the Torlesse and Lake Heron faults capable of rupturing together due to their structural relationships and prehistoric earthquake records?
7. Does the structure and kinematics of the Torlesse fault and other faults int eh region support the plate boundary scale “flower structure” model?

This research used high resolution Unmanned Aerial Vehicle (UAV)-derived Digital Surface Model (DSM) for precise mapping, surveying and paleoseismic trenching to answer these questions. The findings are summarised in Figures 5-1 and 5-2, and discussed in more depth below.

5.1 Surface expression of faults

The surface expression of faulting along the Torlesse and Lake Heron faults is highly varied. In some places, deformation is concentrated on a single strand (e.g. Ede Stream), while in others faulting is distributed over wide zones. For the Torlesse fault, contrasting styles of deformation might be faulting might be due to a function of accessibility of pre-existing discontinuities (e.g., bedding). Here, faults are able to use discontinuities for slip and propagation to reach the surface in steep terrain. Similar trends were observed in North Canterbury in the Kaikoura earthquake (Brough 2019; Bushell 2022), where the location and orientation of surface ruptures were controlled by bedding. On a smaller scale, faults can trade displacement with folds, as deformation gets expressed through unconsolidated sedimentary deposits of variable properties and thicknesses (i.e. through gravels in the Paddle Hill Creek area). Alternatively, faults can accommodate folding, as observed on flexural slip

faults in the Porter trench area. An important takeaway is that detailed field study is required to understand the style and distribution of deformation associated with active faulting. For faults that passes through critical infrastructure, or properties, it is important to carry out geological and geophysical investigations to characterise surface expression.

5.2 Fault kinematics

The Lake Heron fault was found to host only reverse slip, whereas the Torlesse fault accommodated primarily strike-slip (with a component of vertical offset). Different tectonic domains based on the fault source parameters have been given and the Lake Heron fault and the Torlesse fault fall within border areas of two different tectonic domains (Pettinga et al. 2001; Litchfield et al. 2014). Newly defined tectonic domains, however, show both faults falling within a combined reverse and strike-slip fault domain (Van Dissen et al. 2021). As the plate boundary migrates southwards, it is likely that the Lake Heron fault too will begin to interact with strike-slip systems, and perhaps accommodate strike-slip motion itself.

5.3 Fault geometry

A new contribution from this thesis is the conceptualisation of the Torlesse and Porters Pass faults as two faults within a positive flower structure. Based on field mapping, and in part on paleoseismic data, I propose that oblique strike-slip at depth gets expressed at the surface as the uplift and translation of the fault-bounded Torlesse Range. Ruptures that nucleate at depth may propagate on to one or both faults at the surface – though, based on slip rates, preferentially onto the Porters Pass fault. A similar model was proposed for the Kaikoura earthquake (Lamb et al. 2018), in which elastic strain on the Hikurangi interface gets expressed at the surface as rupture across the family of upper crustal faults at the surface. A key question then, if this model is true in other places in NZ, is whether surface paleoseismic data is really 'unique' to any one fault. Ideally, paleoseismic data and multi-fault rupture models will allow for a range of possible rupture pathways on inter-connected faults.

5.4 Co-rupture likelihood magnitude source

Multi-fault earthquake events have been identified in New Zealand (e.g., Quigley et al. 2012; Hamling et al. 2017). At least three faults involved in different five earthquakes since 1840 have been recorded in different geological setting with irregular displacements in New Zealand (Nicol et al. 2022) and this supports the multi-fault ruptures in New Zealand is usual. Structural and paleoseismological evidence in the Torlesse fault, Porters Pass fault, North Esk fault shows the possibility of multi-fault ruptures in mid-Canterbury. Walsh (2022) developed a model to quantify the relative likelihood of multi-fault ruptures stemming from an initial 'seed' fault. The method includes a Monte Carlo

simulation of rupture scenarios, based on empirical relationships between bend angles, step distances, and kinematic changes with co-rupture probability of adjacent fault sections.

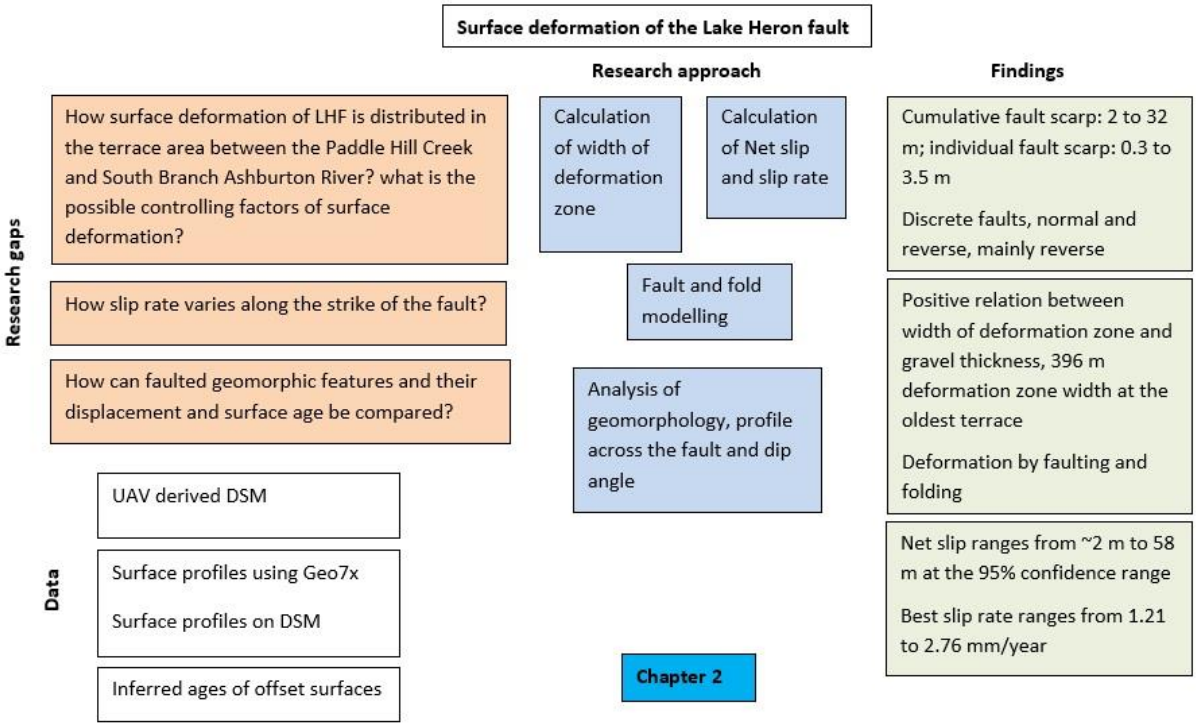

Figure 5-1. Summary of findings related to surface deformation of the Lake Heron fault.

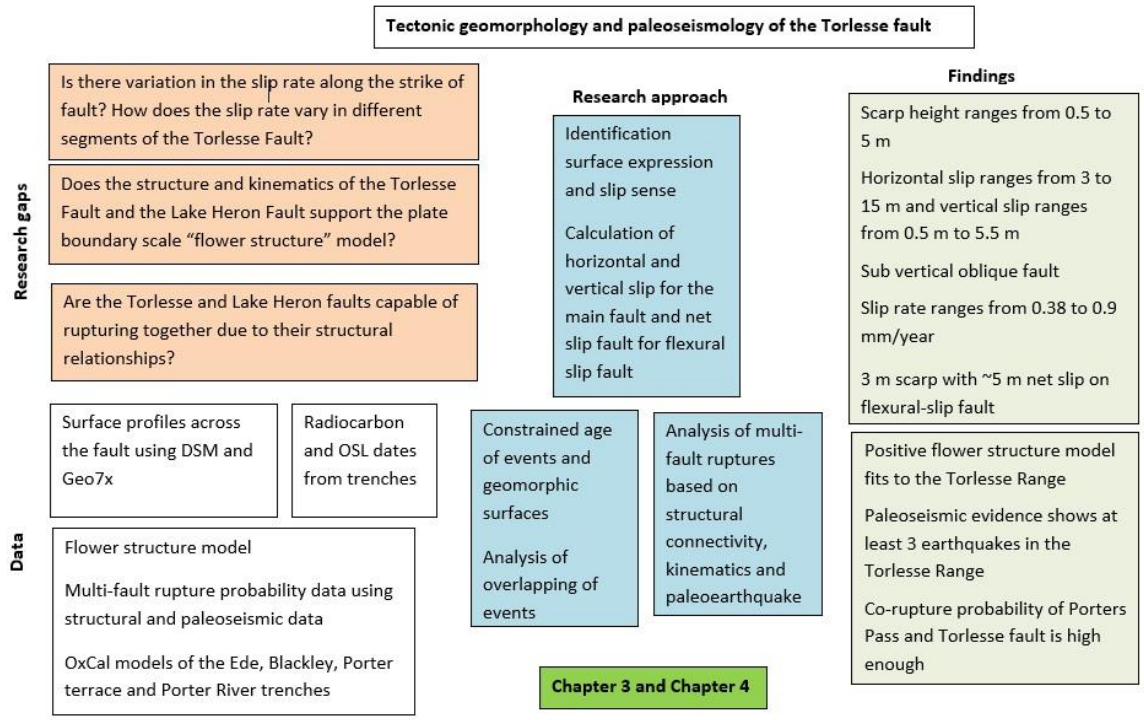

Figure 5-2. Summary of finding related to the tectonic geomorphology and paleoseismology of the Torlesse fault

The same model (Walsh 2022) ran by seeding either of the Torlesse and Porters Pass fault shows a high probability of rupturing both faults (Fig. 5-5). However, rupture on the Lake Heron fault has only a small chance to induce rupture on the Torlesse and Porters Pass faults (Fig. 5-3). This supports my findings of possible multi-fault ruptures from structural connectivity within a "flower structure" and overlapping of paleoseismic events in the Torlesse Range, but ultimately makes ruptures between tectonic domains (between Lake Heron and faults to the North) very unlikely. Histograms showing the length-based magnitudes of multi-fault ruptures in the model are thus higher in the Porters Pass-Torlesse fault area (Fig. 5-4 and 5-6), and generally consistent with estimates from Chapters 3 and 4.

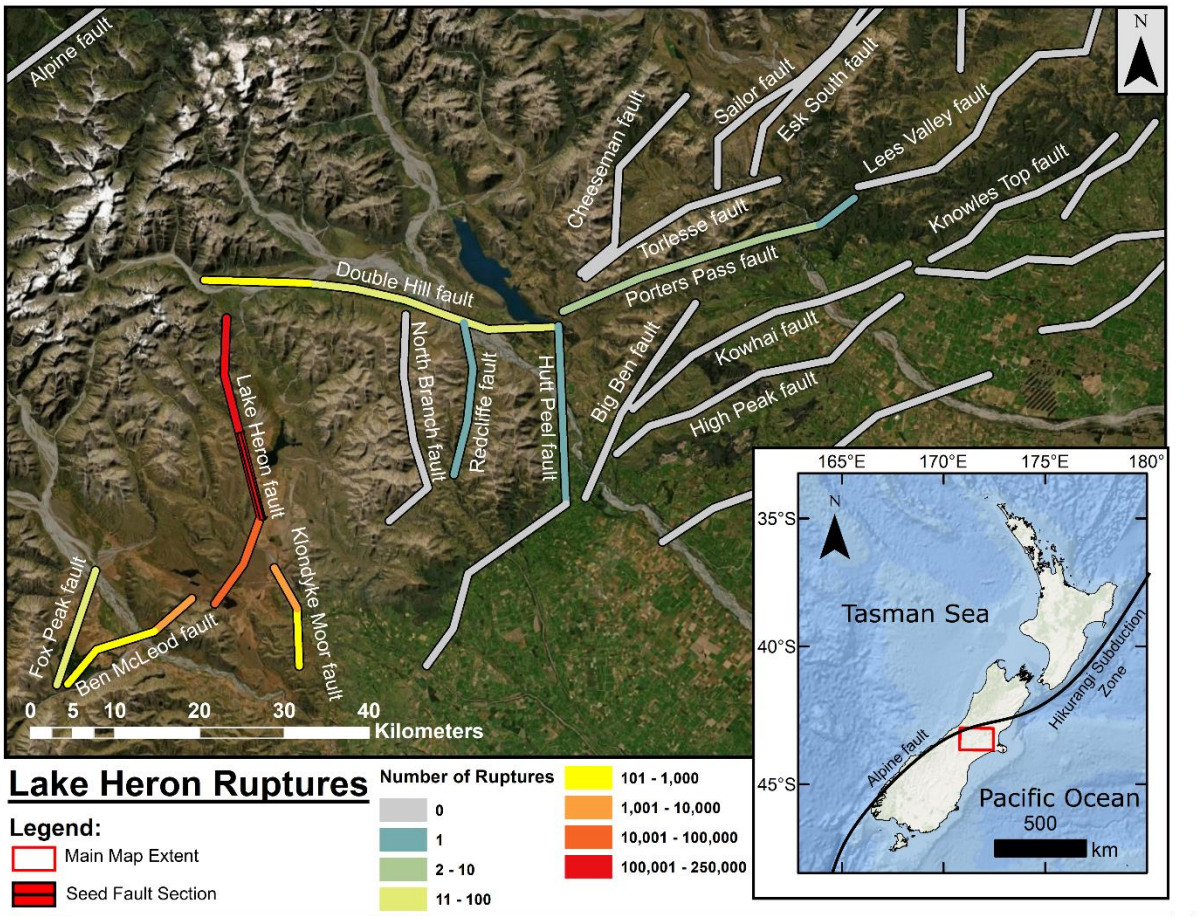

Figure 5-3. Rupture frequency map of mid-Canterbury area. Seed section for the fault is middle part of the Lake Heron fault.

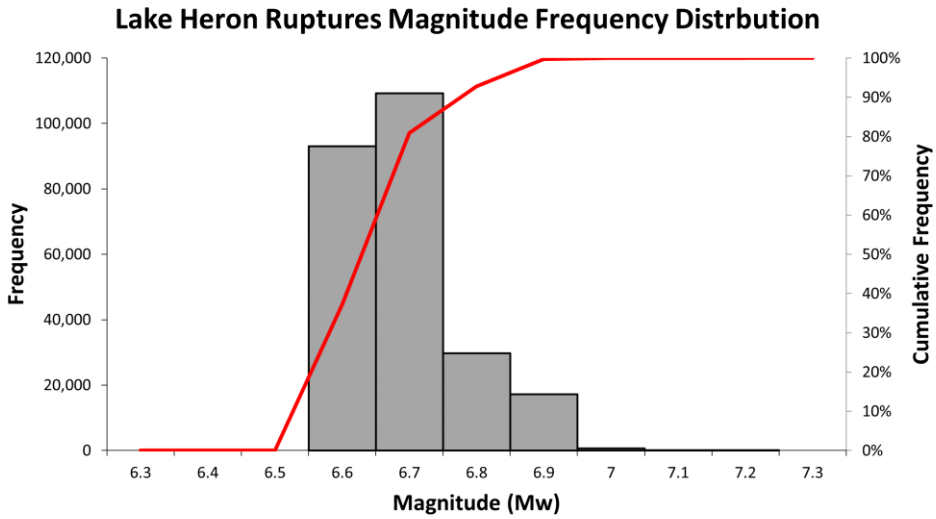

Figure 5-4. Magnitude-frequency distribution for the Lake Heron fault.

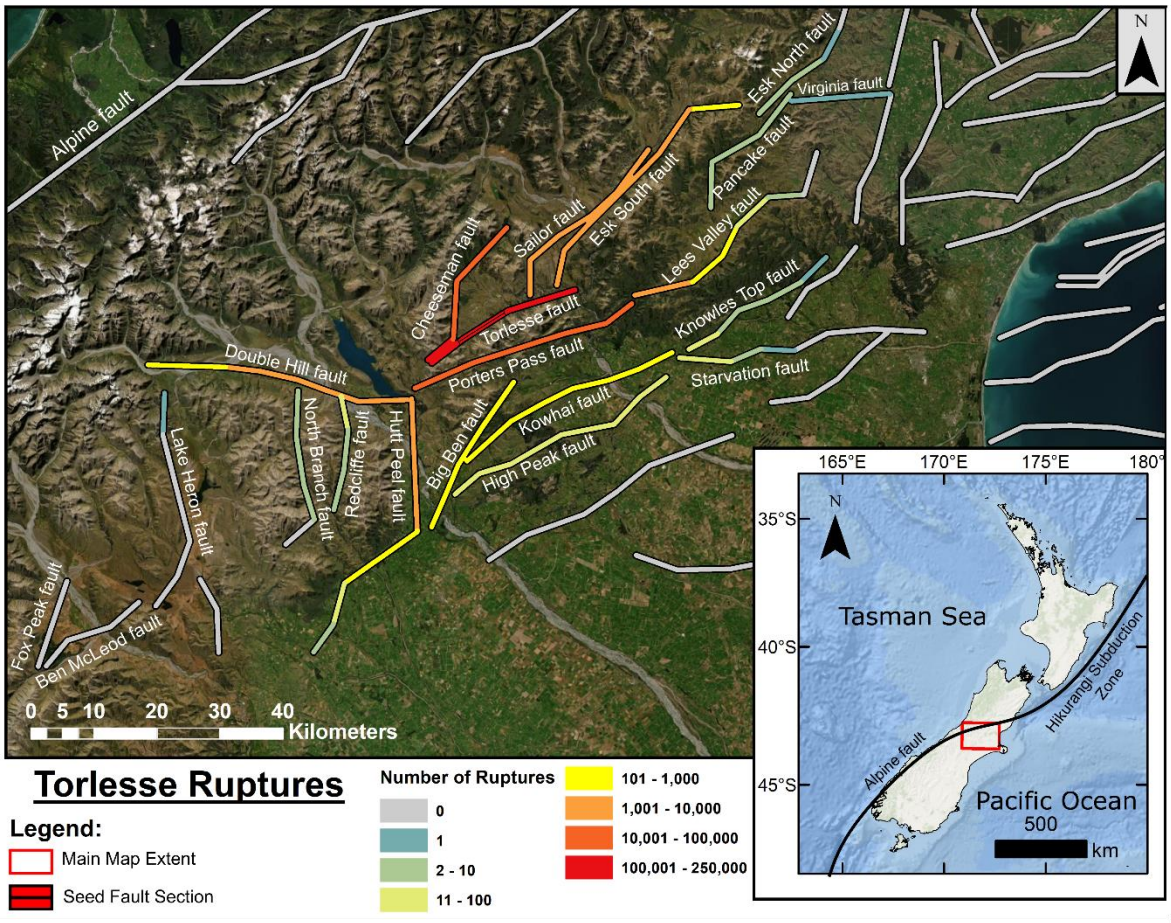

Figure 5-5. Rupture frequency map of mid-Canterbury area. Seed section for the fault is middle part of the Torlesse fault.

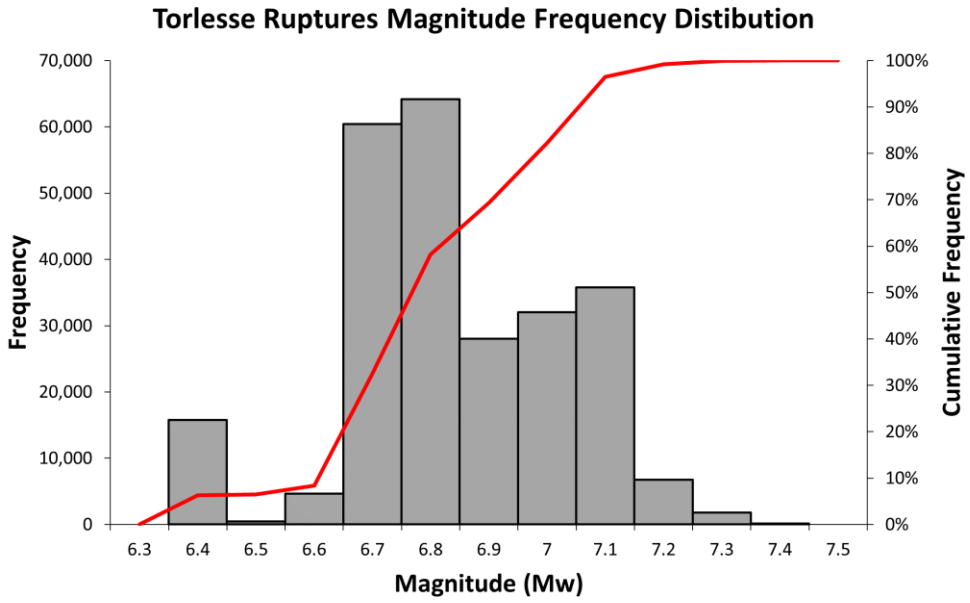

Figure 5-6. Magnitude-frequency map for the Torlesse fault.

5.5 Summary and Future work

Historically, Canterbury has experienced many damaging earthquakes (e.g., Cowan 1992; Howard et al. 2005; Quigley et al. 2012; Hornblow et al. 2014) and is one of the most seismically hazardous regions in New Zealand. This work has improved our knowledge of active faults in mid-Canterbury and ultimately provides useful information for seismic hazard assessments. In future years, New Zealand will have near- or full lidar coverage, and the details of fault surface expression will be further investigated. Future work may focus on using this improved dataset to investigate how faults interact and the variable ways in which deformation gets expressed at the surface, both spatially and temporally. Detailed field studies will still be required to build paleoseismic records and structural models that can explain and refine our knowledge of active faulting in mid-Canterbury.

5.6 References

Brough T 2019. Tectonic geomorphology and paleoseismology of The Humps Fault Zone, North Culverden Basin.

Bushell T 2022. Geometry, kinematics and paleoseismology of the humps and leader faults which ruptured during the 2016 Kaikōura earthquake, North Canterbury, New Zealand. Unpublished thesis, University of Canterbury, Christchurch, New Zealand.

Cowan HA 1992. Structure, seismicity and tectonics of the Porter's Pass-Amberley fault zone, North Canterbury, New Zealand.

Hamling IJ, Hreinsdóttir S, Clark Ket al. 2017. Complex multifault rupture during the 2016 M<inf>w</inf> 7.8 Kaikōura earthquake, New Zealand. Science 356.

Hornblow S, Quigley M, Nicol A, Van Dissen R, Wang N 2014. Paleoseismology of the 2010 Mw 7.1 Darfield (Canterbury) earthquake source, Greendale fault, New Zealand. Tectonophysics 637: 178-190.

Howard M, Nicol A, Campbell J, Pettinga JR 2005. Holocene paleoearthquakes on the strike-slip porters pass fault, Canterbury, New Zealand. New Zealand Journal of Geology and Geophysics 48: 59-74.

Lamb S, Arnold R, Moore JDP 2018. Locking on a megathrust as a cause of distributed faulting and fault-jumping earthquakes. Nature Geoscience 11: 871-875.

Litchfield NJ, Van Dissen R, Sutherland Ret al. 2014. A model of active faulting in New Zealand. New Zealand Journal of Geology and Geophysics 57: 32-56.

Nicol A, Khajavi N, Humphrey J, VanDissen R, Gerstenberger M, Stirling M 2022. Geometries and slip of historical surface-ruptureing earthquakes in New Zealand and their application to seismic hazard analysis. Earthquake Commission, New Zealand. 41 p.

Pettinga JR, Yetton MD, Van Dissen RJ, Downes G 2001. Earthquake source identification and characterisation for the Canterbury region, South Island, New Zealand.

Quigley M, Van Dissen R, Litchfield Net al. 2012. Surface rupture during the 2010 Mw 7.1 darfield(canterbury) earthquake: Implications for fault rupture dynamics and seismic-hazard analysis. Geology 40: 55-58.

Van Dissen R, Seebeck H, Litchfield Net al. 2021. Development of the New Zealand Community Fault Model–version 1.0. 96.

Walsh E 2022. Modelling Complex Multi-fault Ruptures: A 2D Empirical Approach. Unpublished thesis, University of Canterbury, Christchurch, New Zealand. 126 p.